Extending the NV Quantum Sensing Toolbox: All-Optical Nuclear Sensing and Surface Spin NMR

Inauguraldissertation

zur
Erlangung der Würde eines Doktors der Philosophie
vorgelegt der
Philosophisch-Naturwissenschaftlichen Fakultät
der Universität Basel

von

Beat Bürgler

Basel, 2025

Originaldokument gespeichert auf dem Dokumentenserver der Universität Basel
https://edoc.unibas.ch

This work is licensed under a Creative Commons
Attribution-NonCommercial-NoDerivatives 4.0 International License.
The complete text may be reviewed here:
http://creativecommons.org/licenses/by-nc-nd/4.0/

Genehmigt von der Philosophisch-Naturwissenschaftlichen Fakultät
auf Antrag von

Erstbetreuer: Prof. Dr. Patrick Maletinsky
Zweitbetreuer: Prof. Dr. Patrick Potts
Externer Experte: Prof. Dr. Dominik Bucher

Basel, den 15. April 2025

Prof. Dr. Heiko Schuldt
Dekan

Omnipotent, I am the One
Icarus, I'll Touch the Sun

– Lorna Shore –

Abstract

Spin-based quantum sensors have demonstrated significant potential for sensing applications, for instance in fundamental science, medical diagnostics or navigation; where they excel due to their abundance of potential observables and their extraordinary sensitivity at the nanoscale. The nitrogen-vacancy (NV) center in diamond is a particularly promising platform for spin-based quantum sensing, because it hosts a single electron spin with long coherence times even at room temperature, that can be optically initialized and readout. As such, the NV center has received a lot of experimental attention which resulted in a large toolbox of specialized sensing protocols.

In this thesis, we add to the development of the NV sensing toolbox. First, we present a purely optical approach to coherent NV quantum sensing. Our scheme utilizes the NV center's ^{15}N nuclear spin as a sensor, and exploits NV spin dynamics in oblique magnetic fields near the NV's excited state level anti-crossing. We demonstrate all-optical free induction decay measurements – the key protocol for low-frequency quantum sensing – and estimate that for gyroscopy applications, our sensing protocol could achieve sensitivities competitive with the state-of-the-art.

In the second half of this thesis, we turn to the detection of surface spins via NV nuclear magnetic resonance (NMR). We report on an ubiquitous presence of ^{1}H nuclear spins on oxygen terminated diamond surfaces, and based on our experimental results, we speculate that these spins are provided by either surface-bound chemical groups containing hydrogen, or a nanometer thin adsorbate layer of water in a solid-like phase. Then, using these surface spins as an NMR target, we make a technical comparison of NMR with the Spin-Lock sequence and the more established XY8-k protocol, and thereby demonstrate that spin-locking not only solves key issues with XY8-k, such as harmonic frequency contamination of the NMR spectrum and limited spectral resolution, but we also show that Spin-Lock NMR is about 2.5 times more sensitive than XY8-k NMR. Finally, we derive a theoretical description of Spin-Lock NMR with which single NV depth determination can be realized, similar to the XY8-k approach of Pham et al. By fitting these two models to our experimental data, we reveal that both suffer from weaknesses in that they make approximations that are invalid for our experiments. Nonetheless, we attempt to use the models to further characterize the ubiquitous presence of surface protons, and we thereby find the preliminary result that just a collection of hydrogen rich chemically bonded groups is not enough to explain our data, and that a contact layer of solid-like water is likely involved. In conclusion, our results contribute to improving NMR-based NV depth determination, and to a better understanding of water adsorbate layers on diamond.

Contents

Introduction **1**

1 Basics of NV Quantum Sensing **5**
1.1 Electronic Structure of the NV Center 6
1.1.1 Orbital Structure 6
1.1.2 The Effect of a Magnetic Field 7
1.1.3 Hyperfine Structure 10
1.2 Dynamics under Green Illumination 13
1.2.1 Optical Initialization and Readout 14
1.2.2 Nuclear Dynamics at the ESLAC 15
1.3 Spin Control with AC Magnetic Fields 17
1.3.1 Microwave Interaction Hamiltonian 17
1.3.2 Coherent Spin Manipulation 19
1.3.3 Rabi Oscillations 21
1.4 NV Magnetometry Schemes 23
1.4.1 Optically Detected Magnetic Resonance 23
1.4.2 Ramsey Free Induction Decay 26
1.5 Noise Spectroscopy 27
1.5.1 Spin-Lattice Relaxation 29
1.5.2 Ramsey Free Induction Decay (Again) 31
1.5.3 Spin-Echo 33
1.5.4 XY8-k Multipulse Sequence 35
1.5.5 Spin-Locking 37

2 All-Optical Nuclear Quantum Sensing **41**
2.1 Theoretical Description 43
2.1.1 Effective Nuclear Hamiltonian 43
2.1.2 Origin of All-Optically Induced Nuclear Spin Precession 46
2.1.3 Numeric Simulation in Liouvillian Space 48
2.1.4 Comparison of Theoretical Approaches 51
2.2 Analysis of All-Optical Precession Data 53
2.2.1 Frequency of the Observed Nuclear Precession 54
2.2.2 Contrast of the Observed Nuclear Precession 56
2.2.3 Lifetime of the Observed Nuclear Precession 60

2.3 Extension to an NV Ensemble 60
2.4 Sensitivity Estimation 62
2.5 Outlook 64

3 Surface Proton NMR via NV Spin-Locking 65
3.1 Spin-Lock NMR Technique 67
  3.1.1 NMR Data Processing 68
  3.1.2 SNR Optimization 70
  3.1.3 Choice of Magnetic Bias Field 73
3.2 Proton Presence on Bare Diamond 73
  3.2.1 Validation of the Proton Larmor Frequency 74
  3.2.2 NV Statistics 75
  3.2.3 NMR Linewidth Limitation 76
  3.2.4 Temperature Dependence 77
3.3 Deuterium Termination 80
3.4 Towards Water Ice NMR 83
3.5 Outlook 87

4 Comparison of Spin-Lock and XY8 for NMR 89
4.1 Harmonic Frequency Contamination 90
4.2 Sensitivity 93
4.3 Spectral Resolution 95
4.4 Further Technical Differences 97
4.5 Outlook 98

5 Depth Determination via Proton NMR 101
5.1 Theory of Depth Determination 103
  5.1.1 Depth Determination via Spin-Lock NMR 103
  5.1.2 Depth Determination via XY8 NMR 105
5.2 Comparison and Evaluation of the two Models 107
  5.2.1 Evaluation of the Spin-Lock Model 109
  5.2.2 Evaluation of the XY8 Model 111
5.3 Characterization of the Surface Proton Spin Density 113
  5.3.1 Density of the Unidentified Surface Protons 113
  5.3.2 Density of the Deuterium Terminated Surface 120
5.4 Outlook 121

6 Slow Beatings in XY8 Time Traces 124
6.1 Dependency on Detuning and Magnetic Field 125
6.2 Dependency on Experiment Hardware 127
6.3 Outlook 127

Appendix 128
A.1 Home-Built Measurement Setup 128
  A.1.1 The Optical Setup 128
  A.1.2 Goniometric Magnet Stage 130
  A.1.3 Sequence Generation with the SHFSG 131

A.2 Diamond Samples 134
A.2.1 NV Creation and Nanopillar Fabrication 135
A.3 Spin-Lock NMR Depth Determination 140
A.3.1 Hamiltonian Description in the Lab Frame 140
A.3.2 First Rotating Wave Approximation 141
A.3.3 Second Rotating Wave Approximation 145
A.3.4 Plus State Population 146
A.3.5 Spin Bath Noise Statistics 146
A.3.6 Final Result 150
A.4 Redfield Relaxation Theory 152
A.4.1 Derivation of the Redfield Superoperator 152
A.4.2 Derivation of T_1 and T_2^* 155
A.4.3 Derivation of $T_{1\rho}$ 157
A.5 Construction of Transition Superoperators 160
A.6 Magnetic Field Map for All-Optical Precession Data 162
A.7 Optimization of SNR in Immersion Oil NMR 163

Bibliography **180**

Acknowledgements **181**

Curriculum Vitae **183**

Introduction

Quantum physics is an essential part of modern science that evolves around the study of systems on the atomic or even subatomic scale. At such tiny length scales, a multitude of counter-intuitive quantum phenomena such as superposition and entanglement can be observed, and classical physics fundamentally fail to describe them. Only with the formulation of the quantum theory in the 20th century, the properties and behaviour of these quantum systems could be described in a meaningful manner. Nowadays, almost a hundred years later, the investigation of these quantum systems and their properties has grown to a highly active and wide-spread field of research. Most importantly, the accumulated knowledge from decades of quantum research has paved the way to substantial technological advances; in particular in computing, communication and sensing.

In quantum computing [1], quantum properties are harnessed to build information processing platforms that promise to exceed the capabilities of classical computers. Quantum communication [2] makes use of the entanglement between spatially separated quantum systems to provide secure exchange of information that is protected from eavesdropping. Finally, in quantum sensing [3] – the field that this thesis is all about – quantum systems are employed as a sensor to measure physical quantities at the nanometer scale. Contrary to other quantum technologies where the quantum systems' extraordinary sensitivity to external disturbances is a central weakness, it is this high sensitivity that is exploited in quantum sensing techniques. As a result, state-of-the-art quantum sensors surpass the qualities of classical sensing approaches in terms of not only spatial resolution, but also sensitivity.

Quantum sensors can be realized in many different ways. Among these different physical implementations there are for example photonic systems that use squeezed states of light for the detection of signals below the standard quantum limit, for instance in gravitational wave detectors [4]. Other examples include superconducting devices that utilize quantized electric charge or flux in Josephson junctions to measure weak electromagnetic fields [5]; motional states of trapped ions sensitive to force and displacement [6]; or phonons in optomechanical devices that can detect mass [7] and acceleration [8]. Last but not least, there is a large group of quantum sensors that make use of the spin associated with quantum objects such as atoms, nuclei or electrons. It has successfully been demonstrated that these spin-based quantum sensors can be used to measure a wide range of relevant physical quantities, such as magnetic [9] or electric fields [10], frequency [11], temperature [12], pressure [13], mechanical stress [14], or rotary motion [15]. This abundance of potential observables, combined with their high sensitivity at the nanoscale, makes spin-based quantum sensors highly interesting for many fields of application, such as life sciences [16], geological sciences [17], material sciences [18] and navigation [19].

The nitrogen-vacancy (NV) center in diamond [20] is a particularly suitable platform for spin-based quantum sensing applications, due to the excellent properties it provides: First, it hosts a single electron spin with exceptionally long coherence times [21, 22] even at room temperature [23], which boosts the sensitivity compared to shorter lived spin systems [3]. Second, the NV electronic spin can be optically accessed with visible light. Upon such illumination, the NV spin is pumped into a specific eigenstate, enabling all-optical spin initialization [24, 25]. At the same time, the defect emits a spin-dependent amount of red photoluminescence, allowing for robust optical spin readout [26]. Such initialization and readout of the spin state is a key prerequisite for sensing, and the fact that the NV provides the means to do this in a robust, reliable and room temperature compatible fashion drastically facilitates sensing applications. Third, the NV center is located in the crystal lattice of diamond, a highly robust material that can not only be nanofabricated into experimentally advantageous nanostructures; but that also ensures the electric stability of the NV defect even in tiny nanodiamonds. For example, the fabrication of NV scanning probes has enabled magnetic field imaging with 25 nm resolution [27], and nanodiamonds have successfully been deployed for in-vivo thermometry in living organisms [28]. Finally, the NV center provides not only an electronic spin, but also a nuclear spin associated with the defect's nitrogen atom. This nuclear spin is coupled to the electron spin, and can thus be indirectly accessed optically for facile initialization [29] and readout [30]. Importantly, due to its much smaller gyromagnetic ratio, this nuclear spin exhibits significantly longer coherence times compared to the NV electron spin [31, 32], and therefore it offers another interesting resource for quantum technology applications, particularly in magnetometry [32, 33] and gyroscopy [34, 35].

Because of all these fantastic properties, the NV center has received a lot of attention in recent years, which has resulted in the development of a large toolbox of specialized and sophisticated sensing protocols, utilizing either or both of the spins in the NV center. In particular, by deploying AC magnetic fields for coherent spin control, dynamical decoupling pulse sequences have successfully been introduced to NV-based sensing [36, 37]. These sequences are comprised of a series of microwave pulses that manipulate the NV electron spin in a way that alters its response to the environment, effectively acting like a noise filter [38]. This way it is possible to decouple the spin from specific noise sources to further boost the spin coherence time and thereby increase the sensitivity in sensing applications [39, 40]. Alternatively, pulsed dynamical decoupling can maximize the NV spin's sensitivity to a target AC signal, enabling frequency selective spectroscopy of the nearby environment [41, 42], and in particular nuclear magnetic resonance (NMR) measurements [43–45]. Such NV NMR is especially interesting for the characterization of the diamond surface [45–47]; and its ability to image individual molecules [48, 49] or even single spins [50] sees opportunities in chemistry, biology and the medical sciences. Moreover, one already widely employed use case of NV NMR is the determination of an individual NV center's depth in the diamond crystal via NMR of immersion oil on the diamond surface, as proposed by Pham et al. [51]. Such depth determination via surface NMR is one focus of this thesis.

Apart from various microwave spin manipulation sequences, the NV sensing toolbox has also been equipped with meaningful advances in other aspects of the experimental routine. For example, the available diamond nanofabrication techniques are continuously pushed forward, resulting in more intricate and sensitive devices [52]. Specifically, there is significant progress in the chemical engineering of the diamond surface to reduce surface-induced noise and simultaneously facilitate the deposition of NMR targets on the diamond surface [53]. In addition, there are advances towards enhanced spin readout techniques that are based on either the NV's nitrogen nuclear spin [48, 54], or on spin-to-charge conversion [55–57]. Finally, while most sensing protocols are designed for single NVs, it is possible to extend them to entire ensembles of NVs [9, 15]. This drastically increases the optical signal and thus the sensitivity, however it comes at the cost of massively reduced spacial resolution and – for very dense NV ensembles – shorter spin coherence times [58].

In this thesis, we add to the development of the NV sensing toolbox by introducing a purely optical, coherent NV sensing protocol; and by contributing new insights in NV NMR, specifically for NV depth determination via surface proton NMR.
First, in chapter 1, we give an extensive introduction to the basics of NV quantum sensing. Then, in chapter 2, we present a novel all-optical nuclear spin-based sensing scheme that does not require any AC magnetic fields. This scheme utilizes the NV center's ^{15}N spin as a sensor, and exploits NV spin dynamics in small transverse magnetic fields near the NV's excited state level anti-crossing. Without the need for microwave or radio-frequency radiation, our scheme lends itself to integration in portable devices, or for studying samples that are adversely affected by said radiation. We estimate that for gyroscopy applications, our scheme could achieve sensitivities competitive with the state-of-the-art.
Afterwards, we turn to NMR measurements. In chapter 3, we report on an ubiquitous presence of ^{1}H nuclear spins on oxygen terminated diamond surfaces. We attempt to characterize the origin of these spins, and based on our experimental results, we speculate that these spins are provided by either chemical groups containing hydrogen that are bonded to the diamond surface; or a nanometer thin adsorbate layer of water in a solid-like phase. Raising awareness of this proton presence is important, because negligence of these surface spins can be detrimental in applications that rely on ^{1}H NMR measurements, such as for example quantitative depth determination as proposed by Pham et al. [51]. Moreover, a proper characterization of these surface proton spins would pave the way to depth determination via NMR using only these spins, thus omitting the need for coating the diamond with hydrogen-rich substances. This would be especially advantageous in applications that rely on fragile diamond structures from which these substances cannot easily be removed, such as for example in scanning NV magnetometry [27].
Next, in chapter 4, we make a technical comparison of NMR with the Spin-Lock sequence and the more established XY8-k protocol. We demonstrate that spin-locking not only solves major issues with XY8-k, such as harmonic ^{13}C contamination of the NMR spectrum and limited frequency resolution, but we also show that Spin-Lock NMR is up to 2.5 times more sensitive than XY8-k NMR. These results suggest that for any NV sensing application that is based on measuring the NMR signal of a single nuclear species in a quantitative fashion, such as NV depth determination or

surface noise spectroscopy, spin-locking is a better choice than the XY8-k sequence, especially when measuring with ^{13}C-rich diamond samples and at high magnetic bias fields exceeding 400 G.

Finally, in chapter 5, we derive a detailed theoretical description of Spin-Lock NMR with which we can fit the NV depth and the NMR target's spin density, similar to the XY8-k NMR model of Pham et al. [51]. By carefully comparing these models to each other and fitting them to our experimental data, we reveal that both of them suffer from weaknesses in that they make approximations that are invalid for our experiments. Qualitatively accurate depth determination with either model is therefore not possible until these weaknesses are addressed. This is a critical finding, as there are many people who are already using the XY8-k model for NV depth determination [59–69]. Finally, despite these weaknesses, we attempt to use both NMR models to further characterize the ubiquitous presence of surface protons, and we thereby find the preliminary result that a collection of hydrogen rich chemically bonded groups alone is not enough to explain our data, and that a contact layer of solid-like water is very likely involved. Our results contribute towards achieving quantitatively accurate single NV depth determination, and to a better understanding of water adsorbate layers on oxygen-terminated diamond.

CHAPTER 1

Basics of NV Quantum Sensing

The nitrogen-vacancy (NV) center [20] is a paramagnetic defect in the carbon lattice of diamond. It consists of a substitutional nitrogen atom adjacent to a lattice vacancy, as illustrated in Figure 1.1. The four lattice sites neighbouring this vacancy, namely three carbon atoms and that one nitrogen atom, form a tetrahedral structure with a rotational symmetry axis along the (111) crystal direction, mathematically described by the C_{3v} symmetry group.

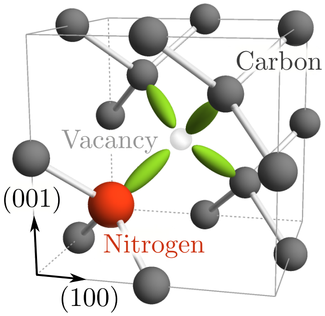

Figure 1.1: Crystal structure of the NV center. Diamond is a face-centered cubic lattice with two carbon atoms (grey) per primitive unit cell. The NV consists of a substitutional nitrogen atom (red) neighbouring a lattice vacancy (transparent) with four dangling electron bonds (green). This tetrahedral structure exhibits a C_{3v} symmetry along the axis connecting the nitrogen and vacancy, in this case the (111) crystal axis.

There are five electrons associated with the NV center that are contributed by the four dangling bonds surrounding the vacancy. To be specific, each carbon atom contributes one electron, and the nitrogen atom contributes two of them. This particular configuration is charge-neutral and denoted as NV^0. An additional sixth electron from other dopants or nearby impurities in the lattice can be trapped in the NV defect, leading to the formation of the negatively charged state, NV^-. As we will discuss in this chapter, this negatively charged state offers highly attractive quantum properties, that make it ideal for spin-based quantum sensing applications [3,20]. For this reason, we work exclusively with NV^- defects in this thesis, and for simplicity, we will refer to the NV^- charge state simply as NV hereafter.

The negatively charged NV center has a well understood electronic structure, with orbital degrees of freedom that can experimentally be addressed by laser radiation; and with spin degrees of freedom whose transitions can be accessed with microwave magnetic fields. Together, these tools offer all the experimental prerequisites to perform dynamical decoupling based quantum sensing with the NV spin as quantum sensor. In this first chapter, we introduce and discuss the theoretical foundations for such sensing with the NV center. We start with presenting the electronic structure of the NV center in section 1.1. Then, we discuss the dynamics of the system under green laser illumination in section 1.2, where we investigate how to use laser light to initialize and readout the spin state all-optically. Afterwards, we have a detailed look at coherent spin manipulation with microwave fields in section 1.3, where we discuss how to employ such AC fields to control the spin in order to perform quantum sensing experiments. Finally, we introduce all the relevant magnetometry and noise spectroscopy protocols in sections 1.4 and 1.5 respectively.

1.1 Electronic Structure of the NV Center

The electronic structure of the NV center consists of both orbital and spin degrees of freedom, and is affected by a wide range of external perturbations, such as magnetic or electric fields, microwave radiation or spins in the environment, to name a few. In this section we will derive this electronic structure by discussing all involved interactions, in order of their magnitude. We start with the structure that emerges from the orbital degrees of freedom of the six electrons in the NV, leading to orbital states split by hundreds of THz. Since the electrons carry a spin, these orbital states have an internal electronic spin structure with energy splittings of a few GHz. Next, we consider external magnetic fields that strongly affect these spin states, giving rise to energy shifts on the order of a few MHz to GHz. Finally, there is an interaction of the electronic spin with the nuclear spin of the NV center's nitrogen atom, resulting in a hyperfine structure with energies of only a few kHz to MHz.

1.1.1 Orbital Structure

The available orbital states of the NV center can be calculated via symmetry considerations exploiting the defect's C_{3v} rotation symmetry [70], or by *ab initio* theory [71, 72]. The six NV electrons occupy the resulting states in a way such that only two electrons remain unpaired. By minimization of the Coulomb interaction between these two electrons, one finds the electronic ground state to be an orbital singlet spin triplet state ($^3A_2$). In addition, there is an an excited state, an orbital doublet spin triplet state (^3E). At room temperature, the orbital degrees of freedom of this excited state are mixed by spin-conserving electron-phonon interactions, leading to the averaging to an effective orbital singlet spin triplet state [73]. As shown in Figure 1.2 (A), the ground state and excited state are split by 1.945 eV [74], and they can be coupled via an optical electric dipole transition. Experimentally, this optical transition can be accessed resonantly with visible light with a wavelength of 637 nm, or non-resonantly with wavelengths between 500 nm and 637 nm. We will discuss the dynamics of the NV system under such illumination in detail in section 1.2.
In addition, there are two spin singlet states ($^1E_{1,2}$ and $^1A_1$) located energetically between ground and excited states, as illustrated in Figure 1.2 (A), with an energy splitting in the infrared of 1.18 eV [75]. Since all four of the orbital states are located deep within the roughly 5.5 eV wide bandgap of the diamond lattice, the negatively

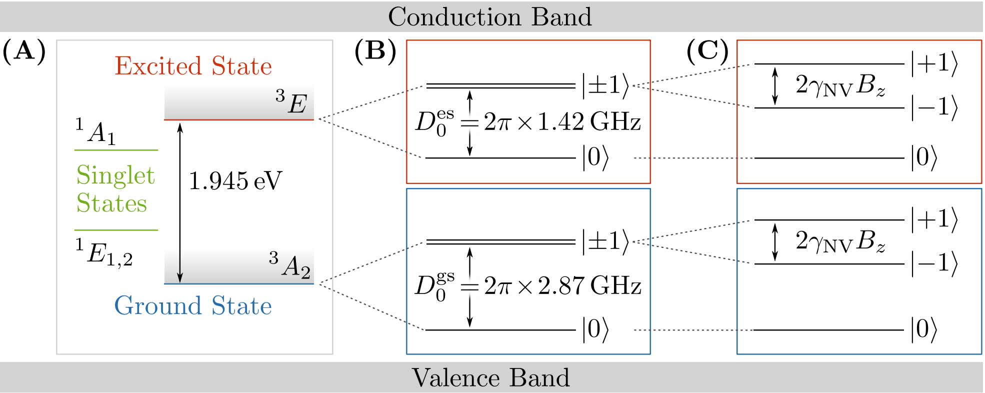
Conduction Band
(A)
Excited State
^3E
$^1A_1$
Singlet States
$^1E_{1,2}$
1.945 eV
$^3A_2$
Ground State
(B)
$|\pm1\rangle$
$D_0^{\text{es}} = 2\pi \times 1.42\,\text{GHz}$
$|0\rangle$
$|\pm1\rangle$
$D_0^{\text{gs}} = 2\pi \times 2.87\,\text{GHz}$
$|0\rangle$
(C)
$|+1\rangle$
$2\gamma_{\text{NV}} B_z$
$|-1\rangle$
$|0\rangle$
$|+1\rangle$
$2\gamma_{\text{NV}} B_z$
$|-1\rangle$
$|0\rangle$
Valence Band

Figure 1.2: Orbital and fine structure of the NV center in diamond at room temperature, illustrated not quite to scale. **(A)** Four orbital states are located deep within the diamond bandgap; two spin singlets, $^1E_{1,2}$ and $^1A_1$ (green), and two spin triplets, $^3A_2$ and ^3E, which are identified as ground state (blue) and excited state (red). **(B)** Each of the two spin triplets has an internal spin fine structure due to spin-spin interaction, leading to a zero-field splitting denoted by $D_0^{\text{gs,es}}$. **(C)** By applying an external magnetic field along the NV symmetry axis, $\boldsymbol{B}_{\text{ext}} = (0, 0, B_z)$, the longitudinal Zeeman effect lifts the degeneracy of the $|\pm1\rangle$ states.

charged state NV$^-$ is stable even at room temperature [76], where $k_B T \approx 25\,\text{meV}$. In addition, due to low spin-orbit coupling in the ground state [20] and the high Debye temperature of diamond [77], the NV center features excellent spin coherence times, even at ambient conditions. For these reasons, it is a great platform for room temperature spin physics.

Both the ground and excited state are spin triplets, where the two unpaired electrons form a total electronic spin $S = 1$. These triplets exhibit an internal fine structure that is best described in the eigenbasis $|\{m_S\}\rangle$ of the spin projection operator $\hat{S}_z$ onto the NV center's symmetry axis $\boldsymbol{e}_z$, where $m_S \in \{0, \pm1\}$ are the three $\hat{S}_z$ eigenvalues. Due to spin-spin interactions, the state $|0\rangle$ is split in energy from $|\pm1\rangle$ by a zero-field splitting of $D_{\text{gs}} = 2\pi \times 2.87\,\text{GHz}$ [20, 78] in the ground state, and $D_0^{\text{es}} = 2\pi \times 1.42\,\text{GHz}$ [79] in the excited state respectively, as shown in Figure 1.2 (B).

1.1.2 The Effect of a Magnetic Field

External magnetic fields interact with the NV center by coupling to the permanent magnetic moment of the electron spin. This fundamental interaction is called the Zeeman effect. Mathematically, the effective, room temperature spin Hamiltonian for the ground (gs) and excited (es) state triplets in the presence of a magnetic field is

$$\hat{\mathcal{H}}^{\text{gs,es}}/\hbar = D_0^{\text{gs,es}}\,\hat{S}_z^2 + \gamma_{\text{NV}} \boldsymbol{B}_{\text{ext}} \cdot \hat{\boldsymbol{S}}\,, \tag{1.1}$$

where the first term describes the zero-field splitting based on spin-spin interactions, while the second term describes the electronic Zeeman effect. Here, $\gamma_{\text{NV}} = 2\pi \times g_e \mu_B \approx 2\pi \times 2.80\,\text{MHz/G}$ is the gyromagnetic ratio of the NV center's electron spin, and $D_0^{\text{gs,es}}$

is the zero-field splitting as introduced in the previous section. Furthermore, the vector $\boldsymbol{B}_{\text{ext}} = (B_x, B_y, B_z)$ is the applied external magnetic field in the NV's coordinate system where the unit vector $\boldsymbol{e}_z$ lies along the NV's symmetry axis. Therefore, B_z is the longitudinal on-axis magnetic field component, and B_x and B_y are the transverse components perpendicular to the NV axis. The dimensionless spin operators $\hat{\boldsymbol{S}} = (\hat{S}_x, \hat{S}_y, \hat{S}_z)$ for the electron spin ($S = 1$) are given with respect to the same NV coordinate system, and in the basis $\{|{+1}\rangle, |0\rangle, |{-1}\rangle\}$ they are represented by the following three dimensional matrices,

$$\hat{S}_x = \frac{1}{\sqrt{2}} \begin{pmatrix} 0 & 1 & 0 \\ 1 & 0 & 1 \\ 0 & 1 & 0 \end{pmatrix}, \ \hat{S}_y = \frac{i}{\sqrt{2}} \begin{pmatrix} 0 & -1 & 0 \\ 1 & 0 & -1 \\ 0 & 1 & 0 \end{pmatrix}, \ \hat{S}_z = \begin{pmatrix} 1 & 0 & 0 \\ 0 & 0 & 0 \\ 0 & 0 & -1 \end{pmatrix}. \tag{1.2}$$

To better differentiate between the longitudinal Zeeman effect based on B_z and the transverse Zeeman effect due to B_x and B_y, equation (1.1) can be rewritten as

$$\hat{\mathcal{H}}^{\text{gs,es}}/\hbar = D_0^{\text{gs,es}}\, \hat{S}_z^2 + \gamma_{\text{NV}} B_z \hat{S}_z + \frac{\gamma_{\text{NV}}}{\sqrt{2}} \begin{pmatrix} 0 & B_\perp e^{-i\phi} & 0 \\ B_\perp e^{+i\phi} & 0 & B_\perp e^{-i\phi} \\ 0 & B_\perp e^{+i\phi} & 0 \end{pmatrix}, \tag{1.3}$$

where $B_\perp = (B_x^2 + B_y^2)^{1/2}$ is the absolute value of total transverse external magnetic field, and $\phi = \tan^{-1}(B_y/B_x)$ is its azimuthal angle in the plane spanned by the unit vectors $\boldsymbol{e}_x$ and $\boldsymbol{e}_y$. In this form of the Hamiltonian, the second term describes the longitudinal Zeeman effect, and the third term describes the transverse Zeeman effect. These two terms have a very different effects on the eigenstates of $\hat{\mathcal{H}}^{\text{gs,es}}$. In the following, we discuss these terms separately.

Longitudinal Magnetic Fields

Applying a magnetic field $\boldsymbol{B}_{\text{ext}} = (0, 0, B_z)$ that is perfectly aligned with the NV center's symmetry axis splits up the $m_S = \pm 1$ eigenstates by the longitudinal Zeeman splitting $\Delta E = 2\gamma_{\text{NV}} B_z$, effectively lifting the degeneracy of the $|\pm 1\rangle$ doublet, as illustrated in Figures 1.2 (C) and 1.3 (A). Notably, for such a perfectly aligned magnetic field the last term of equation (1.3) disappears, such that $\hat{\mathcal{H}}^{\text{gs,es}}$ commutes with $\hat{S}_z$, meaning that $|\{m_S\}\rangle$ remains a good eigenbasis for the system.

The longitudinal Zeeman effect has two key experimental advantages: First, it opens direct pathways to spin-based magnetometry by measuring the splitting between the states $|\pm 1\rangle$. This can be done spectroscopically with a laser, a technique we will discuss in detail in section 1.4.1. Second, by controlling the strength of the aligned magnetic field, one can isolate $|0\rangle$ and $|{-1}\rangle$ into an effective two-level quantum system with an arbitrary energy splitting. This is something which we will do throughout this thesis, particularly in chapters 3 to 6 where we require two isolated spin quantum states split by a few MHz to GHz.

For certain specific axial magnetic field values, level anti-crossings occur. In the excited state, the states $|{-1}\rangle$ and $|0\rangle$ cross at $B_z = D_0^{\text{es}}/\gamma_{\text{NV}} \approx 507\,\text{G}$ at what is called the excited state level anti-crossing (ESLAC). In the ground state, these states are degenerate in energy at $B_z = D_0^{\text{gs}}/\gamma_{\text{NV}} \approx 1025\,\text{G}$, at the ground state level anti-crossing (GSLAC). These anti-crossings are highlighted in Figure 1.3 (A). Note that the same physics take place for negative magnetic fields, however in this case $|0\rangle$ is crossing with $|{+1}\rangle$ instead. In this thesis, we always work with positive magnetic fields, and therefore we do not consider this case hereafter.

Transverse Magnetic Fields

Opposite to the longitudinal Zeeman effect, which conserves the $|\{m_S\}\rangle$ eigenbasis, the transverse Zeeman effect can couple the $|m_S\rangle$ states and thereby mix them into new eigenstates $|\Psi_k\rangle$. Importantly, two states are only significantly mixed if they are near-degenerate, that is if they are split in energy by less than $\hbar\gamma_{\mathrm{NV}}B_\perp$. Otherwise, the transverse Zeeman effect is suppressed by the large energy splitting. As shown in Figure 1.3 (A), this means that mixing due to small transverse magnetic fields is only relevant in the proximity of three particular values of B_z: At zero field (I+II), at the ESLAC (III), and at the GSLAC (IV).
The degree of state mixing at these three three points is shown in Figure 1.3 (B), where the expectation value of the spin quantum projection number m_S of the eigenstates $|\Psi_k\rangle$ is plotted as a function of $B_\perp$. It is clear from the plot that at the three degeneracy points, near-degenerate states are mixed by $B_\perp$, which leads to the loss of a well-defined m_S quantum number; while for states that are well separated in energy, no appreciable mixing is taking place for $B_\perp < 50\,\mathrm{G}$, as indicated by the conservation of m_S. Importantly, note how just a few Gauss of transverse field are sufficient to fully mix two states at any of the B_z values I-IV, highlighting how very sensitive the system is to transverse magnetic fields. In our experiments, we benefit greatly from this high sensitivity when we utilize the mixing of $|0\rangle$ and $|{-1}\rangle$ at the ESLAC to

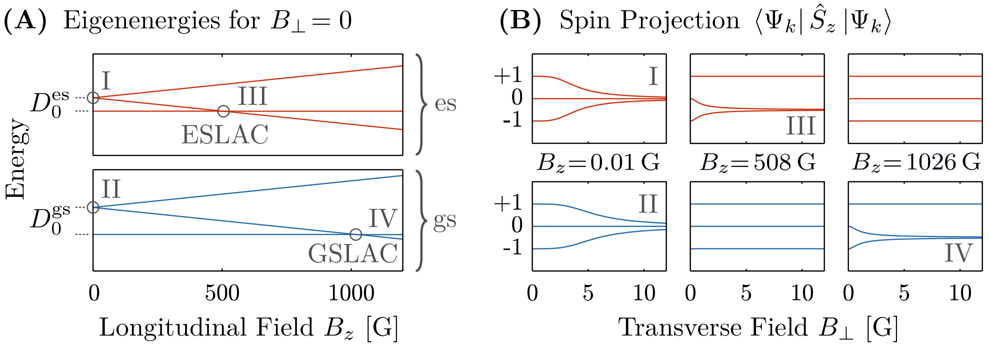

Figure 1.3: Diagonalization of the magnetic field dependent Hamiltonian $\hat{\mathcal{H}}^{\mathrm{gs,es}}$ yields the eigenstates $|\Psi_k\rangle$. **(A)** For $B_\perp = 0$, these eigenstates $|\Psi_k\rangle$ are just the $\hat{S}_z$ eigenstates $|m_S\rangle$. Here, we plot their eigenenergies as a function of B_z, demonstrating the linear nature of the longitudinal Zeeman effect. Importantly, there are only three points (grey circles) where two states are degenerate: At zero field (I+II), at the ESLAC (III), and the GSLAC (IV). **(B)** The expectation value of the spin quantum number m_S for the states $|\Psi_k\rangle$ as a function of $B_\perp$ for values of B_z close to the degeneracy points (I-IV). States that are near degenerate for the given B_z are mixed, leading to a loss of a well defined quantum number m_S, demonstrating the mixture of $|\{m_S\}\rangle$ into a new eigenbasis.

align the magnetic field with the NV axis by minimizing the degree of mixing. This technique is discussed at the end of section 1.2.1.

1.1.3 Hyperfine Structure

In addition to the fine structure and interaction with external magnetic fields, ground and excited state exhibit a hyperfine structure based on the interaction of the electron spin with the NV center's intrinsic nitrogen nuclear spin, as well as ^{13}C spins in the lattice. Here, we focus on just the nitrogen hyperfine interaction.
Nitrogen occurs in two different stable isotopes with different nuclear spins: either ^{15}N with $I = 1/2$, or ^{14}N with spin $J = 1$. Depending on which of these isotopes form the NV defect, two different hyperfine structures emerge. For ^{15}N, the spin Hamiltonian of ground (gs) and excited (es) spin triplet state reads

$$\begin{aligned}\hat{\mathcal{H}}^{\mathrm{gs,es}}_{\mathrm{N15}}/\hbar &= D_0^{\mathrm{gs,es}}\,\hat{S}_z^2 + \gamma_{\mathrm{NV}}\boldsymbol{B}_{\mathrm{ext}}\cdot\hat{\boldsymbol{S}} + \gamma_{\mathrm{N15}}\boldsymbol{B}_{\mathrm{ext}}\cdot\hat{\boldsymbol{I}}\\ &\quad + A_{\parallel}^{\mathrm{gs,es}}\,\hat{S}_z\hat{I}_z + A_{\perp}^{\mathrm{gs,es}}\left(\hat{S}_x\hat{I}_x + \hat{S}_y\hat{I}_y\right). \end{aligned} \tag{1.4}$$

On the other hand, for an NV formed by ^{14}N, due to its nuclear spin $J = 1$ larger than 1/2, there is a non-zero quadrupolar moment, leading to an additional term in the Hamiltonian:

$$\begin{aligned}\hat{\mathcal{H}}^{\mathrm{gs,es}}_{\mathrm{N14}}/\hbar &= D_0^{\mathrm{gs,es}}\,\hat{S}_z^2 + \gamma_{\mathrm{NV}}\boldsymbol{B}_{\mathrm{ext}}\cdot\hat{\boldsymbol{S}} + \gamma_{\mathrm{N14}}\boldsymbol{B}_{\mathrm{ext}}\cdot\hat{\boldsymbol{J}}\\ &\quad + A_{\parallel}^{\mathrm{gs,es}}\,\hat{S}_z\hat{J}_z + A_{\perp}^{\mathrm{gs,es}}\left(\hat{S}_x\hat{J}_x + \hat{S}_y\hat{J}_y\right) + Q\,\hat{J}_z^2\,, \end{aligned} \tag{1.5}$$

In this Hamiltonian, the first two terms are the same as in equation (1.1). The third term describes the nuclear Zeeman effect, imposing the same physics on the nuclear nitrogen spin as previously discussed for the electron spin in section 1.1.2. The fourth and fifth term describe the axial and transverse hyperfine interaction, that couples $\hat{\boldsymbol{S}}$ to the respective nuclear spin $\hat{\boldsymbol{I}}$ or $\hat{\boldsymbol{J}}$. Finally, the sixth term is the aforementioned interaction of the electron spin with the quadrupolar moment of the ^{14}N nuclear spin.
The hyperfine parameters coefficients for these Hamiltonians are shown in table 1.1. Particularly, note that these parameters have opposite signs for the two different nitrogen isotopes, because these isotopes have different signs in their gyromagnetic ratios [80]. Furthermore, the nuclear electric quadrupolar parameter of ^{14}N NVs is $Q = 2\pi \times (-4.945)\,\mathrm{MHz}$ [31, 81]. The dimensionless spin operators $\hat{\boldsymbol{J}} = (\hat{J}_x, \hat{J}_y, \hat{J}_z)$ for the ^{14}N spin ($J = 1$) in the $\{|{+1}\rangle, |0\rangle, |{-1}\rangle\}$ basis are represented by the same three dimensional Pauli matrices as previously defined for the electron spin,

$$\hat{J}_x = \frac{1}{\sqrt{2}}\begin{pmatrix}0&1&0\\1&0&1\\0&1&0\end{pmatrix},\quad \hat{J}_y = \frac{i}{\sqrt{2}}\begin{pmatrix}0&-1&0\\1&0&-1\\0&1&0\end{pmatrix},\quad \hat{J}_z = \begin{pmatrix}1&0&0\\0&0&0\\0&0&-1\end{pmatrix}, \tag{1.6}$$

Similarly, the spin operators for the ^{15}N ($I = 1/2$) nuclear spin operators $\hat{\boldsymbol{I}} = (\hat{I}_x, \hat{I}_y, \hat{I}_z)$ in the $\{|{+1/2}\rangle, |{-1/2}\rangle\}$ basis are the two dimensional Pauli matrices,

$$\hat{I}_x = \frac{1}{2}\begin{pmatrix}0&1\\1&0\end{pmatrix},\quad \hat{I}_y = \frac{1}{2i}\begin{pmatrix}0&1\\-1&0\end{pmatrix},\quad \hat{I}_z = \frac{1}{2}\begin{pmatrix}1&0\\0&-1\end{pmatrix}. \tag{1.7}$$

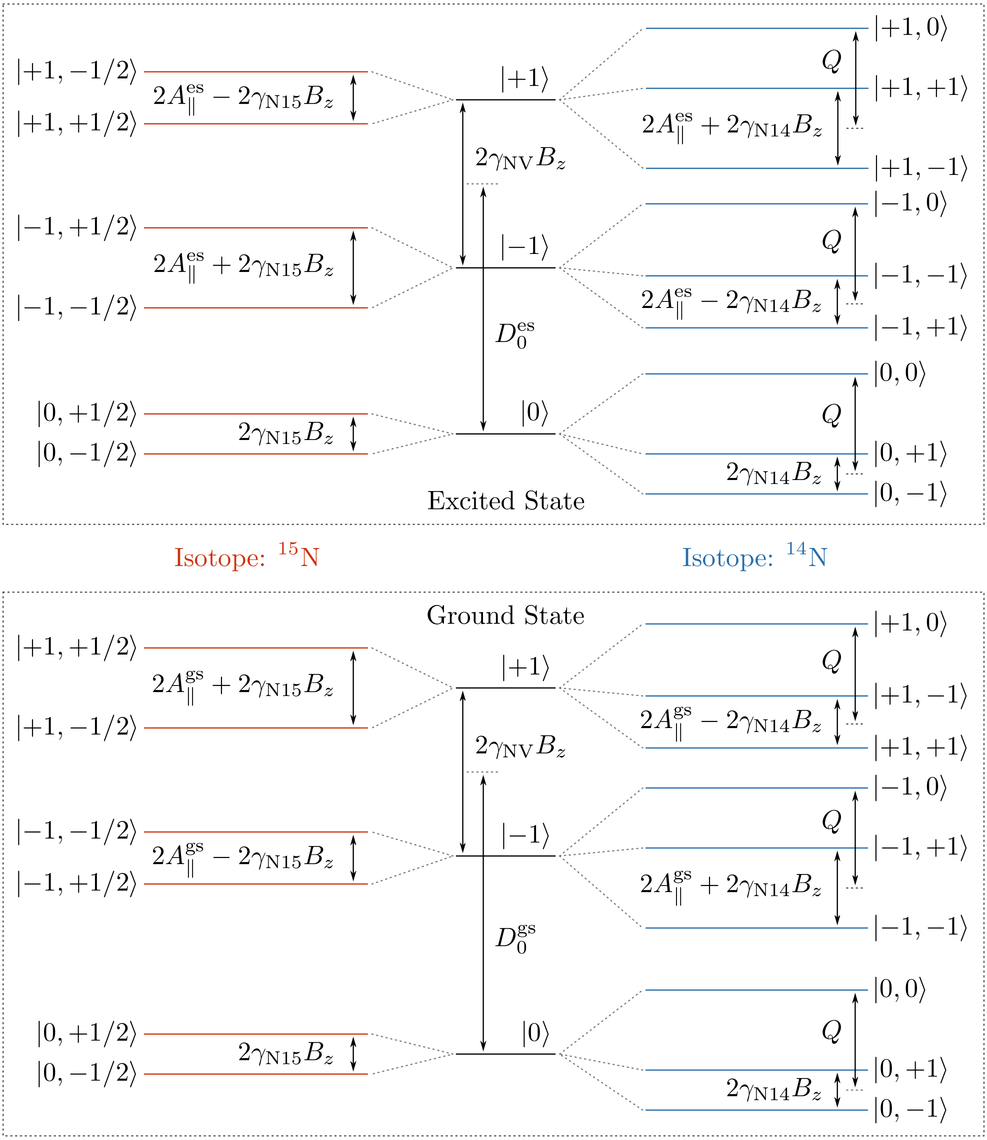
Excited State
$|+1,-1/2\rangle$
$|+1,+1/2\rangle$
$2A_{\parallel}^{\text{es}} - 2\gamma_{\text{N15}}B_z$
$|-1,+1/2\rangle$
$|-1,-1/2\rangle$
$2A_{\parallel}^{\text{es}} + 2\gamma_{\text{N15}}B_z$
$|0,+1/2\rangle$
$|0,-1/2\rangle$
$2\gamma_{\text{N15}}B_z$
$|+1\rangle$
$2\gamma_{\text{NV}}B_z$
$|-1\rangle$
D_0^{es}
$|0\rangle$
$|+1,0\rangle$
Q
$|+1,+1\rangle$
$2A_{\parallel}^{\text{es}} + 2\gamma_{\text{N14}}B_z$
$|+1,-1\rangle$
$|-1,0\rangle$
Q
$|-1,-1\rangle$
$2A_{\parallel}^{\text{es}} - 2\gamma_{\text{N14}}B_z$
$|-1,+1\rangle$
$|0,0\rangle$
Q
$|0,+1\rangle$
$2\gamma_{\text{N14}}B_z$
$|0,-1\rangle$
Isotope: ^{15}N
Isotope: ^{14}N
Ground State
$|+1,+1/2\rangle$
$2A_{\parallel}^{\text{gs}} + 2\gamma_{\text{N15}}B_z$
$|+1,-1/2\rangle$
$|-1,-1/2\rangle$
$2A_{\parallel}^{\text{gs}} - 2\gamma_{\text{N15}}B_z$
$|-1,+1/2\rangle$
$|0,+1/2\rangle$
$|0,-1/2\rangle$
$2\gamma_{\text{N15}}B_z$
$|+1\rangle$
$2\gamma_{\text{NV}}B_z$
$|-1\rangle$
D_0^{gs}
$|0\rangle$
$|+1,0\rangle$
Q
$|+1,-1\rangle$
$2A_{\parallel}^{\text{gs}} - 2\gamma_{\text{N14}}B_z$
$|+1,+1\rangle$
$|-1,0\rangle$
Q
$|-1,+1\rangle$
$2A_{\parallel}^{\text{gs}} + 2\gamma_{\text{N14}}B_z$
$|-1,-1\rangle$
$|0,0\rangle$
Q
$|0,+1\rangle$
$2\gamma_{\text{N14}}B_z$
$|0,-1\rangle$

Figure 1.4: Complete electronic hyperfine structure of the NV center, assuming $B_{\perp} = 0$, for either a ^{15}N atom (red) or a ^{14}N atom (blue), as given by Hamiltonians (1.4) and (1.5). The states are given in the basis $|m_S, m_{I,J}\rangle$. The order of the nuclear states within an electronic manifold differs between orbital states and nuclear spin isotopes because of the different signs of the hyperfine terms (see table 1.1). The axial hyperfine splitting is the dominant term for nuclear splittings, because for the magnetic fields $B_z \leq 600\,\text{G}$ employed our experiments, $2\gamma_{\text{N15/N14}}B_z \ll A_{\parallel}^{\text{gs,es}}$. The transverse hyperfine coupling and Zeeman effect are suppressed by the large energy splitting unless the system is brought to the ESLAC or GSLAC (not shown here).

	$A_{\parallel}^{\mathrm{gs}}$	$A_{\perp}^{\mathrm{gs}}$	$A_{\parallel}^{\mathrm{es}}$	$A_{\perp}^{\mathrm{es}}$	$\gamma_{\mathrm{N15/14}}$
^{15}N	+3.03 [82]	+3.65 [82]	−57.8 [83]	−39.2 [83]	−431.6 [80]
^{14}N	−2.17 [82]	−2.70 [82]	+40 [81]	+40 [81]	+307.7 [84]
units	(2π MHz)	(2π MHz)	(2π MHz)	(2π MHz)	(2π kHz/G)

Table 1.1: List of hyperfine values with the respective literature references.

The hyperfine structure as dictated by (1.4) and (1.5) is depicted in Figure 1.4. In the case of ^{15}N, each electronic manifold is split into a hyperfine doublet, while for ^{14}N, hyperfine triplets are obtained. The nuclear states within each electronic manifold are split by the longitudinal nuclear Zeeman effect, and – for states with non-zero m_S – by the axial hyperfine interaction. In this case, the axial hyperfine interaction is the dominant contribution, because for the magnetic fields $\leq 600\,\mathrm{G}$ that we work with in this thesis, the resulting nuclear Zeeman splitting is $\leq 500\,\mathrm{kHz}$ while the axial hyperfine term is a few MHz to tens of MHz (see table 1.1). Note that the energetic order of nuclear states within a manifold depends not only on the orbital degree of freedom, but also on the given nitrogen isotope. That is because the sign of the hyperfine parameters is different for these cases.

The basis $|\{m_S\},\{m_{I,J}\}\rangle$ we have used in Figure 1.4 is a good eigenbasis of the hyperfine Hamiltonians (1.4) and (1.5) as long as the system is not close to the ESLAC or GSLAC. Near these two level anti-crossings, states of different m_S are near-degenerate, such that the transverse Zeeman effect as well as the transverse hyperfine interaction are no longer suppressed by a large energy splitting. This leads to a mixture of states, and thus to the formation of a new eigenbasis. We have already discussed the nature of the mixing due to transverse magnetic fields at the ESLAC and GSLAC in section 1.1.2, and we now briefly turn to the physics of hyperfine-mediated state mixing.

The transverse hyperfine coupling near a level anti-crossing is a flip-flop interaction, that moves one spin quantum from either spin to the other. In the case of ^{15}N, this can easily be seen by rewriting the transverse hyperfine term from (1.4) in terms of the spin raising and lowering operators, $\hat{S}_{\pm} = \hat{S}_x \pm i\hat{S}_y$, respectively $\hat{I}_{\pm} = \hat{I}_x \pm i\hat{I}_y$,

$$A_{\perp}^{\mathrm{gs,es}}\left(\hat{S}_x\hat{I}_x + \hat{S}_y\hat{I}_y\right) = \frac{1}{2}\,A_{\perp}^{\mathrm{gs,es}}\left(\hat{S}_+\hat{I}_- + \hat{S}_-\hat{I}_+\right)\,. \tag{1.8}$$

Applying this term to a state $|m_S, m_I\rangle$ will transform it into $|m_S \pm 1, m_I \mp 1\rangle$ by raising one spin quantum number and simultaneously lowering the other, hence the name “flip-flop” interaction. In consequence, $|0,-1/2\rangle$ and $|-1,+1/2\rangle$ are coupled with each other, while neither $|0,+1/2\rangle$ nor $|-1,-1/2\rangle$ are affected by (1.8). We plot the eigenenergies of these four states near the ESLAC in Figure 1.5 (A). The coupled pair of states exhibits an anti-crossing with an energy gap of $A_{\perp}^{\mathrm{es}}$ plus a small nuclear Zeeman shift. The same flip-flop interaction takes place for NVs formed by the nuclear ^{14}N isotope, however, in this case there are two coupled pairs, as shown in Figure 1.5 (B). In the ground state near the GSLAC this flip-flop interaction also occurs, though with smaller coupling strengths (see table 1.1).

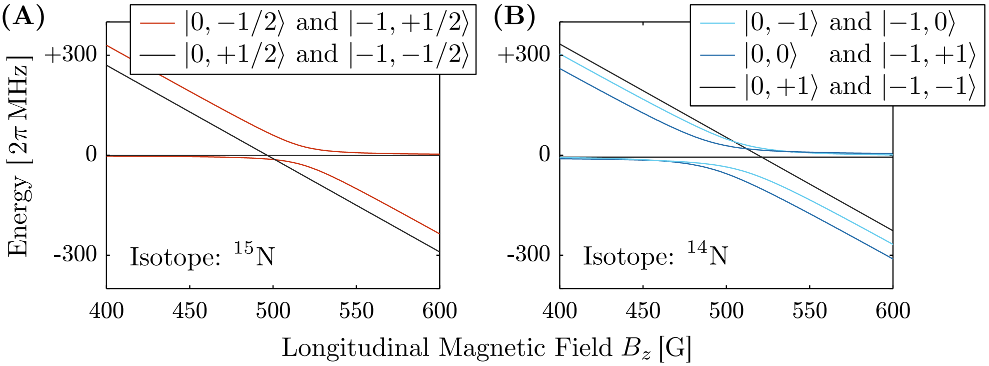

Figure 1.5: Hyperfine resolved eigenenergies at the ESLAC, where the $|0\rangle$ and $|-1\rangle$ electronic spin manifold are degenerate in the excited spin manifold, for $B_\perp = 0$, shown for either **(A)** a nuclear ^{15}N spin, or **(B)** a ^{14}N spin. In each case, there are two states that are not coupled by the transverse hyperfine coupling, and then there is either one or two pairs of states that are coupled, giving rise to anti-crossings with an energy separation of a few tens of MHz.

The hyperfine coupling at the ESLAC is coherently transferring spin polarization between the electronic and nuclear spins, which makes it an interesting mechanism to address the nuclear spin via the electron spin or vice versa. As we will discuss in section 1.2.1, it is easy to optically initialize and readout the electron spin with a green laser. By bringing the system into proximity of the ESLAC, such a laser can be employed to grant optical access to the nuclear spin via the coupled electron spin, giving rise to nuclear spin hyperpolarization [29, 81] and, by virtue of the same mechanism, nuclear spin state readout [30]. We will discuss these nuclear dynamics in detail in section 1.2.2.

1.2 Dynamics under Green Illumination

The NV center offers the intriguing possibility to access the electron spin state through purely optical means by driving the optical transition between ground and excited state with a laser. It turns out that such laser illumination can be utilized to not only initialize the electronic spin via optical pumping [24, 25], but also read out the electron spin state via spin-dependent photoluminescence (PL) [26, 85]. In addition, near the ESLAC at approximately 500 G, the electron and nitrogen spin are coherently coupled in the excited state, ultimately leading to optical access to the nuclear nitrogen spin via the electron spin, and thereby paving the way to optical nuclear spin hyperpolarization [29, 81, 86] and optical readout of the nuclear spin [30]. All these techniques are cornerstones for spin-based experiments with NV centers in diamond, as they allow simple and robust spin initialization and readout, for both the electron and nitrogen spin, even at room temperature.

In this section, we discuss the exact dynamics of the NV center under such laser illumination, both under default conditions and in the special case of operating near the ESLAC at $B_z \approx 500\,\mathrm{G}$.

1.2.1 Optical Initialization and Readout

The NV center can be driven with light by addressing the optical electric dipole transition between the ground state ($^3A_2$) and the excited state (^3E). In particular, the NV can be excited off-resonantly with green light with a wavelength of 500 nm to 637 nm. For example, in our experiments we use a laser with 515 nm. Such green illumination brings the ground state population into vibronic states slightly above the energy of excited state, from where it decays into the excited spin manifold due to radiationless, phonon-mediated decay processes, as illustrated in Figure 1.6. This entire excitation mechanism operates only on the orbital degrees of freedom of the NV quantum state, and is therefore highly spin-conserving. In other words, such off-resonant optical excitation of an NV center that is polarized into a spin state $|m_S, m_{I,J}\rangle$ brings the system into the exact same state in the excited state manifold.

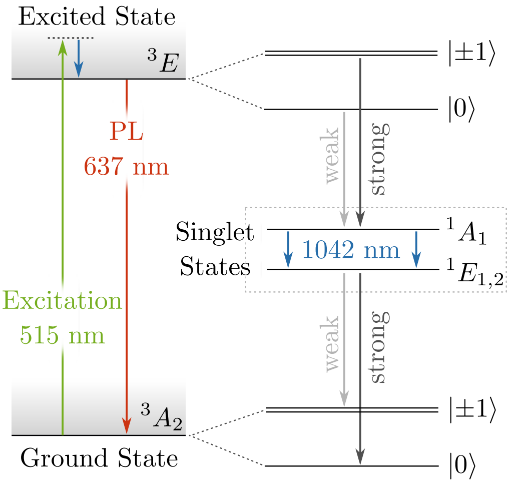

Figure 1.6: A green laser excites the system in a spin-conserving fashion into vibronic states slightly above the excited state (green), from where it transitions into the excited state (blue). From there, spin-conserving radiative relaxation back to the ground state gives rise to the emission of PL (red). Alternatively, a non-radiative transition through the metastable singlet states can occur; a transition is much more likely to occur for $|\pm1\rangle$ population and preferentially ends up in $|0\rangle$. This means that continuous optical pumping with green light produces spin-dependent PL, and ultimately polarizes the system into $|0\rangle$.

From the excited state, there are two possible competing relaxation paths. On one hand, there is a spin-conserving radiative decay directly back to the ground state. This decay causes the emission of a photon, a phenomenon called photoluminescence (PL), as shown in Figure 1.6. In case of a resonant decay, this photon has a wavelength of 637 nm, corresponding to visible red light. Consequently, in the emission spectrum of the NV, there is a zero-phonon line at 637 nm [74]. In addition, non-resonant decay into vibronic states above the ground state leads to a large phononic sideband at larger wavelengths [20].

On the other hand, the system can relax back into the ground state by transitioning through the intermediate electronic singlet states ($^1A_1$ and $^1E_{1,2}$). This is also depicted in Figure 1.6. The decay from the excited state into these singlets is often called "inter-system crossing", it is mediated by spin-orbit interaction, and it is much more likely to occur for population in the $|\pm1\rangle$ states [87, 88]. These singlets are split by 1.18 eV, corresponding to an infrared transition of 1024 nm [75]. From the singlet state, a radiationless decay brings the system back to the electronic ground state. This

process is not yet fully understood, and the reported transition probabilities into the three possible spin projections vary a lot from study to study, however, most people claim to find either no spin selectivity at all [85,87], or a slight preference for decaying into the $|0\rangle$ state [25,89–92]. See table 2.1 for a collection of reported values.
The combination of the spin-conserving optical cycle between ground and excited state and the spin-selective inter-system crossing through the singlet states leads to a polarization of the electronic spin into the $|0\rangle$ state. Typically, at saturated optical excitation, the system is well polarized to more than 90 % to after pumping for at least 1 µs [55]. In our experiment, we apply 3 µs of green light for initialization. This optical spin initialization is a crucial property of the NV center that we use in every single experiment throughout this thesis, and it is the reason why the initial state of the sensing protocols in always the $|0\rangle$ state.
The excited state has a radiative lifetime of about 10 ns [89, 93], leading to a very fast optical cycle between ground and excited state that is mostly limited by the available green excitation power. In comparison to that, the singlet states have very long lifetimes. For example, depending on the temperature, the lower singlet ${}^1E_{1,2}$ has a lifetime of approximately 150 to 450 ns [94]. In consequence, if population moves into these singlets, it is trapped there for many optical cycles, and does therefore not contribute to any PL emission. Since the $m_S = \pm 1$ states are much more likely to move into those optically inactive singlet states, the PL intensity resulting from an NV in a $|\pm 1\rangle$ state is significantly lower than from an NV in the $|0\rangle$ state. In an optimized setup, an optical contrast of up to 30 % can be achieved [57].
This spin-dependent PL provides a tool for differentiating $|0\rangle$ from $|\pm 1\rangle$ by purely optical means. Note that this spin measurement technique cannot discriminate between the $|\pm 1\rangle$ states. In our experiments, however, we exclusively work on an effective two-level system comprised of $|0\rangle$ and $|-1\rangle$ where this optical spin readout is unambiguous. In our protocols, the readout laser pulse after an experiment is 350 ns long, followed by re-initialization into $|0\rangle$ for 3 µs to prepare for the next experiment repetition.

Finally, we briefly describe a useful experimental technique that combines the discussed photo-physics of the NV with the physics of electronic state mixing due to $B_\perp$ as previously discussed in section 1.1.2. By measuring the PL of the NV under continuous green illumination, assuming a perfectly aligned magnetic field of 500 G, the electron spin is brought into the $|0\rangle$ state and thus a high rate of PL is observed. Misaligning the magnetic field by less than one degree introduces a transverse field $B_\perp$ of a few Gauss, which is enough to mix the bright $|0\rangle$ state with the darker $|-1\rangle$ state, see Figure 1.3 (B), leading to an overall reduction in PL. This can be exploited to align an external magnetic field of about 500 G with the NV symmetry axis, simply by maximizing PL. For all experiments that we conduct near the ESLAC, the magnetic field is first aligned with the NV axis with exactly this procedure.

1.2.2 Nuclear Dynamics at the ESLAC

The optical properties of the NV center that we discussed in the previous section remain largely unchanged if the hyperfine interaction with the NV's nitrogen atom is taken into consideration. That is because the nuclear spin has no orbital degrees of freedom itself, and can therefore not be directly addressed with a laser. In addition, the nuclear spin state is conserved when the system is optically cycled between ground and excited state; in fact it is even conserved when the system transitions through the singlet states. Therefore, it is in general true that illumination with green light leads to nuclear spin-independent electron spin-dependent PL, and to initialization from $|\phi_S, \phi_I\rangle$ into $|m_S = 0, \phi_I\rangle$, where $|\phi_S\rangle$ and $|\phi_I\rangle$ are arbitrary electron and nuclear spin states respectively.

However, there is an exception to this: At the ESLAC, hyperfine-mediated coupling between electron and nuclear spin (see section 1.1.3) gives rise to a hyperpolarization of the nuclear spin [29]. For the ^{15}N isotope, this works as follows: $|0, -1/2\rangle$ and $|-1, +1/2\rangle$ are coupled near the ESLAC, meaning that the transverse hyperfine interaction causes flip-flop interactions between the coupled states. On the other hand, continuous optical pumping brings the electron spin into $|0\rangle$; a process that works in only one direction. The combination of these two processes results in a continuous pumping of the system into the steady-state $|0, +1/2\rangle$, as shown in Figure 1.7 (A). In other words, while the laser slowly polarizes the electron spin, the flip-flop coupling in the excited state transfers polarization to the nuclear spin, ultimately leading to the polarization of both spins. For a ^{14}N-based NV, the same nuclear hyperpolarization can be realized, albeit with two additional steps, as illustrated in Figure 1.7 (B). The steady-state in this case is $|0, +1\rangle$.

The described mechanism achieves exceptional nuclear polarization quality of more than 98 % for single NVs [29]. Notably, the process still works reasonably well at magnetic fields that are substantially far away from the ESLAC. For instance, at

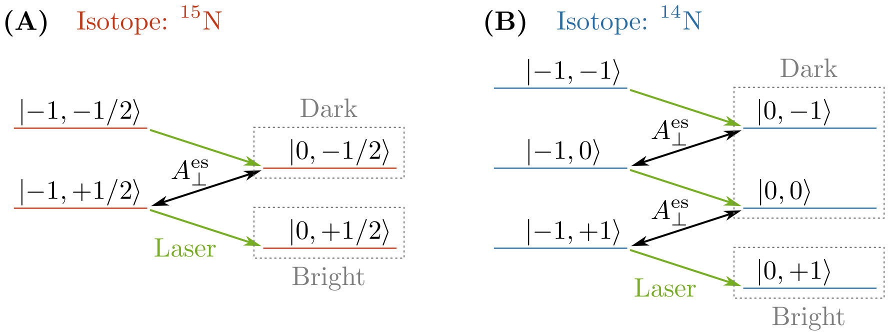

Figure 1.7: Schematic depiction of the nuclear hyperpolarization process under green illumination near the ESLAC. Under these conditions, $m_S = 0$ and $m_S = -1$ spin state manifolds are near-degenerate in the excited state, leading to a hyperfine-based flip-flop interaction between certain spin state pairs (black arrows). At the same time, the green laser light shelves the system into $m_S = 0$ in a nuclear spin-conserving fashion (green arrows). The combination of these two processes leads to hyperpolarization of the nuclear spin into **(A)** the steady-state $|0, +1/2\rangle$ for NVs formed by ^{15}N, and into **(B)** the state $|0, +1\rangle$ in the case of ^{14}N. These hyperpolarized states emit more PL when probed with a green laser compared to other states within the $m_S = 0$ manifold, because they are not coupled to a dark $m_S = -1$ state. This allows for optical readout of the nuclear spin state. Note that for simplicity, the levels are not depicted in their correct energetic order, and the far-detuned $m_S = +1$ states are omitted.

150 G offset from the ESLAC, the polarization efficiency decreases by only about 20 % [29]. The technique can be extended from single NVs to entire NV ensembles, where nuclear hyperpolarization of up to 90 % has been reported [86].
As discussed in the previous section, the system emits red PL upon green illumination, and the amount of emitted photons is high if the system is in a state with electron spin projection $m_S = 0$, and low if it is in a state with $m_S = \pm 1$, up to a contrast of about 30 % [57]. Usually, the nuclear spin projection does affect the emitted PL. Near the ESLAC, however, the nuclear spin matters in that it introduces a PL difference for states within the same m_S manifold. In particular, among the $m_S = 0$ states, the hyperpolarized state is the brightest, because it is the only state that is not mixed with a state from the darker $m_S = -1$ manifold. Experimentally, an optically detected nuclear contrast of up to roughly 4 % can be achieved [30]. This nuclear spin-dependent PL near the ESLAC enables all-optical nuclear spin readout, a technique that is of paramount importance for obtaining the results of chapter 2.
Finally, note that nuclear hyperpolarization and readout can be implemented near the GSLAC by exploiting the same mechanisms, however, within the scope of this thesis we only work near the ESLAC and thus skip the GSLAC discussion.

1.3 Spin Control with AC Magnetic Fields

When it comes to the experimental realization of NV spin-based quantum sensing technologies, the optical initialization and readout discussed in the previous section are key ingredients. However, most spin-based quantum sensing protocols require the spin sensor to be initialized in a very specific state, mostly a superposition state, that is different from the optically pumped $|0\rangle$ state. Moreover, many sensing schemes perform unitary operations on the spin state between sensing periods for sensitivity enhancement, or for frequency filtering in AC sensing techniques. Therefore, to realize such advanced sensing schemes with the NV spin, exploiting just the optical properties of the NV is not sufficient, but it is crucial to additionally implement a robust experimental way to coherently control the spin state in any arbitrary way. In this section we explore how microwave radiation can be utilized to provide just such coherent spin manipulation.

1.3.1 Microwave Interaction Hamiltonian

Let's consider an NV center that is exposed to electromagnetic radiation in the radio-frequency (RF) to microwave (MW) regime, meaning a few MHz up to a few GHz. In this case, the dominant interaction is the coupling of the time-varying magnetic field component $\boldsymbol{B}_{\mathrm{MW}}(t)$ to the spin magnetic dipole moment $\hat{\boldsymbol{\mu}} = -\hbar\gamma_{\mathrm{NV}}\hat{\boldsymbol{S}}$ of the NV's electron spin. The corresponding time-dependent interaction Hamiltonian reads

$$\hat{\mathcal{H}}_{\mathrm{MW}}(t) = -\hat{\boldsymbol{\mu}} \cdot \boldsymbol{B}_{\mathrm{MW}}(t) = \hbar\gamma_{\mathrm{NV}}\boldsymbol{B}_{\mathrm{MW}}(t) \cdot \hat{\boldsymbol{S}} \,. \tag{1.9}$$

Technically, $\boldsymbol{B}_{\mathrm{MW}}(t)$ would also interact with orbital magnetic dipole moments, but since the ground state (always) and the excited state (only at room-temperature due to orbital averaging) are orbital singlets, there is no such orbital moment. The electric component $\boldsymbol{E}_{\mathrm{MW}}(t)$ of the electromagnetic field is in principle also coupling to the

NV spin degrees of freedom via the Stark effect [95], though this effect is negligibly weak and we thus omit it in this thesis.
Interaction with an AC magnetic field as described by the $\hat{\mathcal{H}}_{\mathrm{MW}}(t)$ will couple certain spin eigenstates. Specifically, by evaluating the matrix elements of $\hat{\mathcal{H}}_{\mathrm{MW}}(t)$ one can derive selection rules for these magnetic dipole transitions, and thereby find that only states with $\Delta m_S = \pm 1$ are coupled. For the NV ground state, this implies that a MW field can drive only two distinct transitions, namely either $|0\rangle \leftrightarrow |+1\rangle$ or $|0\rangle \leftrightarrow |-1\rangle$. Therefore, for simplicity's sake, it makes sense to consider only an effective two-level subsystem comprised of either of these pairs. Since we experimentally work exclusively with the $|0\rangle$ and $|-1\rangle$ states, let us continue with this particular two-level system, where we call its energy splitting $\hbar\omega_0$.
Let us consider the case where the electromagnetic MW field generates a linearly polarized AC magnetic field at the NV position, mathematically given by $\boldsymbol{B}_{\mathrm{MW}}(t) = \boldsymbol{B}_{\mathrm{MW}} \cos(\omega t + \phi)$, where $\boldsymbol{B}_{\mathrm{MW}} = (B_x^{\mathrm{MW}}, B_y^{\mathrm{MW}}, B_z^{\mathrm{MW}})$ describes the MW field's constant vector magnetic amplitude, ω denotes its frequency, and ϕ is its phase. Furthermore, we omit static transverse magnetic fields and the hyperfine interaction for now. Overall, for these conditions, the MW driven ground state two-level system comprised of $|0\rangle$ and $|-1\rangle$ is well described by

$$\hat{\mathcal{H}}^{\mathrm{gs}} = \hbar\omega_0 \hat{\sigma}_z + \hbar\gamma_{\mathrm{NV}} \hat{\boldsymbol{\sigma}} \cdot \boldsymbol{B}_{\mathrm{MW}}(t)\,, \tag{1.10}$$

where the first term defines the energy splitting of $\hbar\omega_0$ and the second one describes the interaction with the MW field as given by equation (1.9). Here, $\hat{\boldsymbol{\sigma}} = (\hat{\sigma}_x, \hat{\sigma}_y, \hat{\sigma}_z)$ are the spin operators for the $\{|0\rangle, |-1\rangle\}$ two-level system, that have the same matrix representations as the operator $\hat{\boldsymbol{I}}$ in (1.7).
Ultimately, we aim to describe the dynamics of the spin under MW excitation, and for this reason the goal is to solve the Schrödinger equation for the Hamiltonian $\hat{\mathcal{H}}^{\mathrm{gs}}$ from equation (1.10). To that end, we first eliminate the time dependencies in that Hamiltonian. This can be done by transforming to the rotating interaction frame with the transformation rule

$$\hat{\mathcal{H}} \to \hat{U}\hat{\mathcal{H}}\hat{U}^\dagger + i\hbar \frac{\partial \hat{U}}{\partial t} \hat{U}^\dagger := \hat{\mathcal{H}}_{\mathrm{rot}}\,, \tag{1.11}$$

using the unitary transformation operator $\hat{U} = \exp(i\omega t\, \hat{\sigma}_z)$, which results in

$$\begin{aligned} \hat{\mathcal{H}}^{\mathrm{gs}}_{\mathrm{rot}}(t) = \hbar \left(\omega_0 - \omega + \gamma_{\mathrm{NV}} B_z^{\mathrm{MW}} \cos(\omega t + \phi)\right) \hat{\sigma}_z \\ + \frac{\hbar\gamma_{\mathrm{NV}}}{4} (B_x^{\mathrm{MW}} - iB_y^{\mathrm{MW}})\, e^{-i\phi} \left(1 + e^{2i(\omega t + \phi)}\right) (\hat{\sigma}_x + i\hat{\sigma}_y) \\ + \frac{\hbar\gamma_{\mathrm{NV}}}{4} (B_x^{\mathrm{MW}} + iB_y^{\mathrm{MW}})\, e^{+i\phi} \left(1 + e^{2i(\omega t + \phi)}\right) (\hat{\sigma}_x - i\hat{\sigma}_y)\ . \end{aligned} \tag{1.12}$$

Next, we perform the rotating-wave approximation (RWA) by dropping the fast oscillating terms $e^{2i(\omega t+\phi)}$. What this means is the following: In the lab frame, the linearly polarized field can be decomposed into two circularly polarized components that rotate with equal frequency ω in opposite directions; such that in the rotating frame that matches their frequency ω, these components have frequencies of either 0 or 2ω. The RWA states that it is approximately valid to neglect the latter fast rotating term as it averages to zero on the time scale where the relevant dynamics occur.

In addition to the RWA, we also drop the magnetic B_z^{MW} component of the MW field, because this component – as is evident by equation (1.12) – is only producing time-varying shifts of the spin levels, and not transferring any population between spin states. Furthermore, we write the complex transverse components of the MW field as $(B_x^{\mathrm{MW}} \pm iB_y^{\mathrm{MW}}) = B_\perp^{\mathrm{MW}} e^{\pm i\alpha}$ with complex phase α. Together with applying the RWA, these simplifications lead to the time-independent rotating frame Hamiltonian

$$\hat{\mathcal{H}}_{\mathrm{rot}}^{\mathrm{gs}} = -\hbar\delta\hat{\sigma}_z + \frac{\hbar}{2}\left(\Omega_R^*\hat{\sigma}_+ + \Omega_R\hat{\sigma}_-\right) = \frac{\hbar}{2}\begin{pmatrix} -\delta & \Omega_R^* \\ \Omega_R & +\delta \end{pmatrix}, \tag{1.13}$$

where we have introduced the spin raising and lowering operators $\hat{\sigma}_\pm = (\hat{\sigma}_x \pm i\hat{\sigma}_y)$, the detuning $\delta = (\omega - \omega_0)$, and the so-called Rabi frequency Ω_R that is given by

$$\Omega_R := \left(\frac{1}{2}\gamma_{\mathrm{NV}} B_\perp^{\mathrm{MW}} e^{i(\phi-\alpha)}\right) \xrightarrow[\text{along x}]{\text{fix } B_\perp^{\mathrm{MW}}} \left(\frac{1}{2}\gamma_{\mathrm{NV}} B_\perp^{\mathrm{MW}} e^{i\phi}\right), \tag{1.14}$$

with Ω_R^* being the complex conjugate of Ω_R. The detuning δ describes the offset between the MW frequency and the spin transition frequency, the Rabi frequency Ω_R is a measure of the coupling strength between MW field and spin system. Note that by exploiting the rotation symmetry of the NV system, one can chose the $\boldsymbol{e}_x$-axis to be aligned with $B_\perp^{\mathrm{MW}}$ such that $\alpha = 0$. We will always work under this assumption hereafter.

The eigenstates $|\pm\rangle$ of the driven system are often called "dressed states", and can be obtained by diagonalization of Hamiltonian (1.13). These dressed states possess an energy splitting given by the effective Rabi frequency $\hbar\Omega = \pm\hbar\sqrt{\delta^2 + |\Omega_R|^2}$, an energy splitting that is crucial in Spin-Lock experiments (see section 1.5.5 for an introduction to that sequence, and chapters 3 to 5 for experimental results).

Before we close this section, let us note that the same Hamiltonian could be derived for the interaction of an electromagnetic field with a nuclear spin. However, in this case, the required field needs to be in the radio-frequency regime (only a few MHz) to hit the resonance with nuclear spin transitions, and in addition, due to the much smaller gyromagnetic ratio of nuclear spins, the field needs to have a drastically larger amplitude to induce similar dynamics with MHz bandwidth. For our experiments, there is no need for such nuclear spin control, and we therefore stick to discussing only the case of electron spin manipulation.

1.3.2 Coherent Spin Manipulation

The dynamics invoked by Hamiltonian $\hat{\mathcal{H}}_{\mathrm{rot}}^{\mathrm{gs}}$ from (1.13) are unitary rotations of the spin state, as one can see by considering the corresponding time evolution operator

$$\hat{\mathcal{U}}(t) = \exp\left(\frac{-it}{\hbar}\hat{\mathcal{H}}_{\mathrm{rot}}^{\mathrm{gs}}\right) = \exp\left(-i\Omega t\,\hat{\boldsymbol{\sigma}} \cdot \boldsymbol{e}_{\mathrm{MW}}\right), \tag{1.15}$$

where we introduced the normalized unit vector

$$\boldsymbol{e}_{\mathrm{MW}} = \frac{1}{\Omega}\begin{pmatrix} +|\Omega_R|\cos\phi \\ -|\Omega_R|\sin\phi \\ -\delta \end{pmatrix}. \tag{1.16}$$

Equation (1.15) demonstrates that the system's spin propagator $\hat{\mathcal{U}}(t)$ has the mathematical form of a rotation operator, that rotates the spin about the axis $\boldsymbol{e}_{\mathrm{MW}}$ by an angle of Ωt in the three-dimensional space spanned by $\hat{\sigma}_x$, $\hat{\sigma}_y$, and $\hat{\sigma}_z$.
To illustrate these spin rotations generated by $\hat{\mathcal{U}}(t)$, it is convenient to consider the Bloch sphere representation. To that end, the state of the two-level system is mapped onto the unit sphere in three-dimensional space. Specifically, a spin state described by the density matrix $\hat{\rho} = \boldsymbol{a} \cdot \hat{\boldsymbol{\sigma}} + \mathbb{I}_2/2$, where $\mathbb{I}_2$ is the two-dimensional unitary operator, is represented on the Bloch sphere by the real-valued vector $\boldsymbol{a}$. This means that the poles of the Bloch sphere are identified as the bare states $|0\rangle$ and $|-1\rangle$, other points on the surface correspond to pure superposition states, and points inside the Bloch sphere are attributed to mixed states. In this Bloch sphere representation, in the rotating frame, the MW field is represented by a static vector pointing along $\boldsymbol{e}_{\mathrm{MW}}$, with a length of $\Omega = \sqrt{\delta^2 + |\Omega_R|^2}$. The evolution of the spin as dictated by the propagator from equation (1.15) is a rotation of the spin vector $\boldsymbol{a}$ about $\boldsymbol{e}_{\mathrm{MW}}$ by Ωt radiants. Two examples of such rotations are shown in Figure 1.8.

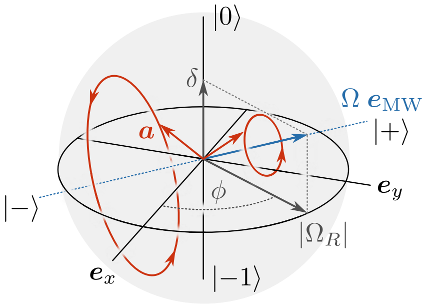

Figure 1.8: Bloch Sphere representation of the two-level system spanned by the ground state spin states $|0\rangle$ (north pole) and $|-1\rangle$ (south pole). In the rotating frame, the MW can be represented by the vector $\Omega\, \boldsymbol{e}_{\mathrm{MW}}$ (blue), characterized by azimuthal angle ϕ equal to the MW field's phase, z-component equal to the system's detuning δ and a length of Ω. The resulting dynamics of a spin state represented by $\boldsymbol{a}$ (red arrows) is a rotation about $\boldsymbol{e}_{\mathrm{MW}}$ by an angle of Ωt. Here, the solid red line shows the trajectory of a continuous rotation with $t \in \{0, \infty\}$.

Ultimately, this precessional motion of the spin state under MW irradiation means that it is possible to generate any arbitrary spin rotation by choosing appropriate values for Ω_R, ϕ, δ, and t. These four values describe the MW field strength, phase, frequency and uptime, which can all be easily controlled experimentally. Therefore, MW pulses are perfectly suited to provide the necessary coherent spin control required for implementing quantum sensing schemes. In fact, for the sequences employed in this thesis, they form the basic building blocks.
In the following, we define the MW pulses that are later used to compile the sensing protocols discussed in sections 1.4 and 1.5. To that end, let's consider a MW field that is resonant with the NV spin transition we are aiming to drive, e.g. we set $\delta = 0$. In this special case, the vector $\boldsymbol{e}_{\mathrm{MW}}$ lies in the equatorial plane of the Bloch sphere, with an azimuthal angle of ϕ and length $\Omega = |\Omega_R|$. What is so special about this configuration is that such a field can rotate $|0\rangle$ into $|-1\rangle$ and vice versa. Specifically, for a pulse duration of $t = \pi/|\Omega_R|$, the system undergoes exactly one such spin-flip; a microwave pulse we call a π-pulse. This can be seen by computing the evolution of

$|0\rangle$ for $\delta = 0$, which yields

$$\hat{\mathcal{U}}\left(t = \frac{\pi}{|\Omega_R|}\right)|0\rangle = ie^{-i\phi}\,|-1\rangle \ . \tag{1.17}$$

For $\phi = 0$, the $\boldsymbol{e}_{\mathrm{MW}}$ vector lies on the $+\boldsymbol{e}_x$ axis. In this case, we call such a π-pulse a $+\pi_x$-pulse. Alternatively, for $\phi = \pm\pi/2$, the vector $\boldsymbol{e}_{\mathrm{MW}}$ is collinear with $\pm\boldsymbol{e}_y$ axis in which case we talk about a $\pm\pi_y$-pulse. An example trajectory of the NV spin under a $+\pi_y$-pulse is shown in Figure 1.9 in blue.
Similarly, for $t = (\pi/2)/\Omega_R$, we obtain a so-called $\pi/2$-pulse, that causes the system to perform a quarter rotation on the Bloch sphere, which would rotate a bare state such as $|0\rangle$ into an equal superposition state on the sphere equator and vice versa, as becomes clear by inspecting the expression

$$\hat{\mathcal{U}}\left(t = \frac{\pi}{2|\Omega_R|}\right)|0\rangle = \frac{1}{\sqrt{2}}\left(|0\rangle + ie^{-i\phi}\,|-1\rangle\right) \ . \tag{1.18}$$

Analogous to the nomenclature introduced above, depending on the direction of the corresponding MW field, we call these pulses $\pm\pi_x/2$-pulses and $\pm\pi_y/2$-pulses respectively. Figure 1.9 shows the Bloch sphere spin trajectory under a $-\pi_x/2$-pulse.

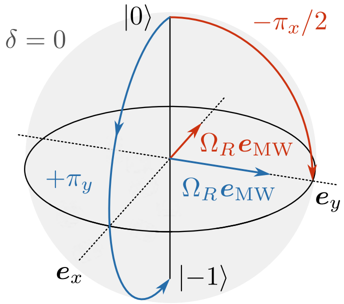

Figure 1.9: Bloch Sphere representation of a π and $\pi/2$-pulse performed on the two-level system spanned by the ground state spin states $|0\rangle$ and $|-1\rangle$, with a resonant MW drive ($\delta = 0$). The $+\pi_y$-pulse is generated by a MW field along the $+\boldsymbol{e}_y$ direction (blue) and causes one entire spin flip from the initialized state $|0\rangle$ into $|-1\rangle$. Alternatively, a $-\pi_x/2$-pulse applied along $-\boldsymbol{e}_x$ (red) rotates $|0\rangle$ into an equal superposition state on the sphere equator.

Such π and $\pi/2$-pulses are the basic blocks for building spin-based quantum sensing sequences. While in general, microwaves can do any arbitrary spin rotation, the sequences we employ in this thesis do only require π-pulses, $\pi/2$-pulses, and continuous resonant microwave irradiation. We will introduce these sequences in sections 1.4 and 1.5. Before we get there though, we will have a look at how to experimentally measure the spin rotations generated by $\hat{\mathcal{U}}(t)$, which is particularly important because these measurements allows us to determine Ω_R and thereby calibrate π and $\pi/2$-pulses.

1.3.3 Rabi Oscillations

Let us now discuss how we experimentally measure Rabi oscillations, i.e. how we observe the MW-driven spin dynamics we have mathematically described in the previous sections. First, in any NV experiment, the spin is initially always prepared in the $|0\rangle$ state by optical pumping, a process we have discussed in section 1.2.1. This means for the two-level system spanned by $\{|0\rangle, |-1\rangle\}$, a MW pulse following this initialization will cause a rotation into the state $\hat{\mathcal{U}}(\tau)\,|0\rangle$, where τ denotes the duration of the MW pulse at hand and $\hat{\mathcal{U}}(\tau)$ is the time evolution operator defined in equation (1.15). At the end of this MW pulse, the probability $P_{|0\rangle}(\tau)$ to find the system in $|0\rangle$ is thus given by

$$P_{|0\rangle}(\tau) = \left| \langle 0| \hat{\mathcal{U}}(\tau) |0\rangle \right|^2 = \cos^2\left(\frac{\Omega\tau}{2}\right) + \frac{\delta^2}{\Omega^2}\sin^2\left(\frac{\Omega\tau}{2}\right) , \tag{1.19}$$

where $\Omega = \sqrt{|\Omega_R|^2 + \delta^2}$. On resonance, $\delta = 0$, this equation simplifies to

$$P_{|0\rangle}(\tau) = \frac{1}{2} + \frac{1}{2}\cos\big(|\Omega_R|\tau\big) . \tag{1.20}$$

Next, remember that spin-dependent PL allows us to experimentally differentiate the bright $|0\rangle$ state from the darker $|\pm 1\rangle$ states, see section 1.2.1, meaning that the larger the probability $P_{|0\rangle}$, the more photons are emitted by the system. Therefore, the amount of detected PL is directly related to $P_{|0\rangle}$.

A measurement thus work as follows: First, we apply a 3 µs long green laser pulse for spin initialization into the $|0\rangle$ eigenstate, directly followed by a MW pulse of variable length τ. Afterwards, the laser is immediately turned back on for 350 ns during which we readout the NV PL. This sequence of pulses is illustrated in the top

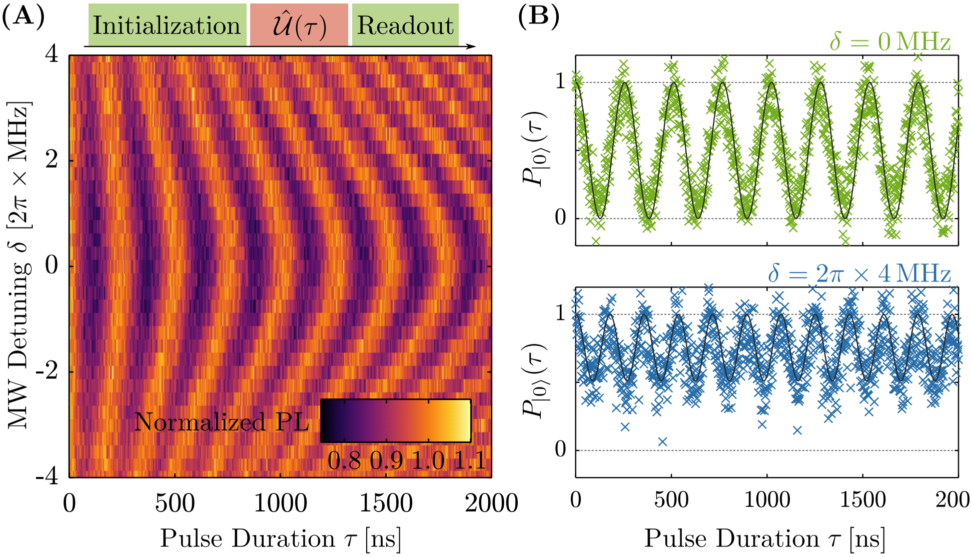

Figure 1.10: Rabi oscillations measured on the electronic $|0\rangle$ to $|-1\rangle$ spin transition, taken on NVA1 (see table A.6). **(A)** Normalized PL as a function of microwave detuning δ and pulse duration τ, exhibiting clear Rabi oscillations, detected as PL modulations. A sketch of the sequence employed to take these data is shown at the top. **(B)** Line cuts of (A) at 0 and 4 MHz detuning. After assigning the optical contrast obtained on MW resonance to the full spin transition, the PL can be linearly mapped to the probability $P_{|0\rangle}(\tau)$. The data agree well with the prediction of equation (1.19) (black line), for whose evaluation we used the fitted value of $|\Omega_R| = (3.906 \pm 0.004)$ MHz.

of Figure 1.10 (A). The resulting PL as a function of τ is linearly related to $P_{|0\rangle}$ and commonly called Rabi oscillation. Consequently, we call this kind of measurement a Rabi experiment.

In Figure 1.10 (A) we show the PL resulting from such a Rabi experiment, as a function of MW pulse duration τ and detuning δ, where $\delta = 0$ corresponds to the resonance with the $|0\rangle$ to $|-1\rangle$ transition. The PL data is normalized via division by the largest obtained PL value. To demonstrate that these data are well described by equation (1.19), we have a look at two particular line cuts, $\delta = 0$ and $2\pi \times 4\,\text{MHz}$. Using least-squares fitting, we find that on resonance the oscillation frequency is $|\Omega_R| = (3.906\pm0.004)\,\text{MHz}$ with a contrast of about (0.21 ± 0.03) in units of normalized PL. Assigning this contrast to the full transition of $|0\rangle$ to $|-1\rangle$, we can map the normalized PL to $P_{|0\rangle}(\tau)$ in a linear fashion, and can thus compare both line cuts to equation (1.19). This comparison is shown in Figure 1.10 (B) where the black lines are the theoretical predictions, demonstrating great agreement with the data.

Importantly, such Rabi experiments can be used to not only measure $|\Omega_R|$, but also to calibrate π and $\pi/2$-pulses. To that end, one measures a Rabi oscillation on resonance, and takes the duration τ required to reach the first local PL minimum as the π-pulse duration. Half that duration corresponds to a $\pi/2$-pulse.

In conclusion, we have discussed how MW radiation can be used to perform arbitrary spin state manipulation, and in particular we have defined π and $\pi/2$-pulses that will be crucial building blocks for the quantum sensing sequences introduced in the next two sections. In addition, we have demonstrated how to measure Rabi oscillations and thereby experimentally calibrate π and $\pi/2$-pulses.

1.4 NV Magnetometry Schemes

While spin-based quantum sensors such as the NV center are capable of sensing a multitude of different physical quantities, they naturally lend themselves to magnetometry applications, because these spin-sensors carry a magnetic moment that is highly susceptible to magnetic fields. The NV center in diamond – due to its atomic size, its room temperature compatibility, and its location in robust diamond host material that can be nanofabricated – is especially suited for high-resolution nanoscale magnetic sensing [96, 97], such as scanning probe magnetometry [27] and nanoscale magnetic resonance imaging [98]. Most of these DC magnetometry applications rely on either of two key protocols for magnetic field measurements: Optically detected magnetic resonance (ODMR) and Ramsey free induction decay (FID). In this section, we discuss these two techniques.

1.4.1 Optically Detected Magnetic Resonance

The simplest, most straight forward way to measure an externally applied longitudinal magnetic field component B_z is to determine the ground state transition frequencies of the electron spin levels. This is because a magnetic B_z component splits up the $|m_S = \pm1\rangle$ states by $2\gamma_{\text{NV}}B_z$ (see section 1.1.2), and therefore the transition frequency from $|0\rangle$ into either of these states is given by $\omega_\pm = D_0^{\text{gs}} \pm \gamma_{\text{NV}}B_z$.

These transition frequencies $\omega_\pm$ can experimentally be determined by continuously applying both green laser light and a MW field to the NV center, as shown Figure 1.11 (A). This scheme is called continuous-wave (CW) optically detected magnetic resonance (ODMR). The laser continuously pumps the system into $|0\rangle$, and simultaneously causes the emission of spin-dependent PL. At the same time, the MW field drives the spin transition from the bright $|0\rangle$ state to either of the dark $|\pm1\rangle$ states and thereby reduces the obtained PL intensity, but only if the MW is resonant with the respective transition. Therefore, by sweeping the frequency of the MW and monitoring the PL intensity, the transition frequencies can be probed.

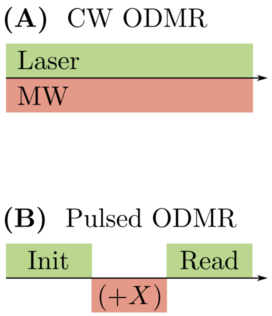

Figure 1.11: Optically detected magnetic resonance experiments can be conducted in two different modes. **(A)** The continuous wave scheme is comprised of a laser and microwave component that are both active all the time. While simple to implement, this scheme can lead to power broadening of the resulting spectral lines. **(B)** The pulsed approach decouples laser and microwave by playing only a π-pulse between initialization and readout, which drastically reduces overall power broadening at the cost of some experimental complexity.

In Figure 1.12 (A), we present the PL spectrum from such a CW ODMR experiment, taken on a single NV at a magnetic field of 80 G aligned with the NV symmetry axis. The two dips in PL are attributed to the $\omega_\pm$ transition frequencies, and their splitting is given by $2\gamma_{\mathrm{NV}}B_z$. Measuring the spectral position of these lines thus accounts to a direct measure of the applied magnetic field B_z.

The line shape of the CW ODMR lines are Lorentzian, with a width that is intrinsically limited by the electron spin's inhomogeneous dephasing time T_2^* [99] (see section 1.5.2). However, most of the time, CW ODMR experiments exhibit much broader lines, because both the laser and the MW drive can lead to significant power broadening. To minimize this power broadening, one has to reduce both laser intensity and MW power. Such a low power CW ODMR experiment is shown in Figure 1.12 (B), recorded at magnetic field of $B_z = 1.8\,\mathrm{G}$. Here, the two electronic lines are narrow enough to reveal the underlying ^{15}N hyperfine structure, given by two lines each with a splitting of $A_\parallel^{\mathrm{gs}}$ (the nuclear Zeeman effect is negligible for such low fields). Unfortunately though, applying such low MW powers also reduces the contrast of the lines, while low optical intensity increases the photon shot-noise, overall leading to significantly worse contrast and signal-to-noise ratio (SNR). For example, the data shown in panel (A) was integrated for only about two minutes, while the experiment in panel (B) ran for multiple hours.

In order to achieve the best of both worlds, that is ODMR with high contrast and narrow linewidth, one can employ pulsed ODMR [100]. Here, instead of continuously exposing the NV to both the laser and the MW field, the system is first pumped by the laser to prepare it in $|0\rangle$, followed by a MW π-pulse of variable frequency, and finally a short laser pulse is played for PL readout. This sequence is illustrated in

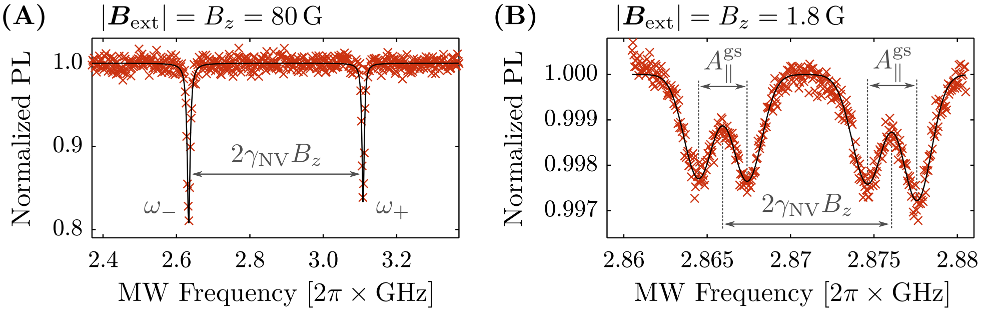

Figure 1.12: Optically detected magnetic resonance (CW mode) on the electron transitions $|0\rangle \leftrightarrow |-1\rangle$ and $|0\rangle \leftrightarrow |+1\rangle$. **(A)** Two dips in PL represent the resonance with either of above transitions, here measured on NVA2 (see table A.6 for a list of NVs) at an aligned magnetic field of $|\boldsymbol{B}_{\mathrm{ext}}| = 80\,\mathrm{G}$. The splitting of the two features is directly proportional to the longitudinal magnetic field component B_z. Lorentzian fits are shown in black. **(B)** Employing low laser and MW power reduces power broadening on the ODMR lines, such that the underlying ^{15}N hyperfine structure of the single NV at hand can be resolved, here measured on NVA1 at a small field of $B_z = 1.8\,\mathrm{G}$. The slight asymmetry with respect to $D_0^{\mathrm{gs}} = 2\pi \times 2.87\,\mathrm{GHz}$ is attributed to strain or stress in the diamond nanopillar.

Figure 1.11 (B). With this protocol, the laser is off during the MW spin manipulation, such that the laser power broadening is fully eliminated. In addition, by choosing low MW power for the π-pulse, the MW induced power broadening is minimized [100]. Figure 1.13 (A) shows a the PL spectrum of the $|0\rangle \leftrightarrow |-1\rangle$ transition of a single NV at an aligned field of 84 G, measured with each the CW and pulsed approach, with a π-pulse length of 800 ns. While both approaches can resolve the hyperfine structure, the data demonstrate how pulsed ODMR achieves significantly better contrast and linewidths within a fraction of the measurement time.

At magnetic fields near the ESLAC, the nuclear spin is hyperpolarized (see section 1.2.2). This can be verified with ODMR measurements, as shown in Figure 1.13 (B) where we repeat the same experiment as in panel (A), but at an aligned magnetic field of 512 G. Only one hyperfine line with approximately twice the contrast compared to panel (A) is detected, indicating that the entire nuclear spin population has been accumulated in one nuclear spin state. Here, the pulsed ODMR is measured with an even longer π-pulse compared to panel (A), namely 2400 ns, leading to a super narrow pulsed ODMR line with a width of less than 350 kHz. However, this is still ten times more than the intrinsic limit $(\pi T_2^*)^{-1}$, where $T_2^* \approx 11.3\,\mu\mathrm{s}$ is NVA2's spin dephasing time (see section 1.5.2), which indicates that there is still a significant amount of power broadening.

Figure 1.13 (B) highlights the advantages of operating the NV near the ESLAC. First, there is only one hyperfine line, meaning that quantum sensing experiments can be conducted on a single transition without any interference from off-resonantly driven hyperfine transitions. Second, this hyperpolarized transition has an increased contrast which leads to faster and more sensitive quantum sensing experiments.

Finally, we note that while we here introduced ODMR as a magnetometry scheme

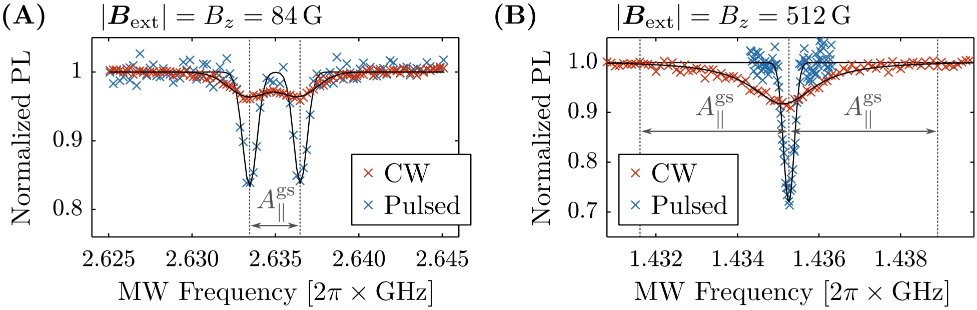

Figure 1.13: Comparison of CW ODMR to pulsed ODMR measurements, taken on NVA2, see table A.6 for a list of NVs. **(A)** Zoom onto one electronic transition at an aligned magnetic field of $|\boldsymbol{B}_{\text{ext}}| = 84\,\text{G}$. Low power CW ODMR can resolve the ^{15}N hyperfine lines, however, such a low power measurement has low contrast and therefore low SNR. Employing pulsed ODMR, here with a π-pulse length of 800 ns, drastically reduces power broadening effects and thereby boosts the contrast and SNR. The black line is a Lorentzian (Gaussian) fit of the CW (pulsed) data. **(B)** Same experiment as in (A), but at a magnetic field near the ESLAC. Under these conditions, the nuclear spin is hyperpolarized such that there is only one line in the ODMR spectrum with approximately twice the contrast. Here, the pulsed ODMR is measured with an even longer π-pulse compared to (A), 2400 ns, leading to a super narrow pulsed ODMR line of less than 350 kHz.

for measuring the axial magnetic field component B_z, it can also be used to measure the transverse field component $B_\perp$, because the spin energy levels are shifted by such transverse fields and thus the transition frequency is changing too. We utilize this in the appendix A.6 where we determine the entire vector $\boldsymbol{B}_{\text{ext}}$ for different tilt angles of a goniometric magnet stage. Last but not least, we comment that strain or stress in the diamond lattice [14], temperature [12] or electric fields [10] all affect the spin energy levels, and can thus be detected by ODMR as well.

1.4.2 Ramsey Free Induction Decay

An alternative yet largely equivalent way to measure magnetic fields is to investigate the quantum phase pick-up of a superposition state. On the Bloch sphere, without any active MW field, a superposition state will rotate about the $\boldsymbol{e}_z$ axis with an angular frequency equal to the MW detuning δ (as is evident from the discussion presented in section 1.3.2). This detuning can directly be related to a shift of the energy levels due to a deviation of the applied magnetic field from the calibrated bias field, and thereby enables DC magnetometry.

The pulse sequence that allows for the measurement of the described spin dynamics is called the Ramsey free induction decay (FID) [99, 101]. A schematic of this sequence is shown in Figure 1.14 (A), with the corresponding Bloch sphere trajectory in 1.14 (B). First, the optically initialized state $|0\rangle$ is rotated by a $+\pi_x/2$-pulse into an equal superposition state on the Bloch sphere's equatorial plane. During a subsequent free evolution of variable duration τ, the system accumulates a phase of $\varphi = \tau \cdot \delta$.

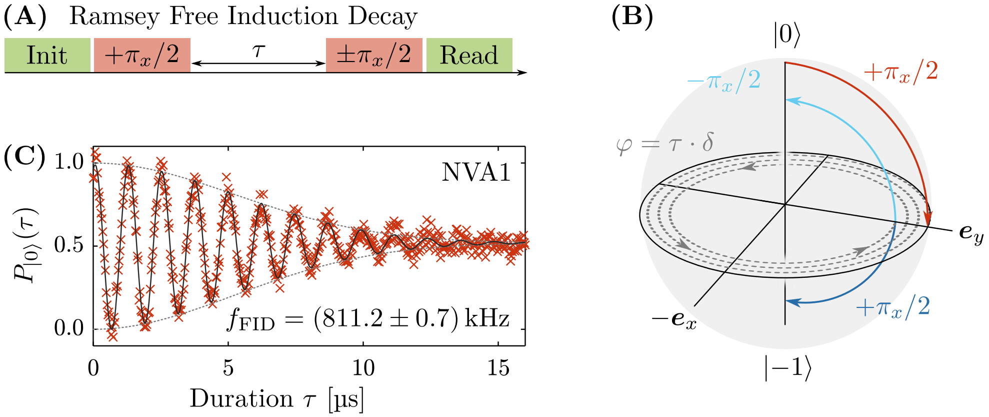

Figure 1.14: Ramsey free induction decay **(A)** Employed pulse sequence, comprised of an initial $+\pi_x/2$-pulse, a free evolution of variable duration τ, and a final $\pi_x/2$-pulse in either positive or negative direction. **(B)** Visualization of the corresponding Bloch sphere dynamics. After the initial $+\pi_x/2$-pulse the spin vector lies on the equatorial plane. In the subsequent free evolution, it rotates about the $\boldsymbol{e}_z$ axis with a frequency given by the detuning δ. Finally, to readout the accumulated quantum phase, the spin vector is rotated back onto the $\boldsymbol{e}_z$ axis by either a positive (dark blue) or negative (light blue) $\pi_x/2$-pulse. **(C)** Example Ramsey FID measurement taken on NVA1 at an aligned magnetic field of 533 G. We plot the difference of PL obtained from the two different $\pi/2$ readout pulses, and assign it to the probability $P_{|0\rangle}$. Least-Square fitting reveals a frequency of $f_{\mathrm{FID}} = (811.2 \pm 0.7)\,\mathrm{kHz}$ which corresponds to the detuning δ of the MW drive.

Afterwards, for optical readout, the spin state is projected back onto the $\boldsymbol{e}_z$ axis with either a positive or negative $\pi_x/2$-pulse. We then calculate the PL difference of the two readout projections, and map this PL difference onto the probability $P_{|0\rangle}$.
Exemplary single NV Ramsey FID data are shown in Figure 1.14 (C). They were taken on a single hyperpolarized ODMR line near the ESLAC at an aligned magnetic field of 533 G. We fit an oscillation frequency of $f_{\mathrm{FID}} = (811.2 \pm 0.7)\,\mathrm{kHz}$, indicating a magnetic offset of $\Delta B_z = 2\pi f_{\mathrm{FID}}/\gamma_{\mathrm{NV}} \approx (289.7 \pm 0.3)\,\mathrm{mG}$.
Finally, we point out that the oscillation presented in Figure 1.14 (C) exhibits a decaying Gaussian envelope with a characteristic decay constant denoted by T_2^*, in this case fitted to $(7.403 \pm 0.003)\,\mu\mathrm{s}$. This decay stems from interaction with the noisy environment. The characterization of this environment, as well as the art of dynamically decoupling the spin from it, is a large field of quantum research and the focus of the next section, where we discuss various different noise spectroscopy approaches.

1.5 Noise Spectroscopy

In the context of spin-based quantum sensing, noise spectroscopy describes the study of the spin's environment based on measurements of the lifetime of spin population and quantum phase. Both these quantities have finite lifetimes that are limited by the noisy environment that solid-state spins like the NV center are constantly exposed to. In the specific case of the NV, such environmental noise sources can be phonons or other spins in the diamond lattice, fluctuations in amplitude or frequency of applied magnetic fields, and especially for shallow NVs surface-bound spins and magnetic materials on the diamond surface. All these different kind of noise sources in the environment affect the spin in different ways and thus lead to different kinds of spin deterioration, specifically either a loss of spin population (= relaxation) and/or a randomization of the spin state's quantum phase (= dephasing). Therefore, by measuring how fast specific properties of the NV spin are altered, one can characterize the NV center's noise environment.

The challenge in such noise spectroscopy is to tell different noise sources of the environment apart from each other. One solution for this is so-called dynamical decoupling [36, 37], where specific MW pulse sequences are employed to manipulate the spin in a way that alters its response to the environment, effectively filtering what kind of noise is still perceived by the spin [38]. Depending on what pulse sequence is played, it is possible to either decouple the spin entirely from particular noise frequencies, or to tune it especially receptive to a target noise frequency. While the former is typically used to increase the spin coherence time in sensing applications to boost sensitivity [39, 40], the latter is very useful for frequency selective spectroscopy of the environment [41, 42] and in particular for nuclear magnetic resonance (NMR) experiments [43–45].

For shallow NVs, while there are relevant non-magnetic noise sources like electric fluctuations [102], the most important noise contribution is the magnetic environment [41, 42, 103], typically originating from spins in the lattice or most importantly, paramagnetic impurities on the surface. Mathematically, these magnetic fluctuations are described by the magnetic noise spectral density, which – according to the Wiener-Khinchin theorem – is equal to the Fourier transformation of the autocorrelation function $G(\tau)$ of the corresponding magnetic noise field [104, 105]. For the environmental spin baths considered in this thesis (i.e. statistically polarized nuclei for nanoscale NMR) the key dephasing mechanism is molecular diffusion of spins in and out of the NV sensing volume, which leads to a decay of the bath's autocorrelation function that is typically considered to be exponential [51, 103–106]. Therefore, we describe the autocorrelation function $G(\tau)$ with an exponential decay of characteristic time scale τ_c, called the autocorrelation time. Fourier transformation then yields the magnetic noise spectral density

$$S_k(\omega) = B^2_{\mathrm{rms},k} \, \frac{\tau_c}{1+\omega^2\tau_c^2} \,, \tag{1.21}$$

where $B^2_{\mathrm{rms},k}$ is the root mean square magnetic noise amplitude along unit vector $\boldsymbol{e}_k$ with $k \in \{x, y, z\}$. Alternatively, $B^2_{\mathrm{rms},k}$ can be identified as the variance of the magnetic field fluctuations along $\boldsymbol{e}_k$. Equation (1.21) states that the noise spectrum in each coordinate direction is a Lorentzian distribution around zero, with a FWHM of $2/\tau_c$ (sometimes called random telegraph noise). Note that there are different conventions for the normalization of $S_k(\omega)$; we are here using the definition from [104]. A sketch of $S_k(\omega)$ is shown in Figure 1.15.

In the following, we will introduce five different pulse sequences that can be used for relaxometry or noise spectroscopy. For each of these five sequences, we will define

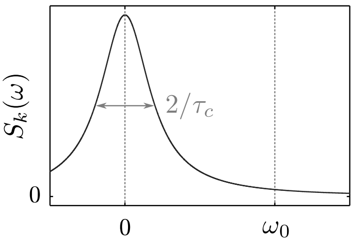

Figure 1.15: The magnetic noise spectral $S_k(\omega)$ is a Lorentzian distribution centered at zero, with a width of $2/\tau_c$. For spin baths surrounding the NV center, the correlation time τ_c is typically on the order of a few microseconds for electronic spins, up to milliseconds for nuclear spins, such that the corresponding width is expected to be narrow compared to the NV resonance frequency w_0 of a few GHz.

the characteristic NV spin decay time, discuss what kind of noise they tune the NV spin sensitive to, and in particular, we investigate what spectral components of the magnetic noise spectral density $S_k(\omega)$ are the dominant magnetic noise contributions for the given pulse sequence. An overview of these results in shown at the end of the chapter in table 1.2.

1.5.1 Spin-Lattice Relaxation

The first sequence we investigate is the simplest sequence possible: Doing nothing to the spin at all. To be specific, after preparing the spin in state $|0\rangle$ with the laser, the system is left to evolve freely for a duration τ, after which the spin state is optically read out. This sequence essentially measures how eigenstate $|0\rangle$ is behaving under unprotected exposure to the noisy environment. In order to conduct the same measurement on the other eigenstate of the two-level system at hand, $|-1\rangle$, one can insert a π-pulse before the free evolution. These two pulse sequences are depicted schematically in Figure 1.16 (A).

During the free evolution τ, the prepared eigenstate is only sensitive to noise that can transfer spin population between the two eigenstates; and the presence of such noise leads to a decay of the eigenstate into a thermally mixed state with a characteristic time scale called T_1. This T_1 decay takes the functional form of a simple exponential decay $\propto \exp(-\tau/T_1)$, which can be derived with spin temperature considerations [104] or *ab initio* calculations [107]. Furthermore, to study the exact dependency of the exponential T_1 relaxation on the noise spectral density $S_k(\omega)$, one can employ the Redfield theory of relaxation [104, 105, 108]. As we show in detail in the appendix A.4, the Redfield theory reveals that the noise spectral density $S_k(\omega)$ and the resulting T_1 decay time are related by the expression [104]

$$\frac{1}{T_1} = \gamma_{\mathrm{NV}}^2 \Big(S_x(\omega_0) + S_y(\omega_0) \Big) . \tag{1.22}$$

Equation (1.22) demonstrates that the magnetic contribution to T_1 is generated by magnetic fluctuations transverse to the NV quantization axis with a frequency that is resonant with the spin transition ω_0. This also follows trivially from the results of section 1.3 where we have shown that the necessary Hamiltonian to perform a spin flip is given by just such a resonant AC transverse magnetic field. Importantly, at room temperature the magnetic noise components at frequency ω_0 are predominantly generated by phonons in the diamond lattice. Consequently, T_1 exhibits a strong temperature dependence [109]. Depending on the given temperature, but also the purity of the diamond and the NV depth, NV T_1 times can vary from a few hundreds of microseconds up to minutes [110]. Note that due to this strong dependence on the phononic environment, T_1 is often called the spin-lattice relaxation time.

At room temperature, thermal excitation and phonon-mediated spin relaxation are competing against each other. This means that T_1 relaxation transfers the spin into a thermal equilibrium state that is usually close to the equal 50:50 mixture, i.e. the Bloch sphere origin. The Bloch sphere trajectory of such spin-lattice relaxation at room temperature is illustrated in Figure 1.16 (B). At cryogenic temperatures in the mK regime, however, thermal excitation is ineffective since $k_B T \ll \hbar D_0^{\mathrm{gs}}$, such that the thermal equilibrium is shifted close to $|0\rangle$.

An example of a T_1 measurement is shown in Figure 1.16 (C), taken on NVA2 (see table A.6 for a list of NVs), where we measure the PL as a function of τ with each of the two sequences in Figure 1.16 (A), subsequently take the difference of the two PL curves and assign it to the probability $P_{|0\rangle}$. The data show a clear exponential decay, to which we fit $T_1 = (590 \pm 64)\,\mu\mathrm{s}$. This is a typical value for shallow NVs in diamond sample A (see appendix A.2 for a description of our diamond samples). NVA1 is another shallow NV in this diamond, for which we have determined $T_1 = (298 \pm 11)\,\mu\mathrm{s}$. For deeper NVs in diamond A, such as NVA3 and NVA4, however, we find much longer T_1 times of more than two milliseconds.

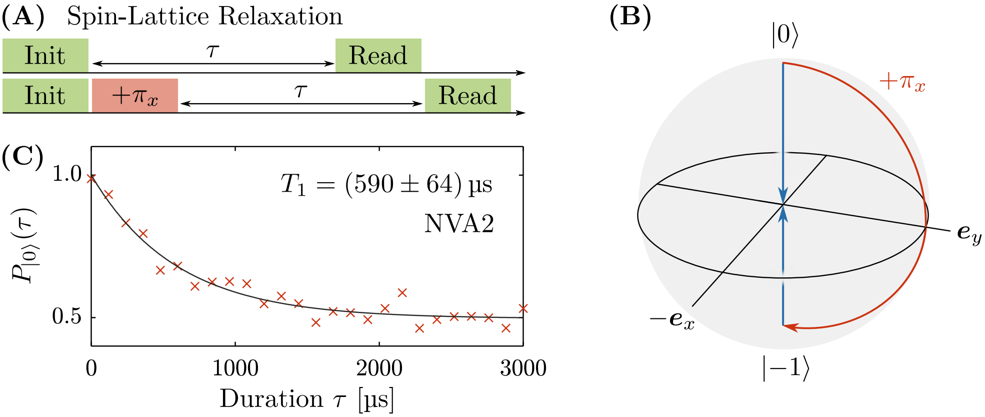

Figure 1.16: Spin-Lattice Relaxation **(A)** The T_1 spin-lattice relaxation time is measured by a pulse sequence that is simply a free evolution combined with the usual optical initialization and readout. To take T_1 on the $|-1\rangle$ state, a π-pulse can be added. **(B)** Corresponding Bloch sphere trajectory for either of the sequences shown in (A). At room temperature, the spin decays along the $\boldsymbol{e}_z$ axis towards a thermal equilibrium state close to the Bloch sphere origin. **(C)** Example T_1 measurement, taken on NVA2, a shallow single NV in a diamond nanopillar. The measured PL of both sequences from (A) is subtracted from each other and mapped onto the probability $P_{|0\rangle}$. The black line is a single exponential fit yielding $T_1 = (590 \pm 64)\,\mu\mathrm{s}$.

1.5.2 Ramsey Free Induction Decay (Again)

In addition to the longitudinal relaxation of the spin population due to T_1 processes, there is also decay of the transverse spin component. Since this component is given by the phase of the quantum state, people commonly refer to such transverse decay processes as dephasing. One way to measure such spin dephasing is to employ the Ramsey FID sequence [99,101], shown in Figure 1.17 (A), that we have previously introduced in section 1.4.2 as a magnetometry tool. However, it also serves as a simple measure of dephasing, since the superposition state prepared by the initial $\pi/2$-pulse acquires a phase of $\tau \cdot \delta$ during the free evolution τ, meaning that any noise on the detuning δ leads to a slightly different accumulated phase in each experiment repetition. This "fanning out" of spins corresponding to separate experiment runs is illustrated in Figure 1.17 (B). Ultimately, when averaging over many of such experimental runs, one observes a decay of the spin vector length, demonstrating the loss of phase information due to noise on the detuning. The corresponding decay time is called the T_2^* coherence time.

The noise on the detuning that causes a T_2^* decay is mainly originating from magnetic fluctuations that introduce fluctuations of the energy of the spin levels, such as noise on the magnetic bias field, the interaction of the NV spin with other spins in the lattice such as ^{13}C nuclei, or surface-bound magnetic impurities. Apart from such magnetic noise sources, there are various other things that could in principle also affect the spin energy levels and thus contribute to T_2^*, such as fluctuations in the electric, mechanical or phononic environment, however, we here focus on just the magnetic environment.

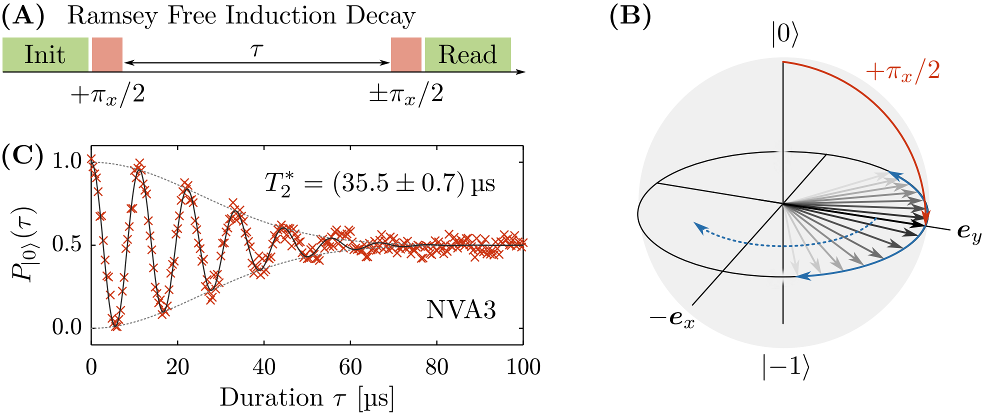

Figure 1.17: Ramsey free induction decay **(A)** Pulse sequence employed to measure the T_2^* dephasing time. **(B)** The corresponding Bloch sphere trajectory for different experimental runs at an average detuning of zero. Due to magnetic fluctuations, the detuning is different in each experiment repetition, as indicated by the different spin vectors. On average, this leads to a loss of phase information (solid blue), combined with a net rotation for a non-zero average detuning (dashed blue). **(C)** Example T_2^* measurement, taken on NVA3 at an aligned field of 507 G, a deep single NV, where the PL difference from either readout projection pulse is assigned to $P_{|0\rangle}$. Fitting a cosine function with a Gaussian decay envelope yields $T_2^* = (35.5 \pm 0.7)$ µs.

We can once more evoke the Redfield relaxation theory to relate T_2^* to the magnetic noise spectral density $S_k(\omega)$, resulting in [104]

$$\begin{aligned}\frac{1}{T_2^*} &= \gamma_{\mathrm{NV}}^2\, S_z(0) + \frac{1}{2}\gamma_{\mathrm{NV}}^2\Big(S_x(\omega_0) + S_y(\omega_0)\Big) \\ &= \gamma_{\mathrm{NV}}^2\, S_z(0) + \frac{1}{2T_1}\,.\end{aligned} \tag{1.23}$$

A detailed derivation of this expression is presented in the appendix A.4.2. This equation implies three important things. First, any relaxation of the spin population does always also cause some degree of dephasing, as is evident by the appearance of T_1 in the expression for T_2^*. Second, this means that T_2^* is always shorter than $2T_1$. Third, any excess dephasing rate exceeding $1/(2T_1)$ stems from magnetic noise at zero frequency. Notably, this is exactly where the noise spectral density $S_z(\omega)$ is maximal, meaning that the Ramsey FID sequence is sensitive to the spectral window where the most noise is expected to be present. In this sense, because it decouples the NV spin from everything but the main noise peak, one could consider the Ramsey FID the least effective noise filter possible.

Another approach to describing T_2^* dephasing is to treat the Ramsey FID as a dynamical decoupling filter problem [3, 38], wherein the employed sequence is described by a filter function $F(\omega)$ that filters the longitudinal noise spectral density $S_z(\omega)$ to obtain the spin coherence $C(\tau)$ as a function of sequence length τ, given by

$$C(\tau) = \exp\left(-\frac{2}{\pi}\int_0^\infty S_z(\omega)F(\omega)\mathrm{d}\omega\right)\,. \tag{1.24}$$

For the Ramsey FID, one can derive the filter function [3, 38, 111]

$$F_{\mathrm{FID}}(\omega) = \frac{1}{\omega^2}\sin^2\left(\frac{\omega\tau}{2}\right)\,. \tag{1.25}$$

Note that [111] has an additional factor of 2 in the definition of their filter function that needs to be removed to match the convention of [3] and [38] that we are using in this thesis.

Equation (1.25) describes how sensitive the spin is to noise at the frequency ω under the Ramsey FID sequence. The sequence thus acts like a sinc-filter, centered at zero and with a low-pass cut-off of roughly π/τ, meaning that predominantly zero frequency noise is allowed to affect the spin under the Ramsey sequence. The filter function formalism is therefore in agreement with the Redfield result from above, however, $F_{\mathrm{FID}}(\omega)$ has higher harmonic peaks at non-zero frequencies and thus accurately describes the pick-up of higher frequency noise; physics that the Redfield approach is not describing. On the other hand, the filter formalism considers only magnetic fluctuations in $\boldsymbol{e}_z$ direction and can therefore not account for the $1/(2T_1)$ contribution of transverse noise at frequency ω_0 which the Redfield theory is very much capable of describing.

Figure 1.17 (C) shows a T_2^* measurement, and we fit a Gaussian decay to find a dephasing time of $T_2^* = (35.5 \pm 0.7)\,\mu\mathrm{s}$. Such a Gaussian envelope $\propto \exp\left[-(\tau/T_2^*)^2\right]$ is to be expected for Ramsey FID in the presence of a Lorentzian noise source, which can be derived by evaluating (1.24) with the expressions from (1.21) and (1.25). The

T_2^* time of a few tens of microseconds observed here is pretty representative for what we usually measure on deep single NVs in diamond A, such as NVA3 and NVA4. Shallow NVs in the same diamond, such as NVA1 and NVA2, show T_2^* times of only up to ten microseconds (see table A.6), demonstrating the significant influence that surface proximity has on the resulting T_2^* time.

1.5.3 Spin-Echo

To improve the dephasing time T_2^* obtained via Ramsey FID, one can employ the so-called Spin-Echo sequence [112, 113]. It is constructed by inserting a π-pulse into the Ramsey sequence, such that the free evolution time is split into two equal parts of duration τ each, as shown in Figure 1.18 (A). This additional π-pulse effectively inverts the sign of the phase accumulation during the second evolution time. Consequently, there is no phase randomization as long as the noise-induced detuning is constant throughout the entire sequence.

In the Bloch sphere picture, as shown in Figure 1.18 (B), this can be well illustrated by considering the spin trajectories of individual experiment repetitions. As we have discussed in the context of Ramsey FID, the spin vectors corresponding to different experiment runs are "fanning out" during the first evolution period. After being flipped by the π-pulse, they continue to rotate with the same individual angular velocities, leading to a refocussing of all vectors by the end of the second free evolution. On taking the average over all experiment repetitions, one finds zero dephasing at the end

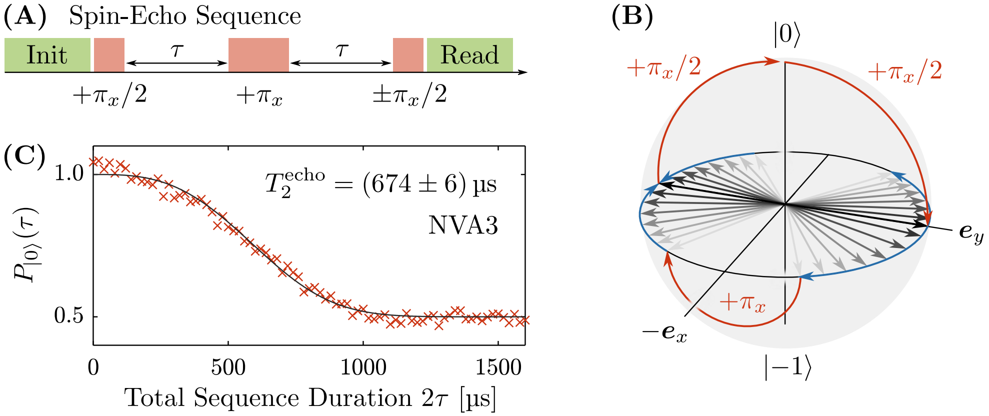

Figure 1.18: Spin-Echo relaxation **(A)** Pulse sequence employed to measure the T_2^{echo} decoherence time. **(B)** The corresponding Bloch sphere trajectory for different experimental runs at $\delta = 0$. The π-pulse in between the two equal free evolution periods inverts the phase accumulation for the second period, causing the spin trajectories of separate experiment repetitions to refocus, effectively eliminating of phase randomization due to low-frequency magnetic noise. **(C)** Example T_2^{echo} measurement, taken on NVA3 at an aligned field of 507 G, a deep single NV, where the PL difference from either readout projection pulse is assigned to $P_{|0\rangle}$. Fitting a decay proportional to $\exp\left[-(\tau/T_2^{\text{echo}})^3\right]$ yields the spin coherence time $T_2^{\text{echo}} = (674 \pm 6)$ µs.

of the sequence, because the average spin vector length has perfectly converged back to one. However, this is only true if the detuning δ is constant throughout each individual experiment repetition, e.g. if there is only zero-frequency noise present. High frequency noise leads to fluctuations in δ throughout the sequence and thus breaks the perfect refocussing by the end of the sequence. This means that measuring $P_{|0\rangle}$ as a function of τ still yields a coherence decay, although a much slower one compared to the Ramsey sequence's T_2^*. We denote this homogeneous decoherence time under the Spin-Echo sequence as T_2^{echo}.

Depending on the depth of the NV center at hand, and the purity of the surrounding diamond material, the T_2^{echo} time can reach up to 2 ms [21]. In our case, we use diamond sample A that is isotopically purified, and as shown in Figure 1.18 (C), we find $T_2^{\text{echo}} = (674 \pm 6)\,\mu\text{s}$ for NVA3. This is clearly longer than the T_2^* time of about 35 µs we have measured on the same NV, see Figure 1.17 (C).

To compare T_2 and T_2^* more quantitatively, we once more employ the filter function formalism. The Spin-Echo sequence is described by the filter function [111]

$$F_{\text{echo}}(\omega) = \frac{4}{\omega^2} \sin^4\left(\frac{\omega\tau}{2}\right) , \tag{1.26}$$

which is exactly zero at $\omega = 0$, demonstrating that Spin-Echo does indeed perfectly decouple from zero frequency noise. At the same time, $F_{\text{echo}}(\omega)$ has a maximum at approximately $\omega \approx \pm\pi/\tau$, highlighting that depending on the choice of τ, there is a frequency component that is picked up especially well. Importantly, evaluation of equation (1.24) with the Lorentzian noise spectral density (1.21) and the filter function (1.26) yields a coherence decay that goes with $\exp\left[-(\tau/T_2^{\text{echo}})^3\right]$, which is what we used to fit the data from Figure 1.17 (C).

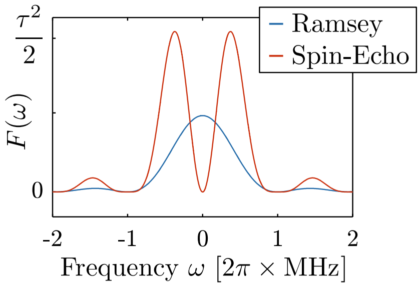

Figure 1.19: Filter functions of the Ramsey FID and Spin-Echo sequences, each plotted for $\tau = 1\,\mu\text{s}$. While the Ramsey function acts like a zero-frequency bandpass filter, the Spin-Echo sequence is efficiently filtering out the zero-frequency noise components and is instead most sensitive to frequencies at roughly $\omega \approx \pm\pi/\tau$, with a bandwidth $\sim \pi/\tau$.

In conclusion, Spin-Echo is a simple technique that elevates the coherence time of the Ramsey FID to significant longer times. As such, it is particularly useful for pulsed quantum sensing applications where the sensitivity relies crucially on long coherence times. Furthermore, while Spin-Echo decouples the spin from zero-frequency noise, it simultaneously maximizes the spin sensitivity to noise at approximately $\pm\pi/\tau$, meaning that by varying τ, the Spin-Echo sequence can in principle be used for frequency selective spectroscopy of the noise environment. However, the width of the probed spectral window does also scale inversely proportional with τ, leading to poor frequency selectivity especially in the high-frequency regime.

In the remainder of this section, we will discuss two more sequences that are both not only exhibiting even longer coherence times, but that are also capable of probing the noise spectral density in a spectral window whose position and width are independent of each other, allowing for sharp noise filtering at arbitrary frequencies. With these sequences, high-resolution noise spectroscopy, and in particular nuclear magnetic resonance experiments can be realized.

1.5.4 XY8-k Multipulse Sequence

A common approach to further improving the coherence time of the Spin-Echo sequence is to build multipulse sequences, where many Spin-Echo blocks of the form $(\tau/2) - (\pi) - (\tau/2)$ are concatenated into a long pulse train of N π-pulses separated by a free spacing of τ. This is the so-called Carr-Purcell-Meibom-Gill (CPMG) sequence [3, 36, 114], the simplest multipulse sequence. And while it provides superior low-frequency noise decoupling compared to the Spin-Echo, as well as better noise spectroscopy properties, it has two very clear weaknesses: First, it only decouples from magnetic noise along the spin symmetry axis, and not from transverse fluctuations. Second, the CPMG sequence is highly susceptible to errors on the π-pulses. For example, using a π-pulse just slightly too long in a CPMG consisting of hundreds of these pulses leads to drastic pulse error accumulation.
Remedy to these two issues is offered by the XY-type sequences [115] where instead of N identical π-pulses, one concatenates pulses that are 90° phase shifted relative to each other. For example, the so-called XY8-k sequence consists of eight π-pulses with a symmetric phase cycle. These eight pulses form one XY8-block, that is then repeated k times. This particular sequence is illustrated in Figure 1.20 (A). Due to the way the phase is alternated between pulses, the sequence is dynamically correcting

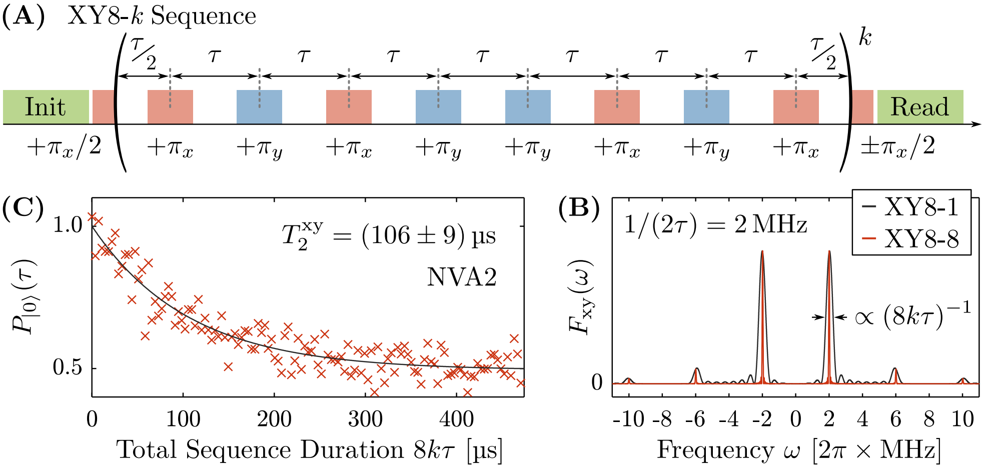

Figure 1.20: The multipulse XY8-k sequence **(A)** Schematic illustration of the XY8-k sequence. **(B)** Normalized plot of the corresponding filter function, plotted for an inter-pulse spacing of 250 ns, once for XY8-1 and XY8-8. The resulting filter function has a main peak at $f = (2\tau)^{-1}$ and a width that scales inversely with k. Higher harmonic peaks live at odd multiples of f. **(C)** Example T_2^{xy} measurement, taken on NVA2 at 308 G with $\tau = 456$ ns (corresponding to $f = 1.1$ MHz). The black line is a single exponential fit ($\alpha = 1$) yielding $T_2^{\mathrm{xy}} = (106 \pm 9)$ µs.

small errors in the spin flip angle induced by the π-pulses (i.e. errors in the pulse frequency, amplitude or phase), and in addition XY8-k is decoupling from magnetic fluctuations along any axis, thus solving both of the common issues with CPMG while inheriting its advantages [116, 117].

The spin decoherence under the XY8-k sequence occurs on a timescale denoted by T_2^{xy}. We measure T_2^{xy} on NVA2 at 308 G by monitoring the PL as a function of k while keeping τ constant at 456 ns. The result is shown in Figure 1.20 (C), and by fitting a single exponential decay we infer that $T_2^{\mathrm{xy}} = (106 \pm 9)\,\mu\mathrm{s}$ (we justify this choice of fitting function further below). This value is very long compared to this NV's T_2^{echo} time of only a few tens of microseconds. For NVs that are located in the same diamond but that are less shallow than NVA2, we find T_2^{xy} times of up to a few milliseconds, see table 1.2.

Let us now investigate the decoupling mechanism of the XY8-k sequence a bit more rigorously. To that end, we once more use the filter function formalism. It turns out that XY8-k filter function is identical to that of a CPMG sequence with $N = 8k$ pulses [3, 51], and yields [111]

$$F_{\mathrm{xy}}(\omega) = \frac{4}{\omega^2} \sin^2\left(8k \cdot \frac{\omega\tau}{2}\right) \sin^4\left(\frac{\omega\tau}{4}\right) \cos^{-2}\left(\frac{\omega\tau}{2}\right) . \tag{1.27}$$

This filter function is plotted in Figure 1.20 (B) for a π-pulse spacing of $\tau = 250$ ns and for k equal to either one or eight. Let us point out a few critical things about this filter function: First, there is a global maximum at the frequency $\omega = \pm\pi/\tau$, respectively at $f = \pm 1/(2\tau)$, indicating that the sequence is tuning the spin sensitive to a noise frequency defined by the π-pulse spacing τ. Consequently, by choosing an appropriate τ, one can probe the noise spectral density at any arbitrary position. On the other hand, for very small values of τ, the main peak of $F_{\mathrm{xy}}(\omega)$ is shifted to high frequencies, meaning that in this case, XY8-k is an excellent filter for decoupling from low-frequency noise. Second, the width of the peaks in $F_{\mathrm{xy}}(\omega)$ scale with the inverse of the total sequence length. This total sequence length can be set independently of τ by tuning k, and therefore one can achieve a narrow noise filter at any given frequency – a key prerequisite for noise spectroscopy applications that is not possible in Spin-Echo. Third, the filter function of such a multipulse sequence is always a periodic function, and as such it exhibits secondary peaks at higher harmonic frequencies. In the case of XY8-k, these harmonic peaks are located at odd multiples of the main peak, namely at $3f$, $5f$, $7f$ etc.

One can use the XY8-k filter function, as dictated by equation (1.24), to compute the spin decoherence as a function of total sequence duration t_{tot}. Specifically, for generalized noise with $S(\omega) \propto \omega^{-\beta}$ where $0 < \beta \leq 2$, it has been shown that the XY8-k filter function from equation (1.27) leads to a coherence decay of $C(t_{\mathrm{tot}}) \propto \exp\left(-[t_{\mathrm{tot}}/T_2^{\mathrm{xy}}]^{\alpha}\right)$, where $T_2^{\mathrm{xy}} \propto (8k)^{\beta/\alpha}$ and $\alpha = (\beta + 1)$ [118]. Consequently, depending on the noise, XY8-k shows a different form of decoherence as characterized by the exponent α. Specifically, in the case of a Lorentzian noise spectral density $S_k(\omega)$ as given by equation (1.21), the ω^{-2} tail typically dominates the decoherence under dynamical decoupling, such that $\alpha \approx 3$. In our experiments, however, we deal with a special case wherein the total amount of π-pulses is not kept constant, because we sweep t_{tot} by tuning k at a fixed value of τ. For such a scenario, above theory predicts a single exponential decay ($\alpha = 1$) independent of β, respectively of the noise environment. This can be derived by substitution of $t_{\mathrm{tot}} = 8k\tau$, which results in $C(8k\tau) \propto \exp(-8k\tau/T_2^{\mathrm{xy}})$ with $T_2^{\mathrm{xy}} \propto \tau^{-\beta}$. This theoretical prediction is consistent with our experimental data, because as shown in Figure 1.20 (C), fitting such a single exponential yields great agreement with the observed PL decay.

Note that equation (1.27) is only valid under the assumption of perfectly sharp π-pulses. In any real-world implementation of the XY8-k sequence, however, the π-pulses have a non-zero length. One consequence of such non-zero pulses is that they introduce additional harmonic peaks in the filter function, due to a phase accumulation stemming from spin rotations during the π-pulse [119]. For the XY8-k sequence, these additional harmonics are fractions either smaller ($\frac{1}{2}f$ and $\frac{1}{4}f$) or larger ($\frac{3}{2}f$, $\frac{5}{2}f$, etc. and $\frac{5}{4}f$, $\frac{7}{4}f$, etc) than the main frequency f. In the context of non-zero π-pulses, we further remark that τ is defined from pulse center to pulse center, meaning that the sequence breaks down when the pulses assume a length comparable to τ.

A famous use-case of the XY8-k sequence is nuclear magnetic resonance (NMR) [43–45], where the sequence is deployed with fixed k and variable τ to probe the noise spectral density and thereby detect the magnetic signal of Larmor precessing nuclear spins located nearby the NV center. This way, one can identify what nuclear species are present on the diamond surface [46, 120], and for known nuclear targets, one can infer the NV depth from the coupling strength [51]. In this thesis, we will perform such NMR experiments based on XY8-k and compare them to Spin-Lock NMR in chapter 4, and ultimately use both for single NV depth determination in chapter 5.

1.5.5 Spin-Locking

So far, we have had an extensive discussion on Ramsey FID, Spin-Echo and XY8-k, that are all ultimately based on the manipulation of a superposition state's phase accumulation. Now, we introduce spin-locking [3, 104] that is a very different relaxometry approach much more similar to the T_1 spin-lattice relaxation in that its core mechanism is an energy relaxation instead of a phase acquisition process.

The key idea behind spin-locking is to bring the spin system into a superposition state with a $+\pi_x/2$-pulse and then apply a resonant continuous MW field whose phase matches the superposition state's phase. On the Bloch sphere in the rotating frame, this means that the field and the spin vector are aligned along the $\boldsymbol{e}_y$ axis, as depicted in Figure 1.21 (B). Such an aligned and resonant field has two important effects on the spin: First, it prevents the spin state from accumulating any phase, effectively locking it along the field vector, hence the name spin-locking. Second, the microwave field defines a new quantization axis in the rotating frame, which results in new eigenstates, i.e. the dressed states $|\pm\rangle$. On the Bloch sphere, these dressed states point along the MW field vector, and they are split in energy by $\hbar\Omega_R$ (see section 1.3.1), where Ω_R denotes the Rabi frequency of the spin-locking MW field. Therefore, in the rotating frame, the phase-locked state is in fact just the eigenstate $|+\rangle$, and its decay is given by an energy relaxation process, and not a dephasing process. We call the characteristic timescale of this decay the rotating frame relaxation time $T_{1\rho}$.

In Figure 1.21 (A), there is a sketch of the entire Spin-Lock sequence, including a final $\pm\pi_x/2$-pulse for projection on the $\boldsymbol{e}_z$ axis for optical spin readout, and in Figure 1.21 (C), we show an exemplary measurement of $T_{1\rho}$. This measurement was

conducted on the shallow NVA2 at a magnetic field of 308 G with a Rabi frequency of $\Omega_R = 1.1\,\text{MHz}$. The resulting spin decay data are fitted with a single exponential function yielding $T_{1\rho} = (115 \pm 10)\,\mu\text{s}$ (we will justify this functional form of spin relaxation under Spin-Lock below). Note how this value is very similar to the T_2^{xy} time we have obtained on the same NV at the same noise frequency, see Figure 1.20 (C), indicating that these sequences exhibit comparable noise sensitivity. We will compare these two sequences, and especially their sensitivity in NMR-type experiments, in more detail in chapter 4. Finally, we note that we obtain $T_{1\rho}$ times of up to a few milliseconds on deeper NVs, see table 1.2.
Analogous to the T_1 relaxation process, the magnetic noise that predominantly contributes to the $T_{1\rho}$ relaxation are fluctuations resonant with the spin transition frequency. The crucial difference is that while for T_1 processes the relevant transition frequency has a magnitude of a few GHz, for the dressed states in a spin-lock scheme it is given by the Rabi frequency Ω_R of the spin-locking field – a frequency that is typically in the MHz regime. Therefore, by experimentally controlling Ω_R, the spin can be tuned sensitive to specific MHz noise frequencies [121,122]. This means that in the context of dynamical decoupling and noise spectroscopy, the spin-locking approach is a promising alternative to the aforementioned phase accumulation based schemes. In this thesis specifically, we will use the Spin-Lock sequence for NMR-type experiments. Note that the underlying idea of Spin-Lock NMR, that is tuning the dressed state energy splitting to the frequency of a nuclear spin precession, was originally proposed

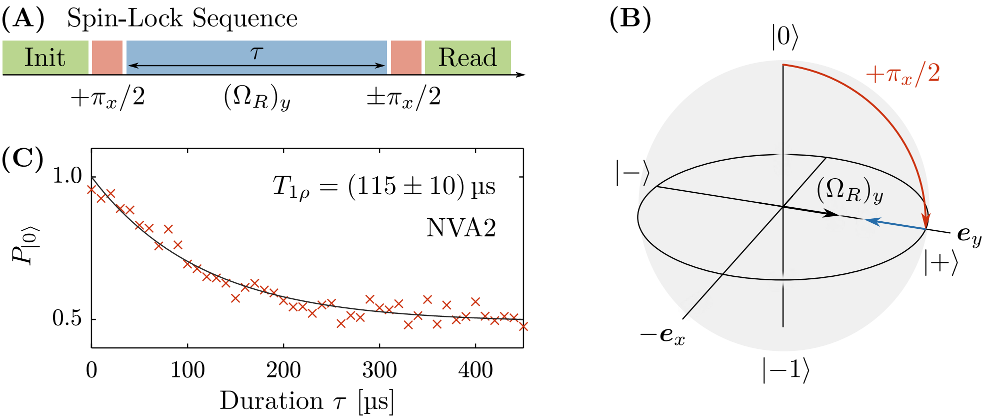

Figure 1.21: Spin-Locking **(A)** The Spin-Lock sequence is identical to the Ramsey FID, but instead of a free evolution between the $\pi/2$-pulses, there is a resonant MW field with a 90° phase-shift relative to the $\pi/2$-pulses. **(B)** On the Bloch sphere, the spin-locking field is aligned with the spin vector after the initial $\pi/2$-pulse, leading to an effective locking of the spin onto the field. Due to the field, there is a new eigenbasis given by the dressed states $|\pm 1\rangle$ that point along the MW field. The resulting energy relaxation along this new quantization axis is the rotating frame relaxation time $T_{1\rho}$. **(C)** Example $T_{1\rho}$ measurement, taken on NVA3 at an aligned field of 308 G and $\Omega_R = 1.1\,\text{MHz}$, where the PL difference from either readout projection pulse is assigned to $P_{|0\rangle}$. Fitting a single eponential decay (black) yields $T_{1\rho} = (106 \pm 9)\,\mu\text{s}$.

by Hartmann and Hahn [123], and for this reason this mechanism is often referred to as Hartmann-Hahn resonance.

To illustrate the physics of spin-locked $T_{1\rho}$ relaxation in a more quantitative way, we use the Redfield theory to derive a proper expression for the $T_{1\rho}$ relaxation time (see the appendix A.4.3 for the full derivation). In the limit of weak driving $\Omega_R \ll \omega_0$, as is the case in our experiments, we find

$$\begin{aligned} \frac{1}{T_{1\rho}} &= \gamma_{\mathrm{NV}}^2\, S_z(\Omega_R) + \frac{1}{2}\gamma_{\mathrm{NV}}^2 \Big(S_x(\omega_0) + S_y(\omega_0) \Big) \\ &= \gamma_{\mathrm{NV}}^2\, S_z(\Omega_R) + \frac{1}{2T_1}\,, \end{aligned} \tag{1.28}$$

where ω_0 is the splitting of the undriven eigenstates. Similar expressions are reported by [3, 103, 121, 124]. The result highlights the dependence of $T_{1\rho}$ on magnetic noise at the frequency Ω_R. Interestingly, it is exactly the same expression as we have seen earlier for T_2^* in equation (1.23), but instead of the $S_z(0)$ term we here obtain $S_z(\Omega_R)$. This makes sense because in the limit of $\Omega_R \to 0$, the Spin-Lock sequence becomes a Ramsey FID. In the limit of infinitely strong driving where $S_k(\Omega_R) \to 0$, the first term vanishes and thus $T_{1\rho}$ is limited by $2T_1$. Conversely, for weak driving (as is the case in our experiments) and for a Lorentzian magnetic noise spectral density as given by equation (1.21), the first term in equation (1.28) is the dominant contribution to $T_{1\rho}$, resulting in $T_{1\rho}$ times that are smaller than T_1. A comparison of typical decoherence time values for shallow and deep NVs in our diamond sample A is presented in table 1.2.

Finally, we point out that the fact that the underlying spin decay process in $T_{1\rho}$ relaxation is the same as in T_1 relaxation, i.e. a population decay along the respective quantization axis caused by transverse noise at the respective spin transition frequency, is why both of these relaxation processes are expected to show the same functional spin decay in the form of an single exponential decay. Indeed, we find that such a single exponential function $\propto \exp(-\tau/T_{1\rho})$ yields great agreement with our Spin-Lock data, as shown in Figure 1.21 (C). For this reason, within this thesis, we always fit such exponential decays to extract $T_{1\rho}$ times.

Let us close this section with a remark that will later motivate the research presented in chapter 4. At first glance, the Spin-Lock sequence seems to be capable of performing

	T_2^*	T_2^{echo}	T_2^{xy}	$T_{1\rho}$	T_1
Main Magn. Noise Contribution	$\omega = 0$	$\omega \approx \frac{\pi}{\tau}$	$\omega = \frac{\pi}{\tau}$	$\omega = \Omega_R$	$\omega = \omega_0$
Typical Value (Shallow NV)	10 µs	50 µs	100 µs	100 µs	500 µs
Typical Value (Deep NV)	30 µs	600 µs	1-5 ms	1-5 ms	>1 ms

Table 1.2: List of different spin decay times, each with the magnetic noise frequency w that is the dominant contribution to the underlying dephasing respectively relaxation process, and with typical values that we observe on diamond A, for shallow NVs such as NVA1 and NVA2, and for deep NVs such as NVA3 and NVA4.

the same sensing experiments as the XY8-k sequence, all while being much simpler to implement. In addition, the Spin-Lock sequence appears to be sensitive to a single magnetic noise frequency, while the XY8-k sequence has many higher harmonic peaks in its filter function. For NMR experiments, these harmonics can lead to issues if there are multiple nuclear species present in the environment, especially when their gyromagnetic ratios are multiples of each other as it is the case for ^{1}H and ^{13}C nuclear spins. Given these nominal advantages of Spin-Lock over XY8-k, the question at hand is therefore how the sensitivity of these sequences compares, and to what extent spin-locking is actually better suited for NMR spectroscopy compared to XY8-k. We address these questions in chapter 4.

CHAPTER 2

All-Optical Nuclear Quantum Sensing

This chapter is based on the following published work:

B. Bürgler, T.F. Sjolander, O. Brinza, A. Tallaire, J. Achard and P. Maletinsky
All-Optical Nuclear Quantum Sensing using Nitrogen-Vacancy Centers in Diamond
npj Quantum Information 9, 56 (2023)

Spin-based quantum sensing with the NV center, using either the electronic or nuclear nitrogen spin, can be realized in many different ways. Almost all established approaches to NV sensing, however, are based the same two key ingredients: The optical properties of the NV for spin initialization and readout (see section 1.2), and AC magnetic fields for coherent spin control (see section 1.3).

This ubiquitous need for AC coherent driving in spin-based quantum sensing is a severe limitation for many applications. Specifically, such AC driving fields can adversely affect investigated samples (for example heat them up), and for integrated or portable sensing devices, the AC field delivery can drastically increase power-consumption and overall complexity, resulting in larger and more expensive systems. Therefore, finding good NV sensing protocols that operate without any AC magnetic fields is highly interesting in the context of sensing application development. Recent experiments have demonstrated microwave-free NV magnetometry schemes that are based on sharp changes in NV PL at level anti-crossings, which occur at specific magnetic fields [125, 126]. However, while these approaches avoid the need for microwave or radio-frequency fields, they do not exploit quantum coherence and are therefore limited in sensitivity, and additionally, they are highly vulnerable to background drifts in the emitted NV PL.

In this chapter, we present a method for coherent, microwave-free quantum sensing using the ^{15}N nuclear spin of the NV center in diamond. Our approach is based on optical driving of the NV center near the ESLAC in the presence of a tiny static magnetic field component $B_\perp$ transverse to the NV symmetry axis. As we will show in section 2.1 below, such a small transverse magnetic field component has a striking effect, in that optical pumping prepares the ^{15}N nuclear spin in a coherent superposition state within the NV's ground state electronic spin manifold $m_S = 0$. To use the nomenclature introduced in chapter 1, the system is brought into a superposition of $|0, +1/2\rangle$ and $|0, -1/2\rangle$. This is very different to optical pumping at $B_\perp = 0$ which results in an initialization of the system into the pure eigenstate $|0, +1/2\rangle$ (see section 1.2.2). Following optical pumping, the laser is turned off, and the nuclear spin starts to Larmor precess about an effective magnetic field; a field we will rigorously derive in section 2.1.1. In that sense, our scheme is a nuclear free induction (FID) experiment, and the spin dynamics can be completely encompassed by a reduced subspace spanned by $\{|0, -1/2\rangle, |+1/2\rangle\}$. Finally, the nuclear precession is measured all-optically by monitoring the ESLAC-mediated nuclear spin state dependent PL (see section 1.2.2). The entire measurement protocol does not require any AC driving fields, but only green laser pulses, as illustrated in Figure 2.1 (A).

In Figure 2.1 (B), we present an example of such an all-optical nuclear free induction (FID) measurement, obtained using the pulse sequence depicted in Figure 2.1 (A). These data were recorded on our home-built confocal optical microscope with magnetic field control (see section A.1); here at a magnetic field of strength $|\boldsymbol{B}_{\text{ext}}| = 540\,\text{G}$, tilted by $\phi = 1°$ away from the NV symmetry axis. The resulting precession frequency is fitted with a sine function, yielding $f_{\text{nuc}} = (251.18 \pm 0.12)\,\text{kHz}$. This frequency is significantly different from the ^{15}N Larmor frequency at the given field, $f_L = \gamma_{\text{N15}} |\boldsymbol{B}_{\text{ext}}| = 233.14\,\text{kHz}$.

In order to understand this discrepancy, and to thereby prove that the observed oscillation is nonetheless attributed to a nuclear precession of the ^{15}N spin, we study the underlying spin dynamics in section 2.1, where we derive an effective Hamiltonian of the subspace spanned by $\{|0, -1/2\rangle, |+1/2\rangle\}$. From this Hamiltonian we deduce an

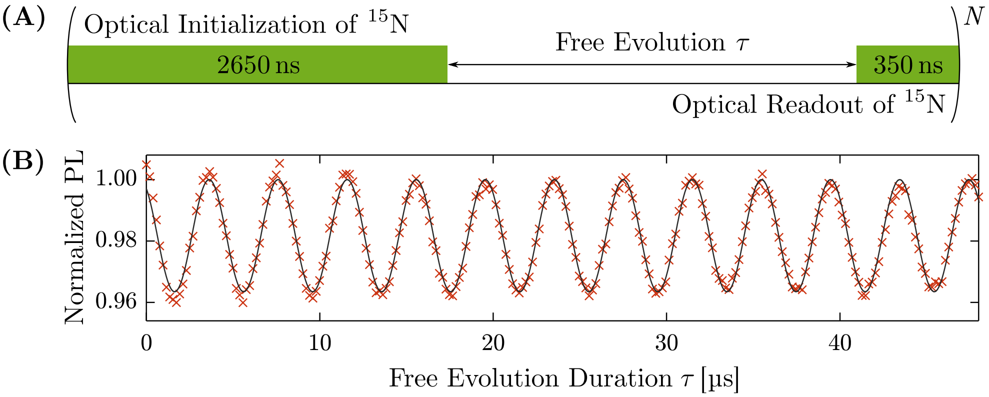

Figure 2.1: All-Optical nuclear spin precession of the ^{15}N nuclear spin. **(A)** Employed pulse sequence, consisting of a 3 µs green laser pulse separated by a varibale delay τ. The first 350 ns of each green pulse are utilized for optical nuclear spin readout, while the remainder of the pulse reinitializes the spin system for the next experiment repetition. **(B)** Example nuclear precession data measured by the all-optical schemes shown in (A), taken at a magnetic field of $|\boldsymbol{B}_{\text{ext}}| = 540\,\text{G}$ tilted away from the NV symmetry axis by $\phi = 1°$. Fitting a harmonically oscillation function (black) yields a precession frequency of $(251.18 \pm 0.12)\,\text{kHz}$.

analytic expression for the expected precession frequency f_{nuc}, which is key to realizing quantitative magnetometry or gyroscopy applications. In addition, we introduce a numerical model that describes the entire NV system under optical pumping in an arbitrary external magnetic field. Using this model, we can not only simulate the FID precession dynamics observed in our experiments, but we can also make a statement about the initialized nuclear state under optical pumping.

In section 2.2, we present more all-optically measured nuclear precession data, and explore how the observed precession depends on experimental parameters such as for example the amplitude and angle of $\boldsymbol{B}_{\mathrm{ext}}$. Crucially, this allows us to identify the ideal working point of our scheme that maximizes the optical precession contrast. Then, in section 2.3 we extend our studies from the single NV case to an entire ensemble of NVs, demonstrating that our all-optical FID sensing scheme is compatible with large nuclear spin ensembles. Finally, in section 2.4, we conclude the chapter with a discussion on the sensitivity of our proposed sensing scheme to address the question how competitive it would be for envisioned quantum sensing applications.

2.1 Theoretical Description

2.1.1 Effective Nuclear Hamiltonian

To derive an effective Hamiltonian for the ^{15}N spin in the electronic $m_S = 0$ ground state manifold, we employ Van Vleck perturbation theory [127, 128]. This theory is applicable to any Hamiltonian that can be written in the form $\hat{\mathcal{H}} = \hat{\mathcal{H}}_0 + \hat{V}$, where $\hat{\mathcal{H}}_0$ is block diagonal, with each block attributed to one subspace of $\hat{\mathcal{H}}_0$, and where $\hat{V}$ is a weak perturbation that couples the initially uncoupled subspaces of $\hat{\mathcal{H}}_0$. In other words, the Hamiltonian $\hat{\mathcal{H}}$ describes a system that is made up of multiple individual subsystems ($\hat{\mathcal{H}}_0$), and the energy difference between states from different subsystems is much larger than the coupling between them ($\hat{V}$). For such a Hamiltonian $\hat{\mathcal{H}}$, the Van Vleck perturbation allows us to calculate the effective Hamiltonian $\hat{\mathcal{H}}^{\alpha}_{\mathrm{eff}}$ for each individual subspace α. Following the notation in [127], to second order, the matrix elements of these effective Hamiltonians are

$$\langle i|\, \hat{\mathcal{H}}^{\alpha}_{\mathrm{eff}}\, |j\rangle = \langle \alpha, i|\, \hat{\mathcal{H}}_0 + \hat{V}\, |\alpha, j\rangle + C_2\,, \tag{2.1}$$

where

$$C_2 = \sum_{k,\beta\neq\alpha} \left(\frac{\langle \alpha, i|\, \hat{V}\, |\beta, k\rangle\langle \beta, k|\, \hat{V}\, |\alpha, j\rangle}{2\,(E_{\alpha,i} - E_{\beta,k})} + \frac{\langle \alpha, i|\, \hat{V}\, |\beta, k\rangle\langle \beta, k|\, \hat{V}\, |\alpha, j\rangle}{2\,(E_{\alpha,k} - E_{\beta,k})} \right) \tag{2.2}$$

is the second order correction term. Here, $|\alpha, i\rangle$ are the eigenstates of the unperturbed Hamiltonian $\hat{\mathcal{H}}_0$ with eigenenergies $E_{\alpha,i}$. The Greek indices (α,β) denote the different subspaces, and Latin indices (i, j, k) count over the states within a given subspace. Equations (2.1) and (2.2) are only valid for weakly coupled subspaces, that is if the energy difference between states from different subspaces is much larger than the coupling between them, e.g. if $|E_{\alpha,i} - E_{\beta,j}| \gg \langle \alpha, i|\, \hat{V}\, |\beta, j\rangle$.

The NV center's ground state Hamiltonian $\hat{\mathcal{H}}^{\mathrm{gs}}_{\mathrm{N15}}$ from equation (1.4) is such a block diagonal Hamiltonian, where the electronic manifolds are identified as the three weakly coupled subspaces. We can bring the $\hat{\mathcal{H}}^{\text{gs}}_{\text{N15}}$ into the required form $\hat{\mathcal{H}}^{\text{gs}}_0 + \hat{V}^{\text{gs}}$ by assigning

$$\hat{\mathcal{H}}^{\text{gs}}_0 = D^{\text{gs,es}}_0 \hat{S}^2_z + \gamma_{\text{NV}} B_z \cdot \hat{S}_z + \gamma_{\text{N15}} B_z \cdot \hat{I}_z \tag{2.3}$$

$$\hat{V}^{\text{gs}} = A^{\text{gs,es}}_{\parallel} \hat{S}_z \hat{I}_z + A^{\text{gs,es}}_{\perp} \left(\hat{S}_x \hat{I}_x + \hat{S}_y \hat{I}_y\right) + \gamma_{\text{NV}} B_{\perp} \cdot \hat{S}_x + \gamma_{\text{N15}} B_{\perp} \cdot \hat{I}_x \tag{2.4}$$

where without loss of generality we defined the direction of the transverse magnetic field as the x-direction, such that $B_y = 0$ and $B_{\perp} = B_x$. It is evident from (2.3) and (2.4) that $\hat{\mathcal{H}}^{\text{gs}}_{\text{N15}}$ fulfils the weak coupling prerequisite, because at an external field of $|\boldsymbol{B}_{\text{ext}}| \approx 500\,\text{G}$, the ground state electronic manifolds are split by $\hat{\mathcal{H}}^{\text{gs}}_0$ by a few GHz, and the interaction $\hat{V}^{\text{gs}}$ couples them with comparably small coupling coefficients in the MHz regime.

We can now evaluate equation (2.1) for Hamiltonian $\hat{\mathcal{H}}^{\text{gs}}_{\text{N15}} = \hat{\mathcal{H}}^{\text{gs}}_0 + \hat{V}^{\text{gs}}$, where we solve for the subspace corresponding to $m_S = 0$. This results in the effective Hamiltonian $\hat{\mathcal{H}}^{m_S=0}_{\text{eff}}$ with the diagonal matrix elements

$$\begin{aligned}\langle 0, \pm 1/2 |\, \hat{\mathcal{H}}^{m_S=0}_{\text{eff}} \,| 0, \pm 1/2 \rangle = \; & \frac{\pm \hbar \gamma_{\text{N15}} B_z}{2} \\ & + \frac{\hbar (A^{\text{gs}}_{\perp})^2}{A^{\text{gs}}_{\parallel} - 2D^{\text{gs}}_0 \pm 2\gamma_{\text{N15}} B_z \mp 2\gamma_{\text{NV}} B_z} \\ & + \frac{4\hbar \gamma^2_{\text{NV}} B^2_{\perp} D^{\text{gs}}_0}{(A^{\text{gs}}_{\parallel} - 2D^{\text{gs}}_0 \pm 2\gamma_{\text{NV}} B_z)(A^{\text{gs}}_{\parallel} + 2D^{\text{gs}}_0 \pm 2\gamma_{\text{NV}} B_z)}\,,\end{aligned} \tag{2.5}$$

and the off-diagonal elements

$$\begin{aligned}\langle 0, \pm 1/2 |\, \hat{\mathcal{H}}^{m_S=0}_{\text{eff}} \,| 0, \mp 1/2 \rangle = \; & \frac{\hbar \gamma_{\text{N15}} B_{\perp}}{2} \\ & + \frac{\hbar \gamma_{\text{NV}} B_{\perp} A^{\text{gs}}_{\perp}/2}{A^{\text{gs}}_{\parallel} - 2D^{\text{gs}}_0 + 2\gamma_{\text{NV}} B_z} + \frac{\hbar \gamma_{\text{NV}} B_{\perp} A^{\text{gs}}_{\perp}/2}{A^{\text{gs}}_{\parallel} - 2D^{\text{gs}}_0 - 2\gamma_{\text{NV}} B_z} \\ & + \frac{\hbar \gamma_{\text{NV}} B_{\perp} A^{\text{gs}}_{\perp}/2}{A^{\text{gs}}_{\parallel} - 2D^{\text{gs}}_0 + 2\gamma_{\text{NV}} B_z - 2\gamma_{\text{N15}} B_z} + \frac{\hbar \gamma_{\text{NV}} B_{\perp} A^{\text{gs}}_{\perp}/2}{A^{\text{gs}}_{\parallel} - 2D^{\text{gs}}_0 - 2\gamma_{\text{NV}} B_z + 2\gamma_{\text{N15}} B_z}\,.\end{aligned} \tag{2.6}$$

Next, we simplify these two expressions by using the approximations $(\gamma_{\text{NV}} \pm \gamma_{\text{N15}}) \approx \gamma_{\text{NV}}$ and $(A^{\text{gs}}_{\parallel} \pm 2D^{\text{gs}}_0) \approx \pm 2D^{\text{gs}}_0$, which are justified by the one respectively three orders of magnitude of difference between these terms. Subsequently, in order to place the resulting energy levels symmetrically around zero, we introduce an energy shift of $\frac{1}{2}\left(D^{\text{gs}}_0 (A^{\text{gs}}_{\perp})^2 + 2D^{\text{gs}}_0 (\gamma_{\text{NV}} B_{\perp})^2\right) / \left((D^{\text{gs}}_0)^2 - (\gamma_{\text{NV}} B_z)^2\right)$. This leads to the final expression for the effective nuclear Hamiltonian, given in the basis $\{|0, +1/2\rangle, |0, -1/2\rangle\}$, reading

$$\hat{\mathcal{H}}^{m_S=0}_{\text{eff}} = \frac{\hbar}{2} \begin{pmatrix} \gamma_{\text{N15}} B_z + \nu_z & \gamma_{\text{N15}} B_{\perp} + \nu_{\perp} \\ \gamma_{\text{N15}} B_{\perp} + \nu_{\perp} & -\gamma_{\text{N15}} B_z - \nu_z \end{pmatrix}, \tag{2.7}$$

where

$$\nu_z = \frac{\gamma_{\text{NV}} B_z (A^{\text{gs}}_{\perp})^2}{(D^{\text{gs}}_0)^2 - (\gamma_{\text{NV}} B_z)^2} \tag{2.8}$$

denotes the correction to the diagonal elements caused by mixing between states of different m_S, and

$$\nu_\perp = \frac{-2\,\gamma_{\mathrm{NV}} B_\perp A_\perp^{\mathrm{gs}} D_0^{\mathrm{gs}}}{(D_0^{\mathrm{gs}})^2 - (\gamma_{\mathrm{NV}} B_z)^2} \tag{2.9}$$

is the corresponding correction to the off-diagonal elements. Note that these expressions for ν_z and $\nu_\perp$ are diverging for $D_0^{\mathrm{gs}} = \gamma_{\mathrm{NV}} B_z$, e.g. near the GSLAC. This is because the Van Vleck formalism is not applicable to that regime since the corresponding electronic subspaces of H_0 are not sufficiently spaced in energy once this condition is approached. In our experiments, we work far away from the GSLAC and thereby avoid this problematic region.

We note that such an effective hyperfine Hamiltonian for ^{15}N-based NV's has been discussed earlier as a perturbation in $A_\perp^{\mathrm{gs}}$ [30], or as a perturbation in $B_\perp$ in the limit $B_z \ll D_0^{\mathrm{gs}}$ [112], but never as a perturbation in both simultaneously as we present it here. Additionally, exact analytic expressions for $\nu_\perp$ have previously been derived in [129]. The main benefit of our expression for $\nu_\perp$ is that we can see very directly that the transverse magnetic field is amplified by $A_\perp^{\mathrm{gs}}$ such that for a very small tilt angle of the magnetic field we get a very large correction $\nu_\perp$ and thus a large off-diagonal term in equation (2.7).

Next, we will discuss the effective magnetic field that represents $\hat{\mathcal{H}}_{\mathrm{eff}}^{m_S=0}$. To that end, we rewrite equation (2.7) in terms of the nuclear spin operators $\hat{I}_k$, and find

$$\hat{\mathcal{H}}_{\mathrm{eff}}^{m_S=0} = \hbar\,(\gamma_{\mathrm{N15}} B_z + \nu_z)\,\hat{I}_z + \hbar\,(\gamma_{\mathrm{N15}} B_\perp + \nu_\perp)\,\hat{I}_x \;:=\; \hbar\gamma_{\mathrm{N15}}\,\boldsymbol{B}_{\mathrm{eff}} \cdot \hat{\boldsymbol{I}}\,, \tag{2.10}$$

where we introduced the effective magnetic field

$$\boldsymbol{B}_{\mathrm{eff}} = \begin{pmatrix} B_\perp + (\nu_\perp/\gamma_{\mathrm{N15}}) \\ 0 \\ B_z + (\nu_z/\gamma_{\mathrm{N15}}) \end{pmatrix} \tag{2.11}$$

experienced by the nuclear spin within the $m_S = 0$ manifold. This effective magnetic field represents the quantization axis of the nuclear spin within $|m_S = 0\rangle$, and therefore describes the axis about which the nuclear spin precesses. Simply put, equation (2.11) states that $\boldsymbol{B}_{\mathrm{eff}}$ is equal to $\boldsymbol{B}_{\mathrm{ext}}$ plus the correction terms given by ν_z and $\nu_\perp$. Note that $\boldsymbol{B}_{\mathrm{eff}}$ is zero in $\boldsymbol{e}_y$ direction, which stems from the fact that we assumed an external field $\boldsymbol{B}_{\mathrm{ext}}$ with $B_x = B_\perp$ and $B_y = 0$. In general, $\boldsymbol{B}_{\mathrm{eff}}$ lies in the plane spanned by $\boldsymbol{B}_{\mathrm{ext}}$ and $\boldsymbol{e}_z$. Within this plane, $\boldsymbol{B}_{\mathrm{eff}}$ is tilted away from the NV symmetry axis $\boldsymbol{e}_z$ by an angle of

$$\vartheta = \tan^{-1}\left(\frac{B_\perp + (\nu_\perp/\gamma_{\mathrm{N15}})}{B_z + (\nu_z/\gamma_{\mathrm{N15}})}\right)\,. \tag{2.12}$$

Importantly, this implies that $\boldsymbol{B}_{\mathrm{eff}}$ is aligned with neither the NV symmetry axis which points along $\boldsymbol{e}_z$, nor with $\boldsymbol{B}_{\mathrm{ext}}$ which is tilted away from $\boldsymbol{e}_z$ by $\phi = \tan^{-1}(B_\perp/B_z)$. And interestingly, ϑ has a sign opposite to ϕ due to the negative sign of γ_{N15}. This is shown in a quantitatively accurate fashion in Figure 2.2, for a magnetic tilt angle of $\phi = 1°$. In the special case of an aligned magnetic field, $B_\perp = 0$, equation (2.9) yields $\nu_\perp = 0$, which in turns causes $\vartheta = \phi = 0$, such that the fields $\boldsymbol{B}_{\mathrm{eff}}$ and $\boldsymbol{B}_{\mathrm{ext}}$ are both perfectly collinear with $\boldsymbol{e}_z$.

Any nuclear spin state not aligned with $\boldsymbol{B}_{\text{eff}}$ will start to precess about $\boldsymbol{B}_{\text{eff}}$. The resulting precession frequency (in units of Hz) is given by

$$f_{\text{nuc}} = \frac{\gamma_{\text{N15}}|\boldsymbol{B}_{\text{eff}}|}{2\pi} = \frac{1}{2\pi\hbar}\sqrt{(\gamma_{\text{N15}}B_z + \nu_z)^2 + (\gamma_{\text{N15}}B_\perp + \nu_\perp)^2}\,. \tag{2.13}$$

Importantly, this precession frequency is strictly larger than the bare Larmor frequency $f_L = \gamma_{\text{N15}}|\boldsymbol{B}_{\text{ext}}|/(2\pi)$. This increase of the precession frequency is once more due to the correction terms ν_z and $\nu_\perp$. Interestingly, even for $B_\perp = 0$, ν_z is still non-zero and therefore leads to an enhanced precession frequency.

To summarize, if there is an external magnetic field $\boldsymbol{B}_{\text{ext}}$ tilted away from $\boldsymbol{e}_z$ by ϕ, the nuclear spin in the $m_S = 0$ manifold experiences an effective magnetic field $\boldsymbol{B}_{\text{eff}}$ that is tilted away from $\boldsymbol{e}_z$ in the opposite direction by an angle $\vartheta \gg \phi$. The resulting precession about $\boldsymbol{B}_{\text{eff}}$ exhibits a precession frequency f_{nuc} that is larger than the bare Larmor frequency that one would expect from precession about $\boldsymbol{B}_{\text{ext}}$.

2.1.2 Origin of All-Optically Induced Nuclear Spin Precession

Based on the analytic results of the previous section, we now discuss how the presence of a small $B_\perp$ affects the ^{15}N nuclear spin dynamics under green laser illumination, and thereby enables all-optical nuclear FID experiments with the sequence shown in Figure 2.1 (A). For this, we will carry on from the Van Vleck perturbation theory framework and continue to approximate the entire coupled and multidimensional electron nuclear spin system as an effective two-level system comprised of $|0, \pm 1/2\rangle$, and thus use the Bloch sphere representation to visualize the corresponding dynamics. To begin, let us remember that in order to initialize and detect a nuclear spin precession in an all-optical fashion, two key ingredients are required: First, on the Bloch sphere of the effective two-level system, the state into which the nuclear spin is initialized must not be collinear with $\boldsymbol{B}_{\text{eff}}$. Otherwise, no spin precession occurs in the first place. This is equivalent with demanding that the initialized state's density matrix must not commute with $\hat{\mathcal{H}}_{\text{eff}}^{m_S=0}$. Second, the axis along which the spin state is optically detected must also not be collinear with $\boldsymbol{B}_{\text{eff}}$, because otherwise the precession would not lead to a modulation of the spin projection onto the measurement axis. It is however perfectly fine if initialization and readout axis are the same (as it will be in our case). In the following, we will develop arguments based on the analytic results from the previous section to explain why in the presence of $B_\perp$ and green light, these two key conditions are fulfilled. This way, we ultimately explain the all-optical FID data shown in Figure 2.1 (B) with the analytic effective Hamiltonian derived in the previous section.
To identify the nuclear spin state resulting from optical pumping, we first note that such optical pumping accumulates the electron spin population in the $m_S = 0$ eigenstate. For $B_\perp = 0$, as discussed in section 1.2.2, this is just the $|0, +1/2\rangle$ state. For non-zero $B_\perp$, when $B_\perp$ and $A_\perp^{\text{es}}$ mix the spin states, population is accumulated in the new eigenstate with the largest $m_S = 0$ character, i.e. the excited state eigenstate $|\psi\rangle$ for which $\langle\psi|\,\hat{S}_z\,|\psi\rangle$ is closest to zero, because this state has the lowest probability of decaying into the NV's singlet state (see section 1.2.1). We denote this state as $|\psi_0^{\text{es}}\rangle$. Importantly, $|\psi_0^{\text{es}}\rangle$ is not just the state the system is initialized into, it is also

the “brightest” excited state eigenstate because it has the largest relative probability of decaying to the ground state by emitting a photon.

After turning off the green laser, relaxation to the ground state happens either directly by emitting a red photon – a process that is highly spin-conserving – or the system decays through the singlet states, which is highly unlikely for $|\psi_0^{\mathrm{es}}\rangle$ due to its large $m_S = 0$ character. Consequently, assuming that no inter-system crossing affects the $|m_S = 0\rangle$ population, the system ends up entirely relaxed to the ground state, with the spin state still perfectly in $|\psi_0^{\mathrm{es}}\rangle$. We actually show in section 2.1.4 that simulating the system with a zero inter-system crossing rate for $m_S = 0$ leads to a state that is perfectly aligned with the Bloch sphere representation of $|\psi_0^{\mathrm{es}}\rangle$, and the numeric result will only deviate significantly from it if the inter-system crossing for $|m_S = 0\rangle$ is allowed.

For the state $|\psi_0^{\mathrm{es}}\rangle$, the expectation value of the nuclear spin lies along a vector that we define as

$$\boldsymbol{e}_{\mathrm{init}} := \langle\psi_0^{\mathrm{es}}|\,\hat{\boldsymbol{I}}\,|\psi_0^{\mathrm{es}}\rangle\,/\hbar\,. \tag{2.14}$$

This unit vector $\boldsymbol{e}_{\mathrm{init}}$ defines both the Bloch sphere direction along which the nuclear spin is initialized under green illumination, as well as the measurement axis for optical readout of the nuclear spin.

Let us now evaluate $\boldsymbol{e}_{\mathrm{init}}$ for the case of $B_\perp = 0$. As discussed previously in section 1.2.2, one finds $|\psi_0^{\mathrm{es}}\rangle = |0, +1/2\rangle$, and therefore in this case, $\boldsymbol{e}_{\mathrm{init}} = \boldsymbol{e}_z$. Also, it is clear from equations (2.8), (2.9) and (2.11) that in the case of $B_\perp = 0$, the effective magnetic field $\boldsymbol{B}_{\mathrm{eff}}$ is aligned with $\boldsymbol{e}_z$. Therefore, for an external magnetic field aligned with the NV axis, the optically initialized state and $\boldsymbol{B}_{\mathrm{eff}}$ are collinear, such that no nuclear precession occurs.

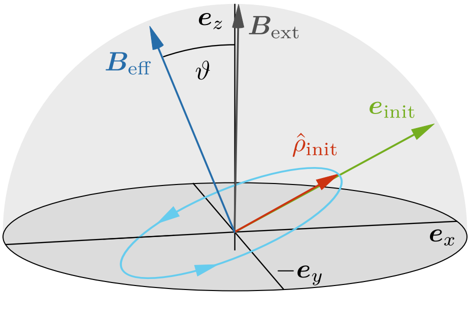
$\boldsymbol{e}_z$
$\boldsymbol{B}_{\mathrm{ext}}$
$\boldsymbol{B}_{\mathrm{eff}}$
ϑ
$\boldsymbol{e}_{\mathrm{init}}$
$\hat{\rho}_{\mathrm{init}}$
$\boldsymbol{e}_x$
$-\boldsymbol{e}_y$

Figure 2.2: Quantitative Bloch-Sphere representation of the ^{15}N spin in the $|m_S = 0\rangle$ ground state manifold, for a magnetic field $|\boldsymbol{B}_{\mathrm{ext}}| = 540\,\mathrm{G}$ tilted away from the NV symmetry axis by $\phi = 1°$. Optical pumping initializes the nuclear spin into $\hat{\rho}_{\mathrm{init}}$. After optical pumping, the nuclear spin precesses freely around an effective magnetic field $\boldsymbol{B}_{\mathrm{eff}}$ tilted in the opposite direction of $\boldsymbol{B}_{\mathrm{ext}}$ by an angle $\vartheta \gg \phi$. The measurement axis for all-optical readout of this precession is given by $\boldsymbol{e}_{\mathrm{init}}$.

For an external magnetic field slightly tilted away from $\boldsymbol{e}_z$, however, the situation is very different. As can be seen from equations (2.7) and (2.9), such a non-zero $B_\perp$ gives rise to a non-zero transverse correction term $\nu_\perp$ in the effective nuclear Hamiltonian. This $\nu_\perp$ leads to increased mixing of the nuclear spin, and thereby to different nuclear eigenstates, which in turn results in a significantly different $|\psi_0^{\mathrm{es}}\rangle$, that is no longer equal to $|0, +1/2\rangle$. In consequence, for $B_\perp \neq 0$, the nuclear spin is initialized along an axis $\boldsymbol{e}_{\mathrm{init}}$ that is no longer aligned with the NV symmetry axis $\boldsymbol{e}_z$. And as shown in the previous section, neither is $\boldsymbol{B}_{\mathrm{eff}}$. Importantly, explicit calculation of $\boldsymbol{e}_{\mathrm{init}}$ and

$\boldsymbol{B}_{\text{eff}}$ shows that for increasing $B_\perp$, these two vectors tilt away from $\boldsymbol{e}_z$ in opposite directions. An example for this is shown in Figure 2.2, where the external magnetic field is $|\boldsymbol{B}_{\text{ext}}| = 540\,\text{G}$, tilted away from the NV symmetry axis by $\phi = 1°$. This corresponds to the experimental conditions from Figure 2.1 (B). In this case, $\boldsymbol{e}_{\text{init}}$ and $\boldsymbol{B}_{\text{eff}}$ are in fact almost perpendicular, giving rise to a precession with a large opening cone which results in a large optical contrast. Since $\boldsymbol{e}_{\text{init}}$ represents both the initialization and readout axis, both key conditions for all-optical nuclear spin precession are fulfilled, enabling this all-optical nuclear precession experiment.

Importantly, we note all these physics only work for NV centers formed with ^{15}N. For ^{14}N-based NVs, the non-zero quadrupolar splitting locks $\boldsymbol{B}_{\text{eff}}$ and $\boldsymbol{e}_{\text{init}}$ onto the NV axis, meaning that the initialized nuclear state is collinear $\boldsymbol{B}_{\text{eff}}$; a scenario in which no nuclear precession occurs. This can be seen by performing the derivation from section 2.1.1 for an NV center formed by ^{14}N, which results in

$$\begin{aligned}\hat{\mathcal{H}}_{\text{eff}}^{m_S=0} &= \hbar\left(\gamma_{\text{N14}}B_z + \nu_z\right)\hat{J}_z + \hbar\left(\gamma_{\text{N14}}B_\perp + \nu_\perp\right)\hat{J}_x \\ &\quad + \hbar\left(Q + \frac{D_0 (A_\perp^{\text{gs}})^2}{(D_0^{\text{gs}})^2 - (\gamma_{\text{NV}}B_z)^2}\right)\hat{J}_z^2\,, \end{aligned} \tag{2.15}$$

where ν_z and $\nu_\perp$ are the same as in equations (2.8) and (2.9), and the nuclear spin operators $\hat{J}_k$ are given as defined by equation (1.6). This effective Hamiltonian is essentially the same as for an ^{15}N NV, see equation (2.10), but with an additional third term that includes the non-zero quadrupolar moment Q. Written in matrix representation, this effective Hamiltonian yields

$$\hat{\mathcal{H}}_{\text{eff}}^{m_S=0} = \hbar\begin{pmatrix} +\gamma_{\text{N14}}B_z + \nu_+ + Q & \frac{\gamma_{\text{N14}}B_\perp + \nu_\perp}{\sqrt{2}} & 0 \\ \frac{\gamma_{\text{N14}}B_\perp + \nu_\perp}{\sqrt{2}} & 0 & \frac{\gamma_{\text{N14}}B_\perp + \nu_\perp}{\sqrt{2}} \\ 0 & \frac{\gamma_{\text{N14}}B_\perp + \nu_\perp}{\sqrt{2}} & -\gamma_{\text{N14}}B_z + \nu_- + Q \end{pmatrix}, \tag{2.16}$$

where $\nu_\pm = (A_\perp^{\text{gs}})^2/(D_0 \mp \gamma_{\text{NV}}B_z)$. In this representation, it is clear to see that Q is the dominant contribution, because $Q = 2\pi \times (-4.945)\,\text{MHz}$ [31, 81], while all the other terms in this matrix are less than $2\pi \times 160\,\text{kHz}$ at $B_z \approx 500\,\text{G}$. Therefore, the non-zero quadrupolar moment Q of the ^{15}N spin fixes the effective field $\boldsymbol{B}_{\text{eff}}$ onto the NV symmetry axis $\boldsymbol{e}_z$.

Finally, we emphasize that all the spin physics discussed in this chapter are only possible in vicinity of the ESLAC (or GSLAC). Moving too far away from 500 G (or 1000 G) eliminates the hyperfine coupling in the excited (ground) state, without which the nuclear spin has no optical contrast for readout. In addition, without said hyperfine coupling, optical pumping does not affect the nuclear spin state, leaving it in a classical mixture of $|\pm 1/2\rangle$ which cannot precess.

2.1.3 Numeric Simulation in Liouvillian Space

To further validate the theory from the perturbative description via Van Vleck theory, and in particular to provide a quantitative theoretical approach to describing the nuclear spin contrast, we now develop a purely numerical model that simulates the dynamics of the ^{15}N NV system during and after optical pumping, at any arbitrary

external magnetic field $\boldsymbol{B}_{\text{ext}}$. To numerically calculate the trajectory of both the electron and nuclear spin under optical pumping on the NV center, it is necessary to consider not only classical rate equation to describe the transitions between the orbital states [25], but to also incorporate the quantum mechanical evolution of the spins within each orbital state via their respective quantum master equation. To achieve this, we build our numerical simulation in Liouvillian space, an approach previously taken to model the effect of chemical reaction kinetics on NMR spectra [130]. In comparison to the discussion in the previous section, that was based on result from a second order perturbative (and therefore approximate) Van Vleck calculation, and on the educated guess that green laser light pumps into $|\psi_0^{\text{es}}\rangle$, this numerical approach is not requiring such significant approximations or assumptions. As we will show below, we still obtain fantastic agreement with the analytical results.
We model the room temperature NV$^-$ center as a system made up of three distinct electronic states: The ground state (gs), the excited state (es), and a metastable singlet state (s). As discussed in section 1.1.1, it is safe to neglect the distinct orbital branches in the excited state as they are efficiently averaged at room temperature. In addition, we assume that there is only one singlet state, a simplification that is justified because the two singlets are identical in terms of spin degrees of freedom, as there are no electronic degrees of freedom within them, and the transition through them singlets is nuclear spin-conserving. Finally, note that we neglect laser induced ionization to the NV^0 state.

We start to build our model by considering a separate spin density operator $\hat{\rho}_\alpha$ for each orbital states $\alpha \in \{\text{es}, \text{gs}, \text{s}\}$. This density operator evolves coherently per the Von Neumann equation of motion under the Hamiltonian $\hat{\mathcal{H}}^\alpha_{\text{N15}}$. However, we aim to work in Liouville space, where a $(n \times n)$ density operator is vectorized and thereby represented as a $(n^2 \times 1)$ vector. In consequence, $(n \times n)$ unitary operators such as the Hamiltonian need to be elevated to so-called superoperators that are $(n^2 \times n^2)$ dimensional. In this Liouville space, the Von Neumann equation becomes the Liouville-Von Neumann equation, which reads

$$\frac{\mathrm{d}}{\mathrm{d}t}\hat{\rho}_\alpha = \hat{\hat{L}}_\alpha \hat{\rho}_\alpha \qquad \text{with} \qquad \hat{\hat{L}}_\alpha := -i\Big(\mathcal{H}^\alpha_{\text{N15}} \otimes \mathbb{I}^\alpha - \mathbb{I}^\alpha \otimes (\mathcal{H}^\alpha_{\text{N15}})^T\Big) \tag{2.17}$$

where $\hat{\hat{L}}_\alpha$ is the superoperator that represents the commutation with the Hamiltonian $\mathcal{H}^\alpha_{\text{N15}}$. Here, carets denote operators (represented by column vectors), double carets denote superoperators (represented by matrices), $\mathbb{I}^\alpha$ is the identity matrix of the same dimensionality as $\mathcal{H}^\alpha_{\text{N15}}$, and T denotes matrix transposition (without complex conjugation). The Hamiltonian $\mathcal{H}^\alpha_{\text{N15}}$ for $\alpha \in \{\text{es}, \text{gs}\}$ is given by equation (1.4), and for the singlet state, it yields

$$\mathcal{H}^{\text{s}}_{\text{N15}} = \hbar\gamma_{\text{N15}}\boldsymbol{B}_{\text{ext}} \cdot \boldsymbol{I}\,, \tag{2.18}$$

where $\boldsymbol{I}$ is the regular space nuclear ^{15}N spin operator as previously defined in equation (1.7). Note that to avoid confusion, we have removed the carets on all regular space operators ($\mathcal{H}^\alpha_{\text{N15}}$, $\boldsymbol{I}$, and $\mathbb{I}^\alpha$) in equations (2.17) and (2.18).
To incorporate the incoherent optical pumping process, we now couple the three independent quantum mechanical master equations from equation (2.17). To that end,

we introduce additional (real valued) superoperators that act to reduce or increase the population of a given spin state, and thus take the role of spin-selective excitation and relaxation superoperators. With them, we can describe all of the optical transitions discussed in section 1.2 that are taking place between the three orbitals. The resulting coupled differential equations read

$$\begin{aligned} \frac{\mathrm{d}}{\mathrm{d}t}\,\hat{\rho}_{\mathrm{gs}} &= \hat{\hat{L}}_{\mathrm{gs}}\hat{\rho}_{\mathrm{gs}} - k_{\mathrm{green}}\hat{\rho}_{\mathrm{gs}} + k_{\mathrm{red}}\hat{\rho}_{\mathrm{es}} + k_{\mathrm{B}}^{1}(\hat{\hat{S}}^{\otimes}_{+1} + \hat{\hat{S}}^{\otimes}_{-1})\hat{\rho}_{s} + k_{\mathrm{B}}^{0}\hat{\hat{S}}^{\otimes}_{0}\hat{\rho}_{\mathrm{s}} \\ \frac{\mathrm{d}}{\mathrm{d}t}\,\hat{\rho}_{\mathrm{s}} &= \hat{\hat{L}}_{\mathrm{s}}\hat{\rho}_{\mathrm{s}} - (2k_{\mathrm{B}}^{1} + k_{\mathrm{B}}^{0})\hat{\rho}_{s} + k_{\mathrm{A}}^{1}\hat{\hat{T}}^{e}(\hat{\hat{P}}_{1} + \hat{\hat{P}}_{-1})\hat{\rho}_{\mathrm{es}} + k_{\mathrm{A}}^{0}\hat{\hat{T}}^{e}\hat{\hat{P}}_{0}\hat{\rho}_{\mathrm{es}} \\ \frac{\mathrm{d}}{\mathrm{d}t}\,\hat{\rho}_{\mathrm{es}} &= \hat{\hat{L}}_{\mathrm{es}}\hat{\rho}_{\mathrm{es}} + k_{\mathrm{green}}\hat{\rho}_{\mathrm{gs}} - k_{\mathrm{red}}\hat{\rho}_{\mathrm{es}} - k_{\mathrm{A}}^{1}(\hat{\hat{P}}_{+1} + \hat{\hat{P}}_{-1})\hat{\rho}_{\mathrm{es}} - k_{\mathrm{A}}^{0}\hat{\hat{P}}_{0}\hat{\rho}_{\mathrm{es}}\,. \end{aligned} \tag{2.19}$$

Here, k_{green} is the excitation rate from the ground state into the excited state due to laser illumination. Similarly, k_{red} is the relaxation back to the ground state, the process responsible for red PL. These two processes are not spin-selective, and the shelved population is therefore directly given by the terms $k_{\mathrm{green}}\hat{\rho}_{\mathrm{gs}}$ and $k_{\mathrm{red}}\hat{\rho}_{\mathrm{es}}$.

The optical transitions through the singlet states, however, are spin-selective, meaning that additional superoperators are required. $P_{\pm 1,0}$ are projection superoperators that project $\hat{\rho}_{\alpha}$ onto the NV-electron spin state with $m_S \in \{\pm 1, 0\}$ while leaving the dimensionality of $\hat{\rho}_{\alpha}$ unchanged. This superoperator ensures that the rate of inter system crossing out of the excited state depends on the instantaneous spin state population of $\hat{\rho}_{\mathrm{es}}$. The corresponding transition rate is given by k_A^0 for $|m_S = 0\rangle$, or k_A^1 for $|m_S = \pm 1\rangle$.

Next, T^e is a partial trace superoperator that acts on a (36×36) joint electron/nuclear density matrix and traces out the NV-electron degrees of freedom, leaving a (4×4) density operator corresponding only to the ^{15}N subsystem. This operator is required to remove the electron degrees of freedom upon an inter-system crossing into the singlet state.

Finally, $S^{\otimes}_{0,\pm 1}$ is a direct product superoperator that reintroduces electron spin degrees of freedom for the transition from the singlet into the ground state. This superoperator acts on a (4×4) ^{15}N density operator and turns it into a joint electron/nuclear density operator with the NV-electron in the state $m_S \in \{0, \pm 1\}$. The superoperator is used for the relaxation from the singlet to the ground state, with a transition rate of k_B^0 for decay into $|m_S = 0\rangle$, and k_B^1 for decay into $|m_S = \pm 1\rangle$.

Note that because their effect changes dimensionality of $\hat{\rho}_{\alpha}$, the matrix representations of T^e and $S^{\otimes}_{0,\pm 1}$ are not square. We give procedures for generating these matrix representations in the appendix in section A.5. Finally, note that the precise values for the different transition rates have been subject to considerable debate. In table 2.1, we present the relevant values from different sources.

By concatenating the vectors $\hat{\rho}_{\mathrm{gs}}$, $\hat{\rho}_{\mathrm{es}}$ and $\hat{\rho}_{\mathrm{s}}$ into a single (76×1) vector $\hat{\rho}$, the entirety of (2.19) can conveniently be cast into matrix form

$$\frac{\mathrm{d}}{\mathrm{d}t}\,\hat{\rho}(t) = \frac{\mathrm{d}}{\mathrm{d}t}\begin{pmatrix}\hat{\rho}_{\mathrm{gs}} \\ \hat{\rho}_{\mathrm{s}} \\ \hat{\rho}_{\mathrm{es}}\end{pmatrix} = \hat{\hat{M}}\begin{pmatrix}\hat{\rho}_{\mathrm{gs}} \\ \hat{\rho}_{\mathrm{s}} \\ \hat{\rho}_{\mathrm{es}}\end{pmatrix}, \tag{2.20}$$

where $\hat{\hat{M}}$ is a (76×76) dimensional matrix that commutes with itself for all values of time t. Therefore, it can easily be integrated and thus the time evolution of the

	Parameter Set 1	**Parameter Set 2**	**Parameter Set 3**	**Parameter Set 4**	**Parameter Set 5**
k_{red}	63.2	62.70	67.4	66	77
k_A^0	10.8	12.97	9.9	0	0
k_A^1	60.7	80.00	96.6	57	30
k_B^0	0.8	3.45	4.83	1.0	3.3
k_B^1	0.4	1.08	1.055	0.7	0
Ref.	[25]	[89]	[90]	[91]	[92]

Table 2.1: Numeric values for of the optical transition rates in our model, given in units of MHz. We consider five different parameter sets. Best agreement with our data is obtained with set 1.

system can be computed by

$$\hat{\rho}(t) = \exp\left(2\pi \hat{\hat{M}} t\right) \hat{\rho}(0)\,. \tag{2.21}$$

Note that because of how we formed $\hat{\rho}(t)$ by concatenation it cannot represent coherences between different orbital states, however such coherences are unlikely to be significant due to the off-resonant laser drive, and they are not necessary to explain the physics of interest in this work. We also note that since we use identity superoperators to represent the radiative processes, spin-spin coherences will be preserved under optical excitation and radiative decay within this model.
The ability to write classically coupled quantum systems of different dimensionality in such a simple linear matrix equation like equation (2.20) with a straight forward solution like (2.21) is the key advantage of rolling out the entire description in the Liouville space. Numerically, (2.21) is simple to solve, drastically reducing computation time and code complexity compared to other approaches.
At any given time t, the first 36 entries of $\hat{\rho}(t)$ correspond to $\hat{\rho}_{\text{gs}}(t)$ written in vector form, the next 4 entries are $\hat{\rho}_{\text{s}}(t)$ and the last 36 are $\hat{\rho}_{\text{es}}(t)$. We take the predicted instantaneous PL for $\hat{\rho}(t)$ as the fractional population in the excited electronic state, namely

$$\text{PL}(t) = \text{Trace}\{\hat{\rho}_{\text{es}}(t)\}\,, \tag{2.22}$$

which is the quantity we ultimately simulate to compare with experimental data.

2.1.4 Comparison of Theoretical Approaches

To compare the results of the analytic description presented in section 2.1.1 and the numeric model presented in section 2.1.3, we look at what these two approaches predict for both the initialized nuclear state and the effective field (respectively the quantization axis) that the initialized spin state precesses about.

Initialized State

We first look back at Figure 2.2 and point out that $\boldsymbol{B}_{\text{eff}}$ (dark blue arrow) and $\boldsymbol{e}_{\text{init}}$ (green arrow) were calculated as given by the analytical approach, see equations (2.14) and (2.11). The shown initialized nuclear spin state $\hat{\rho}_{\text{init}}$ (red arrow), however, has been derived from the numeric model. To be specific, $\hat{\rho}_{\text{init}}$ has been obtained by propagating the system density matrix $\hat{\rho}(t)$ for 3 µs under green illumination at the given magnetic field, followed by a 50 ns dark time to let the system fully relax to the ground state, and by subsequently taking the trace over the NV electron degrees of freedom. The resulting nuclear spin state's direction on the Bloch sphere is showing extraordinary agreement with the initialization axis $\boldsymbol{e}_{\text{init}}$ given by equation (2.14), demonstrating that the different theoretical approaches agree well with each other.
Note that this perfect overlap of $\hat{\rho}_{\text{init}}$ and $\boldsymbol{e}_{\text{init}}$ is only given as long as $k_A^0 = 0$, e.g. if there is zero probability for $m_S = 0$ population to transition into the singlet states. Otherwise, the initialized state directly after the optical pumping is altered during the first few moments of dark time, because excited state $|m_S = 0\rangle$ population is allowed to transition through the singlets and thereby turn into $|m_S = \pm 1\rangle$ population – a process that was not considered in the derivation of $\boldsymbol{e}_{\text{init}}$.
In the case of $\hat{\rho}_{\text{init}}$ as shown in Figure 2.2, we were using the optical parameter set 1 from table 2.1, but for aesthetic reasons fixed $k_A^0 = 0$. In truth, $\hat{\rho}_{\text{init}}$ deviates slightly from $\boldsymbol{e}_{\text{init}}$. This is shown in Figure 2.3 (A), where we plot $\hat{\rho}_{\text{init}}$ for the precise numbers of all five parameter sets listed in table 2.1.

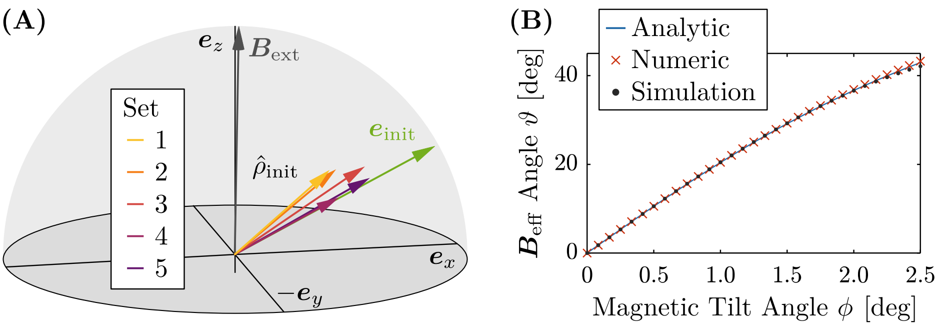

Figure 2.3: Comparison of results from the two different theoretical approaches. **(A)** Initialized nuclear state for $\phi = 1°$ as determined by the numerical model, for each of the parameter sets listed in table 2.1. For models 4 and 5 that have $k_A^0 = 0$, we find the best agreement with the analytical prediction for $\boldsymbol{e}_{\text{init}}$ as given by equation (2.14). **(B)** Tilt angle ϑ of $\boldsymbol{B}_{\text{eff}}$ as a function of the tilt angle ϕ of $\boldsymbol{B}_{\text{ext}}$, calculated in three different ways, showcasing the excellent agreement of our theoretical approaches. The black line shows the analytic result from equation (2.12), green crosses are the result from numerical diagonalization of the full ground state Hamiltonian, and red dots represent the geometrically determined precession axis of the numerically simulated trajectory of $\hat{\rho}(t)$.

Precession Axis

There are three different ways to theoretically predict the axis about which the initialized state precesses. For each of these ways, we compute the angle ϑ of the precession axis with respect to $\boldsymbol{e}_z$ and compare the results.
First, the effective magnetic field $\boldsymbol{B}_{\text{eff}}$ resulting from the perturbation treatment is tilted away from the $\boldsymbol{e}_z$ axis by ϑ as described by equation (2.12). Second, one can compute $\boldsymbol{B}_{\text{eff}}$ with a purely numerical approach by numerically diagonalizing the entire ground state Hamiltonian $\hat{\mathcal{H}}^{\text{gs}}_{15\text{N}}$ from equation (1.4), and by subsequently identifying the eigenvector $|\psi\rangle$ with the largest $|m_S = 0, m_I = +1/2\rangle$ character. The direction of $|\psi\rangle$ in the Bloch sphere of the $|0, \pm 1/2\rangle$ subsystem defines the precession axis, and hence the angle ϑ is given by $\vartheta = \arccos(\boldsymbol{e}_z \cdot \langle\psi| \hat{\boldsymbol{I}} |\psi\rangle /\hbar)$. Finally, ϑ can be inferred geometrically from the trajectory of $\hat{\rho}(t)$ as computed by the numerical model presented in the previous section. To that end, $\hat{\rho}(t)$ is plotted as a three dimensional curve in the Bloch sphere, and the center of mass of this precession trajectory, together with the sphere origin, defines the precession axis.
In Figure 2.3 (B) we show the tilt angle ϑ of the precession axis (respectively $\boldsymbol{B}_{\text{eff}}$) as a function of the tilt angle ϕ of the externally applied magnetic field $\boldsymbol{B}_{\text{ext}}$, as predicted by the three different described approaches to finding ϑ. We find excellent agreement, verifying that the approximations made in the perturbation theory treatment are valid for small angles ϕ, and we once more demonstrate that for small $\phi \leq 2.5°$ we obtain significantly larger ϑ of up to 40°.

2.2 Analysis of All-Optical Precession Data

After developing a well rounded theory framework in the last section, we now present experimental data provided by our all-optical nuclear precession scheme. We will explore how the key properties of the optically detected nuclear spin precession – namely amplitude and frequency – depend on different experimental settings, and we will compare the experimental data with the predictions of our theoretical description. The ultimate goal of this study is to understand the parameter space of our experiment, and to work out ideal conditions for envisioned sensing applications based on our all-optical measurement scheme.
Before we start discussing data, let us point out that all data were recorded on a homebuilt confocal microscope, that was used to focus a green laser on the sample and to simultaneously collect the emitted red PL. A static magnetic field was applied using a permanent neodymium disk magnet, mounted on a linear translation stage to tune the magnetic field strength at the NV location. For precise magnetic field alignment near the ESLAC, the magnet is additionally mounted on a goniometric stage with sub millidegree angular accuracy. Finally, the laser and photon-detectors were gated with pulses which were created and synchronized using a high-frequency signal generator, which also served as a source for microwave pulses used for the characterization of the magnetic field via ODMR experiments. A much more detailed description of the experiment setup is provided in the appendix in section A.1.
All data shown in this chapter (unless explicitly stated otherwise) were measured with NVA1, that is located in a nanopillar of diamond A. See the appendix A.2 for more details on the diamond samples, and table A.6 for a list of NVs. Finally, note that

for the data presented in this section, we always optically excite NVA1 near optical saturation, which for our setup corresponds to a laser power of about 50 µW.

2.2.1 Frequency of the Observed Nuclear Precession

We start with studying the frequency of the nuclear precession we measure. The measured FID frequency is a key quantity in the development of quantum sensing applications based on our protocol, because envisioned magnetometry or gyroscopy techniques would crucially depend on measuring this frequency. Therefore, verifying that our theory framework accurately describes the observed frequency is of great importance.
First, we study the frequency observed in the precession that we have shown in Figure 2.1 (B) in the beginning of the chapter. The black line in the plot is a sine function fit, determined by least-squares fitting, yielding a fitted precession frequency of $f_{\mathrm{nuc}} = (251.18 \pm 0.12)\,\mathrm{kHz}$. Here and elsewhere in this chapter, the given errors are the standard errors of the coefficients in the respective non-linear regression fits. The fit result is in good agreement with what equation (2.13) predicts, namely $f_{\mathrm{nuc}} = 252.71\,\mathrm{kHz}$ for the experimental conditions $|\boldsymbol{B}_{\mathrm{ext}}| = 540\,\mathrm{G}$ and $B_\perp = 10.6\,\mathrm{G}$. We assign the small remaining discrepancy to uncertainties in controlling the tilt angle ϕ and in determining the exact magnetic bias field components $B_\perp$ and B_z.

Precession Frequency as a Function of $|\boldsymbol{B}_{\mathrm{ext}}|$

To validate that our theory approaches predict the correct scaling of the precession frequency with the applied magnetic field, we repeat the same experiment as in Figure 2.1 (B), while varying the amplitude $|\boldsymbol{B}_{\mathrm{ext}}|$ of the external magnetic field. The tilt angle ϕ is fixed to 1° to within experimental accuracy. Figure 2.4 shows the resulting, near-linear dependence of f_{nuc} on $|\boldsymbol{B}_{\mathrm{ext}}|$ and the excellent agreement with the predictions of both equation (2.13), labeled “Analytic”, and the numerical model, labelled “Simulation”. The plot showcases the clear enhancement of f_{nuc} over the bare Larmor frequency $f_L = \gamma_{\mathrm{N15}}|\boldsymbol{B}_{\mathrm{ext}}|/(2\pi)$ one would expect for an isolated nuclear spin at the same field. As discussed in section 2.1.1, this enhancement is due to the correction terms ν_z and $\nu_\perp$. The slope of the analytic or simulated curve represents the effective gyromagnetic ratio, yielding $\gamma_{\mathrm{eff}} \approx 1.2 \cdot \gamma_{\mathrm{N15}}$.

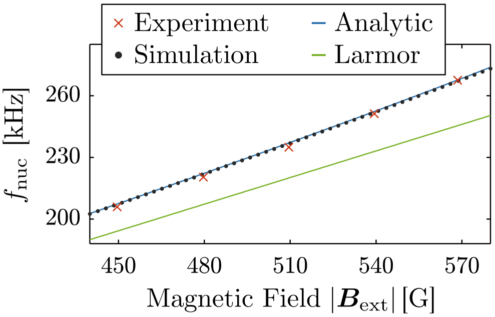

Figure 2.4: Experimentally observed precession frequency at different values of $|\boldsymbol{B}_{\mathrm{ext}}|$ and fixed tilt angle $\phi = 1°$, together with analytic and numerical predictions, demonstrating a near-linear dependence of f_{nuc} on the external magentic field strength. In addition, there is a clear enhancement of the precession frequency of the expected bare Larmor frequency, that is well captured by the theory predictions.

In conclusion, the near linear dependence of f_{nuc} on the applied magnetic field strength does not only underline that we do indeed observe nuclear spin precession, its great agreement with the theoretical framework is also demonstrating that our scheme is well enough described by our theory to be utilized in quantitative magnetometry applications. We will discuss envisioned sensitivities for key applications in section 2.4.

Precession Frequency as a Function of $B_\perp$

Next, we investigate the dependence of f_{nuc} on the transverse magnetic field $B_\perp$. Experimentally, this transverse field is generated by tilting the entire bias field vector away from the NV symmetry axis by an angle ϕ. We can control ϕ in two separate angles, ϕ_x and ϕ_y, applied in the $\boldsymbol{e}_x$-$\boldsymbol{e}_z$ and $\boldsymbol{e}_y$-$\boldsymbol{e}_z$-planes, respectively. For the small angles we investigated, $(\phi_x^2 + \phi_y^2)^{1/2} \approx \phi$.

In Figure 2.5 (A), we show the observed nuclear precession frequency as a function of ϕ_x and ϕ_y, at a fixed total magnetic field of $|\boldsymbol{B}_{\mathrm{ext}}| = 533\,\mathrm{G}$, measured on the nanopillar containing NVA1. For each pixel, an all-optically induced FID trace is taken, and the corresponding precession frequency f_{nuc} is extracted by Fourier analysis. Note that only the pixels with an optical precession contrast of more than 1 % are considered. See section 2.2.2 for a definition of contrast, and Figure 2.6 (A) for the measured contrast of each pixel shown here.

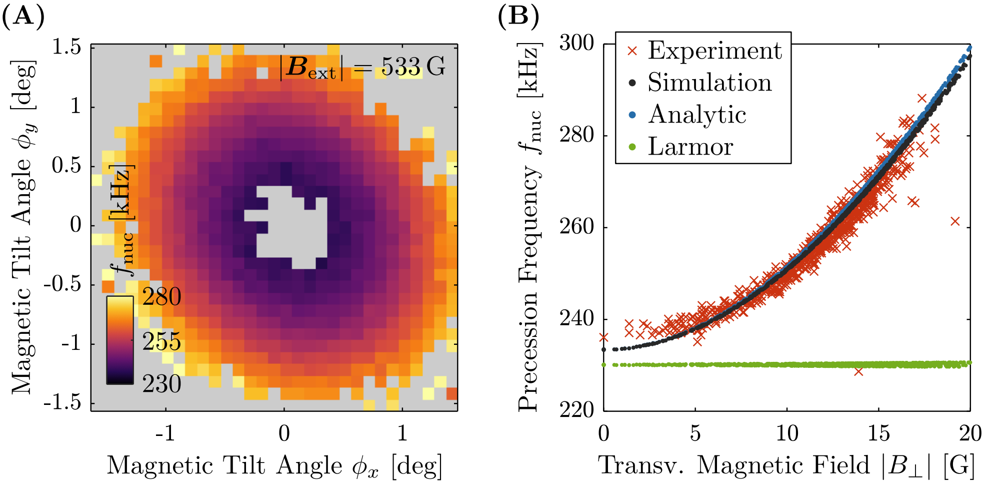

Figure 2.5: Investigation of the observed nuclear FID frequency. **(A)** Measured nuclear precession frequency of NVA1 as a function of magnetic field orientation, for a fixed total field of $|\boldsymbol{B}_{\mathrm{ext}}| = 533\,\mathrm{G}$. Only pixels with a corresponding FID contrast of $C > 1\,\%$ are shown. **(B)** Same data as in (A), but plotted against total transverse magnetic field $B_\perp$. The black dots represent the prediction of our numerical model, the blue dots the prediction of equation (2.13), and the green dots the expected bare larmor frequency $\gamma_{\mathrm{N15}}|\boldsymbol{B}_{\mathrm{ext}}|/(2\pi)$. Our theory framework captures to non-linear dependence of f_{nuc} on $B_\perp$ extremely well.

To relate the tilt angles ϕ_x and ϕ_y to the corresponding transverse magnetic field, we re-plot the same data as a function of $B_\perp$, as shown in Figure 2.5 (B). This transverse field $B_\perp$ was determined for each pixel individually by taking a full ODMR spectrum (see appendix, section A.6). We find that the precession frequency f_{nuc} increases non-linearly with $B_\perp$ in a way that is excellently described by both the analytic result from equation (2.13) and our numerical model. Both analytic and numeric results are generated by using the magnetic field values $B_\perp$ and B_z that were measured experimentally for each pixel. Note that even at $B_\perp = 0$ the observed precession is enhanced with respect to the bare Larmor frequency $f_L = \gamma_{\mathrm{N15}} |\boldsymbol{B}_{\mathrm{ext}}|/(2\pi)$ due to the non-zero ν_z correction term.

For values of $B_\perp$ approaching 20 G, the numerical model and the analytic expression start to slightly deviate from each other, which is due to the perturbative nature of the analytic expression that breaks down for large $B_\perp$. Fortunately, as we will see in the next section, the region of $B_\perp > 20\,\mathrm{G}$ is experimentally inaccessible and thus anyway irrelevant for us.

In conclusion, our theory describes the observed precession frequency outstandingly well, for any given bias field vector that is near the ESLAC and slightly tilted away from the NV symmetry axis. In particular, equation (2.13) excellently describes the near-linear dependence of f_{nuc} on $|\boldsymbol{B}_{\mathrm{ext}}|$ and the non-linear dependence on $B_\perp$.

2.2.2 Contrast of the Observed Nuclear Precession

For any envisioned quantum sensing application, it is not only necessary to quantitatively understand the observed nuclear precession frequency, it is also of great importance to identify ideal measurement conditions to maximize the experiment's sensitivity. In our case, this means maximizing the optical contrast of the observed oscillation. This motivates the question how the FID readout contrast depends on both $B_\perp$ and $|\boldsymbol{B}_{\mathrm{ext}}|$.

Before we dive into answering this question, let us define the optically detected precession contrast C. For a time domain signal $S(t) = A\cos(\omega t) + B$, we define $C = (2A)/B$; or to put it in words, the full range of the PL oscillation ($2A$) with respect to the PL average (B). For example, the oscillation shown in Figure 2.1 (B) has a contrast of $C \approx 4.1\,\%$. However, note that experimentally – in order to reduce the error of the frequency fit – we typically measure with a low time resolution (just about 6 pixels per oscillation), but instead take a lot of periods. This approach can lead to large errors on the fitted amplitude, such that it is better to determine C in Fourier space, where the definition from above translates to

$$C = \frac{4V}{V_0}\,, \tag{2.23}$$

where V is the amplitude of the signal in the Fourier domain (e.g. its Fourier peak height), and V_0 is the amplitude of the Fourier peak at zero frequency. In the following, we will rigorously measure C as a function of $B_\perp$ (respectively ϕ) and $|\boldsymbol{B}_{\mathrm{ext}}|$.

Precession Contrast as a Function of $B_\perp$

Figure 2.6 (A) shows data recorded on NVA1, where we measured C as a function of $(\phi_x^2 + \phi_y^2)^{1/2} \approx \phi$ for a fixed field $|\boldsymbol{B}_{\mathrm{ext}}| = 533\,\mathrm{G}$. Each pixel originates from a

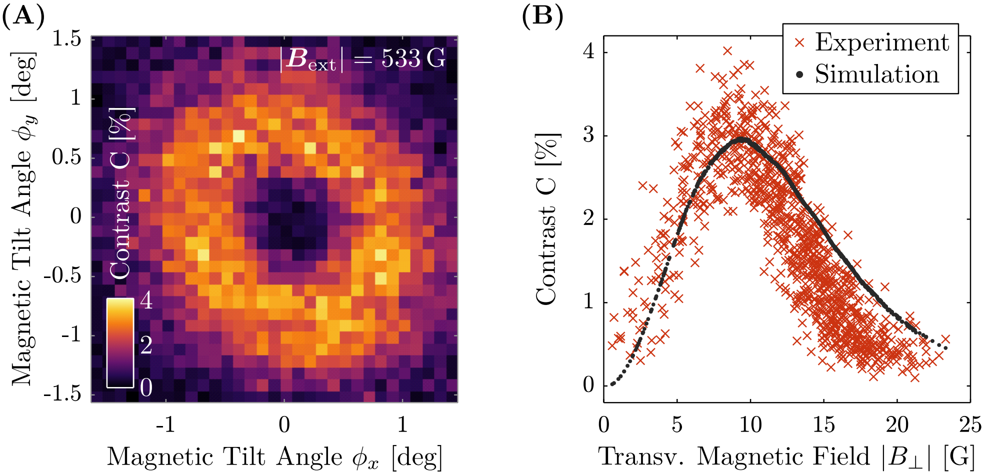

Figure 2.6: Investigation of the observed nuclear FID contrast. **(A)** Measured nuclear precession contrast C of NVA1 as a function of magnetic field orientation, for a fixed total field of $|\boldsymbol{B}_{\mathrm{ext}}| = 533\,\mathrm{G}$. **(B)** Same data as in (A), but plotted against total transverse magnetic field $B_\perp$. The black dots are the prediction of our numerical model, which is normalized to the mean of the data at $\phi_{\mathrm{opt}} \pm 0.03°$. We find great agreement of the numerical model with the data.

single FID trace, in fact the same traces as in Figure 2.5 (A), however here we plot the contrast C instead of the frequency f_{nuc}.

It is clear from Figure 2.6 (A), that when $\phi = 0$, no nuclear FID contrast is observed. This is in line with what we expect based on our theory, because in this case $\boldsymbol{B}_{\mathrm{eff}}$ and $\boldsymbol{e}_{\mathrm{init}}$ are both collinear with $\boldsymbol{e}_z$ such that the nuclear spin is optically pumped into the non-precessing eigenstate $|0, +1/2\rangle$ of the system. Upon increasing ϕ, the vectors $\boldsymbol{B}_{\mathrm{eff}}$ and $\boldsymbol{e}_{\mathrm{init}}$ both tilt away from $\boldsymbol{e}_z$ in different directions, resulting in nuclear precession of increasing contrast C. At the same time, increasing ϕ (i.e. $B_\perp$) tends to reduce the nuclear hyperpolarization efficiency [29, 30] and the NV optical spin readout contrast [25], both of which reduce C. Overall, these counteracting effects imply that there is an optimal tilt angle ϕ_{opt} which maximizes C by balancing the magnitude of the nuclear spin coherences with nuclear spin readout efficiency. From here on, we will call this maximized contrast C_{max}.

To determine ϕ_{opt} and C_{max}, we show in Figure 2.6 (B) the same data as in panel (A), but as a function of transverse field $B_\perp$. This transverse field $B_\perp$ was measured for each pixel individually via ODMR (see appendix A.6). Figure 2.6 (B) reveals a clear maximum in C at $B_\perp \approx 8.6\,\mathrm{G}$, which corresponds to $\phi_{\mathrm{opt}} \approx 0.86°$. These results are in good agreement with the predictions of our numerical model, whose simulated contrast is represented by the black dots in Figure 2.6 (B). These simulation results were generated by using the magnetic field components $B_\perp$ and B_z that were experimentally determined for each pixel individually.

Note that the numerical simulation is normalized to the mean of the data at $\phi_{\mathrm{opt}} \pm 0.03°$. This is because the PL predicted by the numerical model is directly proportional to the nuclear spin state occupation, see (2.22), and does therefore neglect any experimental factors such as for instance the nanopillar's wave-guiding properties, optical collection efficiency, or the amount of background light. To make for a fair comparison, we therefore normalize the simulated contrast to the measured contrast.

Precession Contrast as a Function of $|\boldsymbol{B}_{\text{ext}}|$

Interestingly, we find that our all-optical ^{15}N nuclear FID protocol is relatively resilient to deviations of $\boldsymbol{B}_{\text{ext}}$ away from ideal ESLAC conditions. To demonstrate this, we investigate the dependence of the contrast C on the applied external magnetic field $|\boldsymbol{B}_{\text{ext}}|$ and tilt angle $\phi = (\phi_x^2 + \phi_y^2)^{1/2}$, where for each data point, we ensured that $\phi_y = 0$ is maintained to within experimental accuracy. The resulting data exhibit a non-trivial dependence of C on $|\boldsymbol{B}_{\text{ext}}|$ and ϕ_x, as shown in Figure 2.7 (A). Surprisingly, the data appear to be asymmetric with respect to the ESLAC, and both ϕ_{opt} and C_{max} change with $|\boldsymbol{B}_{\text{ext}}|$ in a non-linear fashion, as shown in Figure 2.7 (B). We find a global maximum of $C_{\text{max}} \approx 4.2\,\%$ for $|\boldsymbol{B}_{\text{ext}}| = 533\,\text{G}$, and a drop of C over a full-width at half maximum (FWHM) range of approximately 50 G. The optimal tilt angle increases by a factor of about three when the external bias field is reduces to 420 G.

The reported non-trivial behaviour of C as a function of external field strength is qualitatively captured quite well by our numerical model, as indicated by the black dots in Figure 2.7 (B). Recall that as discussed above, the numerically simulated PL does not predict quantitatively correct PL numbers, which is why the model's result for C_{max} is normalized to the maximum of the data.

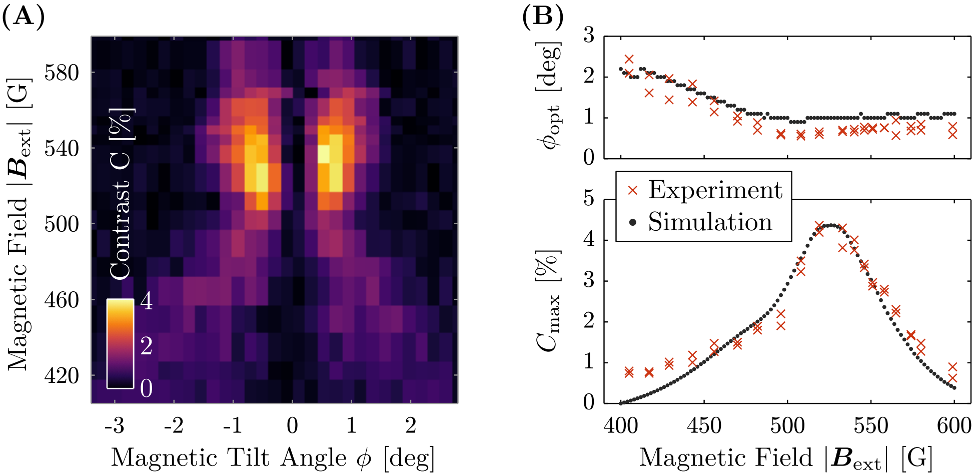

Figure 2.7: Investigation of the observed nuclear FID contrast. **(A)** Measured nuclear precession contrast C of NVA1 as a function of magnetic field orientation and amplitude. **(B)** Maximal observed contrast C_{max} and corresponding tilt angle Φ_{opt} for each value of $|\boldsymbol{B}_{\text{ext}}|$. The prediction of our numerical model is shown in black, which for the case of C_{max} is normalized to the maximal data point.

Matching Optical Rates to the Experimental Data

The quality of the simulation depends sensitively on the optical rates plugged into the numerical model. Specifically, depending on which of the parameter sets listed in table 2.1 is used, we find better or worse agreement with our data. To determine which parameter set returns the output that matches to our data the best, we re-plot the data from Figures 2.6 (B) and 2.7 (B) and compare it to the numerical result using each of the five parameter sets from table 2.1. This comparison is shown in Figure 2.8. Note that as explained above, the numerical results for the contrast C and $C_{\max}$ are normalized to the data.

Depending on the parameter set, we find maximal contrast for $B_\perp$ between 7.9 and 10.2 G, as shown in Figure 2.8 (A). All rate constant parameter sets predict a global maximum in C between 530 and 550 G, as demonstrated by Figure 2.8 (B). Surprisingly, for sets 4 and 5, for which $k_A^0 = 0$, there is a second local maximum in $C_{\max}$ at about 470 G, however there is no such indication of a second maximum in the experimental data. Overall, we conclude that parameter set 1 has the best agreement with our data, and this is why we have used parameter set 1 for the numerical results shown in all previous figures within this section. We assign any remaining discrepancies between data and simulations to uncertainties on the exact values of set 1.

In conclusion, we have not only worked out the numerical model parameters that fit best to our experimental data, but more importantly, the analysis of the observed contrast in PL has allowed us to identify ideal measurement conditions for sensing applications based on our all-optical protocol. Namely, the PL contrast – and thus the predicted sensitivity – is maximized at a total magnetic bias field of $|\boldsymbol{B}_{\text{ext}}| = 533\,\text{G}$ for a tilt angle of $\phi_{\text{opt}} = 0.86°$, where we obtain $C_{\max} = 4.2\,\%$.

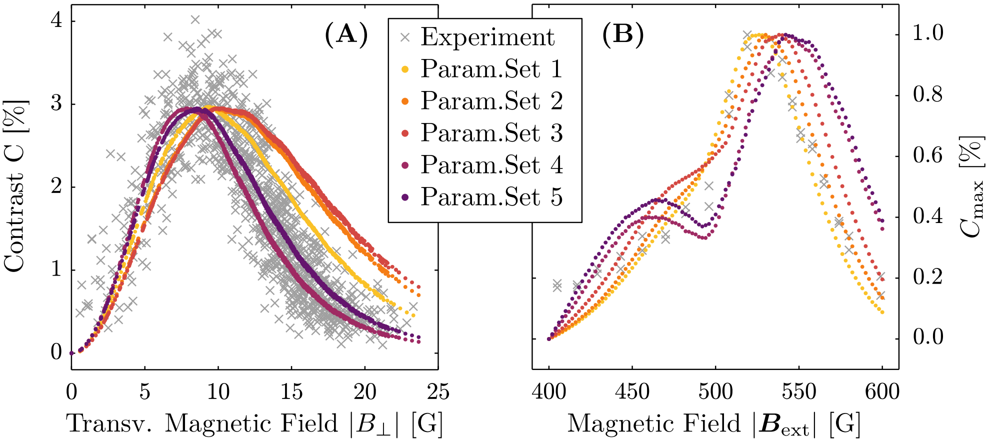

Figure 2.8: Investigation of the observed nuclear FID contrast. **(A)** Measured nuclear precession contrast C of NVA1 as a function of magnetic field orientation and amplitude. **(B)** Maximal observed contrast $C_{\max}$ and corresponding tilt angle Φ_{opt} for each value of $|\boldsymbol{B}_{\text{ext}}|$. The prediction of our numerical model is shown in black, which for the case of $C_{\max}$ is normalized to the maximal data point.

2.2.3 Lifetime of the Observed Nuclear Precession

For almost all spin-based quantum sensing applications, the sensitivity scales with the lifetime of the employed spin [3, 99, 131]. Nuclear spins typically offer much longer coherence times than electron spins [31, 32], and are therefore of particular interest for quantum sensors. It is true, however, that very often the sensitivity is also scaling with the gyromagnetic ratio of the spin system, where nuclear spins are about three orders of magnitude worse compared to electronic spins, meaning that general there is a trade-off to be considered. We will discuss the sensitivity of our protocol in more detail in section 2.4. Here, we focus on measuring our scheme's limiting spin lifetime, that is the inhomogeneous nuclear ^{15}N spin coherence time T_2^*. This time is directly given by the lifetime of the observed oscillation in PL.
Therefore, in order to experimentally determine the nuclear T_2^* time with our all-optical sensing scheme, we extend the measurement pulse sequence shown in Figure 2.1 (A) to much longer FID evolution times τ, until we can fully resolve the entire decay of the signal. The resulting very long FID trace, taken on NVA1, is shown in Figure 2.9. Fitting an exponentially decaying sine function to these data yield $C = (3.09 \pm 0.11)\,\%$ and $T_2^* = (248.1 \pm 12.4)\,\mu\text{s}$ for this single NV under investigation. This decoherence time is somewhat shorter than previously reported values [132], however, it is consistent with the rather short NV electron spin relaxation time of only about $T_1 = (298 \pm 11)\,\mu\text{s}$ we have measured for this shallow NVA1 – a timescale which is known to limit the NV's nuclear spin decoherence time [133, 134].

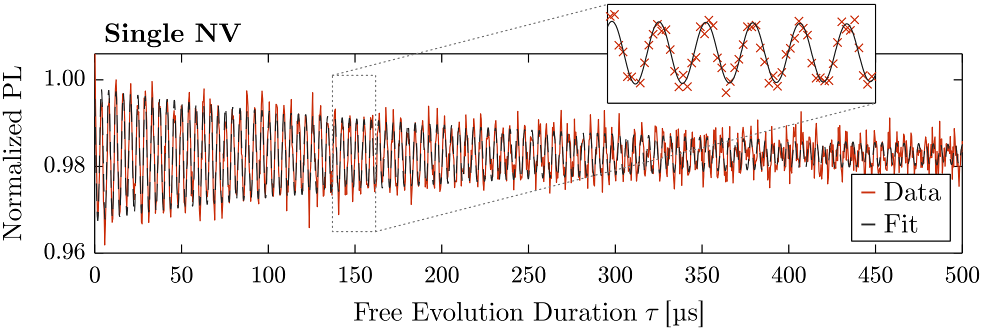

Figure 2.9: All-Optically measured nuclear spin precession of a single NV in a diamond nanopillar (NVA1), measured at $|\boldsymbol{B}_{\text{ext}}| = 533$ G with tilt a tilt angle $\phi = 0.65°$. The FID trace is fitted with a damped harmonic function to determine the nuclear spin coherence time T_2^*, yielding $T_2^* = (248.1 \pm 12.4)\,\mu\text{s}$.

2.3 Extension to an NV Ensemble

All the studies presented in the previous section of this chapter were conducted on the same single NV center (NVA1). For many sensing applications, however, it is advantageous to employ entire spin ensembles instead of single centers. Especially for applications that do not require the high spacial resolution only a single NV can provide, the strong signal and thus enhanced sensitivity of a large collection of NVs is desirable. However, in such ensemble measurements, due to the spacial distribution of the NVs, it can be highly challenging to treat all NVs exactly the same, because for example the optical excitation intensity or microwave driving field amplitudes can vary across a large NV ensemble. Such inhomogeneities can be very problematic because they typically give rise to inhomogeneous broadening of the signal, potentially leading to the failure of a particular sensing technique. In addition, interaction between the NVs can be another hurdle that could lead to the breakdown of a sensing scheme when moving to spin ensembles.

Here, we reproduce the data from the previous section on an (113)-oriented ensemble of NVs with 75 % preferential alignment of NVs (diamond C, see appendix A.2 in the appendix for a more detailed description of the diamond). The resulting data are shown in Figure 2.10, and they convincingly demonstrate that our sensing scheme and the developed theory is compatible with large ensembles of NVs. Note that the reduced quality of the data compared to the single NV case is mostly due to shorter experiment integration times. We also note that our optics were not at all optimized for ensemble measurements, but instead we even used a optical density filter in the collection path to protect our photon detector from the bright signal of this very dense ensemble. In addition, to guarantee magnetic alignment with the NVs in this (113) diamond, the sample was mounted with the top surface not normal to the optical excitation and collection path, further reducing optical readout efficiency due to scattering at the tilted surface and reduced wave-guiding in the nanopillar. All of these experimental circumstances have contributed to increased noise on the observed all-optical FID ensemble data. Nonetheless, the core physics are visible in the data and identical to the single NV case.

Based on the results shown in Figure 2.10, we identify the external magnetic field for which the contrast C is optimized, and find a very similar optimal working point as we previously identified for the single NV: $|\boldsymbol{B}_{\text{ext}}| \approx 533$ G with a tilt angle of $\phi \approx 0.8°$. Under these ideal conditions, we next measure the nuclear T_2^* decoherence time of the NV ensemble, as shown in Figure 2.11. Using a least-squares fit, we find $C_{\text{max}} = (2.08 \pm 0.04)\,\%$ and $T_2^* = (508.5 \pm 17.4)\,\mu\text{s}$ for this NV ensemble. While C has halved compared to the single NV case, a reduction we assign to the minority of non-aligned NVs, the T_2^* time has almost doubled.

This increased ensemble ^{15}N coherence time stems from the fact that the ensemble NVs are much deeper compared to the very shallow single NV in the nanopillar that we

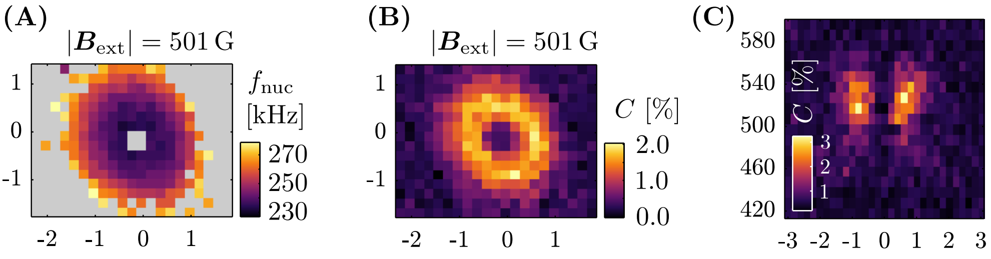

Figure 2.10: Same data as in Figures 2.5 (A), 2.6 (A) and 2.7 (A), but recorded on an entire ensemble (diamond C) instead of a single NV, demonstrating that our all-optical nuclear FID measurement scheme is compatible with large ensembles of NVs.

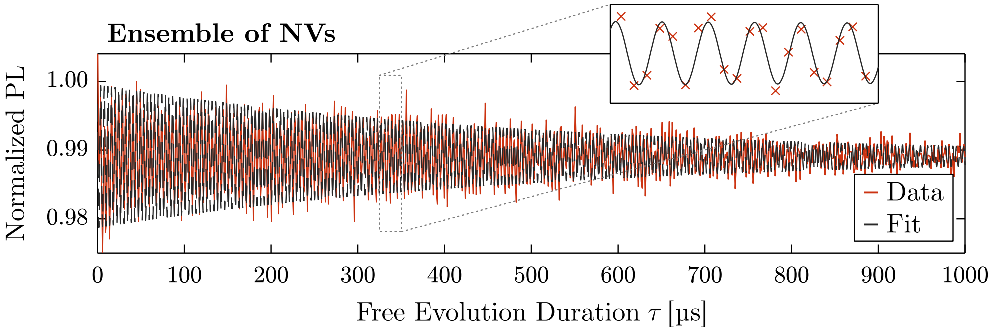

Figure 2.11: All-Optically measured nuclear spin precession of a dense ensemble of NVs in bulk diamond (diamond C), measured at $|\boldsymbol{B}_{\text{ext}}| = 533$ G with tilt a tilt angle $\phi = 0.8°$. The FID trace is fitted with a damped harmonic function to determine the nuclear spin coherence time T_2^*, yielding $T_2^* = (508.5 \pm 17.4)$ µs, about twice the value we obtained on a single shallow NV.

used above, which results in less surface spin noise. However, the observed ensemble T_2^* time is still short of the best reported values of up to 2.2 ms [35,132]. In the single NV case, we argued that the NV electron spin relaxation time T_1 is limiting the nuclear spin coherence time, but for the ensemble at hand, we exclude this argument because it exhibits a very long electron spin lifetime of $T_1 = (5.8 \pm 0.5)$ ms. Instead, possible other sources for nuclear spin dephasing in our ensemble might be fluctuations in the external magnetic field or in temperature [132,134].

2.4 Sensitivity Estimation

Our all-optical ^{15}N FID scheme lends itself to applications in quantum sensing, in particular to magnetometry and gyroscopy, two techniques that can both infer the respective target quantity (magnetic field and rotation frequency) directly from the frequency of the observed nuclear precession. In this section, we discuss the predicted performance of such envisioned all-optical coherent quantum sensing schemes.

Magnetometry

We begin with an estimation of the sensitivity that our scheme could achieve in magnetometry applications. The shot noise limited FID sensitivity for spin-based, low-frequency magnetometry is given by [3,99,131]

$$\eta_{\text{mag}} \approx \frac{1}{\gamma C \sqrt{N T_2^*}} \,. \tag{2.24}$$

Here, N is the average number of detected photons per readout pulse, C is the readout contrast, and γ is the gyromagnetic ratio of the spins employed for sensing. Further sensitivity reductions due to overhead in preparation and measurement of quantum states are not included in this expression, but of little relevance to our conclusion, given the long T_2^* times at hand.

Evaluating (2.24) for our single NV data ($T_2^* \approx 250\,\mu\mathrm{s}$, $C \approx 4\%$, $N = 0.1$) using the effective nuclear gyromagnetic ratio $\gamma = 1.2 \cdot \gamma_{\mathrm{N15}}$ determined from the slope of the data in Figure 2.4 or alternatively from (2.13), we obtain a photon shot noise limited magnetometry sensitivity of $\eta_{\mathrm{mag}} = 154\,\mu\mathrm{T\,Hz}^{-1/2}$. Further, given that our approach scales to NV ensembles, we make predictions on future ensemble NV magnetometry sensitivity. For this, we assume a laser power of 100 mW, a 350 ns readout window, and a conversion ratio of excitation photons to detected PL photons of 3.4 % [135], to obtain $N = 3.2 \cdot 10^9$. Together with the measured ensemble values $T_2^* = 500\,\mu\mathrm{s}$ and $C = 2\,\%$, we estimate that $\eta_{\mathrm{mag}}^{\mathrm{ensemble}} = 1.22\,\mathrm{nT\,Hz}^{-1/2}$.
When comparing nuclear spins to electron spins in terms of their sensitivity in sensing applications, one finds that electron spins are usually preferable. The reason for this is the following: While nuclear spins benefit from larger T_2^* coherence times compared to electron spins, their gyromagnetic ratio γ is smaller by about four orders of magnitude. In most cases, the gain in coherence time is not large enough to outweigh the sensitivity loss due to the small γ, meaning that most of the time nuclear spins are worse magnetometry sensors. This is the case for our protocol too. The nuclear sensitivity of $\eta_{\mathrm{mag}}^{\mathrm{ensemble}} = 1.22\,\mathrm{nT\,Hz}^{-1/2}$ we estimate for our envisioned ensemble magnetometer is nowhere near competitive with the state-of-the-art NV electron spin magnetometry that achieves sensitivities of $\tilde{\eta}_{\mathrm{mag}}^{\mathrm{ensemble}} < 10\,\mathrm{pT\,Hz}^{-1/2}$ [91].

Gyroscopy

For spin-based gyroscopy, however, the situation is very different because the gyroscopic sensitivity does not depend on the gyromagnetic ratio [30],

$$\eta_{\mathrm{gyro}} \approx \frac{1}{C\sqrt{NT_2^*}}\,. \tag{2.25}$$

Nuclear spins are thus extremely attractive for gyroscopy, since their small gyromagnetic ratio is irrelevant and one only profits from their long T_2^* times. For this reason, gyroscopy is the sensing application where our all-optical nuclear approach would arguably excel the most. Employing the same procedure as before, we obtain a projected ensemble gyroscope sensitivity of $\eta_{\mathrm{gyro}}^{\mathrm{ensemble}} \approx 135^\circ\,\mathrm{hour}^{-1/2}$. To place this estimate in context, we note that best reported NV-based nuclear spin gyroscopes have recently achieved sensitivities $\tilde{\eta}_{\mathrm{gyro}}^{\mathrm{ensemble}} = 280^\circ\,\mathrm{hour}^{-1/2}$ [35]. It is important to note that NV-based spin gyroscopes in general is still an emerging technology and not yet competitive with established technologies [35, 136]. Finally, note that the sensitivity we give here is an optimistic estimate on what could be experimentally achievable; they are by no means values we have realized in the lab. This is because our setup is not at all optimized for ensemble measurements, and therefore we are lacking the resources to look into proper sensitivity optimization.

In conclusion, while for magnetometry, our projected sensitivity alone is not competitive with the state-of-the-art, the microwave-free modality we present still lends itself to specific applications, such as for instance remote sensing through optical fibres [137], or for cases where microwave radiation would critically affect the sample of interest. Conversely, for gyroscopy, we project numbers competitive with previous

NV-based approaches. The added feature of all-optical operation is hereby a key asset, which may enable future integrated and power-efficient NV gyroscopes.

2.5 Outlook

To summarize, we have presented an all-optical technique for nuclear quantum sensing with the ^{15}N spin of the NV center in diamond, that relies on optically exciting a nuclear spin precession that is then observed as a modulation in the emitted NV PL. The key ingredient for this is a magnetic field with an amplitude of around 500 G that is very slightly misaligned with the NV symmetry axis. We have theoretically described the measurement scheme both analytically and with a numerical model, and obtain outstanding agreement with experimental data, that we have recorded on both single a NV and an entire ensemble of NVs. We find that the ideal working point in terms of sensitivity is achieved at 533 G and a tilt angle of 0.86°, leading to a maximal contrast in PL of 2 to 4 %. Under these ideal conditions, we estimate an ensemble sensitivity of $1.22\,\mathrm{nT\,Hz}^{-1/2}$ for magnetometry, and $135°\,\mathrm{hour}^{-1/2}$ for gyroscopy applications.

Looking forward, the obvious question at hand is how the observed nuclear FID contrast C could be improved to further boost the scheme's sensitivity. Previous studies have shown that at the ESLAC, the optical contrast between nuclear states in the $|m_S = 0\rangle$ manifold is not expected to be much higher than 4 to maximally 5 % [30], a limit we are already approaching experimentally when we measure at the identified optimal measurement point. Potential approaches to exceed this limit could for instance be alternate high fidelity readout schemes based on spin-to-charge conversion [55–57], which are well compatible with our protocol. Another potential path to improving contrast C is to dynamically pulse the external magnetic field misalignment angle ϕ between spin initialization and readout, to separately optimize the two processes.

Based on the discussion presented in section 2.4, our all-optical sensing scheme is of particular interest for gyroscopy applications. This has sparked interest with researchers from CSEM, who are currently developing an integrated diamond gyroscopy device based on our all-optical sensing scheme. This is an on-going research project in close collaboration with people from our group at the University of Basel, all funded by the SNSF quantum flagship.

CHAPTER 3

Surface Proton NMR via NV Spin-Locking

The previous chapter presented an improved way of configuring the NV center as a quantum sensor. Now, we will shift focus and instead study a particular kind of signal that can be sensed with the NV center – namely the magnetic field originating from the spins of nearby atomic nuclei. The experimental technique that we will be using for this is nuclear magnetic resonance (NMR).

Traditionally, NMR is based on first polarizing the target nuclear spin ensemble in a large magnetic field, subsequently exciting a nuclear precession motion with RF pulses, and finally measuring the resulting induction voltage in a pickup coil. This approach to NMR was discovered by Isidor Rabi in 1938 [138], for which he was awarded the Nobel prize in 1944, and by today, it has become an indispensable tool in a multitude of scientific areas, such as medicine, analytical chemistry, material science and microbiology [139]. Key applications of NMR are on one hand the identification and characterization of molecules by measuring their nuclei's chemical shifts. On the other hand, by introducing a spatial gradient in the bias magnetic field, one can resolve where in space a particular NMR signal comes from, and thereby do magnetic resonance imaging (MRI). The established coil-based inductive detection, however, comes with a substantial drawback in that the coils used to detect the nuclear moments are rather far away from the NMR sample. This restricts the method's application to macroscopic samples, making it practically impossible to study samples at the nanometer scale [140].

This limitation can be overcome by employing the NV center in diamond as an NMR sensor [43–45], because its atomic size allows it to be brought into close proximity to the NMR sample under investigation, which substantially boosts spatial resolution and signal strength [66], enabling nanoscale NMR. The dynamical decoupling sequences that we have introduced in section 1.5 play a central role in NMR with the NV center, because they tune the NV center's sensitivity to specific AC magnetic fields, allowing for frequency selective detection of the target nuclei's magnetic fields. Over the last fifteen years, people have used these pulse sequences to demonstrate NV-based NMR spectroscopy of statistically polarized nuclear spins in surface materials [45–47, 67] with volumes as small as $5\,\mathrm{nm}^3$ [120], as well as the detection of single molecules [48, 49] and even single spins [50].

One prevalent and widely employed application of nanoscale NV NMR is the determination of an individual NV center's depth in the diamond crystal [51]. This depth can in principle be inferred from the NMR coupling strength to a nuclear ensemble on the diamond surface, given that the position, volume and spin density of this ensemble are well-known. It is very common to use ^{1}H nuclei (i.e. proton spins) in immersion oil for this. In chapter 5, we conduct such NMR-based depth measurements with immersion oil, and discuss the underlying mathematics in great detail, specifically for NMR performed with the Spin-Lock and XY8-k sequences.

Here, we study one particular issue that can arise in depth determination via immersion oil NMR. Namely, such depth determination is only working properly under the assumption that the immersion oil on the diamond surface is the only source of nearby hydrogen nuclei. This is not necessarily the case, as some NV NMR studies have reported that there is an observable proton NMR signal even when the diamond is not nominally coated with immersion oil or any other hydrogen-rich substance [42, 46, 66, 67, 69]. This observation indicates a presence of unidentified protons near the NV, either in the diamond lattice or on its surface. Disregarding these additional protons in any depth determination technique based on ^{1}H NMR is highly problematic, as this leads to an underestimation of the NV depth. Judging by the literature, the NV community seems often unaware of such an ubiquitous and measurable proton spin ensemble, as there is a long list of publications where depth determination based on protons in immersion oil was done without characterizing the NMR signal before applying oil, or at least NMR experiments on clean diamond are not mentioned [59–65]. There are a handful of papers that do mention the existence of proton NMR on un-coated diamond, yet it appears that these protons are not accounted for when computing the NV depth from the NMR obtained after applying oil [66,67,69].

The goal of this chapter is to verify and characterize the presence of proton spins in tri-acid cleaned diamond samples. Given such a characterization, including a quantitative analysis of the location and density of the proton spin ensemble, one could account for these spins in the conventional depth determination protocol to avoid depth underestimation. Even better, if these protons are not only well characterized but also always present, it would be possible to determine the depth of single shallow NV centers using only these protons, thus eliminating the need for coating the diamond with immersion oil or other proton-rich substances. This would be highly advantageous for depth determination in applications that employ fragile diamond structures from which these substances cannot be easily removed, such as for example mounted diamond scanning tips for scanning NV magnetometry [27].

For this reason, we perform nanoscale NMR spectroscopy with single NV centers in diamond, using the Spin-Lock sequence we have introduced in section 1.5.5. Notably, we are not employing the XY8-k sequence, because as we will demonstrate in chapter 4, XY8-k NMR has a few crucial weaknesses that can be overcome by using the Spin-Lock sequence instead. And indeed, for shallow NVs, our Spin-Lock NMR experiments reveal a clear proton signature, even if the diamond surface is clean. Here, whenever we say “clean”, we mean tri-acid cleaned, i.e. boiled in a equal mixture of nitric, sulphuric and perchloric acid, which is known to result in an oxygen terminated diamond surface [53, 141]. An example of such proton Spin-Lock NMR on clean diamond is shown in Figure 3.1, taken on a single shallow NV at 490 G. The data exhibit a dip at 2.078 MHz ± 0.411 kHz which is very close to the expected proton Larmor frequency of $\omega_L = 2.086\,\mathrm{MHz}$, a small discrepancy that we assign to an inaccurate B-Field measurement. Based on the characterization experiments that we will present in this chapter, we speculate that this proton signal arises from either a sub-nanometer thin film of water on the diamond surface [142–144], or from surface-bound hydrogen atoms that are expected to be present on oxygen terminated diamond surfaces [141].

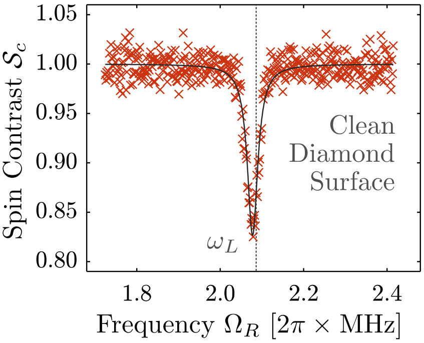

Figure 3.1: Spin-Lock NMR spectrum on tri-acid cleaned diamond (oxygen surface terminated surface). Data were taken on the shallow NVA1 at an aligned magnetic field of $|\boldsymbol{B}_{\mathrm{ext}}| \approx 490\,\mathrm{G}$ and for a spin-locking duration of $\tau = 30\,\mu\mathrm{s}$. The obtained NMR dip is fitted with a Lorentzian lineshape function, revealing a dip position of 2.078 MHz ± 0.411 kHz. This matches the expected proton Larmor frequency of $\omega_L = 2.086\,\mathrm{MHz}$, indicating a presence of protons in the NV vicinity.

This chapter is organized as follows: First, in section 3.1, we explain the principle of Spin-Lock NMR, how to process the PL data to arrive at a spectrum as shown in Figure 3.1, and how to optimize the resulting signal-to-noise ratio. Then, in section 3.2, we study the proton presence observed on tri-acid cleaned diamond by measuring how the corresponding NMR dip scales with NV depth, spin-locking duration and temperature. Finally, in sections 3.3 and 3.4, we undertake two more attempts to further characterize the observed proton signal, namely by deuterium terminating the diamond surface, and by freezing liquid water on the diamond surface.

3.1 Spin-Lock NMR Technique

To perform nanoscale NV NMR spectroscopy of statistically polarized nuclear spins, we employ the Spin-Lock sequence we have previously introduced in section 1.5.5. Specifically, we first apply an external magnetic field that is aligned with the NV symmetry axis to set the nuclear ensemble's noise frequency to its Larmor frequency. Then, we play a Spin-Lock sequence with a fixed spin-locking duration τ (see section 3.1.2 for a discussion on how to choose a good value for τ), while sweeping the amplitude of the spin-locking field. For amplitude values where the corresponding Rabi frequency Ω_R matches the Larmor frequency ω_L of a nearby nuclear spin ensemble – that is, at the Hartmann-Hahn resonance – the Spin-Lock sequence picks up the nuclear spins' magnetic signal, and thus the resulting $T_{1\rho}$ time is reduced, as described by equation (1.28).

To further illustrate this mechanism, we sketch in Figure 3.2 (A) an envisioned Spin-Lock filter function together with the noise spectral density $S_z(\omega)$ from equation (1.21) where we added an additional noise feature at the nuclear Larmor frequency ω_L that represents the proton spin bath. Sweeping the MW amplitude and thereby its Rabi

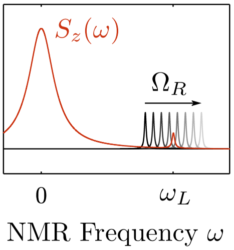

Figure 3.2: Principle of Spin-Lock NMR. By sweeping the Rabi frequency Ω_R of the spin-locking MW pulse, the peak of an envisioned filter function is shifted in frequency space. This way, it can be swept across a nuclear noise peak at the nuclear Larmor frequency ω_L in the noise spectral density $S_z(\omega)$. On Hartmann-Hahn resonance, $\Omega_R = \omega_L$, the overlap of the two functions is maximized, resulting in increased noise pick-up and thus a reduction in $T_{1\rho}$. In an NMR spectrum, this reduction manifests as a dip in PL.

frequency Ω_R tunes the filter function's peak across the nuclear noise peak, such that on resonance $\Omega_R = \omega_L$, the two functions show a large overlap. This means that there is increased noise pick-up and a concomitant reduction in $T_{1\rho}$. Consequently, we observe a dip in NV PL when $\Omega_R = \omega_L$, leading to an NMR spectrum as shown in Figure 3.1.

3.1.1 NMR Data Processing

In this section, we explain the data processing necessary to obtain an NMR spectrum as depicted in Figure 3.1. In particular, we will discuss how we calibrate the x-axis to units of Rabi frequency, how we transform the measured NV PL into units of spin contrast, and we explain what we mean by the spin contrast $\mathcal{S}_c$ in the first place. For this, we use the exemplary dataset shown in Figure 3.1.

Whenever we perform a Spin-Lock NMR experiment, as discussed in section 1.5.5, we always finish the sequence with either a positive or negative $\pi/2$-pulse, resulting in two distinct PL curves that we denote as $I_{\mathrm{PL}}^{\pm}$. These PL curves are plotted in Figure 3.3 (A). The x-axis of this plot is given by the amplitude of the applied spin-locking MW field, which is experimentally controlled by our microwave signal generator with a waveform amplitude with values between 0 and 1 in (see the appendix A.1.3 for a detailed description of the MW generation in our setup). In a first data processing step, we combine the two curves $I_{\mathrm{PL}}^{\pm}$ to a relative difference in PL that we denote as ΔI_{PL}, using the same definition as Pham et al. [51], which yields

$$\Delta I_{\mathrm{PL}} = \frac{I_{\mathrm{PL}}^{-} - I_{\mathrm{PL}}^{+}}{I_{\mathrm{PL}}^{-} + I_{\mathrm{PL}}^{+}} \,. \tag{3.1}$$

We plot ΔI_{PL} in Figure 3.3 (B). By working with this relative difference ΔI_{PL} we remove common mode noise such as drifts in the background PL, and we ensure that in the absence of coherent oscillations, $\Delta I_{\mathrm{PL}} = 0$ corresponds to a fully decayed spin state. Next, to normalize the data, we fit a linear function to the background of ΔI_{PL}. For this we omit all pixels that are closer to the peak than two times its width. This range is highlighted in grey in Figure 3.3 (B), and the resulting linear fit is represented by the black line. Dividing the entire data set by this linear background fit leads to a normalized NMR spectrum with a flat background and with values between 0 and 1. This normalization essentially removes the "background" relaxation due to noise sources at frequencies outside the measured NMR window (in particular at 0 Hz),

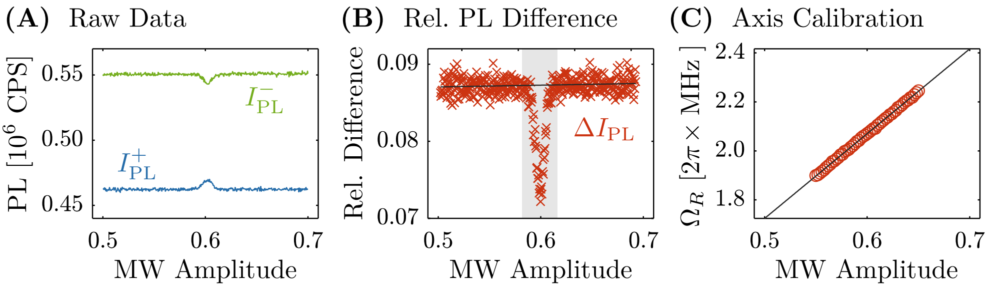

Figure 3.3: Spin-Lock NMR Data Processing **(A)** The obtained raw PL data as a function of MW amplitude for $\tau = 30\,\mu\mathrm{s}$. We always measure two separate PL traces, for either a final + or $-\pi/2$-pulse. **(B)** Taking the relative PL difference ΔI_{PL} of the two curves in (A) results in an NMR dip where a value of 0 corresponds to a fully relaxed spin system. To normalize the data to 1, we fit a linear function (black line) to the data omitting the pixels in the grey area, and normalize the entire data with this linear fit (not shown here). **(C)** Calibration of the x-axis is done by measuring Rabi oscillations for multiple MW amplitude values, and fitting a linear function to the resulting Rabi frequencies. Dividing the data from (B) by the linear background fit, and then plotting against the x-axis in units of Ω_R ultimately results in the NMR spectrum shown in Figures 3.1 and 3.4.

and for this reason, we identify the normalized PL values as the NV spin contrast caused by the presence of nuclear spins, denoted by $\mathcal{S}_c$. Specifically, a value of $\mathcal{S}_c = 1$ means that no decoherence due to any nuclear spin bath has occurred, whereas $\mathcal{S}_c < 1$ means that some nuclear ensemble is resonant with the NV dressed state transition and is thus reducing the NV coherence. In the extreme case, for $\mathcal{S}_c = 0$, the nuclear spin noise has caused the dressed state to relax into a fully mixed state.

Finally, to convert the MW amplitude on the x-axis to the more meaningful corresponding Rabi frequency Ω_R, we take Rabi experiments (see section 1.3.3) at multiple MW amplitudes. We then transform the resulting Rabi oscillations to Fourier space, where we determine the Rabi frequency Ω_R as the position of the respective Fourier peak. Ultimately, we fit the obtained Rabi frequencies with a linear function, as depicted in Figure 3.3 (C). This linear function serves as a conversion from MW

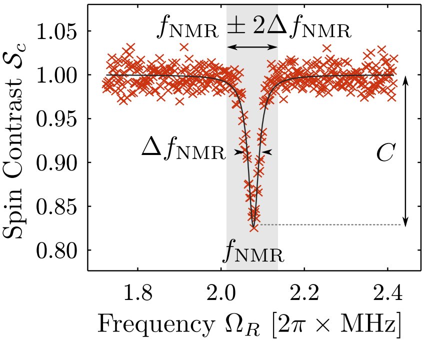

Figure 3.4: Same Spin-Lock NMR spectrum as in Figure 3.1 ($\tau = 30\,\mu\mathrm{s}$), plotted again to define key properties of the NMR spectrum. We define f_{NMR} as the fitted Lorentzian function's position, Δf_{NMR} as its FWHM, and the contrast C as its height. Finally, we define the signal-to-noise ratio (SNR) as the contrast C divided by the standard deviation of all pixels more than $2\Delta f_{\mathrm{NMR}}$ away from the fitted peak position (i.e. outside the grey area).

amplitude to Ω_R. Normalizing ΔI_{PL} as described above and plotting it against the recalibrated x-axis ultimately yields the NMR spectrum shown in Figures 3.1 and 3.4. Note that an alternative way to calibrate the x-axis is to play two artificial MW tones at MHz frequencies, which will show up as separate peaks in the NMR spectrum, and whose positions allows for a conversion of MW amplitude to Rabi frequency. In this thesis, we use this alternative calibration approach only once, specifically in Figure 3.12.

In Figure 3.4 we plot the finalized data once more to define the key properties of such an NMR signal. First, we define the NMR frequency f_{NMR} as the fitted position of the dip in units of Hz, and the NMR width Δf_{NMR} as the FWHM of the fitted Lorentzian lineshape, in units of Hz as well. Next, we define the contrast C of the NMR signal as the height of the NMR dip,

$$C \;=\; \mathcal{S}_c(\Omega_R \neq \omega_L) - \mathcal{S}_c(\Omega_R = \omega_L) \;=\; 1 - \mathcal{S}_c(\Omega_R = \omega_L)\,, \tag{3.2}$$

and the signal-to-noise ratio (SNR) as the contrast C divided by the standard deviation of all pixels outside the grey area,

$$\mathrm{SNR} = \frac{C}{\mathrm{std(background)}}\,. \tag{3.3}$$

This grey are is given by the interval $f_{\mathrm{NMR}} \pm 2\Delta f_{\mathrm{NMR}}$.

3.1.2 SNR Optimization

Optimization of the SNR in Spin-Lock NMR is not only desirable from a purely practical point of view to minimize experiment duration in our lab, it is also of crucial importance when it comes to improving the sensitivity of Spin-Lock NMR for quantum sensing applications. In order to increase the SNR, as is evident by equation (3.3), one can either reduce the noise on the PL readout to minimize the standard deviation STD of the NMR background, or one can increase the contrast C. While both of these depend on various different parameters, we will show in the following that both do crucially depend on the spin-locking duration τ. In fact, we will see that $C(\tau)$ and $\mathrm{STD}(\tau)$ increase with τ in different ways, and therefore there is an ideal value for τ that maximizes their ratio, i.e. the $\mathrm{SNR}(\tau)$.

To identify this optimal value for τ, we now introduce a simple model that describes the SNR as a function of spin-locking duration τ. We begin by considering a normalized NMR spectrum as shown in Figure 3.5 (A), and imagine taking a $T_{1\rho}$ measurement perfectly on resonance, that is fixing $\Omega_R = \omega_L$ and sweeping τ. In units of $|I^+_{\mathrm{PL}} - I^-_{\mathrm{PL}}|$, such $T_{1\rho}$ spin relaxation exhibits a decay of the form

$$\chi^{\mathrm{res}}(\tau) = \Delta_{01}\,\exp\left(-\left[\tau/T_{1\rho}^{\mathrm{res}}\right]^{\alpha}\right)\,, \tag{3.4}$$

where $T_{1\rho}^{\mathrm{res}}$ is the decay time the system exhibits on resonance, and Δ_{01} is the PL difference between the $|0\rangle$ and $|-1\rangle$ states. The exponent α is 1 for Spin-Lock $T_{1\rho}$ relaxation, as we have discussed previously in section 1.5.5. Similarly, taking such a measurement off-resonantly at $\Omega_R \neq \omega_L$ yields a decay of the form

$$\chi^{\mathrm{off}}(\tau) = \Delta_{01}\,\exp\left(-\left[\tau/T_{1\rho}^{\mathrm{off}}\right]^{\alpha}\right)\,, \tag{3.5}$$

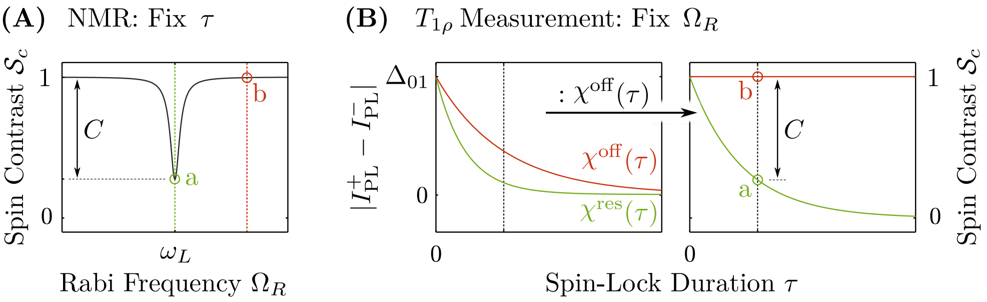

Figure 3.5: Visualization of the scaling of the contrast C with τ. **(A)** Sketch of a normalized Spin-Lock NMR spectrum. **(B)** Time traces taken at the Ω_R values indicated by the linecuts in (A). On resonance, we find a decay given by $\chi^{\rm res}(\tau)$ whereas off-resonance, $T_{1\rho}$ is longer such that a slower decay $\chi^{\rm off}(\tau)$ is obtained. Normalizing these functions in the same way as the NMR spectrum, that is by dividing both PL curves by $\chi^{\rm off}(\tau)$, results in two functions whose difference is exactly $C(\tau)$. The markers a and b indicate identical points in (A) and (B).

where $T^{\rm off}_{1\rho} > T^{\rm res}_{1\rho}$ is the coherence time the system shows off resonance, and $\alpha = 1$. These two $T_{1\rho}$ relaxation curves are plotted on the left-hand side of Figure 3.5 (B). To convert them to units of spin contrast $\mathcal{S}_c$ in the same way as the NMR spectrum, we divide both by the background given by $\chi^{\rm off}(\tau)$. This results in the curves shown on the right-hand side of Figure 3.5 (B). The markers a and b indicate identical working points in panels (A) and (B). Importantly, as can be seen in panel (A), the difference in spin contrast $\mathcal{S}_c$ between a and b is equal to the contrast C, because we have defined C as the amplitude of the normalized NMR dip, see equation (3.2). One can therefore compute C as a function of τ from the difference of the two curves in the right-hand side of panel (B), which is given by

$$C(\tau) = \frac{\chi^{\rm off}(\tau) - \chi^{\rm res}(\tau)}{\chi^{\rm off}(\tau)}\,, \tag{3.6}$$

an expression that is increasing with τ, and approaching one for $\tau \to \infty$. Note that this contrast C is only non-zero as long as $T^{\rm off}_{1\rho} > T^{\rm res}_{1\rho}$.

Next, we model the noise on the experiment readout as a Gaussian random variable with zero mean and standard deviation σ, denoted as $\mathcal{N}(0, \sigma^2)$. For such Gaussian white noise, σ decreases with the square root of the number of experiment repetitions [3]. This is equivalent to saying that σ increases with $\sqrt{\tau}$, where τ is the spin-locking duration, because for longer τ, less repetitions of the sequence can be conducted within the same time. Furthermore, to account for the experimental overhead T_0 given by the laser and waiting times between sequence repetitions, which limits the sequence repetition number and thus the readout noise in the limit of $\tau \to 0$, we modify the scaling factor to $\sqrt{\tau + T_0}$. With this, the standard deviation of the normalized NMR background yields

$$\mathrm{STD}(\tau) = \mathrm{std}\left(\frac{\mathcal{N}\left(0, [\sigma\sqrt{\tau + T_0}]^2\right)}{\chi^{\rm off}(\tau)}\right) = \frac{\sigma\sqrt{\tau + T_0}}{\chi^{\rm off}(\tau)}\,, \tag{3.7}$$

and therefore

$$\mathrm{SNR}(\tau) = \frac{C(\tau)}{\mathrm{STD}(\tau)} = \frac{\Delta_{01}}{\sigma\sqrt{\tau + T_0}} \left(\exp\left(-\tau/T_{1\rho}^{\mathrm{off}}\right) - \exp\left(-\tau/T_{1\rho}^{\mathrm{res}}\right) \right). \tag{3.8}$$

Using this expression, we now aim to find τ that maximizes the SNR, however, the equation $\mathrm{d}/\mathrm{d}\tau\ \mathrm{SNR}(\tau) = 0$ is transcendental, such that we cannot derive an analytic expression for this ideal τ value. It is possible though to evaluate equation (3.8) numerically for our experimental conditions, and thereby compute the value for τ that optimizes the SNR in that specific case.

For example, for NVA2, we have measured that $T_{1\rho}^{\mathrm{off}} = (243 \pm 11)\,\mu\mathrm{s}$, $T_{1\rho}^{\mathrm{res}} = (101 \pm 14)\,\mu\mathrm{s}$, $T_0 = 3464\,\mathrm{ns}$, and $\Delta_{01} = 90\,\mathrm{kcps}$. On the same NV, we have then taken a series of NMR measurements for different values of τ, where each of these experiments ran for exactly one hour, and we have extracted the resulting values for C, STD and SNR. The results of these measurements are shown in Figure 3.6, together with the prediction of equations (3.6), (3.7) and (3.8). The grey area represents the error on the model's prediction based on the measurement errors on the two $T_{1\rho}$ times plugged into our model. The noise variance σ is determined by fitting equation (3.7) to the standard deviation data. We find reasonable agreement of the experimental data with the numerical predictions. In particular, the model predicts that for this particular NV, the SNR is maximal at $\tau = (76.6 \pm 5.5)\,\mu\mathrm{s}$. This is only about 76 % of $T_{1\rho}^{\mathrm{res}}$ and 31 % of $T_{1\rho}^{\mathrm{off}}$.

We close the discussion on SNR optimization in Spin-Lock NMR with four further comments: First, the optimal τ value varies from NV to NV. For example, we have found that for NVA2 that we investigated here, the ideal value is about 31 % of $T_{1\rho}^{\mathrm{off}}$, meanwhile in the next chapter we present a similar measurement on NVB1 (see Figure 4.3), where the model predicts an ideal τ of about 45 % of $T_{1\rho}^{\mathrm{off}}$. Second, while

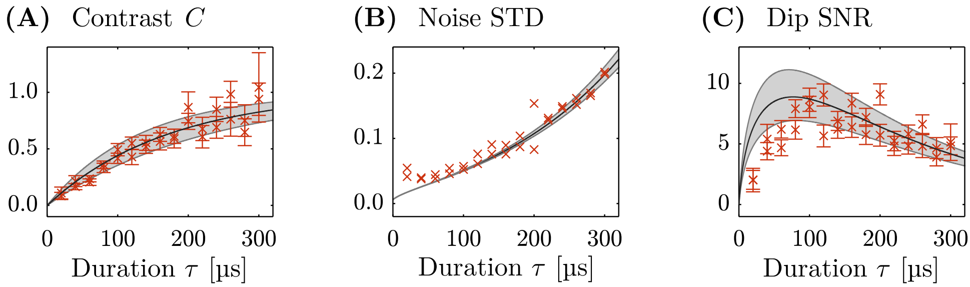

Figure 3.6: Optimization of the Spin-Lock NMR SNR via measurement of **(A)** the contrast $C(\tau)$, **(B)** the readout noise $\mathrm{STD}(\tau)$, and **(C)** the resulting $\mathrm{SNR}(\tau)$. The red crosses are experimental results, taken on NVA2, where each pixel represents a single NMR experiment that ran for exactly one hour. The error bars arise from the fitting uncertainty on the amplitude of the fitted Lorentzian lineshape. Evaluation of equations (3.6), (3.7) and (3.8) for the experimental conditions under which the NMR data were taken results in the solid black line, and the grey area is the model's error based on the uncertainty of the employed experimental values for $T_{1\rho}^{\mathrm{off}}$ and $T_{1\rho}^{\mathrm{res}}$. For this particular NV, SNR is maximized for $\tau \approx 0.76 \cdot T_{1\rho}^{\mathrm{res}}$.

the inclusion of the experimental overhead in our model ensures that the simulated STD is not vanishing for $\tau \to 0$, it seems that the model is slightly underestimating the STD for small τ. This indicates that there are experimental circumstances that the model is currently not accounting for, such as imperfect readout [99], whose addition to the model could improve the overlap of the model with the SNR data. Third, the model is not limited to Spin-Lock NMR, but instead it can be applied to any NMR protocol that relies on faster spin decoherence on resonance with the NMR target. For example, we will show in section 4.2 that the model can be used to describe the SNR of XY8-k NMR. Forth, we will extend this model in the appendix A.7 to study the ideal τ for optimizing the SNR difference between two NMR curves, namely NMR taken with and without immersion oil on the diamond surface.

3.1.3 Choice of Magnetic Bias Field

In this thesis, we always conduct our NMR experiments at a magnetic bias field near the ESLAC, that is at $|\boldsymbol{B}_{\text{ext}}| \approx 500\,\text{G}$. We make this particular choice for the following three reasons: First, due to the nuclear hyperpolarization occurring near the ESLAC (see section 1.2.2), there is only one occupied nuclear state, meaning that we can work with a single spin transition without interference from any off-resonantly driven transitions. Second, this isolated hyperpolarized transition has an optical contrast that is two times (for ^{15}N) or three times (for ^{14}N) larger compared to an unpolarized hyperfine line (see Figure 1.13). This optical contrast, denoted above as Δ_{01}, scales linearly into the SNR of the NMR experiment, as we have shown in equation (3.8), meaning that our experiments are more sensitive and faster when operated near the ESLAC. Third, we always aim to work with a magnetic bias field that is well aligned with the NV axis, and we realize this alignment by monitoring the reduction in PL when tilting the magnetic field away from the NV axis with a goniometric mount (see appendix A.1.2). Since our goniometer has an angular range limited to $\pm 5\,°$, we can only align magnetic fields that are larger than approximately 250 G, because for lower fields the transverse magnetic field component at 5° misalignment is not sufficient to quench the PL in a significant manner. For these three reasons, we always apply aligned magnetic fields near the ESLAC between 400 G and 550 G.

3.2 Proton Presence on Bare Diamond

The Spin-Lock NMR data we have presented previously in Figure 3.1 respectively 3.4 exhibit a clear NMR feature at a frequency that matches the proton Larmor frequency, suggesting that there is a nearby proton ensemble. Such NV proton NMR in itself is nothing new – many people have used NVs to detect protons in nanoscale samples [46,63,67,120] – however in our case we did not deliberately add these protons, neither by coating the diamond with any hydrogen rich material such as polymers, immersion oil or other organic substances, nor by hydrogen terminating the diamond surface. The fact that our Spin-Lock NMR experiments are nonetheless registering a significant proton signature raises the question where these proton spins are located and how they have been introduced in the first place.

In this section, we first provide additional evidence that the observed NMR signature is indeed arising from proton spins, and subsequently we characterize the proton source by investigating how the proton NMR contrast and width scales with various experimental factors.

3.2.1 Validation of the Proton Larmor Frequency

We now present multiple arguments to substantiate the claim that the dip observed in the Spin-Lock NMR spectrum in Figures 3.1 and 3.4 is indeed due to a nearby proton ensemble.

We make this claim based on the observation that the measured NMR frequency of the dip matches the proton Larmor frequency. However, the NMR frequency we measure is highly dependent on the conversion of MW amplitude to Rabi frequency Ω_R (see section 3.1.1), and an improper conversion would lead to a false dip position f_{NMR} and thus to a wrong nuclear spin species identification. To validate that our conversion is correct and that the dip is indeed at the proton Larmor frequency, we apply a 2.5 MHz MW tone with a second antenna and perform Spin-Lock NMR on NVB1 at an aligned magnetic field of $|\boldsymbol{B}_{\mathrm{ext}}|$ of 412 G. The resulting NMR spectrum is shown in Figure 3.7 (A), where we observe not only the proton feature at the expected proton Larmor frequency of about 1.76 MHz, but we do also see a dip at exactly 2.5 MHz that is produced by the applied MW tone. The fact that this dip is showing up at precisely 2.5 MHz verifies that the conversion from MW amplitude to frequency Ω_R is correct.

To further validate that the observed NMR signal stems from proton spins, we check that the measured dip position f_{NMR} scales linearly with the magnetic field, with a

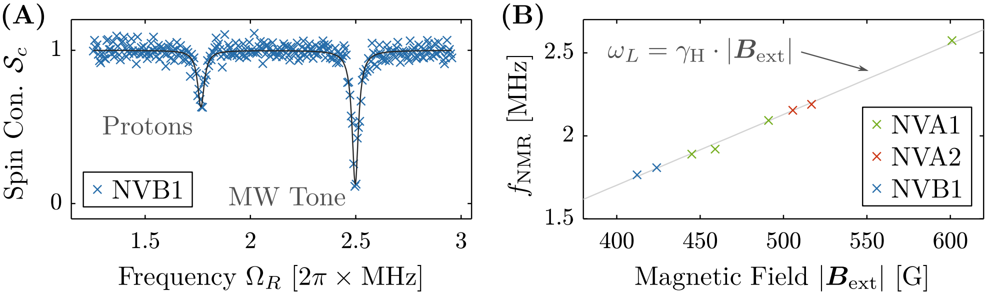

Figure 3.7: Validation that the observed NMR feature is due to protons in the NV's environment. **(A)** Recording a Spin-Lock NMR with a 2.5 MHz MW tone applied to the NV results in an additional dip in the NMR spectrum at exactly 2.5 MHz. This verifies that the conversion from MW amplitude to frequency Ω_R is correct. The data shown here were taken on NVB1 at about 412 G. **(B)** A series of NMR experiments at different magnetic fields reveals that the frequency f_{NMR} of the observed proton dip scales linearly with $|\boldsymbol{B}_{\mathrm{ext}}|$, with a slope that matches the proton gyromagnetic ratio γ_{H} (grey line), further validating that the observed feature is due to noise originating from precessing proton spins. Note that the errorbars on the fitted frequency are less than 1 kHz and not shown here.

slope given by the proton Larmor frequency $\gamma_\mathrm{H} = 4.2577\,\mathrm{kHz/G}$ [80]. For this, we measure f_NMR at different magnetic field amplitudes $|\boldsymbol{B}_\mathrm{ext}|$, using multiple NVs from two different diamond samples, namely diamonds A and B (see appendix A.2). The result of these experiments is shown in Figure 3.7 (B), where the grey line represents the proton Larmor frequency $\omega_L = \gamma_\mathrm{H} \cdot |\boldsymbol{B}_\mathrm{ext}|$. We find good agreement of the data with ω_L, where the small deviations are due to inaccurate magnetic field measurements. In particular for NVA1, these B-field measurements are based on only a single ODMR experiment on one electron spin transition instead of two. Overall, we conclude that these data are not only providing clear evidence that the detected NMR is indeed due to proton spins, the data also demonstrate that there are protons present nearby the NVs of two entirely different diamond samples.

Finally, we point out that in contrast to the XY8-k sequence, the Spin-Lock sequence is not periodic and therefore it is not sensitive to harmonic fractions or multiples of the target noise frequency. For this reason, we rule out that the observed feature is generated by the harmonic frequency of another nuclear spin species such as ^{13}C whose Larmor frequency happens to have harmonics near the proton Larmor frequency. See section 4.1 for a more detailed discussion and experimental validation of this statement.

All these findings together represent strong evidence that we are indeed measuring the noise signature of precessing proton spins in the NV's environment.

3.2.2 NV Statistics

As a first characterization step of the observed proton signal, we acquire some statistics by conducting Spin-Lock NMR experiments on different NVs in two different samples, diamond A and B (see appendix A.2). We find that in both of these samples, there are NVs that show a proton dip in their NMR spectrum, and NVs that do not. Whether a Spin-Lock NMR experiment detects a proton presence is therefore not so much dependent on the diamond itself, but much more on the local environment of the respective NV.

In Figure 3.8, we plot the observed proton NMR contrast C of all these NVs versus their respective $T_{1\rho}^\mathrm{off}$ relaxation time. For NVs without any observable proton feature, we set $C = 0$. The horizontal error bars in the plot represent the largest and smallest $T_{1\rho}^\mathrm{off}$ value we have ever measured for the respective NV, and for NVs where this was measured only once, it represents the error on the least-square fit of the relaxation time of that single experiment. Similarly, vertical errorbars indicate the largest and smallest measured contrast C of the respective NV, each taken with a τ value between $T_{1\rho}^\mathrm{res}$ and $T_{1\rho}^\mathrm{off}$.

The data demonstrate that none of the NVs with relaxation times exceeding $1.5\,\mathrm{ms}$ show a proton signature in their NMR spectrum. On the other hand, the three NVs with short $T_{1\rho}^\mathrm{off}$ exhibit a clear proton NMR signal with contrasts between $20\,\%$ and $40\,\%$. Since spins and magnetic impurities on the diamond surface are the main contributors to magnetic background noise – especially for diamond A that has a negligible amount of ^{13}C spins in the lattice – we directly correlate $T_{1\rho}^\mathrm{off}$ with the NV depth. This means that we expect NVs with long $T_{1\rho}^\mathrm{off}$ times, such as NVA3 and NVA4, to be much deeper in the diamond than NVs with short relaxation times, such as NVA1, NVA2 or NVB1. To further underline the statement that NVA4 is a deep NV, we point out that even if we add immersion oil to the diamond surface, NVA4 is not showing any proton NMR while it detects an artificial MHz tone test signal just fine. This observation indicates that NVA4 is so far away from the diamond surface that even increasing the number of surface protons is not enough for it to sense them. In fact, this oil experiment together with the long relaxation times shown in Figure 3.8 is why we say that NVA3 and NVA4 are deep NVs, and why we claim that NVA1, NVA2 and NVB1 are shallow.

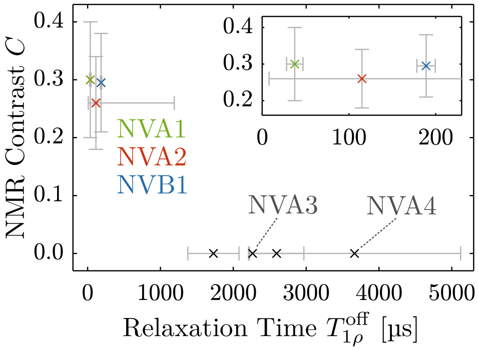

Figure 3.8: Spin-Lock NMR contrast as a function of the employed NV's off-resonant relaxation time $T_{1\rho}^{\text{off}}$. We do only observe proton NMR for the three NVs with $T_{1\rho}^{\text{off}} < 300\,\mu\text{s}$. For all other NVs, we find $T_{1\rho}^{\text{off}} > 1.5\,\text{ms}$ and we do not obtain any proton NMR. Since $T_{1\rho}^{\text{off}}$ is strongly correlated with the NV depth, we conclude that only shallow NVs detect a proton NMR, indicating that the proton ensemble is located on the diamond surface.

To summarize, the data from Figure 3.8 suggest that we do only observe the surface proton NMR on shallow NVs. This leads to the conclusion that the protons are not homogeneously distributed throughout the entire diamond lattice, but they are instead localized on the diamond surface.

3.2.3 NMR Linewidth Limitation

We now investigate how the proton NMR width Δf_{NMR} behaves as a function of the spin-locking duration τ. This width depends on two different parameters: The properties of the proton ensemble that generates the magnetic NMR signal, and the parameters of the Spin-Lock sequence applied to the NV. Both of these are independent of each other, and thus they impose separate limitations on how small Δf_{NMR} can be.

The Spin-Lock sequence itself imposes a Fourier limit of $\sqrt{\pi}/\tau$ on the NMR width. This can easily be derived by Fourier transforming a cosine signal of finite duration τ, which results in a frequency domain sinc-like function with a FWHM of $\sqrt{\pi}/\tau$. Put into words, this Fourier limit dictates that the longer the spin-locking period is, the more precise the NMR frequency measurement becomes. Therefore, if such a Fourier limit is limiting the width Δf_{NMR} in our experiments, we would expect $\Delta f_{\text{NMR}} = \sqrt{\pi}/\tau$. On the other hand, if a property of the proton spin bath is limiting the NMR width, such as for example a nuclear dephasing time $T_2^* < \tau$, we would expect Δf_{NMR} to be larger than $\sqrt{\pi}/\tau$ and independent of τ.

In Figure 3.9 we show a measurement of Δf_{NMR} as a function of τ, taken on both NVA2 and NVB1. The errorbars are given by the uncertainty on the width obtained by a least-square fit of a Lorentzian lineshape. The data suggest that Δf_{NMR} is independent of τ, and in particular for $\tau > 100\,\mu\text{s}$, the measured width Δf_{NMR} clearly exceeds the Fourier limit.

We therefore conclude that for $\tau > 100\,\mu\mathrm{s}$, our experiments are not Fourier limited, but that the spin bath itself is defining the observed NMR linewidth. This means that for our usual experimental conditions, the choice of τ has no effect on Δf_{NMR} and thus τ can be chosen to optimize the SNR as described in section 3.1.2. Interestingly, the NMR linewidth for the two NVs are different, indicating that depending on the diamond sample and/or the NV, the proton spin bath has different intrinsic properties.

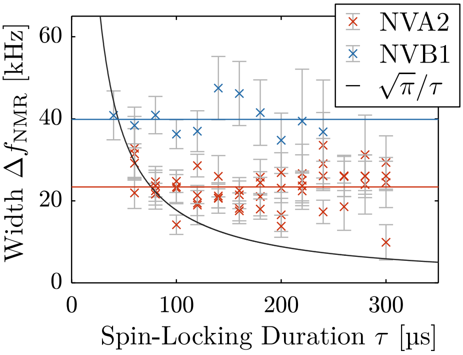

Figure 3.9: Spin-Lock NMR width as a function of spin-locking duration τ, recorded on NVA1 and NVB1. The dashed lines highlight the average width of each NV, while the black line represents the Fourier limit $\sqrt{\pi}/\tau$. The data suggest that the width is independent of τ, indicating that the NMR is not Fourier limited, but instead the width is determined by the spin bath itself. Moreover, the limit imposed by the bath is different for these two NVs.

The question at hand is what one can learn about the proton spin based on the observed width. The key parameters that are typically used to describe a nuclear spin bath such as the protons observed here are the spin density and the bath's autocorrelation time which depends on the proton coherence time and – for non-stationary spins – the molecular diffusion coefficient [51]. However, since all these parameters play into the measured width, it is hard to make a statement about any of these parameters based on just the single Δf_{NMR} value measured here. We will attempt to infer the ^{1}H spin density of the detected source in chapter 5, using a full theoretical description of Spin-Lock NMR.

3.2.4 Temperature Dependence

After having shown that the NMR width Δf_{NMR} is limited by the proton spin bath's properties, we continue to further investigate this width. In particular, we study whether Δf_{NMR} – and thus the underlying spin bath property – changes with temperature, which will be an indicator whether the observed spin bath is subject to temperature dependent processes such as molecular diffusion. For this, we mount the diamond on a thermoelectric peltier element (ThorLabs TECF1S) with a thermistor (ThorLabs TH10K) for temperature control via an electric feedback-loop. This allows us to bring the diamond to any target temperature between $-5\,^{\circ}\mathrm{C}$ and $75\,^{\circ}\mathrm{C}$. Using this experimental setup, we measure the proton NMR width Δf_{NMR} of NVA1 as a function of temperature, the result of which is shown in Figure 3.10.
The data show no clear dependence of Δf_{NMR} on the temperature, and in particular there is no increase in Δf_{NMR} with higher temperature. If the detected proton signal was arising from a liquid whose molecules are free to move, we would have expected that this diffusive molecular motion increased at higher temperature, leading to a shorter autocorrelation time of the bath and thus to an increase in Δf_{NMR}. For example, liquid water has a self-diffusion rate that changes by a factor of more than

three in the investigated range [145, 146]; a difference we would be able to observe in Spin-Lock NMR by monitoring Δf_{NMR}. However, our data suggest that this is not the case, and hence we conclude that the detected proton spins are either fully stationary and bound to the diamond surface in a fixed way, or they are at least bound strong enough such that their molecular dynamics are dominated by the interaction with the diamond surface and not the applied temperature. In either case, we conclude that the proton carriers are in a solid-like surface-bound state, and we estimate a lower bound on the surface binding energy as $k_B T \approx 30\,\mathrm{meV}$ for $T = 70\,°\mathrm{C}$.

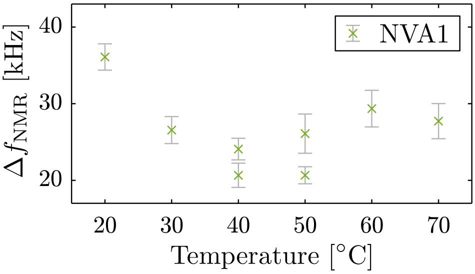

Figure 3.10: Spin-Lock NMR temperature dependence. The width of the proton NMR dip, as measured on NVA1, seems to be independent of the temperature. This indicates that the detected protons are provided by a substance that is solid-like in that its molecules are surface-bound and do not show any temperature dependent molecular diffusion.

To summarize, our studies have provided evidence that the detected proton spin bath is located on the diamond surface, that its properties limit the width of the NMR dip to approximately 20 to 40 kHz, and that it does not show any temperature dependent diffusive motion. Based on this, we suspect the proton carriers to be stationary on the surface in a solid-like bound state, leading to the following two reasonable options: Surface-bound chemical groups containing hydrogen, or a thin layer of immobilized water molecules. Let us now discuss these two scenarios.

Surface-Bound Hydrogen Atoms

The diamond surface termination we usually work with, and in particular the termination with which our shallow NV centers sense a proton presence in Spin-Lock NMR, is the oxygen termination. This oxygen termination is generated by tri-acid cleaning the diamond sample [53, 141]. High resolution XPS measurements have shown that the chemical surface composition generated this way is not a perfect oxygenated diamond surface comprised of only C-O-C and C=O bonds, but that there are also C-OH and (COOH)HO-C=O bonds [141]. These groups contain hydrogen atoms, and it is possible that they are the origin of the proton NMR we observe.

The surface density of these chemically bonded groups is limited by the surface density of available carbon dangling on the (001) surface of our diamond, which is about $32\,\mathrm{nm}^{-2}$. This can be calculated by $2 \cdot [2a \sin(\phi/2)]^{-2}$, where $a = 0.3567\,\mathrm{nm}$ is the C-C bond length, $\phi = 109.5°$ is the angle between C-C bonds in the lattice, and the initial factor of 2 comes from the fact that each carbon atom provides two free dangling bonds. Even if 20 % of all carbon dangling bonds hosted a group with one hydrogen atom (and that is a generous estimate given the results from [141]), the resulting ^{1}H surface density of about $6.4\,\mathrm{nm}^{-2}$ is rather low compared to the volume density of immersion oil, which ranges from $50\,\mathrm{nm}^{-3}$ [42, 50, 120] to $60\,\mathrm{nm}^{-3}$ [63, 66]

or even $(68 \pm 5)\,\mathrm{nm}^{-3}$ [51]. This makes it questionable, yet by no means impossible, that surface-bound hydrogen atoms are the origin of the signal we measure.

A Sub-Nanometer Thin Water Layer

We rule out liquid water as a source for the observed proton signal because its molecular diffusion is expected to show a temperature dependence in the investigated temperature range [145, 146], and even more importantly, the high molecular diffusion of liquid water would broaden the NMR line by much more than what we measure. For example, at room temperature, the self-diffusion rate of liquid water is about $D \approx 2000\,\mathrm{nm}^2/\mu\mathrm{s}$ [145, 146], such that the water molecules move on average by approximately $(2D \cdot 1\,\mu\mathrm{s})^{1/2} \approx 63\,\mathrm{nm}$ per microsecond [106]. Given that the NV center's sensing volume is well approximated by a semi-sphere on the diamond surface with a radius roughly equal to the NV depth [44, 120], i.e about 10 nm for our NV centers, this means that every microsecond most water molecules in the sensing volume are expected to be exchanged with a molecule from outside the sensing volume, leading to a diffusion-limited NMR linewidth of $\Delta f_{\mathrm{NMR}} > 1\,\mathrm{MHz}$. To further highlight how fast the diffusion in liquid water is, we note that immersion oil (with which proton NMR is feasible) has a substantially smaller self-diffusion coefficient of only approximately $0.5\,\mathrm{nm}^2/\mu\mathrm{s}$ [51].

For a water layer that is extremely thin, however, the situation changes drastically. Recent work reports that such two-dimensionally nanoconfined water with less than 2 nm thickness shows strongly suppressed molecular diffusion [142, 147], and that such reduced diffusion in water with only picoliter volumes can in fact be detected by the NV center [143, 144]. Another very recent study claims that there is a non-evaporating sub-nanometer thick water layer on the diamond surface under ambient conditions [147]. In light of these findings, it is a reasonable assumption that the proton signal in our NV NMR experiments is a super-thin, solid-like water contact layer on the diamond surface – a hypothesis that has previously been formulated [42,46,66–68]. To further underline this possibility, we note that the proton density of water is

$$\rho_{\text{water}} \approx 2 \cdot \frac{N_A\, m_{\text{water}}}{M} \approx 67\,\mathrm{nm}^{-3}\,, \tag{3.9}$$

where N_A is Avogadro's number, $m_{\text{water}} \approx 1000\,\mathrm{kg/m^3}$ denotes the mass density of water, $M = 18\,\mathrm{g/mol}$ is the molar mass, and the factor 2 arises from the fact that there are two hydrogen atoms per water molecule. This density is very similar to the proton density of immersion oil that is about $50\,\mathrm{nm}^{-3}$ [42,50,120] to $60\,\mathrm{nm}^{-3}$ [63,66] or even $(68 \pm 5)\,\mathrm{nm}^{-3}$ [51]. Since coating the diamond with such immersion oil is providing enough protons to be detected by NV NMR techniques [51, 120], a thin immobilized water layer on the diamond surface might also supply a sufficient amount of proton spins.

In the next two sections, we will conduct more experiments with the goal to shed further light onto these two hypotheses. To be specific, we will modify the diamond surface by switching from the oxygen termination to a deuterium termination in section 3.3, and we will cool the diamond sample to sub-zero degree Celsius to create frozen water ice on the diamond surface in section 3.4. Both of these approaches could have an effect on the detected proton NMR and thereby potentially provide new avenues to characterizing the protons' origin.

3.3 Deuterium Termination

We have speculated above that the observed proton NMR signal might originate from chemically bonded hydroxyl groups on the oxygen terminated diamond surface, that are introduced when we tri-acid clean the diamond [141], as shown in Figure 3.11. Here, in order to test this hypothesis, we manipulate the diamond's surface termination and measure whether there is any change in the observed proton NMR.
Hydrogen (H) termination of the diamond surface is a well understood process [148–151], and we have access to the necessary facilities in house. However, by hydrogen terminating we would add yet another source of protons to the system which would unnecessarily complicate our study. Instead, we use the in-house facilities to terminate with heavy hydrogen, i.e. deuterium (D), that has a different gyromagnetic ratio than protons and thus appears at a different point in the NMR spectrum. To achieve this D-termination, we follow the H-termination recipe from [148], but replace the water supply with heavy water, such that in the end, the diamond is annealed in a pure D_2 atmosphere at 750 °C for 6 hours. We expect that the resulting deuterium surface termination is predominately defined by C-D bonds (see Figure 3.11), similar to the C-H bonds one would expect from a hydrogen terminated surface [151].

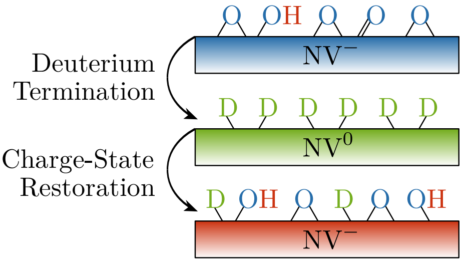

Figure 3.11: Tri-Acid cleaning results in an oxygen terminated surface (blue), that contains hydroxyl groups (OH) which we hypothesize could be the origin of the proton NMR we detect on clean diamond. Deuterium terminating the diamond (green) yields a surface of mostly C-D bonds, however, due to band-bending induced by the H- (or D-) termination, the NVs under such a surface are in the NV^0 charge state that cannot be used for surface NMR experiments. To restore the charge state, we illuminate the sample with green light and thereby obtain a surface (red) of mostly C-O-C, C-OH and C-D bonds.

There is one caveat, however, in that we cannot measure Spin-Lock NMR under a deuterium terminated diamond surface, because the NVs under D-termination have a different charge state. Specifically, only the NV^- charge state is usable for our experiments, and while NV^- is the stable charge state in an oxygen terminated diamond, it is not stable under a H-terminated surface [149, 150]. This is because shallow NV^- centers tend to lose an electron and become NV^0 when the surface is hydrogen terminated, a process that is attributed to the energy band bending induced by the hydrogenated surface [149, 150]. Because hydrogen and deuterium have near identical chemical properties, we assume that the same charge-state stabilization to NV^0 occurs under deuterium termination. We have confirmed this assumption by measuring an absence of NV^- ODMR signatures in nanopillars where there has clearly been NV^- ODMR before D-terminating the diamond.

In order to reset the NV charge-state in deuterium terminated diamond back to NV^- without tri-acid cleaning, we illuminate the diamond sample with a green laser of approximately 2 mW power. Such continuous exposure to green light alters the chemical composition of the surface and thereby affects the surface induced band bending, and in H-terminated diamond specifically it restores the NV^- charge state [152]. In the case of our D-terminated diamond, the same charge-state conversion to NV^- occurs. We observe this conversion process as a gradual increase in PL and ODMR contrast throughout the illumination period until similar ODMR quality is achieved as before the deuterium termination.

Zuber et al. [153] suggest that the surface after laser-assisted restoration of the NV^- charge-state consists of mostly hydroxyl (C-OH) and ether-like (C-O-C) groups, with a small remainder of deuterium bonds (C-D), as depicted in Figure 3.11. Notably, theoretical work suggests that this chemical surface composition (proposed with C-H instead of C-D) is ideal for NV^- spin stabilization [150].

Importantly, this charge-state converted surface exhibits a different chemical composition compared to the O-terminated surface prepared by tri-acid cleaning, and it is thus very likely that the hydrogen surface density is different than before this treatment. Therefore, if the hydrogen nuclei of such surface-bound groups are indeed the origin of the proton NMR we detect, we would expect to observe a different NMR signal on these two surfaces.

To verify this hypothesis, we measure Spin-Lock proton NMR on NVB2 in diamond B, first with an O-terminated surface and subsequently with a D-terminated surface that was illuminated with 2 mW of green light for half an hour to re-stabilize the NV^- charge state. The result of these experiments is shown in Figure 3.12. For each surface, we have first measured Δ_{01}, $T_{1\rho}^{\mathrm{res}}$ and $T_{1\rho}^{\mathrm{off}}$ to determine the ideal value for the spin-locking duration τ, as described in section 3.1.2. The NMR spectrum is then taken at this optimal τ, here being 215 µs for the O-termination, and 280 µs for the D-termination. In addition, we play two coherent MW tones of 2.0 and 2.4 MHz in these experiments, resulting in the two strong dips at these frequencies, which we use to calibrate the x-axis instead of the usual conversion via Rabi experiments (see section 3.1.1) in order to speed up the experimental routine. Each of the two experiments integrated for exactly 4 hours.

The amplitude of the NMR features generated by the artificial MW tones is a much larger than the proton NMR, and two of the dips even show a contrast of $C > 1$. This is attributed to the coherent nature of the MW tone, which effectively drives Rabi oscillations on the dressed states during the Spin-Lock sequence, leading to an NMR contrast that oscillates between values of $C = 0$ and $C = 2$ as a function of τ. Furthermore, the NMR features are much broader than the proton dips. Given that these data were taken on a different setup than all other data presented in this thesis, and specifically than the data from Figure 3.7 (A) where the MW tone has a similar width as the proton feature, we assign the broad linewidth measured here to noise

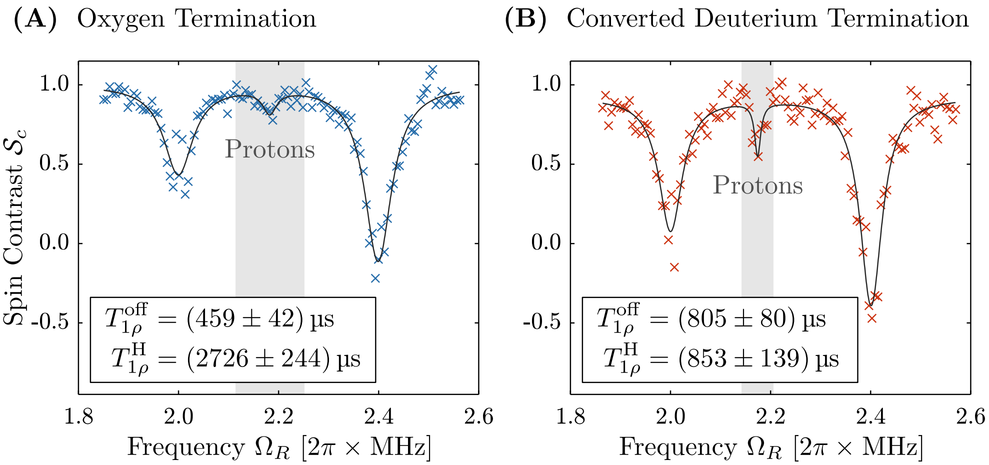

Figure 3.12: Spin-Lock NMR taken on NVB2 near the ESLAC, for **(A)** an oxygen terminated surface obtained from tri-acid cleaning the diamond, and **(B)** a deuterium terminated surface that was exposed to green laser light to restore the NV$^-$ charge state of NVB2. Both NMR spectra were taken at their respective ideal value for τ (see section 3.1.2) and with two artificial MW tones of 2.0 and 2.4 MHz for calibration of the x-axis. We find that the SNR is approximately doubled for the converted D-terminated surface, indicating an increase in the detected protons' density, that is in line with the observed decrease in $T_{1\rho}^{\text{pro}}$ (= the proton contribution to $T_{1\rho}^{\text{res}}$). Furthermore, we observe an increase in the off-resonant relaxation time $T_{1\rho}^{\text{off}}$, suggesting that the D-terminated surface produces less magnetic background noise.

on the MW tone frequency introduced by the cheaper and less high-end signal MW hardware in this secondary setup.

Let us now discuss the proton feature: The data from Figure 3.12 reveals that the SNR of the proton NMR dip has almost doubled after the deuterium treatment, from (1.90 ± 0.65) to (3.66 ± 1.02). This increase in SNR, according to equation (3.8), can be attributed to either or both of the following two factors: An increase in the proton surface density which leads to a stronger proton signal and thus a shortened $T_{1\rho}^{\text{res}}$, or a reduction in magnetic background noise due to the change in the chemical surface composition which leads to a prolonged $T_{1\rho}^{\text{off}}$.

And indeed, we measure that the off-resonant relaxation time of the O-terminated surface is $T_{1\rho}^{\text{off}} = (459 \pm 42)$ µs, and (805 ± 80) µs for the converted D-terminated surface – which is almost twice as long. This indicates that the background noise has significantly reduced, which is consistent with the claim that the laser converted hydrogen terminated surface (respectively deuterium in our case) provides improved NV spin properties for sensing [150].

To investigate to what extend the surface hydrogen spin density has been altered, we calculate its contribution to $T_{1\rho}^{\text{res}}$. The faster decay on resonance compared to the off-resonant case ($T_{1\rho}^{\text{off}}$) can be attributed to an additional decay component $T_{1\rho}^{\text{H}}$ that is solely due to the proton presence. Mathematically, these decay rates are related by

$$\frac{1}{T_{1\rho}^{\mathrm{res}}} = \frac{1}{T_{1\rho}^{\mathrm{off}}} + \frac{1}{T_{1\rho}^{\mathrm{H}}} \qquad \text{such that} \qquad T_{1\rho}^{\mathrm{H}} = \left(\frac{1}{T_{1\rho}^{\mathrm{res}}} - \frac{1}{T_{1\rho}^{\mathrm{off}}} \right)^{-1} . \tag{3.10}$$

Using the measured values for $T_{1\rho}^{\mathrm{off}}$ and $T_{1\rho}^{\mathrm{res}}$, equation (3.10) yields that $T_{1\rho}^{\mathrm{H}} = (2726 \pm 244)\,\mu\mathrm{s}$ for the O-terminated surface, and $(853 \pm 139)\,\mu\mathrm{s}$ on the converted D-terminated surface. This drastic reduction in $T_{1\rho}^{\mathrm{H}}$ indicates that there is a stronger proton signal originating from the converted D-terminated surface, suggesting a larger proton density compared to the O-terminated surface. In addition, the width of the NMR dip has approximately halved, reducing from $\Delta f_{\mathrm{NMR}} = (33.3 \pm 18.1)\,\mathrm{kHz}$ on the O-terminated surface to $(14.6 \pm 6.1)\,\mathrm{kHz}$ on the converted D-terminated surface, indicating that the width-limiting properties of the proton spin bath (see section 3.2.3) have changed. For example, if the observed proton spins are provided by a thin layer of immobilized water, the reduction in Δf_{NMR} could be explained by a reduced molecular diffusion rate on the new surface, for example because of a smaller surface hydrophilicity (leading to a thinner water layer and thus more strongly suppressed diffusion), or because of a larger water to surface binding energy (which directly decreases the water self-diffusion rate).

We conclude that the surface treatment performed here is indeed affecting the source of the protons we detect. Specifically, we find evidence that the proton density of the proton bath seems to have been increased by the deuterium termination and subsequent green illumination. Later, in section 5.3.2, we will revisit these data and fit them with theoretical models for depth determination, where we will conclude that the surface proton density increases by a factor of about two during the conducted surface treatment – which agrees with the conclusion drawn from the analysis done here. Furthermore, the data presented here provide evidence that the surface treatment with deuterium and laser light causes not only an increased proton density, but also reduced magnetic background noise. For envisioned depth determination based on the NMR signal of these protons, the converted D-terminated surface would therefore be superior compared to the O-terminated surface in terms of SNR and thus sensitivity. Overall, these results suggest that if the observed protons are due to surface-bound groups containing hydrogen, then D-terminating and subsequently illuminating the surface with a laser would increase the density of these hydrogen-rich groups. Alternatively, if the observed protons are due to a layer of immobilized water, then our data indicates that on the laser treated D-terminated surface, the amount of water molecules in this adsorbate layer is increased, for example because this surface might be more hydrophilic than the O-terminated surface.

3.4 Towards Water Ice NMR

The proton NMR we observe in our Spin-Lock experiments could originate from a sub-nanometer thin contact layer of water on the diamond surface. As we have already mentioned above, recent studies have shown that the molecular diffusion in such a two-dimensionally nanoconfined layer of water is strongly suppressed [142,

143], leading to a solid-like molecular behaviour that is well in agreement with our findings from section 3.2. In addition, there is evidence that such a nanoconfined layer of non-evaporating water is always present on diamond surfaces under ambient conditions [147].
Here, we investigate the possibility that we are indeed measuring the NMR signal of protons in such a water layer. To that end, we aim to bring the diamond sample to a temperature below 0 °C in order the freeze the surface water layer to water ice. The molecular structure of the water layer is expected to change during the phase transition to ice, and therefore key properties relevant to the resulting NMR width could be altered, in particular the water-water interaction strength, the ^{1}H spin density and the molecular self-diffusion rate. Therefore, if the proton NMR we observe is indeed originating from such a water layer, there is a chance that we can discern the different states of aggregation with Spin-Lock NMR by monitoring the linewidth Δf_{NMR}. On the other hand, if the protons were to stem from surface-bound OH groups, we expect no significant change in the NMR width. This experiment is very exploratory in nature, because the molecular properties of a nanoconfined water layer with suppressed diffusion are not well understood, and they could actually be very similar to those of ice, in which case we might not see a any difference in NMR between these two water phases.
To freeze water on the diamond surface, we aim to stabilize the diamond sample at −5 °C in our ambient room-temperature setup. For this, we use the same thermoelectric arrangement as described earlier in section 3.2.4. However, keeping the diamond at sub-zero temperatures for an extended amount of time leads to the condensation of water from the surrounding air, that then freezes to a thick layer of ice, as shown in Figure 3.13. This layer of ice prevents us from focusing the green laser onto the NV, and it complicates antenna positioning for MW delivery.

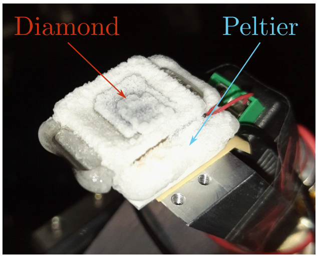

Figure 3.13: In order to bring the diamond to −5 °C, we mount the diamond on a thermoelectric peltier element (ThorLabs TECF1S) with a thermistor (ThorLabs TH10K) for temperature control via an electric feedback-loop. However, under ambient conditions, within just one hour, water condensation leads to the formation of ice all over the sample holder, making it impossible to focus the laser onto the NV.

We attempt to overcome this problem by continuously blowing nitrogen gas onto the diamond sample. This N_2 gas is dry and can therefore prevent ambient humidity from condensing on the cold diamond. Note that the diamond sample is mounted upside-down, i.e. the nanopillars containing the NVs are on the bottom surface to provide proper wave guiding. Consequently, while the nitrogen gas keeps the top surface dry to ensure a good laser focus, the water layer on the lower surface is expected to be unaffected by the stream of N_2 and can freeze to ice.
However, this flow of room-temperature warm N_2 gas is heating up the diamond. To still achieve an equilibrium temperature of less than 0 °C, we build a contraption to cool the nitrogen gas with dry ice before blowing it onto the diamond. In addition, we

add CPU cooling fans to the sample stage that serves as the heat sink for the peltier element, which improves the overall cooling power of our system.

To test whether this new thermal arrangement is working as intended, e.g. whether it provides water ice in a thermally stable fashion on the bottom surface, and a dry top surface at the same time, we mount the diamond such that the nanopillars are pointing into a thin slit, that we then fill with de-ionized water. This way, we work with a macroscopic amount of ice instead of just a nanometer thin layer, and can thus check by eye if the setup performs well. As shown in the images in Figure 3.14, we begin at $\Delta t = 0\,\text{min}$ with freezing the water in the slit, which takes roughly ten minutes. At this point, $\Delta t = 10\,\text{min}$, we turn on the nitrogen flow. About 50 minutes later, $\Delta t = 1\,\text{hour}$, we can see that there is still frozen water ice underneath the diamond sample, while the top surface is dry enough for the laser to be focused onto the NV under investigation. This is where we can start measuring, and we find that our arrangement does indeed work well for a timescale of about one to two hours. However, after $\Delta t > 3\,\text{hours}$, the ice in the slit starts to disappear. For example, the situation at $\Delta t = 4.5\,\text{hours}$ is shown in Figure 3.14 (D).

The fact that ice is first forming but then vanishes again after a few hours is indicative of a overheated heat sink that reduces the cooling power of the Peltier element for $\Delta t > 2\,\text{hours}$. In addition, the formation of ice on the sample holder increases the total mass that needs to be cooled, which is further reducing the effective heating as a function of time. We therefore conclude that our setup is never arriving in a thermal equilibrium where water ice can exist in a stable manner underneath the diamond. Moreover, the time window of one to two hours where the ice persists is not satisfactory for us, because we often integrate NMR experiments much longer to achieve SNR > 5. For these reasons, our setup is not suited for freezing water on the diamond nanopillars in a thermodynamically stable fashion. Consequently, we did not

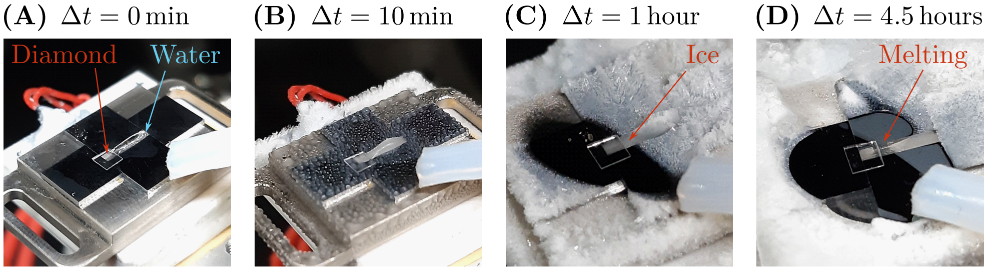
(A) $\Delta t = 0\,\text{min}$ **(B)** $\Delta t = 10\,\text{min}$ **(C)** $\Delta t = 1\,\text{hour}$ **(D)** $\Delta t = 4.5\,\text{hours}$

Figure 3.14: Images of the water ice experiment **(A)** We begin with filling the slit underneath diamond A with DI water to submerge its diamond nanopillars in water, and then we start to cool down the diamond. **(B)** After ten minutes, the water is frozen, and we turn on a nitrogen gas flow (plastic tube) of about two liters per hour to keep the top diamond surface dry. **(C)** About fifty minutes later, there is still water ice on the lower diamond surface, while the top surface seems clean and dry. **(D)** Roughly 4.5 hours since we first started to cool down, we observe that the ice has begun to vanish from underneath the diamond, indicating that the heat sink of the Peltier element is overheating, such that the system is no longer in a thermal equilibrium where ice can exist.

even try to cool down without first adding lots of water, and thus have no data for freezing just the nanometer thin layer of water we propose might be located on the diamond surface.

We did, however, attempt to measure NMR on the macroscopic amount of ice that was visible in the slit for a few hours. These experiments require constant recalibration of the NV position, the ODMR resonance and the MW power at the NV position, because various elements of the setup are moving due to thermal expansion and contraction of the involved metal components (which is one more indicator that the system is not in an equilibrium state). Consequently, we measure NMR in only 13-minute-long experiments between which it takes about 5 minutes to recalibrate the Spin-Lock sequence. We start the first of these repetitions at around $\Delta t = 1\,$hour. Averaging the first three individual NMR experiments, spanning Δt from 1.5 to approximately 2.5 hours yields the NMR spectrum shown in Figure 3.15 (A). Similarly, in Figure 3.15 (B) we plot the average of the seventh to ninth repetitions, corresponding to Δt from 3.3 to 4.2 hours, where the ice has at least started to melt or is already entirely gone. Even though the NMR spectra are quite noisy, we do find that they show different NMR linewidths that lie outside each other's fit error range.

Therefore, we do indeed observe a change in Δf_{NMR} between the two aggregate states of water, indicating that we are indeed measuring a signature of water ice ^{1}H NMR. Specifically, the measured width is smaller for the liquid state compared to the solid state, which is consistent with the concept of motional narrowing [104, 139]. Motional narrowing can be understood as follows: The dipole-dipole interaction, as shown in equation (A.16), depends on the relative orientation of the two interacting spins.

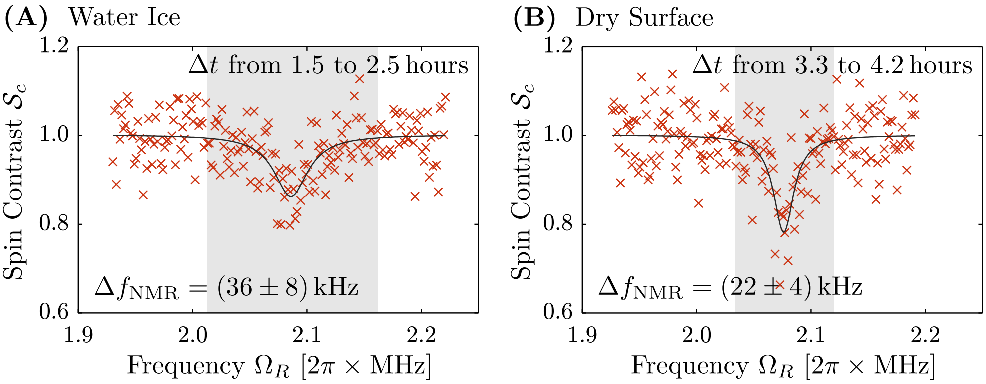

Figure 3.15: Spin-Lock NMR recorded on NVA1 at a magnetic bias field near the ESLAC, using the thermal setup shown in Figure 3.14. **(A)** Measuring Spin-Lock NMR for one hour in a time range where we assume that the NV nanopillar is surrounded by a macroscopic amount of water ice yields $\Delta f_{\mathrm{NMR}} = (36 \pm 8)\,$kHz. **(B)** Conversely, measuring in a time interval where the ice appears to have vanished (or has at least started to melt), reveals $\Delta f_{\mathrm{NMR}} = (22 \pm 4)\,$kHz. Due to strong fluctuations and drifts in the system, the experiment had to be recalibrated every 13 minutes. Each of the spectra shown here are the average of three such 13-minute NMR measurements.

Consequently, for nuclear spins in neighbouring liquid-state molecules that are quickly rotating and tumbling, this interaction averages out on the timescale of an NMR experiment. Meanwhile in a solid, the molecules are relatively frozen in orientation, such that the magnetic dipole-dipole interaction between nuclei is not vanishing in the time average. Instead, it is non-zero and takes on different values for all the different molecule pairs in the NMR sample. As such, it leads to a homogeneous broadening of the NMR line compared to the liquid case. Our data might indicate this motional narrowing effect between the liquid and solid phases of the macroscopic amount of water.

Let us close this section with three more comments. First, we point out that our NMR linewidth measurements are very noisy. Comparison with the results shown in Figure 3.10, where we measured Δf_{NMR} of the same NV at higher temperatures, reveals that the observed width varies between 20 and 40 kHz, such that one needs to be careful with making any definitive conclusion based on just the two widths measured here. Second, we note that multiple experimental runs of forming and subsequently melting macroscopic amounts of water ice on the diamond nanopillars has not damaged these pillars. Instead, all nanostructures seem unchanged, no significant amount of dirt is deposited during the ice process, the optical properties of the NVs inside the pillars remain the same, and even the crystal bond used to glue to diamond sample to the sample holder survives the sub-zero temperatures and potential exposure to liquid and frozen water. Finally, we note that once a stable setup for freezing water on the diamond surface has successfully been engineered, it could not only be used to study the nanometer thin layer of water we hypothesize might be on the diamond surface, but also to create a proton environment on the diamond surface in a controlled fashion for NMR depth determination – similar to applying immersion oil, but with the great benefit that water ice can easily be removed simply by heating the sample.

3.5 Outlook

In conclusion, in this chapter we have introduced the Spin-Lock sequence as an alternative approach to NMR compared to the established XY8-k protocol, and we have used it to measure a presence of ^{1}H nuclear spins in tri-acid cleaned diamond samples. Based on the experimental results from section 3.2 we have proposed two reasonable options for what the origin of these spins might be: Either chemical groups that contain hydrogen and are attached to the O-terminated diamond surface, and/or a thin layer of nanoconfined water. In section 3.3, we have modified the surface termination and thereby observed a change in the ^{1}H NMR signature, meaning that the chemical composition of the diamond surface seems affect the proton spin bath that we measure via NMR. In particular, our results suggest that on the laser-treated D-terminated surface, the density of surface proton spins is increased compared to the O-terminated surface. The water ice experiments from section 3.4 failed to shed any light on the origin of the ubiquitous surface spins, yet we report progress towards engineering a system that allows for freezing water on the diamond surface in a controlled manner, and we even provide first preliminary data of water ice NMR.

Looking forward, there are multiple ways to proceed with the characterization of the proton spins' origin. To further study the possibility that hydrogen related chemical surface groups are responsible for the proton NMR we observe, we propose to perform a different method for oxygen termination instead of tri-acid cleaning, for example by annealing in an oxygen atmosphere, which could lead to a different OH concentration on the diamond surface [141]. Alternatively, while X-ray photoelectron spectroscopy (XPS) cannot detect hydrogen [154], it can detect OH groups. If such OH groups are the dominant contribution to the proton spin bath that we measure in NV NMR, assessing the surface density of these groups with XPS spectroscopy could give a good initial estimate on the overall proton density. Finally, as an alternative way towards determining the surface density of the detected protons, it could be worthwhile to experiment with adding immersion oil to the diamond surface, measure XY8-k proton NMR, and analyse the resulting NMR spectra with the established depth determination method [51]. We will follow this route in in chapter 5.

In order to continue the investigation of NMR on both macroscopic and nanometer thin water ice on the diamond surface, we propose to cool down the diamond to sub-zero degrees in a closed environment (essentially a small fridge) with a nitrogen atmosphere. Such an enclosure would not only prevent the condensation of water from the ambient air, but it would also allow for thermal isolation from the environment and would therefore drastically facilitate the thermal control of the system, making it much easier to achieve a thermal equilibrium.

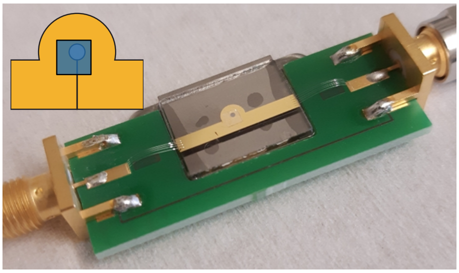

Figure 3.16: On-Chip MW delivery line, following the design of Opaluch et al. [155]. An omega-shaped gold strip line (true-to-scale sketch in the top left, with the diamond shown in blue) is evaporated onto a glass plate, that is glued to a titanium sample holder with crystal bond. To connect to the SMA cables carrying the MW signal, we attach a PCB board with a ground backplane, and contact it with wire bonds.

The main engineering challenge in constructing such a fridge is to deliver the laser and in particular the MW signal to the diamond inside the enclosure. Specifically, the gold wire loop antenna we are currently working with is not suitable for this. For this reason, have already worked towards an on-chip strip line antenna, that could be placed underneath the diamond in the envisioned thermal enclosure, following the design from Opaluch et al. [155]. We show a picture of one of our latest prototypes in Figure 3.16. However, the on-chip delivery lines we have made so far do only provide rather small MW amplitudes leading to maximal NV Rabi frequencies of $\Omega_R^{\max} \approx 2.8\,\mathrm{MHz}$, which is significantly less than what Opaluch et al. have achieved. Moreover, our prototypes suffer from mechanical instability, and it is yet to be confirmed whether there is sufficient thermal conductivity for cooling to sub-zero degrees Celsius. Further development of the on-chip antenna is required to realize water ice NMR in a closed nitrogen gas environment.

CHAPTER 4

Comparison of Spin-Lock and XY8 for NMR

Nanoscale NMR with NV centers in diamond [43–45] is a technique that is capable of detecting magnetic radio-frequency signals of precessing nuclear spins in nanoscale samples. We have demonstrated this in the previous chapter, where we employed NV NMR to characterize an ubiquitous presence of ^{1}H nuclear spins on oxygen terminated, clean diamond surfaces. In this chapter, we continue to do such NMR experiments, but we now focus on the measurement technique itself, i.e. the employed spin manipulation sequence. This sequence is key to the success of NV NMR experiments, because it is this pulse sequence that makes the NV spin sensitive to the target nuclear spins in the first place (see section 1.5), and that therefore enables the necessary frequency selective spectroscopy of nuclear magnetic signals.

There are two intrinsically different types of sequences that can be employed for NMR. The one that is most commonly encountered in NV NMR related research is the family of pulsed dynamical decoupling schemes. These protocols consist of a sequence of equally spaced MW π-pulses, often with alternating phases. Many people who employ such pulsed dynamical decoupling for their NMR experiments use the XY8-k sequence [45, 46, 50, 66–68, 120], that we have previously introduced in section 1.5.4. The operating mode of XY8-k NMR is very well understood, as it has not only been described in detail with the filter function formalism [3, 38, 111], but people have also rigorously modelled the resulting NMR coupling to nuclear spin baths [51]; a model that we present later in section 5.1.2.

The second type of NMR protocols are continuous dynamical decoupling sequences, that induce the coupling of NV spin and NMR target during a single MW pulse, with the prominent example being the Spin-Lock sequence. We have introduced this sequence in section 1.5.5, and we have used it for the NMR experiments presented in the previous chapter. Besides the results of this thesis, there is other work that has utilized spin-locking for NMR. For example, it has been demonstrated that spin-locking can be used for measuring the NMR signal of hydrogen in immersion oil on the diamond surface [63], that it can access high frequency NMR regions that cannot be probed with XY8-type protocols [156], and there is theoretical work that proposes that Spin-Lock NMR could be utilized to resolve the molecular structure of nanoscale NMR samples [49].

Despite all this NMR work conducted with both the XY8-k and the Spin-Lock sequences, there is a lack of knowledge in how these two sensing schemes compare to each other in terms of NMR sensitivity, frequency resolution, ease of use, and/or general applicability to nanoscale NMR. Given that these sequences operate entirely differently – that is a pulsed dynamical decoupling approach based on the randomization of the NV spin's quantum phase, versus a continuous decoupling technique that relies on spin population relaxation in the rotating frame – it is entirely possible that these two sequences differ substantially with regard to the aforementioned properties; meaning that either of them could be significantly better suited for NV NMR applications than the other.

Here, we measure the proton NMR signal that we characterized in the previous chapter, using both the XY8-k and the Spin-Lock sequence, and rigorously compare the resulting NMR spectra. We thereby demonstrate that the Spin-Lock sequence is insensitive to undesirable harmonic frequencies (section 4.1), achieves up to 2.5 times higher sensitivity (section 4.2), and yields a higher spectral resolution (section 4.3), all while being simpler to implement experimentally (section 4.4). Based on these results, we conclude that Spin-Lock is superior to XY8-k for nanoscale NMR applications.

4.1 Harmonic Frequency Contamination

When we introduced the XY8-k sequence in section 1.5.4, we have discussed how its filter function does not only exhibit a main peak at the frequency $f_{\mathrm{NMR}} = 1/(2\tau)$ where τ is the π-pulse spacing, but there are also harmonic side peaks at odd multiples of f_{NMR}. Furthermore, due to the non-zero width of the π-pulses, there are many additional peaks, including $\frac{1}{2}f_{\mathrm{NMR}}$ and $\frac{1}{4}f_{\mathrm{NMR}}$ [119]. For NMR applications, all these harmonics are problematic when there are multiple nuclear spin species in the NV center's proximity, because it can drastically complicate the identification of individual NMR dips. This issue becomes especially inconvenient when the gyromagnetic ratios of two different nuclei are multiples of each other, because in this case the main NMR feature of one spin overlaps with the harmonic dip of another spin.

For the proton NMR measurements that we perform with NV centers in diamond, ^{13}C spins in the diamond lattice cause exactly this problem: Their gyromagnetic ratio is $\gamma_{\mathrm{C}} = 2\pi \times 1.07\,\mathrm{kHz/G}$, which is pretty close to one fourth of the proton gyromagnetic ratio $\gamma_{\mathrm{H}} = 2\pi \times 4.2577\,\mathrm{kHz/G}$ [80]. Consequently, at the magnetic fields of 400 to 500 G we are working with, the ^{1}H main peak and ^{13}C fourth harmonic peak only differ by 10 to 13 kHz, which is on the order of the NMR linewidth Δf_{NMR} we observe; meaning that it is near impossible to tell the two resonances apart in XY8-k NMR. This is a major problem for any NMR application that requires a quantitatively accurate measurement of the proton NMR feature, such as for example single NV depth determination [51].

The Spin-Lock sequence, on the other hand, is not a periodic function and as such, we do not expect it to be sensitive to higher harmonics. Therefore, it appears likely that it is a remedy to the described problem in XY8-k NMR spectroscopy. To test this, we measure NMR of the surface protons characterized in chapter 3 with both an XY8-k and a Spin-Lock sequence. For this, we use NVB1 that is hosted in diamond sample B, which is not isotopically purified and is thus expected to contain a natural abundance of ^{13}C nuclei (see the appendix A.2 for a detailed description of the diamond samples). The resulting spectra are shown in Figure 4.1 (A), where the XY8-k data are normalized in the same way as the Spin-Lock data (see section 3.1.1). The data are demonstrating quite clearly that the spin-locking measurement is only detecting a single NMR dip with a frequency $f_{\mathrm{NMR}} = (2.145 \pm 0.820)\,\mathrm{MHz}$ that matches the expected proton Larmor frequency $\omega_L = \gamma_{\mathrm{H}} |\boldsymbol{B}_{\mathrm{ext}}| = 2.150\,\mathrm{MHz}$ (dashed line), where for this experiment $|\boldsymbol{B}_{\mathrm{ext}}| = 505\,\mathrm{G}$. The XY8-$k$ spectrum, however, reveals a multitude of overlapping NMR features. Based on this, we conclude that there are plenty of spurious magnetic signals that the XY8-k is collecting in addition to ^{13}C harmonics, while the Spin-Lock sequence is protecting the NV spin from them.

Taking the same experiments at a lower magnetic field of $|\boldsymbol{B}_{\mathrm{ext}}| = 417\,\mathrm{G}$, further away from the ESLAC, results in the NMR spectra depicted in Figure 4.1 (B). While the Spin-Lock NMR is still showing just a single Lorentzian NMR dip at the proton Larmor frequency, the XY8-k measurement is once more showing multiple features. However, there are less NMR signals compared to the 505 G case, such that it is possible to make out the NMR dip generated by the main resonance with ^{1}H nuclei and the forth harmonic of ^{13}C nuclei (dashed line). In addition, we obtain a clear NMR dip at a slightly higher frequency of approximately $f_{\mathrm{NMR}} = 1.976\,\mathrm{MHz}$ which corresponds to a gyromagnetic ratio of roughly 4.74 kHz/G. This matches neither the gyromagnetic ratio, nor the 2nd, 3rd, 4th, or 5th harmonic of any relevant nuclear spin [80], in particular not of ^{13}C, ^{14}N, ^{15}N, ^{17}O, ^{19}F, or ^{29}Si which are the elements most likely to be present in the diamond lattice or on its surface.

Our other sample, diamond A, is isotopically purified and contains a negligible amount

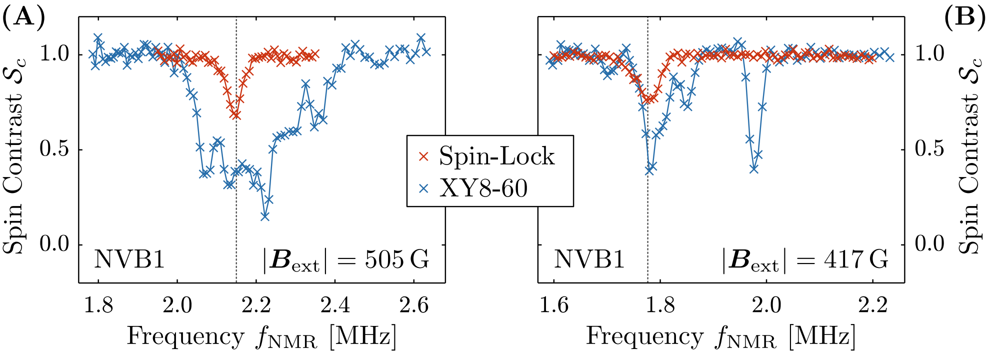

Figure 4.1: Comparison of the Spin-Lock and XY8-k NMR spectra recorded on NVB1 in diamond B, a sample that contains a natural abundance of ^{13}C spins. **(A)** At 505 G, the NMR taken with an XY8-60 sequence results in a spectrum that exhibits a multitude of different features around the proton Larmor frequency, while the Spin-Lock sequence returns a clean, single-frequency NMR dip at the expected proton Larmor frequency (dashed line). **(B)** Taking the same experiment at a lower field of 417 G yields an XY8-60 NMR spectrum with less perturbing features, such that a single Lorentzian dip at the proton Larmor frequency can be identified. This indicates that the NMR contamination in XY8-k might depend on the hyperfine coupling at the ESLAC near 500 G.

of ^{13}C isotopes in its lattice (less than 10 ppm). If we perform the same NMR measurements on NVA2 in this diamond, we find that both sequences result in a plain NMR spectrum with a single dip at the proton Larmor frequency, as shown in Figure 4.2. Since diamond A and B were both cleaned in the same way prior to these measurements (tri-acid boiling), we assume that their surfaces are identical, and thus conclude that the XY8-k NMR contamination that we obtain on diamond B originates from defects and/or spins within the diamond lattice that do not exist in the isotopically purified diamond A. Crucially, on the purified diamond A the two sequences yield very similar NMR contrasts C, meanwhile on diamond B the XY8-k sequence returns a significantly higher contrast at the proton Larmor frequency than Spin-Lock. This is indicative that on diamond B, there is indeed a harmonic ^{13}C contribution to the dip in XY8-k NMR that is not present on diamond A.

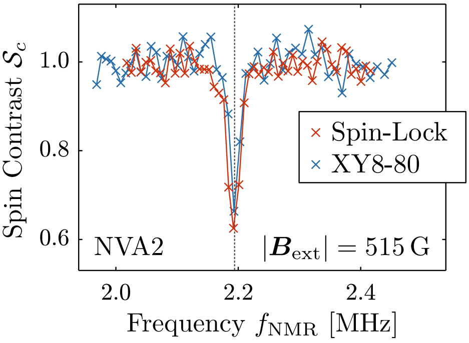

Figure 4.2: Comparing the NMR spectra of Spin-Lock and XY8-k on NVA2, that is hosted in the isotopically purified diamond A, reveals that there are none of the spurious signals present that were observed with NVB1 (see Figure 4.1). This is a strong indicator that the ^{13}C spin bath of diamond B is responsible for the features observed on NVB1. The data were recorded at 515 G with a spin-locking duration of $\tau = 150\,\mu\mathrm{s}$ and an XY8-k block repetition amount of $k = 80$.

We now make speculations on the origin of the spurious signals that surround the proton dip in Figure 4.1 (A). Since these signals are broader and more numerous near the ESLAC at 515 G, we propose that their source might be inhomogeneous hyperfine coupling between the NV spin and nearby ^{13}C nuclei in the lattice, whose precession frequency is known to be modified if the ^{13}C atom is very close to the NV center [112]. Alternatively, it could be ESLAC-mediated cross-resonances with the electron spins of nearby substitutional nitrogen atoms [157], so-called P1 centers, which hyperfine couple to the ^{13}C bath at magnetic fields near the ESLAC. However, the P1 spin transition frequencies do not match the NMR frequencies that we measure unless some sort of frequency down-conversion occurs. An alternative explanation for the observed NMR features in NVB1 might be beatings in XY8-k time traces, a phenomenon that we measure and discuss in chapter 6.

In conclusion, while we cannot properly explain the origin of the NMR contamination in XY8-k based on our data, we provide experimental evidence that it stems from impurities and/or ^{13}C spins in the diamond lattice that are sensed by the XY8-k sequence as harmonic frequencies. The Spin-Lock sequence, on the other hand, seems to protect the NV spin from the signal of these impurities and/or spins, as it produces a single NMR line independent of the purity of the diamond sample. For any NV NMR application that relies on measuring a single NMR signature, our data therefore suggest that – especially whenever a diamond without isotopic purification is used – the spin-locking approach is the better choice than XY8-k.

4.2 Sensitivity

We will now investigate how the sensitivity achieved by NMR with the Spin-Lock and XY8-k sequences compares to each other. In section 3.1.2 we have seen that for Spin-Lock NMR, the SNR depends strongly on the total sequence duration – that is the spin-locking duration τ – and we have developed a model that describes the functional dependency of SNR(τ), the result of which is given by equation (3.8). At its core, the model is based on the fact that the NMR dip in Spin-Lock is ultimately caused by a decrease in the rotating frame spin relaxation time $T_{1\rho}$ when the resonance condition with the NMR target is met. Similarly, in XY8-k NMR, the fundamental mechanism is a decrease in the spin coherence time T_2^{xy} on NMR resonance, and for this reason it is possible to model the XY8-k SNR in the exact same fashion. To that end, we follow the derivation we have presented in section 3.1.2, but we replace the two $T_{1\rho}$ decay times with the corresponding T_2^{xy} times, and substitute the spin-locking time τ with the XY8-k sequence duration $8k\tau$, where τ denotes the π-pulse spacing. This π-pulse spacing is swept to generate the NMR spectrum, however the XY8 repetition number k is a free parameter that we can use to modify the total sequence length. This results in a functional dependency SNR(k), yielding

$$\mathrm{SNR}(k) = \frac{\Delta_{01}}{\sigma\sqrt{8k\tau + T_0}} \left(\exp\left[-\left(\frac{8k\tau}{T_2^{\mathrm{xy,off}}} \right)^{\alpha} \right] - \exp\left[-\left(\frac{8k\tau}{T_2^{\mathrm{xy,res}}} \right)^{\alpha} \right] \right) . \tag{4.1}$$

Importantly, as discussed in section 1.5.4, the exponent α is equal to one for a coherence decay as a function of k and with a constant value for τ as is the case here [118]. Thus, we hereafter fix $\alpha = 1$. In conclusion, based on equations (3.8) and (4.1), we predict that both Spin-Lock and XY8-k exhibit a SNR that depends strongly on the total sequence duration. Consequently, in order to compare their SNR in a fair manner, it is necessary to first maximize the SNR of each sequence by tuning the respective sequence length.

Under such ideal conditions, we then expect the Spin-Lock sequence to provide a higher SNR. This is because the NV spin is coupled to the proton spin bath throughout the entire Spin-Lock sequence, while in a XY8-k sequence of equal total duration, the effective interaction time is shorter due to the non-zero π-pulses during which no coupling with the nuclear spin bath occurs – instead the relevant quantum phase is acquired in the free evolution between the pulses. Differently put, when ignoring experimental overhead, the Spin-Lock sequence is coupling the NV spin to the NMR target with a 100 % time efficiency, while the XY8 sequence “wastes” a certain amount of time playing π-pulses. In the following, we will denote the fraction of time that is spent playing pulses as $\mathcal{P}_\pi := (\pi\text{-pulse length})/(\pi\text{-pulse spacing})$, and for any $\mathcal{P}_\pi > 0$, we expect XY8-k to show a lower SNR within the same measurement time – and thus a lower sensitivity – than the Spin-Lock sequence.

To test this hypothesis, we measure the proton NMR on NVB1 at 417 G with both Spin-Lock and XY8-k as a function of sequence duration, where every NMR spectrum is taken with 51 pixels, and is integrated for exactly two hours. The resulting SNR of these NMR spectra is shown in Figure 4.3, where the solid lines are the predictions of equations (3.8) and (4.1). Clearly, the model is capturing the correct functional dependency of the SNR on the respective sequence length. Moreover, the model predicts maximal SNR at $52\,\mu s \approx 0.45 \cdot T_{1\rho}^{\mathrm{off}}$ for Spin-Lock, and $60.6\,\mu s \approx 0.39 \cdot T_2^{\mathrm{xy,off}}$ for XY8-k. Note that we have here only measured the respective off-resonant decay times, and have obtained the resonant coherence times by fitting equation (3.6) to the experimental contrast data.

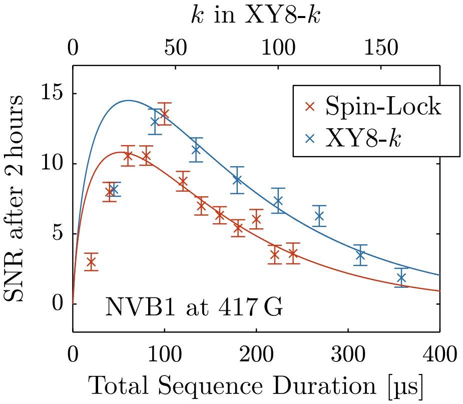

Figure 4.3: Comparison of the SNR achieved by Spin-Lock and XY8-k NMR experiments, measured as a function of total sequence duration. In the case of Spin-Lock, the sequence length is given by the spin-locking duration τ, and for XY8-k it is $8k$ times the π-pulse spacing. The solid lines are fits of equation (3.8) and (4.1). We expect Spin-Lock to achieve a higher SNR than XY8-k, due to its higher relative interaction time, however, the data demonstrate the opposite. We think this is due to harmonic contaminations adding to the fitted NMR contrast in XY8-k.

Importantly, for the XY8-k sequence employed here, we used $\mathcal{P}_\pi = 31\,\%$, such that the free evolution time between π-pulses makes up only about 69 % of the total sequence duration. As explained above, we thus expect that the SNR maximum of XY8-k is lower than the Spin-Lock SNR maximum. However, the data demonstrate quite the opposite in that XY8-k actually achieves the higher SNR values. Since we are using NVB1, we suspect that this is due to the harmonic ^{13}C contaminations in XY8-k which we have discussed in the previous section, that lead to XY8-k acquiring a stronger signal (^{13}C and ^{1}H) than Spin-Lock (^{1}H only). In other words, it is very likely that there are harmonic ^{13}C contributions to what we identify and fit as the proton dip, essentially increasing the fitted contrast C and thus overestimating the XY8-k proton SNR.

In order to remove these harmonic disturbances, we continue our SNR study with NVA2 that is not showing any such harmonic features (as we have demonstrated in Figure 4.2). This allows us to investigate the SNR resulting from just the isolated proton signal. For this, we first experimentally maximize the SNR of each sequence by sweeping τ and k respectively, and then take a single spectrum at these ideal points. The result of this is shown in Figure 4.4 (A,B). Importantly, both of these spectra have been integrated for exactly 10 hours, and were taken with equal amounts of data points. The experiments reveal that the SNR of the Spin-Lock dip, (25.5 ± 1.4), is more than twice the SNR achieved by XY8-k, (9.9 ± 1.3). This demonstrates that if one measures proton NMR without error on the fitted contrast due to the overlap with harmonic ^{13}C features, Spin-Lock is indeed more sensitive than XY8-k because of its increased contact time with the proton bath.

In the specific case shown in Figure 4.4 (A), the XY8-k sequence spent about $\mathcal{P}_\pi = 31\,\%$ of the time playing π-pulses, resulting in an integration time efficiency of 69 %. Since the SNR scales with the square root of the experiment integration time, we expect the XY8-k SNR to be $\sqrt{0.69} \approx 0.83$ times smaller than the Spin-Lock SNR.

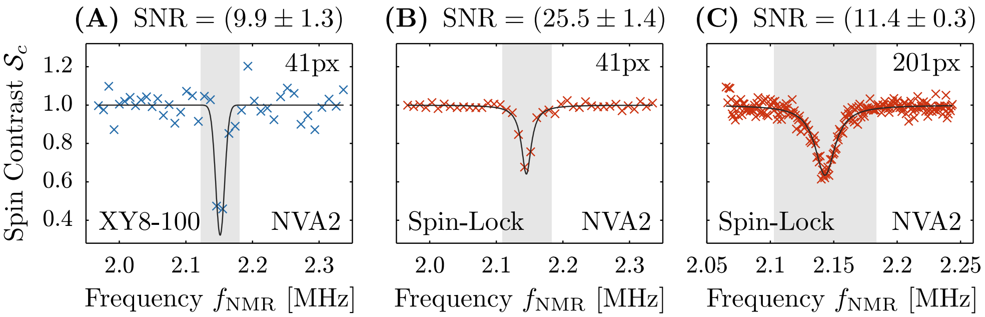

Figure 4.4: Comparison of SNR and spectral resolution in XY8-k and Spin-Lock NMR. All spectra shown here were recorded on NVA2, integrated for exactly 10 hours, and ran at ideal τ respectively k values that optimize SNR, see equations (3.8) and (4.1). **(A)** XY8-100 NMR with 41 pixels achieves a spectral resolution of $\Delta f = 9.45\,\mathrm{kHz}$ and an SNR of about 10. The dip is captured by only 2 pixels. This is the XY8-k spectral resolution limit for our current experimental setup at magnetic fields near the ESLAC. **(B)** Spin-Lock with $\tau = 100\,\mu\mathrm{s}$ with identical pixel density, equal integration time, and a similar spectral resolution of $\Delta f = 9.15\,\mathrm{kHz}$ achieves a 2.5 times higher SNR and thus sensitivity than XY8-k. **(C)** Spin-Lock with 201 pixels distributed on a more narrow spectral window, demonstrating a spectral resolution of $\Delta f = 1.27\,\mathrm{kHz}$ that exceeds the XY8-k resolution limit by a factor of at least four.

However, in our experiment, the observed XY8-k SNR amounts to only 0.39 times the Spin-Lock SNR. This mismatch indicates that there are more aspects to the difference in SNR than the non-zero $\mathcal{P}_\pi$, however, the absolute difference in SNR is clear as a stand-alone result.

4.3 Spectral Resolution

We now study the spectral resolution that can be achieved by the Spin-Lock and XY8-k sequences respectively. This resolution is key to meaningful fits of the NMR dip, especially when the dip is very narrow. Such fitting is important for applications where the contrast and width of the dip need to be determined in a quantitatively accurate manner, as for instance in NV depth determination [51].

For XY8-k, the resolution of the NMR spectrum is ultimately limited by the sampling rate of the pulsing hardware. In our case, we use a Zurich Instruments SHFSG with a state-of-the-art sampling rate of 2 GHz, corresponding to a pulsing resolution of half a nanosecond. Due to the way we set up the XY8-k sequence, the free evolution between π-pulses is controlled in increments of twice that value, such that our effective time resolution is $\Delta t = 1\,\mathrm{ns}$. The π-pulse spacings we typically work with to measure proton NMR at 500 G, where $f_{\mathrm{NMR}} \approx 2\,\mathrm{MHz}$, are about $\tau = 1/(2f_{\mathrm{NMR}}) \approx 250\,\mathrm{ns}$. Therefore, for our experiments, we estimate a spectral frequency resolution of

$$\Delta f = \left(\frac{1}{2\tau}\right) - \left(\frac{1}{2(\tau + \Delta t)}\right) \approx \left(\frac{\Delta t}{2\tau^2}\right) = 2\Delta t \cdot f_{\mathrm{NMR}}^2 = 8\,\mathrm{kHz}\,, \tag{4.2}$$

and about half of that could be achieved if the π-pulse spacing was incremented by $\Delta t = 0.5\,\text{ns}$ instead of 1 ns. For the typical NMR linewidths that we observe (that is, 10 to 50 kHz), a resolution of $\Delta f \approx 8\,\text{kHz}$ means that the dip is captured by only 2 to 5 pixels. For example, in the XY8-k spectrum that we show in Figure 4.4 (A), we measured at the time resolution limit of $\Delta t = 1\,\text{ns}$, resulting in a spectral resolution of $\Delta f = 9.45\,\text{kHz}$. The observed dip has a width of $\Delta f_{\text{NMR}} = (13.3 \pm 2.3)\,\text{kHz}$ and is thus defined by only two pixels.

Spin-Lock NMR on the other hand, has a spectral resolution that is limited by the resolution with which the MW amplitude (respectively the MW power) can be controlled. For the SHFSG device we are using, the output power is ranging from -30 to 0 dBm, multiplied with a modulation amplitude between 0 and 1 for fine tuning. We can set this modulation amplitude with at least six decimal digits, such that at our typical working point of $-5\,\text{dBm}$, we can control the output power well enough to achieve a resolution on the resulting Rabi frequency of less than 2 kHz (in principle even much less, but we have not tried, see the comment at the end of the section). This can be seen in Figure 4.4 (C), where we repeat the Spin-Lock experiment from panel (B), but we take five times the pixel density distributed over a smaller spectral range, revealing a resolution of $\Delta f = 1.27\,\text{kHz}$, almost 7.5 times better than what XY8-k could achieve. This demonstrates that at magnetic fields near the ESLAC, Spin-Lock can achieve far higher spectral resolutions than XY8-k.

Importantly, the spectral resolution of XY8-k depends on the probed spectral window, and therefore on the applied magnetic bias field. For instance, evaluating equation (4.2) for protons at a lower field of 200 G would result in $\Delta f \approx 1.5\,\text{kHz}$ which is comparable to what we obtained with spin-locking. For higher magnetic fields, however, the XY8-k resolution worsens drastically. At 750 G already, equation (4.2) predicts $\Delta f \approx 20\,\text{kHz}$, such that it would be impossible to resolve the NMR feature from Figure 4.4 (A). For the Spin-Lock sequence, on the other hand, the spectral resolution is magnetic field independent. Therefore, given the necessary MW power, Spin-Lock can achieve the same $\sim 1\,\text{kHz}$ resolution at fields where XY8-k fails to resolve the NMR dip.

Finally, we point out one particularly neat thing about the spectrum in Figure 4.4 (C). It has integrated for precisely 10 hours just as the spectra from panels (A) and (B), but since there are five times more pixels, each data point was effectively measured for only a fifth of the time. This reflects very nicely in the resulting SNR, which is pretty exactly a factor of $\sqrt{5}$ lower than the SNR in panel (B).

Before we close the discussion on the spectral resolution, we make the important remark that we could very likely achieve even higher resolutions in Spin-Lock NMR than presented here, though we have not tried. Technically, given the appropriate electronic hardware, it is possible to reach a resolution on the MW power down to the noise limit. For our SHFSG device, the MW output noise density is about -144 to $-135\,\text{dBm/Hz}$, which is many orders of magnitude lower than the estimated step width of $(-13 \pm 2)\,\text{dBm}$ that we employed in Figure 4.4 (C), indicating that one should reasonably be able to achieve sub 10 Hz resolution in Spin-Lock NMR.

4.4 Further Technical Differences

We now list a few more rather technical differences between the XY8-k and the Spin-Lock sequence, that we learned about when working with them in our lab. Some of these aspects are well known in the NV community already, yet for completeness we nonetheless mention them here.

Available MW Power

For Spin-Lock NMR it is irrelevant how fast the initial and final $\pi/2$-pulses are, and for the spin-locking pulse, any MW power is sufficient as long as the corresponding Rabi frequency Ω_R exceeds the Larmor frequency of the target NMR spin. In our case, the NMR resonance is at around $f_{\mathrm{NMR}} \approx 2\,\mathrm{MHz}$, and the NMR linewidth is on the order of a few tens of kHz, such that a Rabi frequency of 2.5 MHz is sufficient to monitor the NMR feature in its entirety.
For XY8-k however, it is important to reduce the duration of the individual π-pulses, because long pulses reduce the effective contact time of the NV with the spin bath and thereby reduce the SNR (as we have discussed in section 4.2). Moreover, long π-pulses can shift the NMR position and distort the NMR signal [158], and give rise to the collection of undesirable additional harmonic frequencies [119]. In our case, where $f_{\mathrm{NMR}} \approx 2\,\mathrm{MHz}$, the π-pulse spacing is approximately $\tau = 250\,\mathrm{ns}$. For the reasons listed above, the employed π-pulses should be significantly shorter than this, ideally by a factor of four or more, such that we require Rabi frequencies of $\Omega_R > 8\,\mathrm{MHz}$. This is far more than the 2.5 MHz that Spin-Lock NMR would require under equal conditions. Therefore, the available MW power is much more limiting for XY8-k experiments.

Pulse Imperfections

Employing well calibrated pulses is crucial for both XY8-k and Spin-Lock to ensure proper sequence functionality. Any errors in MW pulse length, phase or frequency lead to improper spin flips. The XY8-k is expected to correct for small systematic pulse imperfections [115, 116] in that it prevents them from accumulating throughout the entire multipulse sequence, yet it is not resistant to random noise or drifts throughout the sequence. The Spin-Lock sequence, on the other hand, is quite sensitive to any kind of pulsing errors because for imperfect pulsing, the NV spin is no longer “locked” by the spin-locking pulse. Instead, it precesses about the spin-locking field which manifests as an oscillation in the NMR spectrum’s background. This concerns not only errors on pulse timing and amplitude, but crucially also errors on the phase relation between the $\pi/2$-pulses and the spin-locking pulse. Hence, we conclude that pulse calibration is particularly important for Spin-Locking, marking one weakness of Spin-Lock compared to XY8-k which can correct small calibration errors.

Pulse Timing

The XY8-k protocol is highly timing sensitive, because the π-pulse spacing τ is defining which NMR frequency the NV spin is sensing. To guarantee that the signal identification is unambiguous, it is necessary to control the pulse timing with nanosecond precision. Moreover, random noise on τ can cause the entire XY8-k sequence to break down in the sense that the noise frequency selectivity is lost, especially when k is large. For spin-locking, however, the timing between the two $\pi/2$-pulses and the spin-locking pulse is not that important, as long as these pulses do not overlap. While we have not measured this directly, we suspect that random delays of less than 5 ns between the $\pi/2$-pulses and the spin-locking pulse have little effect, while random errors on this time scale are expected to cause a notable degradation of the NMR frequency accuracy in XY8-k experiments. For these reasons, we hypothesize that Spin-Lock is more robust to systematic and random timing errors than XY8-k.

Pulse Shape

The pulse shape can be relevant for NMR, particularly when employing square pulse envelopes. This is because many microwave components, such as switches, circulators, amplifiers and coaxial cable interfaces can lead to overshoots on the sharp edges of such square pulses. For XY8-type sequences where there are many pulses, these random errors on the edges can accumulate and thereby degrade the NMR quality. For Spin-Lock, on the other hand, there are only three pulses, and we therefore expect the sequence to be rather insensitive to such pulse-shape dependent errors, highlighting yet another advantage of Spin-Lock over XY8-k. We note that in our experiments, to avoid overshoots on pulse shape edges entirely, we play smooth Gaussian ramps of 16 ns each instead of sharp edges.

Loop Antenna Movement

For our experiments, we use a gold wire loop to deliver the microwave (see the appendix A.1 for a detailed description of the setup). Depending on the MW signal running through this wire, it is prone to heat up and move. In particular, we observe that there is significant movement during ODMR experiments where the MW frequency is changing, and during pulsed experiments where the MW is quickly turned on and off. Consequently, during an XY8-k NMR experiment that is requiring higher power and fast pulsing, we expect more antenna movement than during a Spin-Lock NMR measurement. For this reason, we expect more noise on the MW pulse amplitude in XY8-k compared to Spin-Lock. This is yet another advantage of Spin-Lock over XY8-k, however, this issue can be solved by employing more robust antenna solutions such as for example on-chip designs [155].

4.5 Outlook

In summary, we have compared Spin-Lock and XY8-k by investigating their applicability to nanoscale NMR on a technical level. We found that using the Spin-Lock sequence has multiple significant advantages over the XY8-k sequence.

First, while the XY8-k technique is picking up various spurious signals including harmonics of other nearby nuclear spins – resulting in a contamination of the NMR spectrum – the Spin-Lock sequence is protecting the NV spin from such frequencies and thus guarantees an isolated proton signature in the NMR spectrum. Specifically, we have demonstrated that for a non-isotopically purified diamond with ^{13}C spins in its lattice, XY8-k NMR exhibits many NMR features near the proton resonance; in fact many more than just the fourth harmonic of ^{13}C, indicating the collection of further spurious signals. All these contaminations disappear when using an isotopically purified diamond. For this reason, we have formulated the hypothesis that the underlying physics might either be inhomogeneous hyperfine coupling between the NV spin and nearby ^{13}C nuclei with enhanced gyromagnetic ratios [112], or ESLAC-mediated cross-resonances with the electron spins of nearby substitutional nitrogen atoms which hyperfine couple to the ^{13}C bath at magnetic fields near the ESLAC [157].

We have demonstrate that Spin-Lock NMR is not sensing these contaminations at all, highlighting a key advantage of spin-locking over XY8-k. However, it is possible to modify the XY8-k sequence in order to suppress the collection of such unwanted signals, such as adaptive XY sequences that employ non-equally spaced pulses to eliminate low-order harmonics [159], or controlled randomization of the π-pulse phase to mitigate spurious signals [160, 161], or so-called cyclic geodesic driving that generates a repeated adiabatic evolution of the NV spin to suppress both harmonics and other spurious signals [162], or the so-called "PulsePol" sequence that has been demonstrated to be entirely insensitive to any harmonic frequencies [163]. However, all these modifications come at the cost of drastically increased pulsing complexity, longer sequence durations and thus prolonged experiment integration times.

To further look into the XY8-k NMR features that we observe in non-isotopically purified diamond, it might be worthwhile to employ some of these sequences to characterize the observed features' origin. Alternatively, we suggest taking a systematic study of how the NMR spectrum depends on the applied magnetic field to pin down the exact role that the ESLAC plays in the generation of these features. Furthermore, to study which order of harmonic frequencies we might observe, one could employ different XY-type sequences, such as XY4-k or XY16-k, that show slightly different harmonic peaks in their filter functions, especially for non-zero π-pulses [119]. Finally, we remark that the features might also be related to slow kHz-frequency beatings that we sometimes obtain in XY8-k time traces. We present and discuss these beatings in chapter 6.

Second, we demonstrate experimentally that spin-locking achieves up to 2.5 times higher NMR sensitivity than XY8-k, given ideal choices for the spin-locking time τ and the XY8 repetition number k. We assign this difference in sensitivity to the fact that spin-locking is coupling the NV spin to the nuclear spin bath with a 100 % time efficiency, while the XY8-k spends a significant fraction $\mathcal{P}_\pi$ of the time playing π-pulses during which the relevant interaction with the nuclear spin bath is paused. Based on this hypothesis, it would be interesting to drastically reduce $\mathcal{P}_\pi$, either by using much more MW power (to shorten the π-pulses), or by measuring at lower magnetic fields (to prolong the π-pulse spacing), and study whether this does indeed increase the resulting XY8-k sensitivity as expected.

Third, we have shown that Spin-Lock achieves a much higher spectral resolution for NMR, being technically limited only by the accuracy with which the MW amplitude respectively MW power can be controlled. We experimentally demonstrate spectral resolutions of less than 2 kHz, and predict that substantially better resolutions of less than 10 Hz should be achievable with our hardware. XY8-k on the other hand is limited by the sampling rate of the pulsing hardware, and for state-of-the-art AWG cores that provide two giga-samples per second (such as our SHFSG device), we estimate a spectral resolution limit for proton NMR at the ESLAC of about 4 kHz, which can be further increased by measuring at lower magnetic fields. To entirely overcome this reciprocal relation of sampling rate and spectral resolution, one could employ XY8 correlation spectroscopy [45, 164, 165] whose NMR frequency resolution is limited by the NV spin lifetime. However, at the same time such correlation spectroscopy has a total sequence duration that is more than twice as long as standard XY8-k, leading to a significant reduction in SNR and thus sensitivity.

Overall, our findings suggest that Spin-Lock is much better suited for NV NMR applications that rely on measuring a single NMR feature, such as for example depth determination of single NVs. We will perform such depth determination with both XY8-k and Spin-Lock NMR in the next chapter.

CHAPTER 5

Depth Determination via Proton NMR

So far, we have measured NMR on single NV centers to characterize a specific source of hydrogen nuclei present on tri-acid cleaned diamond surfaces (chapter 3), and we have studied the technical differences between Spin-Lock and XY8-k proton NMR (chapter 4). Now, we turn to an actual application of NV NMR, in particular the depth determination of single shallow NV centers in diamond. Such depth determination is of great interest, because there are many NV sensing schemes that depend critically on this NV depth, for example nanoscale NV magnetometry [96, 97] such as scanning probe magnetometry [27] or magnetic resonance imaging [98]. Precise a priori knowledge of the deployed NV's depth would improve the quality and quantitative precision of these applications [68]. For example, in scanning probe magnetometry, the quantitative reconstruction of the sample magnetization from the measured magnetic stray fields is a function of the NV depth [166, 167].

For NV centers formed by ion implantation, a common tool for depth estimation is the stopping range of ions in matter (SRIM) Monte-Carlo simulation [168], however, SRIM returns a statistical prediction and not a precise measurement of an individual NV center's depth. Moreover, SRIM does not consider certain effects such as crystal channelling of ions, and it thus systematically underestimates the implantation depth by a factor of up to two [51, 169]. For these reasons, SRIM is not satisfying the need for a quantitatively accurate depth determination technique.

In 2016, Pham et al. have published a promising protocol for depth determination of individual NV centers [51], that is based on measuring XY8-k NMR of ^{1}H spins in immersion oil on the diamond's surface. By carefully modelling the interaction of the NV spin with the magnetic signal of these spins under XY8-k, one can fit the proton NMR spectrum and thereby obtain the depth of the NV defect. Over the last few years, many people have used this technique to identify the depth of single NVs [59–69]. However, as we have demonstrated in chapter 4, there are critical issues with XY8-k NMR that complicate this depth determination scheme, such as harmonic frequency contamination and limited NMR frequency resolution. There are ways to avoid these problems, for example one can eliminate ^{13}C harmonics by working with isotopically purified diamond material, or it is possible to boost the spectral resolution of XY8-k by measuring at lower magnetic bias fields; however, these workarounds restrict the technique's application to specific diamonds and magnetic fields. A solution to these issues that works independent of diamond purity and bias field – and we have validated this experimentally in chapter 4 – is to use the Spin-Lock sequence instead of XY8-k, and on top of that, Spin-Lock NMR even comes with the additional benefit of higher sensitivity. In light of these arguments, we suspect that depth determination via Spin-Lock NMR offers significant advantages over the established XY8-k protocol.

However, the necessary mathematical framework to rigorously describe Spin-Lock NMR and the resulting NV depth analysis does not yet exist. Deriving this framework is a challenge because Spin-Lock is not a pulsed dynamical decoupling sequence relying on the manipulation of the quantum phase accumulation caused by transverse fields, but instead Spin-Lock NMR is based on spin relaxation due to fields parallel to the respective spin quantization axis. For this reason, common theoretical approaches to dynamical decoupling, in particular the filter function formalism [3, 38], cannot be applied to the Spin-Lock sequence. People have nonetheless already made first steps towards a mathematical description of AC magnetometry under spin-locking [103, 121], yet there is still a lack of a complete and quantitatively accurate Spin-Lock model that could be used for depth determination. We are aware of one single paper that performs such spin-locked depth determination [63], however this publication is not providing the fitting functions that were used to extract the NV depth.

Here, we derive a theoretical description of Spin-Lock NMR, that can be deployed to fit the depth of individual NVs or the density of the detected nuclear spin ensemble. By comparing this Spin-Lock model to the established XY8-k model of Pham et al., we identify issues with both approaches introduced by assumptions made in their respective derivation that are invalid for our experimental conditions. Most importantly, we demonstrate experimentally that these poor assumptions lead to a substantial error on the fitted depth. Our results thus suggest that both models need to be reworked for quantitatively accurate depth determination.

In the second half of this chapter, despite the limitations of these models, we nonetheless use them to attempt to further characterize the source of ^{1}H spins that we have previously studied in chapter 3. Specifically, we show that by adding immersion oil, it is possible to simultaneously fit the NV depth and the spin density of the unidentified proton ensemble. If we fit a two-dimensional surface ensemble to the data in this way, the resulting surface density exceeds the density of available carbon dangling bonds by far, which excludes the scenario that the observed proton signal is originating from only surface-bound chemical groups. On the other hand, when fitting a three-dimensional proton layer with only a few nanometers thickness – a length scale that has been proposed for adsorbate water layers on diamond under ambient conditions [142, 147] – the resulting volume spin density is substantially larger than the density of liquid water. While it is unclear how accurate these fits are until the theoretical models are reworked, our preliminary results indicate that a very dense layer of solid-like water suits better to our data than a just 2D ensemble of chemically bonded groups containing hydrogen, which is in accordance with other NV NMR results [42, 46, 66–68] and recent adsorbate water layer analysis [142, 147].

5.1 Theory of Depth Determination

We now present the math behind the two depth determination schemes that we work with in this chapter. First, we discuss our own protocol based on Spin-Lock NMR that we have developed from scratch, and then we briefly present the established protocol based on XY8-k NMR that has been published by Pham et al. [51].

5.1.1 Depth Determination via Spin-Lock NMR

To derive our theoretical model of Spin-Lock NMR, we have worked together with Aaron Daniel and Patrick Potts from the quantum thermodynamics group in Basel, a collaboration that resulted in what we will present in the following. Note that we are here only discussing the approach, the key assumptions and the final result of this model. The full derivation is presented in detail in the appendix A.3.

In a Spin-Lock sequence, applied to the two-level system spanned by the NV electronic states $|0\rangle$ and $|-1\rangle$, the initial $\pi/2$-pulse brings the system into an eigenstate of $\hat{\sigma}_x$, specifically into the dressed state $|+\rangle = \frac{1}{\sqrt{2}}(|0\rangle + |-1\rangle)$. During the subsequent spin-locking pulse the system then evolves according to the Hamiltonian

$$\hat{\mathcal{H}} = \hbar\omega_0\hat{\sigma}_z + \hbar\gamma_{\mathrm{NV}}\boldsymbol{B}_{\mathrm{MW}}\cdot\hat{\boldsymbol{\sigma}} + \hbar\gamma_{\mathrm{NV}}\boldsymbol{B}_{\mathrm{N}}\cdot\boldsymbol{\sigma} + \hbar\omega_L\sum_j \hat{I}_z^j\,, \tag{5.1}$$

where the first term describes the splitting of the electronic $|0\rangle$ and $|-1\rangle$ states, the second term is the coupling of the NV to the MW magnetic field $\boldsymbol{B}_{\mathrm{MW}}$ that constitutes the spin-locking field, the third term represents the coupling of the NV to the magnetic field $\boldsymbol{B}_{\mathrm{N}}$ produced by the nuclear spin ensemble on the diamond surface, and finally the fourth term describes the Zeeman splitting of the nuclear spins (indexed by j) due to the applied magnetic bias field. Here, $\hat{\boldsymbol{\sigma}} = (\hat{\sigma}_x, \hat{\sigma}_y, \hat{\sigma}_z)$ are the spin operators of the two-level system, as defined previously in section 1.3.1.

As we demonstrate in appendix A.3.2 and A.3.3, the Spin-Lock Hamiltonian from equation (5.1) becomes time-independent in a doubly rotating frame under two rotating wave approximations. Therefore, in this specific frame, it is straight forward to compute the time evolution of $|+\rangle$, and by doing so, we derive the probability to find the system in $|+\rangle$ by the end of the spin-locking pulse as

$$P_{|+\rangle} = \frac{1}{2}\left(1 + \frac{\Delta^2 + \gamma_{\mathrm{NV}}^2 B^2\,\cos\left(\frac{1}{2}\tau\sqrt{\Delta^2 + \gamma_{\mathrm{NV}}^2 B^2}\right)}{\Delta^2 + \gamma_{\mathrm{NV}}^2 B^2}\right)\,, \tag{5.2}$$

where τ is the duration of the spin-locking pulse, $\Delta = \Omega_R - \omega_L$ is the detuning between the spin-locking Rabi frequency Ω_R and the proton Larmor frequency ω_L, and $B := |\boldsymbol{B}_{\mathrm{N}}^{\mathrm{rotrot}}|$ is the time-independent amplitude of the magnetic field that the proton spins generate at the NV position in the doubly rotating frame. We note that the performed rotating wave approximations are only valid for weak driving ($\Omega_R \ll \omega_0$) and near the Hartmann-Hahn resonance ($\Omega_R \approx \omega_L$); two conditions that are always well fulfilled in our experiments, because we sweep Ω_R across a $\sim 200\,\mathrm{kHz}$ range centered around $\omega_L \approx 2\,\mathrm{MHz}$, while $\omega_0 \approx 1.4\,\mathrm{GHz}$.

Importantly, in the derivation of (5.2) we assumed that the protons in the ensemble are a collection of non-interacting pure magnetic dipoles, such that there is no dephasing in the bath. Later, in section 5.2.1, we will see that this approximation does not apply to our experiments. Instead one ought to either assign a phenomenological nuclear T_2^* dephasing time to the proton spins, or directly treat the spin-spin interactions and/or molecular diffusion by adding these mechanisms to Hamiltonian (5.1).

Next, we add fluctuations in the magnetic field produced by the nuclear spin ensemble. For this, we assume that the nuclear magnetic field components in the doubly rotating frame (B_x, B_y, B_z) are each described by a Gaussian distribution with variance σ^2 and zero mean. In this case, the fluctuations on their Euclidean norm $B = (B_x^2 + B_y^2 + B_z^2)^{1/2}$ are given by the Rayleigh distribution,

$$R(B, \sigma^2) = \frac{B}{\sigma^2} \exp\left(\frac{-B^2}{2\sigma^2} \right) . \tag{5.3}$$

Furthermore, we assume that the fluctuations of the nuclear spins are slow compared the spin-locking duration τ, such that B can be assumed to be constant throughout one repetition of the Spin-Lock sequence. Under this assumption, we can express the expectation value of $P_{|+\rangle}$ as

$$E\left[P_{|+\rangle}\right] = \int_0^\infty P_{|+\rangle}\ R(B, \sigma^2)\ \mathrm{d}B\,. \tag{5.4}$$

Finally, in order to evaluate equation (5.4), we need to quantitatively describe the magnetic field variance $\sigma^2 = \langle \hat{B}_i^2 \rangle - \langle \hat{B}_i \rangle^2$ at the NV's position, where $i \in \{x, y, z\}$. To that end, we describe the proton spin bath with an infinite temperature thermal state (we justify this choice at the end of this section), and then evaluate the expectation values $\langle \hat{B}_i^2 \rangle$ and $\langle \hat{B}_i \rangle^2$ by integration over all spins in the ensemble. Depending on whether we consider a proton ensemble that is two-dimensional (A), three-dimensional (V), or a combination of both (AV), we find (see appendix A.3.5)

$$\sigma_A^2 = \frac{(\hbar\gamma_\mathrm{H}\mu_0)^2}{4096\,\pi} \cdot \left(3\,\frac{\rho_A}{d^4} \right) , \tag{5.5}$$

$$\sigma_V^2 = \frac{(\hbar\gamma_\mathrm{H}\mu_0)^2}{4096\,\pi} \cdot \left(\frac{\rho_V}{(d+Z_1)^3} - \frac{\rho_V}{(d+Z_2)^3} \right) , \tag{5.6}$$

$$\sigma_{AV}^2 = \sigma_A^2 + \sigma_V^2 , \tag{5.7}$$

where d is the depth the of NV center used to sense the proton spin bath, ρ_A and ρ_V are the surface and volume spin densities, Z_1 and Z_2 are the boundaries of the three-dimensional proton layer (such that the layer is located at a distance $d + Z_1$ to $d + Z_2$ relative to the NV), γ_H is the proton Larmor frequency, and μ_0 is the vacuum permeability. Note that σ_V^2 equals σ_A^2 in the limit of $Z_2 \to Z_1$ with $Z_1 = 0$, given the constraint that $\lim_{Z_2 \to 0}(\rho_V \cdot Z_2) = \rho_A$.

Finally, to directly fit the model to our NMR data that is normalized as discussed in section 3.1.1, we map the the expectation value $E\left[P_{|+\rangle}\right]$ onto the corresponding spin contrast $\mathcal{S}_c$. As explained in appendix A.3.6, this is done through the relationship,

$$\mathcal{S}_c = 2 \cdot E\left[P_{|+\rangle}\right] - 1\,. \tag{5.8}$$

We have not yet been able to analytically solve the integral in equation (5.4) and therefore we cannot give an analytic solution for equation (5.8). However, we can nonetheless fit (5.8) to our NMR data numerically.

We close this section with a few comments on our model, and suggestions on how to further improve it. First, we note that the model is not restricted to protons, but it can be used to describe NV NMR with any nuclear spin species. For this, one would need to change equation (A.17) to describe the dipolar field of the new nucleus, which ultimately changes the prefactor of σ_A^2 and σ_V^2 in equations (5.5) and (5.6).
Second, we made the assumption that the protons are non-interacting pure dipoles, and as already mentioned above, this means that our model does not account for molecular diffusion, nuclear spin dephasing, or other effects that would introduce a finite nuclear T_2^* time. In section 5.2.1, we will demonstrate that this causes the model to predict a Fourier limited NMR linewidth of $\sqrt{\pi}/\tau$. This is not consistent with our experimental NMR data, which in turn introduces a significant error on the fitted NV depth d. In the future, the model should therefore be reworked to account for a phenomenological finite T_2^* time, or to directly treat the underlying mechanisms by adding nuclear spin-spin interactions and/or diffusion to the Hamiltonian (5.1).
Finally, we point out that we assumed an infinite temperature quantum state for the proton bath, an approximation that forbids any thermal polarization in this spin bath. This is a good approximation, because the thermal polarization of protons at 500 G is negligibly small. To illustrate this, we compute the thermal polarization P_{thermal} as the ratio between the total net magnetization of N thermally polarized protons, M_z, and the magnetization achieved by a fully polarized proton ensemble, $M_{\text{full}} = N\hbar\gamma_{\text{H}}I$. In the high-temperature approximation, this yields [170]

$$P_{\text{thermal}} = \frac{M_z}{M_{\text{full}}} = \frac{\hbar\gamma_{\text{H}}B(I+1)}{3k_B T}\,, \tag{5.9}$$

and evaluation for $B = 500\,\text{G}$ and $T = 300\,\text{K}$ results in $P_{\text{thermal}} \approx 1.8 \cdot 10^{-7} \ll 1$.

5.1.2 Depth Determination via XY8 NMR

To determine the depth d of a single NV via XY8-k NMR, we use the mathematical framework that has been derived and published by Pham et al. [51]. Here, we first present the key results of their work expressed in our own notation, and we then extend these results to the three different spin ensemble types we have considered above, i.e. a two-dimensional surface ensemble (A), a three-dimensional layer (V), or the combination of both (AV).
Pham et al. use the same NMR data normalization as we do (see section 3.1.1), and they show that the spin contrast $\mathcal{S}_c$ of a single NV under an XY8-k sequence is

$$\mathcal{S}_c = \exp\left(-\frac{2}{\pi^2}\,\gamma_{\text{NV}}^2\sigma^2\,K(\Delta,k,\tau)\right)\,, \tag{5.10}$$

where σ^2 denotes the variance of the magnetic field produced by the nuclear spin bath at the NV's position. Note that in equation (5.10), Pham et al. actually give the root mean square magnetic field amplitude $B_{\text{RMS}}^2 = \langle\hat{B}_z^2\rangle$ instead of the variance $\sigma^2 =$

$\langle\hat{B}_z^2\rangle - \langle\hat{B}_z\rangle^2$ that we use here, however, as we show in the appendix in equation (A.39), for the infinite temperature nuclear spin bath at hand, the expectation value $\langle\hat{B}_z\rangle$ is zero, such that $B_{\mathrm{RMS}}^2 = \sigma^2$. Finally, the term $K(\Delta, k, \tau)$ is a function describing how susceptible the NV is to such AC magnetic field fluctuations under the XY8-k sequence. Pham et al. derive that under the assumption of instantaneous π-pulses with zero duration, K is given by

$$\begin{aligned} K(\Delta, k,\tau) \;=\; & \frac{2\,(T_2^*)^2}{\Big[(T_2^*\Delta)^2+1\Big]^2} \Bigg(\Big[(T_2^*\Delta)^2-1\Big] + \frac{8k\tau}{T_2^*}\Big[(T_2^*\Delta)^2+1\Big] \\ & - \exp\Big(-\frac{8k\tau}{T_2^*}\Big)\Big\{\Big[(T_2^*\Delta)^2-1\Big]\cos(8k\tau\Delta) + 2\,T_2^*\Delta\,\sin(8k\tau\Delta)\Big\}\Bigg)\,, \end{aligned} \tag{5.11}$$

where τ is the π-pulse spacing, $\Delta = (\frac{\pi}{\tau} - \omega_L)$ is the detuning between the probed NMR frequency $\frac{\pi}{\tau}$ and the proton Larmor frequency ω_L, the integer k is the XY8-k block repetition number such that $8k\tau$ is the total sequence duration, and T_2^* denotes the nuclear proton spin dephasing time. If one assumes that T_2^* is much longer that the duration $8k\tau$ of the entire XY8-k sequence, it is valid to work in the limit $T_2^* \to \infty$, and Pham et al. show that in this case, equation (5.11) becomes

$$K(\Delta, k, \tau) \;\approx\; (8k\tau)^2 \cdot \mathrm{sinc}^2\Big(4k\tau\Delta\Big)\,. \tag{5.12}$$

However, as we will show below in section 5.2.2 and specifically in Figure 5.1 (B), this approximation is not consistent with our experimental NMR data, and we will therefore exclusively work with K as given by equation (5.11).

To compute the magnetic variance σ^2, Pham et al. make the same basic assumptions about the position and volume of the nuclear spin ensemble as we have made above in section 5.1.1; namely they consider a three-dimensional layer of spin density ρ_V, located on the diamond surface at a distance $(d + Z_1)$ to $(d + Z_2)$ relative to the NV center, such that the proton layer thickness is given by $(Z_2 - Z_1)$. However, contrary to our approach where the full vector of the nuclear magnetic field at the NV position is taken into account, Pham et al. only consider the projection of the nuclear magnetic field onto the NV axis. Therefore, they obtain a different expression for the volume integral over the spin bath,

$$\begin{aligned} \sigma_V^2 \;&=\; \frac{9\rho_V(\hbar\gamma_{\mathrm{H}}\mu_0)^2}{64\,\pi^2}\int_0^{2\pi}\int_0^{\pi/2}\int_{\frac{d+Z_1}{\cos(\theta)}}^{\frac{d+Z_2}{\cos(\theta)}} \frac{\big(\boldsymbol{e}_{\mathrm{NV}}\cdot\boldsymbol{e}_{\mathrm{H}}\big)^2 - \big(\boldsymbol{e}_{\mathrm{NV}}\cdot\boldsymbol{e}_{\mathrm{H}}\big)^4}{r^4}\,\sin(\theta)\,\mathrm{d}r\,\mathrm{d}\theta\,\mathrm{d}\phi \\ &=\; \frac{5\,\big(\hbar\gamma_{\mathrm{H}}\mu_0\big)^2}{1536\,\pi}\cdot\left(\frac{\rho_V}{(d+Z_1)^3} - \frac{\rho_V}{(d+Z_2)^3}\right)\,, \end{aligned} \tag{5.13}$$

where $\boldsymbol{e}_{\mathrm{H}} = [\sin(\theta)\cos(\phi), \sin(\theta)\sin(\phi), \cos(\theta)]$ is a unit vector denoting the orientation of the proton spin that is located at a distance r from the NV center, and $\boldsymbol{e}_{\mathrm{NV}} = [\sin(\alpha)\cos(\beta), \sin(\alpha)\sin(\beta), \cos(\alpha)]$ is the orientation of the NV itself. Here, the coordinate system is chosen such that the z-axis is normal to the diamond surface, and such that the NV is located in the coordinate system's origin. Since we exclusively perform NMR on diamond samples A and B that have a (001) surface, we have fixed $\alpha = [\frac{\pi}{2} - \cos^{-1}(\sqrt{2/3})] \approx 54.7°$ to solve equation (5.13).

What Pham et al. are not showing in their publication is an expression for the magnetic field variance produced by a two-dimensional surface layer of protons. We derive this by changing the volume integral in (5.13) to a surface integral. For this, we fix r to $d/\cos(\theta)$, substitute the ρ_A for ρ_V, and integrate only over the two angular degrees of freedom, such that

$$\begin{aligned}\sigma_A^2 &= \frac{9\,(\hbar\gamma_{\mathrm{H}}\mu_0)^2}{64\,\pi^2}\,\rho_A \int_0^{2\pi}\int_0^{\pi/2} \frac{(\boldsymbol{e}_{\mathrm{NV}}\cdot\boldsymbol{e}_{\mathrm{H}})^2-(\boldsymbol{e}_{\mathrm{NV}}\cdot\boldsymbol{e}_{\mathrm{H}})^4}{[\,d/\cos(\theta)\,]^4}\,\sin(\theta)\,\mathrm{d}\theta\,\mathrm{d}\phi \\ &= \frac{41\,(\hbar\gamma_{\mathrm{H}}\mu_0)^2}{5040\,\pi}\cdot\left(\frac{\rho_A}{d^4}\right). \qquad (5.14)\end{aligned}$$

For a combination of both a two-dimensional surface ensemble (A) and a three-dimensional volume ensemble (V), one obtains $\sigma_{AV}^2 = \sigma_A^2 + \sigma_V^2$.

Finally, we note that this model comes with a crucial intrinsic problem: As we will show experimentally in section 5.2.2, the fitted NV depth d depends strongly on the employed π-pulse duration, demonstrating that the assumption of infinitely sharp π-pulses is highly invalid for our experiments. Therefore, to provide quantitatively accurate depth determination, it is necessary to extend the model to account for non-zero π-pulse lengths.

5.2 Comparison and Evaluation of the two Models

We now compare the two NMR depth determination protocols that we have introduced in sections 5.1.1 and 5.1.2. We begin by comparing the magnetic field variances predicted by the two models. These variances do not depend on the pulse sequence, and as such, they should be the same. However, while it is true that the expressions for σ_A^2 and σ_V^2 of the two models show the same scaling with the relevant physical quantities (in particular the NV depth d), they differ significantly in the numerical prefactor. An overview of these prefactors in shown in table 5.1 (A).

These differences in σ^2 arise from the fact that Pham et al. consider only the projection of the protons' magnetic field onto the NV axis (which is a valid assumption for XY8-k), whereas we do not make this projection and instead work with a general magnetic field vector. Consequently, in Pham et al.'s model, the term that is integrated to obtain σ^2 has a geometric dependency on the orientations of the NV and the individual protons, while this is not the case for the term we integrate in our derivation. For this reason, the two models result in different magnetic field variances for the same proton bath.

Furthermore, the models differ crucially in their treatment of dephasing in the proton bath, in that Pham et al. work with a finite nuclear T_2^*, where we work in the limit $T_2^* \to \infty$ by assuming that the protons are non-interacting dipoles.

To derive how the magnetic fluctuations σ^2 of the proton bath are affecting the NV spin, the models describe the respective NMR detection scheme, and ultimately result in an expression for the NMR spin contrast $\mathcal{S}_c$. Specifically, our description of Spin-Lock NMR is based on computing the time evolution of the NV dressed state in a doubly rotating frame by solving the Schrödinger equation, while Pham et al.'s XY8-k model is based on the filter function formalism to model the quantum phase

(A) Spin Bath	**This Work**	**Pham et al. [51]**
Proton spin dephasing	No, non-interacting dipoles	Yes, finite proton T_2^*
Nuclear magnetic field	Work with full $\boldsymbol{B}_\mathrm{N}$	Use only $B_{\mathrm{N},z}$
Numeric prefactor in σ_A^2	$\mathcal{N}_A = 3/4096$	$\mathcal{N}_A = 41/5040$
Numeric prefactor in σ_V^2	$\mathcal{N}_V = 1/4096$	$\mathcal{N}_V = 5/1536$

(B) NMR Detection	**This Work**	**Pham et al. [51]**
Pulse sequence	Spin-Lock	XY8-k
Employed theory	Time evolution analysis	Filter function
Non-Zero pulse lengths	Irrelevant	No, zero duration

Table 5.1: Comparison of the two NMR models **(A)** To describe the proton spin bath, Pham et al. consider a finite nuclear T_2^* time for proton bath, while we assume that the proton spins are non-interacting pure dipoles. Moreover, the models use different projections of the magnetic field $\boldsymbol{B}_\mathrm{N}$ produced by the nuclear spins at the NV position, which leads to different numerical prefactors in the nuclear magnetic field variance. **(B)** The NMR detection is realized with different pulse sequences, Spin-Lock and XY8-k respectively, and different theoretical approaches are used to describe them. Finally, Pham et al. assume that the π-pulses are instantaneous.

pick-up under XY8-k. Finally, we note that Pham et al. make the assumption of instantaneous π-pulses.

Given that the two depth determination techniques rely on different assumptions and different pulse sequences, it is an important sanity check to verify that they nonetheless yield the same NV depth d. We will verify this now. The data we have shown in the previous chapter in Figure 4.2 are ideal for this, because it is a Spin-Lock and XY8-k NMR spectrum, recorded on the same NV center (NVA2), under equal conditions and even on the same day. The NMR target in these two measurements is the ubiquitous ^{1}H nuclear surface ensemble that we have studied in chapter 3 (i.e. there is no immersion oil). Here, we treat these spins as a two-dimensional ensemble, which is why we use the variance σ_A^2 from equations (5.5) and (5.14) for the fits. For the surface spin density ρ_A, we use the value of immersion oil, that is $50\,\mathrm{nm}^{-3}$ [42,50,120], and scale it down to two dimensions, meaning that we plug in $\rho_A = (50)^{2/3}\,\mathrm{nm}^{-2}$. While there is no proper justification for this arbitrary choice of density, both models scale with (ρ_A/d^4) in the same way, such that an incorrect nuclear spin density leads to the same multiplicative error on d in both models, and thus this arbitrary choice for ρ_A does not affect the qualitative comparison we are making here.
Fitting the models to the data in this way results in what is plotted in Figure 5.1. Crucially, the two models reveal different NV depths d far outside each other's error margin; an error interval that we compute as the square root of the fit covariance matrix's diagonal entries. The fact that these models return such different depths is significant because it means that at least one of the models yields an incorrect depth.

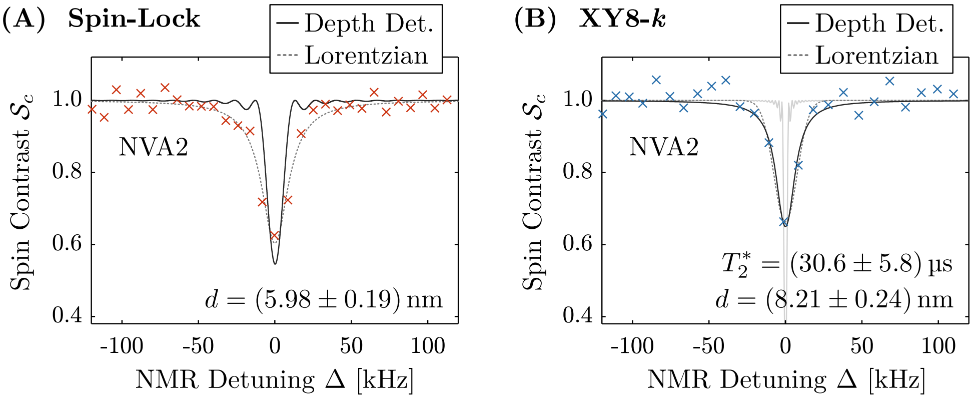

Figure 5.1: Comparison of the NV depth d as fitted by the two depth determination techniques. Both NMR spectra shown here were recorded on NVA2 within the same day and under equal conditions. The dashed lines are Lorentzian lineshape fits. **(A)** In the case of Spin-Lock with $\tau = 150\,\mu\text{s}$, the model fits a depth $d = (5.98 \pm 0.19)\,\text{nm}$. **(B)** The XY8-$k$ data were recorded with $k = 80$ and a π-pulse of 64 ns (such that $\mathcal{P}_\pi = 28.1\,\%$), and the fit yields $d = (8.21 \pm 0.24)\,\text{nm}$. Assuming that $T_2^* \to \infty$, the model fits a similar depth of $(8.19 \pm 0.32)\,\text{nm}$, but the resulting fit is much to narrow (light grey). We conclude that clearly, the depth fitting results of the two models do not agree, and we study this mismatch in sections 5.2.1 and 5.2.2, where we show that both models are intrinsically flawed, and thus fit incorrect NV depths.

Note that the XY8-k model fits a very similar depth independent of whether a finite or infinite nuclear T_2^* time is employed, i.e. $d = (8.21 \pm 0.24)\,\text{nm}$ and $(8.19 \pm 0.32)\,\text{nm}$ for these two cases. However, for $T_2^* \to \infty$, the resulting NMR lineshape has a width that is much too narrow and a contrast that is way to large, as shown by the light grey line in Figure 5.1 (B). On the other hand, if we fit a finite T_2^* in addition to the depth d, the lineshape matches extremely well to the data (black line). For this reason, we will hereafter always include a finite nuclear T_2^* as a fitting parameter XY8-k depth determination.

In the next two sections, we will study the depth mismatch of the two models by investigating how key assumptions and approximations made in either model's derivation affect the resulting depth fit. This way, we will reveal that each of the two models is making one critical assumption about the physical system that does not apply to our experiments, and we will demonstrate experimentally that this in turn leads to a substantial error on the fitted depth d.

5.2.1 Evaluation of the Spin-Lock Model

Our model assumes that the protons in the spin bath are non-interacting pure dipoles. This means that we essentially neglect any nuclear dephasing and molecular diffusion processes, and treat the protons as nuclear spins with an infinite coherence time, $T_2^* \to \infty$. For such an infinite T_2^* that significantly exceeds the spin-locking duration τ, we expect our model to result in a Fourier limited NMR linewidth, given by $\sqrt{\pi}/\tau$.

Conversely, if the protons were subject to some form of interaction or noise that reduced their coherence time to $T_2^* \leq \tau$, the linewidth would instead be limited by T_2^* and be independent of τ. As we have seen in section 3.2.3 (specifically Figure 3.9), the latter case is true for our Spin-Lock experiments, meaning that there is indeed a finite $T_2^* \leq \tau$ associated with the detected surface proton ensemble. This is further supported by the results of Pham et al. who report that protons in immersion oil exhibit $T_2^* \approx 60\,\mu\text{s}$ [51]. Moreover, as discussed above, for the surface protons that we measure on clean diamond, Pham et al.'s model fits best with a finite dephasing time of $T_2^* \approx 30\,\mu\text{s}$. Both of these values are shorter than our typical spin-locking times of $\tau \approx 100\,\mu\text{s}$. For these reasons, we suspect that the assumption of $T_2^* \to \infty$ is a central weakness of our Spin-Lock model, which might lead incorrect depth fits.

To validate this hypothesis experimentally, we fit the data from Figure 3.9 with our Spin-Lock NMR model. And indeed, as shown in Figure 5.2 (A), the model results in a width Δf_{model} that perfectly matches the Fourier limit of $\sqrt{\pi}/\tau$, while the data exhibit a constant linewidth Δf_{NMR}. Here, Δf_{NMR} is determined by the FWHM of a fitted Lorentzian lineshape, and Δf_{model} is the FWHM of the NMR dip as fitted by our Spin-Lock model. For these fits, we have used the spin density of immersion oil, i.e. $\rho_V = 50\,\text{nm}^{-3}$ [42, 50, 120] and $\rho_A = (\rho_V)^{2/3}$ respectively. Since we have not applied any oil here but are instead measuring the surface protons on clean diamond, these density values are likely incorrect. However, for the qualitative study we are doing here, we do not need quantitatively accurate depth fits. The inferred width

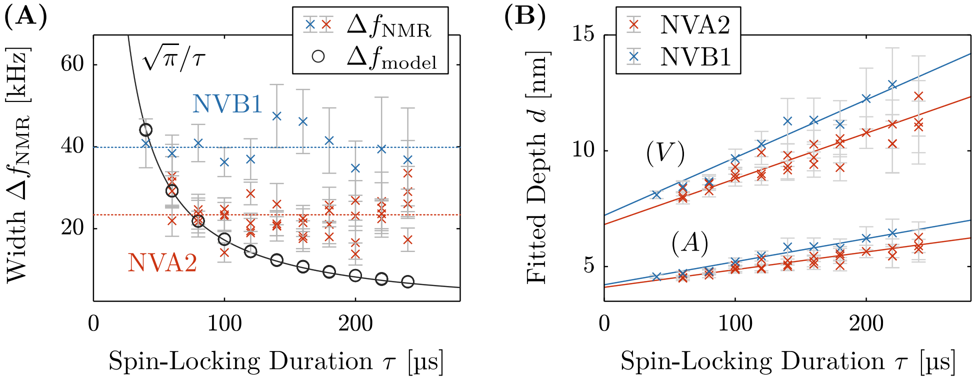

Figure 5.2: Our Spin-Lock depth determination protocol assumes zero proton spin dephasing, which leads to an incorrect prediction on the NMR width. **(A)** While the experimentally determined proton NMR linewidth Δf_{NMR} of NVA2 and NVB1 is independent of the spin-locking duration τ, fitting our model to the data yields a fit with a width Δf_{model} that fits very well to the Spin-Lock Fourier limit of $\sqrt{\pi}/\tau$. This clearly indicates that while the data is limited in width by a decoherence process in the bath, our model predicts a Fourier limited NMR width. **(B)** The fitted NV depth d increases linearly with τ, yet in reality the depth is constant. We assign this slope in $d(\tau)$ to the incorrect linewidth predicted by our model. To enable quantitatively accurate depth determination, we suggest to incorporate a finite nuclear T_2^* into the Spin-Lock NMR model.

Δf_{model} is the same for fitting a two-dimensional ensemble (using σ_A^2) or an infinitely large three-dimensional proton ensemble (using σ_V^2).

The results shown in Figure 5.2 (A) demonstrate that our Spin-Lock NMR model is Fourier limited as expected. As such, our model is underestimating the NMR width, especially for our typical spin-locking durations of $\tau \geq 100\,\mu\text{s}$. To investigate how this this mismatch in linewidth affects the fitted NV depth d, we plot the inferred value of d against the spin-locking duration τ. This is shown in Figure 5.2 (B), where it is clear to see that $d(\tau)$ increases linearly with τ as indicated by the linear fits (represented by solid lines). In reality, the NV depth d is constant, because we only change the spin-locking duration τ and not the physical system itself. Hence, such a non-zero slope $\frac{\partial d}{\partial \tau}$ is unphysical and a clear problem with our model.

Interestingly, when comparing NVA2 and NVB1, we find that NVA2 actually yields a smaller slope $\frac{\partial d}{\partial \tau}$. At the same time, NVA2 has a narrower linewidth Δf_{NMR} that matches the model's prediction slightly better. This suggests that the discrepancy in NMR width between data and model is related to the slope $\frac{\partial d}{\partial \tau}$, in the sense that a larger width mismatch causes a larger slope.

To quantify the error in d, we note that for the range of $\tau = 20\,\mu\text{s}$ up to $240\,\mu\text{s}$ that we probed here, the fitted depth almost doubles. Therefore, the result of our Spin-Lock depth determination technique is currently afflicted by an error in depth d on the order of approximately a factor of two.

In summary, we conclude that the Spin-Lock model's assumption of zero dephasing in the bath leads to a Fourier limited NMR width that underestimates the true linewidth, and consequently, the model fits an incorrect NV depth d. In order to solve this issue, the model needs to be extended to include decoherence in the proton spin ensemble. To that end, we propose to either assign a phenomenological nuclear T_2^* dephasing time to the proton spins, similar to the approach by Pham et al. [51]; or even better, to directly treat the spin-spin interactions and/or molecular diffusion by adding these mechanisms to Hamiltonian (5.1).

5.2.2 Evaluation of the XY8 Model

For the model derived by Pham et al., the π-pulses of the XY8-k sequence are assumed to be instantaneous, i.e. of zero duration. This assumption is often made in mathematical descriptions of pulsed dynamical decoupling [3, 38, 111], however, in reality these pulses always have a non-zero width.

We now investigate how valid it is to assume such instantaneous π-pulses in XY8-k depth determination, by studying how the fitted depth d depends on the employed π-pulse length. To that end, we determine the depth of NVB1 by fitting the XY8-k NMR model to corresponding NMR data that we measure with different π-pulse durations. The result of these fits is shown in Figure 5.3. These experiments were conducted at 412 G using an XY8-10 sequence, and the proton NMR target is the ubiquitous surface proton presence we have characterized in chapter 3 (again, no immersion oil has been applied). The fitting routine was executed for either a two-dimensional (A) or an infinitely large three-dimensional (V) proton ensemble, and the fitting parameters are the depth d and the finite nuclear coherence time T_2^*. For the proton spin density, we plug in the value for immersion oil, $\rho_V = 50\,\text{nm}^{-3}$ [42, 50, 120], and for the 2D case we use $\rho_A = (\rho_V)^{2/3}$. As explained above, these are probably not the correct densities for the surface proton ensemble, however, we are studying how the fitted depth depends on the π-pulse length and thus we do not mind a systematic error on d.

The data in Figure 5.3 are clearly showing that the fitted depth d increases with longer π-pulses in a linear fashion (as indicated by the linear fits). This increase in d is of course not physical, because nothing about the NV system changes when the π-pulse duration is altered, and thus the model should fit the same depth d for all these data points. We speculate this this increase in the inferred value of d is caused by the increase of $\mathcal{P}_\pi = (\pi\text{-pulse length})/(\pi\text{-pulse spacing})$ via the following mechanism: For larger $\mathcal{P}_\pi$, the system has a shorter direct interaction time with the spin bath, and does thus acquire less quantum phase from the interaction with the nuclear spin bath. The model is then incorrectly interpreting this reduced phase pick-up as a weaker nuclear magnetic signal at the NV position, which manifests in an increased NV depth.

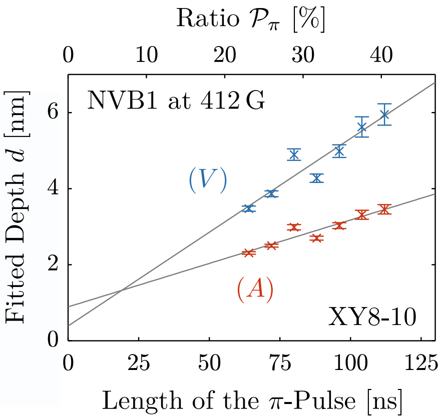

Figure 5.3: Fitted NV depth d as a function of π-pulse duration respectively $\mathcal{P}_\pi$, obtained by fitting equation (5.10) to XY8-10 NMR data recorded on NVB1 at about 412 G, where the π-pulse spacing is $\tau = 285$ ns. The fit was done for either (V) an infinite volume of proton spins on the surface with a proton spin density $\rho_V = 50\,\text{nm}^{-3}$, or ($A$) a two-dimensional surface layer with a spin density of $\rho_A = (\rho_V)^{2/3}$. Both approaches result in a depth d that increases with π-pulse duration, as indicated by the linear fits (solid gray lines). This demonstrates that the model's assumption of sharp π-pulses leads to a massive overestimation of the NV depth.

Based on our results, we conclude that the XY8-k model of Pham et al. is incorrectly describing XY8-k NMR if non-zero π-pulse lengths are not explicitly considered. Consequently, the model needs to be modified to account for such non-zero pulse lengths. We propose that this could for instance be done with a similar treatment as presented in [119], where NV spin rotations during the π-pulses are added to the spin evolution under XY8-k.

We speculate that the actual depth of the NV is the depth obtained by extrapolating the data to a π-pulse duration of zero, that is by intersecting the linear fits with the y-axis, because in this limit ($\mathcal{P}_\pi \to 0$) the model is accurate. For the data shown here, that would be roughly 0.4 nm respectively 0.9 nm. This is extraordinarily shallow, however, we might be underestimating the depth because we are using NVB1, where harmonic ^{13}C contaminations in the XY8-k NMR spectrum might add to what we treat as the proton dip (see section 4.1), causing an overestimation of the nuclear magnetic signal. Also, keep in mind that we are using inappropriate spin densities for the analysis of this data, such that neither the absolute depth values, nor the slopes of the linear fits are quantitatively accurate.

Finally, given that the model is accurate in the limit of $\mathcal{P}_\pi \to 0$, it is possible to mitigate the error introduced by the non-zero π-pulse lengths by minimizing $\mathcal{P}_\pi$. This can be done either by employing drastically more MW power than we use here (to shorten the pulses), or by operating at much lower magnetic fields (to reduce f_{NMR} and thereby prolong the π-pulse spacing).

To summarize, we have shown that the assumption of instantaneous π-pulses in the XY8-k depth determination protocol of Pham et al. is invalid for our experiments where the π-pulses make up about 20 to 40 % of the sequence duration. We show experimentally that this gives rise to an error on the fitted NV depth. For the data presented here, this error manifests as an overestimation of the depth by a factor of 2 to 6. To improve the model and enable quantitatively accurate depth determination, we suggest to extend the model to account for non-zero π-pulses.

5.3 Characterization of the Surface Proton Spin Density

Although we have just provided strong evidence that both the Spin-Lock and the XY8-k depth determination protocols show conceptional weaknesses and therefore return incorrect fitting results, we nonetheless will now use these models to further characterize the surface ensemble of ^{1}H nuclear spins that we have previously studied in chapter 3, in particular by fitting its proton density. We justify the usage of these incomplete models with the following three arguments: First, while the fits of the models are not quantitatively accurate, they at least provide the correct order of magnitude for the depth, and thus it is worth trying to use them to estimate the magnitude of the proton density. Second, while a direct comparison of the two models is not feasible, it is possible to qualitatively compare the results of the same model as long as the corresponding sequence is unchanged (i.e. equal spin-locking duration and π-pulse spacing respectively), since in this case the introduced error on the fitting results is the same. Third, even if we should find unphysical proton densities, we do at least demonstrate how to employ our models to fit the spin density; a routine that would remain unchanged once the models themselves are updated to provide a complete description of proton NMR.

In section 5.3.1, we first study the density of the proton spins that we observe on tri-acid cleaned diamond. Afterwards, in section 5.3.2, we make a qualitative statement on how this density changes during the Deuterium termination that we have discussed in section 3.3.

5.3.1 Density of the Unidentified Surface Protons

We now attempt to use the two NMR models to make an estimate of the density of the ^{1}H nuclear spin ensemble that we consistently measure on tri-acid cleaned diamond. In chapter 3, we have already investigated this source of protons, and based on our experimental results, we have concluded that these surface spins are either a collection of surface-bound hydrogen-rich chemical groups and/or a nanometer thin contact layer of water molecules. Therefore, we will now treat this source as either a two-dimensional ensemble with a surface density ρ_A, or as a three-dimensional layer of finite thickness and volume density ρ_V, or a combination of both. Given the corresponding experimental NMR data, we can then employ our theoretical description of NMR to fit ρ_A and/or ρ_V. In the following, we will present such fits for each of these three cases.

(Case 1) : A Two-Dimensional Surface Ensemble

We start with the case where we treat the unidentified surface ^{1}H nuclei as a two-dimensional surface layer of density ρ_A. In this case, the nuclear magnetic field variance σ_A^2 generated by these spins at the NV position is directly given by equation (5.5) for our approach, respectively by equation (5.14) for Pham et al.'s model, reading

$$\sigma_A^2 = \mathcal{N}_A \, \frac{(\hbar\gamma_{\mathrm{H}}\mu_0)^2}{\pi} \cdot \left(\frac{\rho_A}{d^4}\right) , \tag{5.15}$$

where $\mathcal{N}_A$ is the respective numerical prefactor, as listed in table 5.1. With this variance, we can in principle evaluate the outcome of both models numerically, and thereby attempt to determine ρ_A. However, it turns out that there is a major caveat, namely, that we do not know the depth d of the NV, and it is impossible to fit both d and ρ_A simultaneously. This is because they appear in both models only via equation (5.15) as the ratio (ρ_A/d^4), and consequently, we can only fit this ratio in an unambiguous manner, but not the individual values of d and ρ_A.

We solve this issue by adding immersion oil to the diamond surface. In this way, the NV senses two different spin baths at the same time; the surface protons of unknown origin and the ^{1}H nuclei in the oil. Since we apply a macroscopic amount of oil, we describe the oil with an infinitely large three-dimensional spin ensemble of volume density $\rho_{\mathrm{oil}} = 50\,\mathrm{nm}^{-3}$ [42, 50, 120], such that its magnetic variance is given by (5.6) and (5.13) respectively, with $Z_1 = 0$ and $Z_2 = \infty$. The total magnetic variance detected by the NV is then given by the sum of both ensembles, and yields

$$\sigma_{A,\mathrm{oil}}^2 = \sigma_A^2 + \sigma_{\mathrm{oil}}^2 = \frac{(\hbar\gamma_{\mathrm{H}}\mu_0)^2}{\pi} \cdot \left(\mathcal{N}_A \, \frac{\rho_A}{d^4} + \mathcal{N}_V \, \frac{\rho_{\mathrm{oil}}}{d^3}\right) , \tag{5.16}$$

where $\mathcal{N}_A$ and $\mathcal{N}_V$ are the respective numerical prefactors, as listed in table 5.1. Crucially, $\sigma_{A,\mathrm{oil}}^2$ depends on two different ratios, (ρ_A/d^4) and $(\rho_{\mathrm{oil}}/d^3)$. For this reason (and because ρ_{oil} is a known constant), we can unambiguously determine both ρ_A and d by simultaneously fitting equations (5.15) and (5.16) to NMR experiments taken with and without immersion oil.

In Figure 5.4 (A), we present the result of such a fit. Here, we measure Spin-Lock NMR on NVA2 at a bias field of 515 G, once with and once without immersion oil on the diamond surface. Both spectra were recorded with the same spin-locking duration of $\tau = 150\,\mu\mathrm{s}$ that was determined beforehand to maximize the NMR SNR on clean diamond (see section 3.1.2), and both spectra were integrated for exactly 10 hours. Simultaneously fitting these spectra with the Spin-Lock NMR model as described above results in $\rho_A = (1165 \pm 1323)\,\mathrm{nm}^{-2}$ and $d = (18.2 \pm 9.3)\,\mathrm{nm}$.

In addition, we conduct the same measurements and fitting procedure with the XY8-k sequence, as shown in Figure 5.4 (B). Here, the spectra were measured

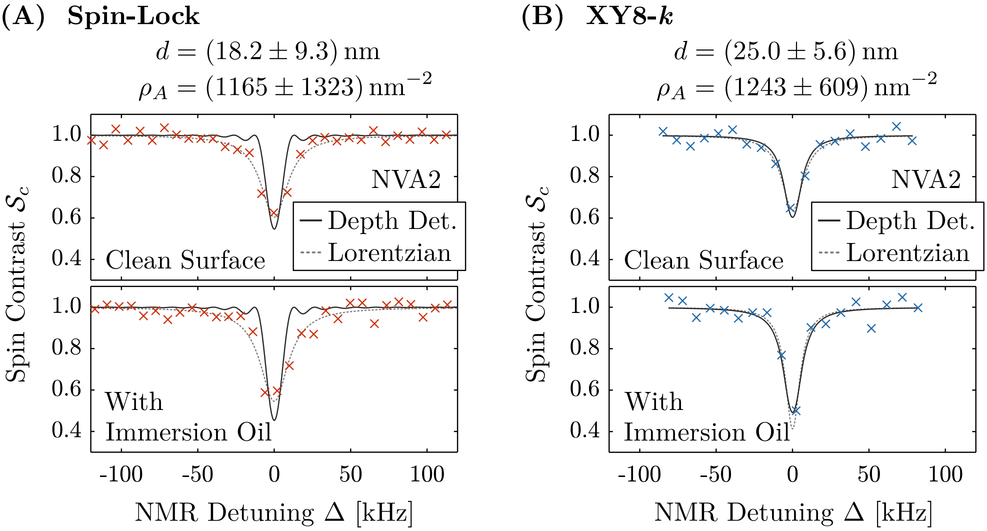

Figure 5.4: Taking NMR measurements with and without coating the diamond surface with immersion oil, and subsequently fitting both spectra simultaneously allows us to determine both the NV depth and the density of the unidentified surface proton spins. Here, we are fitting the data under the assumption that this proton ensemble is a two-dimensional surface ensemble with density ρ_A. **(A)** Fitting of the Spin-Lock NMR experiments reveals a depth of $d = (18.2 \pm 9.3)\,\mathrm{nm}$ and a surface spin density of $\rho_A = (1165 \pm 1323)\,\mathrm{nm}^{-2}$. **(B)** Equal procedure with XY8-k results in $d = (25.0 \pm 5.6)\,\mathrm{nm}$ and $\rho_A = (1243 \pm 609)\,\mathrm{nm}^{-2}$, and additionally, a finite nuclear T_2^* time was fitted to $(34.4 \pm 5.2)\,\mu\mathrm{s}$. These values indicate that the unidentified source of surface spins has a much higher proton density than immersion oil.

with $k = 80$ that was chosen to maximize the SNR on clean diamond (see section 4.2). Furthermore, the π-pulse duration was 64 ns in both experiments, such that $\mathcal{P}_\pi = 28.1\,\%$. Each spectrum was integrated for exactly 10 hours. The fitting is executed with the same variances as described above, but we now use the numerical prefactors $\mathcal{N}_A$ and $\mathcal{N}_V$ from Pham et al.'s model, and we add the nuclear dephasing time T_2^* as a third fitting parameter. Ultimately, a simultaneous fit of both spectra yields $\rho_A = (1243 \pm 609)\,\mathrm{nm}^{-2}$, $d = (25.0 \pm 5.6)\,\mathrm{nm}$ and $T_2^* = (34.4 \pm 5.2)\,\mu\mathrm{s}$.

We now discuss these fitting results. First, the NV depths extracted by the two fits are not equal, but on the same order of magnitude. This was to be expected, since we have shown that the models are not quantitatively accurate in their depth determination for our experimental conditions. However, a depth of 18 nm or 25 nm is reasonable for NVs in diamond A, because SRIM simulations [168] – which are known to underestimate the implantation depth by a factor of up to two due to negligence of ion crystal channelling [51, 169] – predict a nominal NV depth of roughly 9 nm for this diamond. Hence, our fitted NV depths are well in accordance with the statistical prediction of SRIM, which demonstrates that at least the order of magnitude of d is correctly predicted by the two NMR models.

The inferred surface spin density ρ_A, on the other hand, is more than $1000\,\mathrm{nm}^{-2}$. This seems excessively high, given that the corresponding average proton-proton distance on the surface is about $0.3\,\text{Å}$, which is unrealistically small. Moreover, the surface density of carbon atoms on the (001) surface of our diamond is only about $16\,\mathrm{nm}^{-2}$, as can be calculated by $[2a\sin(\phi/2)]^{-2}$, where $a = 0.3567\,\mathrm{nm}$ is the C-C bond length, and $\phi = 109.5°$ is the angle between C-C bonds in the lattice. Since each carbon atom provides two dangling bonds, the surface density of attached atoms or chemical groups should be limited to a maximum of $32\,\mathrm{nm}^{-2}$. Our fit result for ρ_A exceeds this by a factor of roughly 35. Hence, we conclude that just a two-dimensional collection of chemically bonded groups containing hydrogen is not enough to explain the ubiquitous presence of protons we observe on O-terminated diamond.

Next, we point out that the NMR contrast in Figure 5.4 (A,B) is actually only marginally increasing when the immersion oil is added. This indicates that the nuclear magnetic field that the NV detects is dominated by the unidentified proton source. In other words, the effective sensing volume of the NV must essentially contain only protons from the unidentified source and essentially no protons from the immersion oil. Since the NMR sensing volume of a single NV is approximately given by a semi-sphere on top of the diamond surface with a radius roughly equal to the NV depth d [44,120], we can imagine three scenarios that would explain our data: Either, the NV is extremely shallow such that its sensing volume is very tiny and contains basically only the unidentified two-dimensional surface ensemble; or the unidentified ensemble is three-dimensional with a thickness on the order of d such that it fills the entire sensing volume; or the surface spins have a substantially higher proton density than the oil and outnumber the oil protons by far. Our current fitting routine disregards the second case (we are fitting such three-dimensional ensembles later), and suggests that the third case is much more likely than the first case, because both models return $\rho_A \approx 1200\,\mathrm{nm}^{-2}$ that is significantly larger than $(\rho_{\mathrm{oil}})^{2/3} \approx 13.6\,\mathrm{nm}^{-2}$. Moreover, we exclude the case of a super-shallow NV, because when we fit the spectra with the constraints of $d < 4\,\mathrm{nm}$ and $\rho_A < 1000\,\mathrm{nm}^{-2}$, the resulting fits do not agree well with the data. Thus, these arguments further substantiate our conclusion that in case of a 2D layer of protons, this layer would need to be unrealistically dense in order to match our data. Surface-bound groups containing hydrogen alone are therefore unlikely the sole origin of the proton NMR we measure.

However, keep in mind that the utilized fitting functions have limitations. Let us now estimate the worst case scenario for how wrong the fitted density ρ_A might be due to the error on the fitted depth that we have studied in section 5.2. We have seen that for Spin-Lock (XY8-k), depending on the choice of τ (the π-pulse length), the fitted NV depth is modified by a factor of up to 2 (6). Since the depth d and density ρ_A appear in the model as the ratio (ρ_A/d^4), we estimate that the fit of ρ_A might be off by up to $2^4 = 16$ in Spin-Lock, and $6^4 = 1296$ in XY8-k. Therefore, contrary to what we hypothesized in the beginning of this section, in the worst case, the ρ_A density we have determined here is in fact one to three orders of magnitude off. In this worst case, it would be incorrect to exclude chemically bonded groups as the origin of the observed proton spins.

We note that for all the fits presented here and later below, we assume that the nuclear T_2^* dephasing time is the same for the nuclear spins of unknown origin and in the oil molecules. This is not necessarily true, because if the unidentified ^{1}H nuclei are indeed provided by surface-bound chemical groups containing hydrogen (or a solid-like contact layer of water in the fits below), they might actually have very different spin properties and diffusion rates than the ^{1}H nuclei in liquid immersion oil. In the future, these fits should thus be modified to allow for two different T_2^* times. Such an additional fitting parameter, however, can drastically complicate the fitting process because it eventually becomes hard to unambiguously fit all these parameters at the same time.

Finally, the NMR measurement presented here and below are conducted with spin-locking durations τ (respectively XY8 block repetitions k) that were determined beforehand to maximize the SNR on clean diamond without immersion oil, following the procedure we have presented and discussed in sections 3.1.2 and 4.2. However, it turns out that in order to maximize the SNR in experiments with immersion oil, or even more importantly, to maximize the relative difference ΔSNR between the measurements with and without oil, a different choice of τ and k is ideal. We demonstrate this in the appendix A.7. Importantly though, we also show that for our experimental regime, the suboptimal choice of τ and k made here leads to only a negligible reduction in ΔSNR compared to the optimal case.

(Case 2) : A Three-Dimensional Layer of Protons

We now study the case where the unidentified surface proton layer is a three-dimensional layer with finite thickness. To that end, we fit the same NMR data as in Figure 5.4, but with different fitting functions. In particular, we now describe the magnetic field variance generated by the unidentified surface protons with σ_V^2 from equations (5.6) and (5.13), substituting $Z_1 = 0$ and $Z_2 = \Delta Z$, such that

$$\sigma_V^2 = \mathcal{N}_V \, \frac{(\hbar\gamma_{\mathrm{H}}\mu_0)^2}{\pi} \cdot \left(\frac{\rho_V}{d^3} - \frac{\rho_V}{(d+\Delta Z)^3} \right) , \tag{5.17}$$

where we have introduced ΔZ as the thickness of the unidentified ensemble. If there is immersion oil on top of the 3D proton layer, we use $\sigma_{V,\mathrm{oil}}^2 = \sigma_V^2 + \sigma_{\mathrm{oil}}^2$,

$$\sigma_{V,\mathrm{oil}}^2 = \mathcal{N}_V \, \frac{(\hbar\gamma_{\mathrm{H}}\mu_0)^2}{\pi} \cdot \left(\frac{\rho_V}{d^3} - \frac{\rho_V}{(d+\Delta Z)^3} + \frac{\rho_{\mathrm{oil}}}{(d+\Delta Z)^3} \right) , \tag{5.18}$$

where we assume the oil to fill the entire infinite space above the other ensemble, ($Z_1 = \Delta Z$ and $Z_2 \to \infty$). To fit the NMR data with these functions in an unambiguous fashion, we need to make an assumption on what the thickness ΔZ is. In the case of a surface-bound layer of molecules, ΔZ would only be a few angstroms and the two-dimensional approach presented above would very likely be better suited. For a thin adsorbate layer of water, any thickness between the size of a few water molecules to a few nanometers would make sense. This is because in order for water NMR to be feasible in the first place, molecular diffusion needs to be suppressed; and it has been shown that such suppression occurs in water that is confined to less than 2 nm [142, 143]. In addition, it has very recently been reported that there is a non-evaporating sub-nanometer thin layer of water on the diamond surface [147]. For these reasons, we are here investigating the range of $\Delta Z \in [0.1\,\mathrm{nm}, 4\,\mathrm{nm}]$.

By fixing ΔZ to a value within this range, we simultaneously fit ρ_V and d, and the result of this fitting procedure is plotted in Figure 5.5. In the XY8-k fits, we add the nuclear T_2^* time as a third fitting parameter. As above, we use the same T_2^* for both ensembles, which is a weak approximation that should be avoided in the future. We find that independent of the choice of ΔZ, up to numerical precision, the T_2^* time fitted this way is always the same, $T_2^* = (35.0 \pm 5.4)\,\mu\text{s}$. We therefore do not plot this nuclear T_2^* in Figure 5.5.

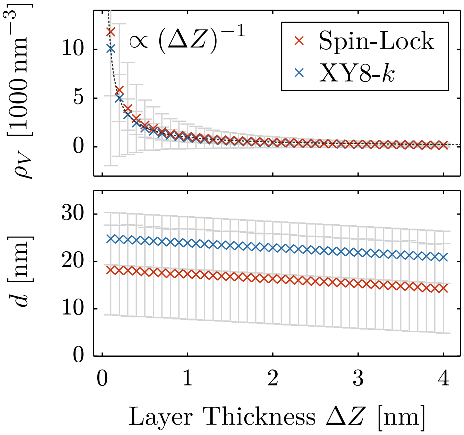

Figure 5.5: Fitting of the same two NMR spectra as in Figure 5.4, but here we instead treat the unidentified surface spins as a three-dimensional layer of thickness ΔZ and volume density ρ_V, and thus use equations (5.17) and (5.18) for the fitting routine. By fixing the value of ΔZ and subsequently fitting ρ_V and d to both NMR spectra simultaneously results in the plotted values. The data indicate that the unidentified proton layer's density scales $\propto (\Delta Z)^{-1}$, as indicated by the dashed black line. In the limit $\Delta Z \to 0$, we obtain the same depth d as in the 2D case.

The fitted NV depth d scales linearly with the layer thickness ΔZ. As expected, for values of $\Delta Z \ll d$ (e.g. $\Delta Z = 0.1\,\text{nm}$) both models return very similar values as when we treated the surface spins as a two-dimensional ensemble. This demonstrates very nicely that in the limit of $\Delta Z \to 0$, where the 3D layer becomes a 2D surface, the fitted depths are equal. Furthermore, similar to before, the two models do not yield the same depth, which we once more assign to their intrinsic weaknesses that affect the depth fit in different ways.

The spin density ρ_V resulting from our fits scales $\propto (\Delta Z)^{-1}$, as indicated by the dashed black line in Figure 5.5. This makes sense, because this scaling guarantees that the total amount of spins is preserved. The numerical value of ρ_V is nearly identical for both sequences. In the case of Spin-Lock, ρ_V is roughly $180\,\text{nm}^{-3}$ at $\Delta Z = 4\,\text{nm}$, slowly increases to about $1075\,\text{nm}^{-3}$ at $\Delta Z = 1\,\text{nm}$, and then rapidly diverges when approaching $\Delta Z \to 0$. All these results for ρ_V are significantly larger than the density of protons in oil, $\rho_{\text{oil}} = 50\,\text{nm}^{-3}$ [42, 50, 120]. The results also exceed the proton density of liquid water, $\rho_{\text{water}} = 67\,\text{nm}^{-3}$; a density we have estimated earlier in equation (3.9). In the case where we are indeed detecting an adsorbate layer of water molecules as we have speculated in chapter 3 and others have hypothesized before us [42, 46, 66–68], our fits suggest that this water is significantly more dense than ordinary liquid water. This is well in agreement with the picture that this water layer is in a solid-like state with entirely different molecular properties compared to liquid water [142, 143, 147]. However, for the same reasons as stated in the discussion of the ρ_A fits above, one should be careful with drawing conclusions from the fitted ρ_V value, because we are using models that are not fully applicable.

Finally, we attempt a different approach to the fitting of our data. Instead of fixing ΔZ and subsequently fitting ρ_V and d, we now fix ρ_V and fit ΔZ and d. Specifically, we set $\rho_V = 67\,\text{nm}^{-3}$ to the density of liquid water. In this case, we obtain $\Delta Z =$

$(6.7 \pm 6.5)\,\mathrm{nm}$ and $\Delta Z = (7.3 \pm 6.4)\,\mathrm{nm}$ from fitting the Spin-Lock and XY8-k data respectively. Abendroth et al. have conducted a similar study [46], where they too observe a proton signal on clean diamond, and also characterize it with single NV XY8-k NMR and Pham et al.'s model, both with and without immersion oil, and with $\mathcal{P}_\pi$ between 7 % and 18 %. They too speculate that these unidentified protons originate from an adsorbate water layer, and assuming a proton density of $\rho_V = 60\,\mathrm{nm}^{-3}$, they report that depending on the NV, the thickness of this water layer is 0.95 nm to 1.8 nm. The fact that they infer a much narrower layer than we do (using the same XY8-k fit function), is an indicator that the detected water layer varies from diamond to diamond, or even locally on the same diamond sample.

(Case 3) : A Combination of Both

Finally, we consider the case where there is a combination of (A) a two-dimensional layer of chemically bonded groups containing hydrogen and (V) a finite layer of water on the diamond surface. In the absence of immersion oil, we thus use the variance

$$\sigma_{AV}^2 = \frac{(\hbar\gamma_{\mathrm{H}}\mu_0)^2}{\pi} \cdot \left(\mathcal{N}_A \frac{\rho_A}{d^4} + \mathcal{N}_V \left[\frac{\rho_V}{d^3} - \frac{\rho_V}{(d+\Delta Z)^3} \right] \right) . \tag{5.19}$$

If immersion oil is applied to the diamond surface, we instead use

$$\sigma_{AV,\mathrm{oil}}^2 = \frac{(\hbar\gamma_{\mathrm{H}}\mu_0)^2}{\pi} \cdot \left(\mathcal{N}_A \frac{\rho_A}{d^4} + \mathcal{N}_V \left[\frac{\rho_V}{d^3} - \frac{\rho_V}{(d+\Delta Z)^3} + \frac{\rho_{\mathrm{oil}}}{(d+\Delta Z)^3} \right] \right) . \tag{5.20}$$

Given that we have obtained extremely high nuclear spin densities for the unidentified proton bath if only one of the possible ensembles types (A or V) is considered, it is conceivable that fitting with both ensemble types at the same time could lead to more reasonable results in terms of proton spin density. However, as we will show below, this is not the case.

If we stick to a layer thickness of $\Delta Z \in [0.1\,\mathrm{nm}, 4\,\mathrm{nm}]$ and fix the surface density ρ_A to the upper bound given by the available surface density of carbon bonds, i.e. to $32\,\mathrm{nm}^{-2}$, and subsequently fit the volume density ρ_V, we obtain values that are only 4 % to 10 % lower than the results plotted in Figure 5.5 where we considered only a three-dimensional proton layer (and the fitted depths are nearly identical). Alternatively, if ρ_V is fixed to $\rho_{\mathrm{water}} = 67\,\mathrm{nm}^{-3}$, we fit surface spin densities ρ_A that still exceed $1000\,\mathrm{nm}^{-2}$.

These results show that in order for the models to match to the data, there have to be a lot of proton spins in the NV detection volume. Consequently, independent of what kind of spatial extension one assumes for the unidentified proton source (A, V or AV), at least one of the involved spin densities (ρ_A and/or ρ_V) needs to be large compared to the density of available carbon dangling bonds or the density of hydrogen in water respectively. While it is impossible that ρ_A of an ensemble of chemically bonded groups exceeds the density of available carbon dangling bonds by a factor of 35, it could well be that the spin density of solid-like water layer is larger than ρ_{water}. In particular at $\Delta Z = 4\,\mathrm{nm}$, this relative difference is "only" a factor of 3. Note that neither of the the recent reports on adsorbate water layers on diamond [142, 147] make a statement on proton spin density, so it is unclear to us how realistic a spin density enhancement of 3 really is.

Based on our preliminary results presented in this section, we hypothesize that the proton signature we detect on tri-acid cleaned diamond originates mostly from a thin adsorbate layer of solid-like water, potentially with a small contribution from hydrogen-rich chemical groups that are part of the oxygen termination. This hypothesis needs to be validated once the models are corrected.

As a final remark, we point out that there could also be protons within the diamond lattice, a scenario that we have not investigated here. Specifically, such protons in the diamond lattice can in principle be very close to the NV center, leading to a strong nuclear magnetic signal that outweighs the contribution obtained by adding oil to the diamond surface – which is exactly what we have measured. The results from section 3.2.2 exclude a homogeneous distribution of protons throughout the entire diamond lattice, however, the scenario where protons have diffused into the diamond from the outside and therefore only exist near shallow NVs would be consistent with our data.

5.3.2 Density of the Deuterium Terminated Surface

We will now discuss the data shown in Figure 3.12, where we have measured how the proton NMR changes when we move from the usual oxygen surface termination to a deuterium terminated diamond surface, after the NV charge state has been restored with laser illumination. The analysis we have provided back in section 3.3 was based on the resonant and off-resonant $T_{1\rho}$ times under these two surfaces, and has lead us to conclude that the surface spin density of protons must be larger on the converted D-terminated surface.

Here, we will validate this hypothesis by fitting our theoretical model of Spin-Lock NMR to the data underlying Figure 3.12. To that end, we treat the surface spins as a three-dimensional ensemble, and then fit the Spin-Lock model to the data in the

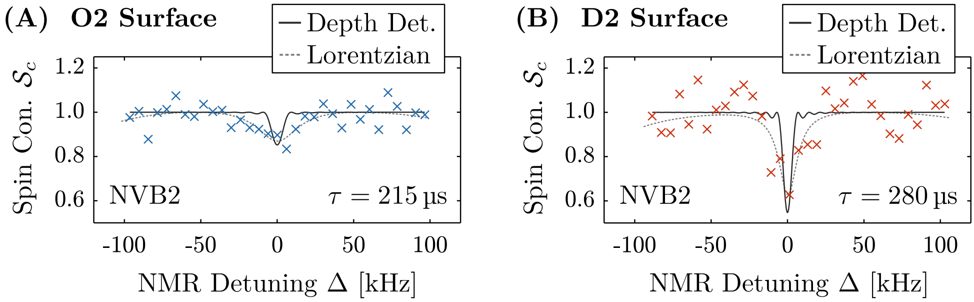

Figure 5.6: Fits of our Spin-Lock model to the from Figure 3.12, where we compared Spin-Lock proton NMR taken on O-terminated diamond to the Spin-Lock NMR measured after D-terminating the diamond and restoring the charge state with laser illumination. For these fits, we treat the surface protons as either a two- or three-dimensional ensemble. We first fit the depth d using the O-terminated surface data, and by fixing this depth, we then fit the D-terminated surface data. The resulting surface densities have a ratio of $(\rho_V^{\mathrm{D}_2}/\rho_V^{\mathrm{O}_2}) = (\rho_A^{\mathrm{D}_2}/\rho_A^{\mathrm{O}_2}) = 2.045$, indicating that the amount of surface proton spins is twice as high on the laser-treated D-terminated surface.

following way: First, we pick an arbitrary value for the proton density $\rho_V^{\mathrm{O}_2}$ of the O-terminated surface. Using this arbitrary value, we then fit the NMR spectrum taken on the O-terminated surface, and thereby infer the depth d. Afterwards, we keep this fitted value for d fixed, and determine $\rho_V^{\mathrm{D}_2}$ by fitting the NMR we have measured on the converted deuterium terminated surface.

While the fit values for d and $\rho_V^{\mathrm{D}_2}$ depend strongly on the initial choice of $\rho_V^{\mathrm{O}_2}$, the resulting NMR curve $\mathcal{S}_c$ predicted by the model is entirely independent of this initial choice. Moreover, we obtain the exact same $\mathcal{S}_c$ curve if we assume that the proton ensemble is two-dimensional. These curves are plotted together with the data and the Lorentzian lineshape fits in Figure 5.6.

Most importantly, not only the fitted curve, but also the ratio between the two resulting densities is independent of the initial density choice and spatial extension of the proton ensemble. Specifically, we find that $(\rho_V^{\mathrm{D}_2}/\rho_V^{\mathrm{O}_2}) = (\rho_A^{\mathrm{D}_2}/\rho_A^{\mathrm{O}_2}) = 2.045$. Therefore, our fits reveal that deuterium termination and subsequent laser-induced charge-state restoration roughly doubles the amount of surface protons. This increase in density agrees with what we discussed in section 3.3.

Once more, we heed a word of caution. The numeric result for the density ratio might be incorrect, due to the limitations of our Spin-Lock model. In particular, we are here comparing the fitting results of two Spin-Lock spectra that were recorded with different spin-locking times τ, such that we expect them to be subject to different errors. However, while the exact value of ratio $(\rho_V^{\mathrm{D}_2}/\rho_V^{\mathrm{O}_2})$ might therefore not be captured well by our analysis here, the model is clear in that there is some non-zero increase in proton density from $\rho_V^{\mathrm{O}_2}$ to $\rho_V^{\mathrm{D}_2}$.

5.4 Outlook

The immediate next step in continuing the studies of this chapter is to further develop the two NMR depth determination models. Specifically, the theoretical description we have derived for Spin-Lock NMR is currently neglecting decoherence in the spin bath, such that it predicts a Fourier limited NMR linewidth. This is not in agreement with our data and leads to a depth overestimation. For this reason, it is necessary to incorporate nuclear spin dephasing and molecular diffusion into the model. We propose to do this in a similar fashion as in Pham et al.'s description of XY8-k, where these processes are accounted for by introducing a phenomenological finite nuclear T_2^* dephasing time.

For the XY8-k model of Pham et al. [51], we have shown that the fitted depth d depends on the duration of the employed π-pulses. This demonstrates that the model's assumption of instantaneous π-pulses is invalid, and we therefore suggest to extend the model to account for non-zero pulse durations. This could for instance be done with a similar treatment as presented in [119], where NV spin rotations during the π-pulses are added to the spin evolution under XY8-k.

Once these changes have been made, we suggest to repeat the experiments of this chapter, and for the fits, one should use different T_2^* times for the nuclear spins of the oil and the unknown origin. We expect this approach, combined with improved NMR models, to yield more accurate results for the depth and spin density.

We now make a final statement on the surface ^{1}H spins that we have studied in chapters 3 and 5. We have observed the presence of these spins on two different diamonds samples, but only with NVs that have short $T_{1\rho}$ relaxation times (i.e. shallow NVs). Furthermore, these surface spins exhibits a bath-limited NMR linewidth of about 20 kHz to 40 kHz, that is independent of temperature between 20 °C and 70 °C. Based on these results, we have speculated in chapter 3 that we are either dealing with an ensemble of chemically bonded groups containing hydrogen, or a thin adsorbate layer of water in a solid-like phase.

In this chapter, we have seen that in either case, these spins appear to be very densely packed. Specifically, if we treat them as a two-dimensional ensemble, our fitting routine reveals a surface spin density that exceeds the density of available carbon dangling bonds by a factor of about 35, which seems highly unphysical. Alternatively, if we assume that the surface spins are located in a three-dimensional layer of less than 4 nm thickness, we fit a spin density that is larger than the proton density of liquid water by a factor of 3 to 100. Specifically for $\Delta Z > 3\,\mathrm{nm}$, where this factor is less than 4, the inferred volume spin densities could be realistic. While it is unclear how accurate these fits are until the theoretical models are reworked, these preliminary results indicate that an ensemble of surface-bound chemical groups alone is not matching our data, and that a dense layer of solid-like water of a few nanometer thickness is likely to be involved. Note that the molecular structure of such a nanometer thin contact layer of water – in particular its density and diffusion rate – are not yet very well quantified. Repeating our experiments with quantitatively accurate NMR models could contribute to the understanding of this exotic state of water.

Finally, we have investigated how the nuclear spin ensemble on the diamond surface changes when the sample is deuterium terminated and irradiated with a strong laser for NV charge-state restoration. We find that on this modified surface, the proton density is about twice as large compared to tri-acid cleaned surfaces, which further underlines that the unidentified proton source is indeed located at the diamond surface and affected by the chemical surface composition. For the case of a water contact layer, this result means that either the molecular structure or the thickness of this adsorbate layer is different on the two investigated surface terminations.

Finally, let us make a few closing comments on depth determination with NV NMR in general. Over the last few years, many people have done such depth determination of individual NV centers with XY8-k [59–69], and they have all used the model of Pham et al. [51]. However, we have shown in this chapter that this model returns incorrect depths if the sequence is played with π-pulses that make out more than $\mathcal{P}_\pi \approx 20\,\%$ of the total sequence duration. For this reason, we suspect that everyone who does not work with sufficiently fast π-pulses or at low enough magnetic fields, such that $\mathcal{P}_\pi$ approaches zero, is overestimating the NV depth.

Furthermore, the experiments presented in this thesis are undoubtedly demonstrating that there is an ubiquitous source of ^{1}H spins on tri-acid cleaned diamond under ambient conditions. In any depth determination based on proton NMR with immersion oil, these surface spins needs to be taken into account, or the resulting depth will definitively be incorrect; especially if these surface spins dominate the nuclear magnetic signal such as is the case in our experiments. Additionally, we have shown in chapter 4 that XY8-k depth determination comes with intrinsic issues such as harmonic contamination of the NMR spectrum and a limited spectral resolution, which further complicates a quantitatively accurate fit of the NV depth when measuring with C^{13}-rich diamond samples and magnetic fields exceeding 400 G. Altogether, the results of this thesis demonstrate that XY8-k depth determination is not as easy as many people in the NV community seem to believe.

We have shown experimentally in chapter 4, that Spin-Lock depth determination provides remedy to all of these issues intrinsic to XY8-k, and it even comes with increased NMR sensitivity. For these reasons, we propose that it is much better suited for NMR depth determination. However, the required theoretical description of Spin-Lock NMR that we have derived in this chapter still needs more refinement. Importantly, it is yet to be verified that the two depth determination approaches do actually yield the same result. Furthermore, it is so far entirely unclear to us how the accuracy of the resulting depth fit compares between these two models. These open questions will be interesting to explore once the weaknesses of the two NMR models have been addressed.

A crucial limitation to the robustness of our fitting routine is the small difference in contrast between NMR with and without applying immersion oil, which we observe on both NVs we have applied oil to (NVA2 and NVB1). So far, we have not yet found an NV where this difference is large, as for example Abendroth et al. have measured [46]. We have also not yet discovered an NV center in our diamonds, where there is no observable ^{1}H NMR after acid cleaning, but there is such a signal after applying oil, such as Mamin et al. have reported [47]. Instead, all the NVs we have investigated do either show both of these NMR signals (shallow NVs with $T_{1\rho}^{\text{off}} < 300\,\mu\text{s}$) or neither of them (deep NVs with $T_{1\rho}^{\text{off}} > 1500\,\mu\text{s}$). We suspect that in order to measure a larger difference in contrast between NMR experiments with and without oil, we would require an NV with intermediate depth, i.e. intermediate $T_{1\rho}$ between 300 µs and 1500 µs.

Finally, to extend the horizon of this outlook, we note that once this ubiquitous surface spin ensemble is well understood in terms of layer thickness and spin density, it will be possible to perform depth determination of shallow NV centers with only these protons, omitting the need for immersion oil. Not only would this simplify the experimental procedure in general, but it would be particularly interesting for applications that employ fragile diamond structures from which immersion oil cannot be removed that easily, such as for instance mounted diamond scanning tips for scanning NV magnetometry [27].

CHAPTER 6

Slow Beatings in XY8 Time Traces

In this last, very short chapter, we will present and discuss experimental XY8-k data that is not directly linked to NMR, but that shows unexpected and surprising behaviour. As an important disclaimer, we note that it is entirely unclear whether the observed behaviour is actually real physics, or whether we are dealing with an experimental artefact originating from broken hardware.

In particular, we observe a beating frequency of a few kHz in XY8-k time traces. With time traces, we mean measuring the PL resulting from XY8-k as a function of sequence duration, i.e. as a function of k with fixed π-pulse spacing. Usually, for such a measurement, we would expect to obtain an exponential decay, as shown in Figure 1.20 (C), where the exponential decay constant equals the coherence time T_2^{xy}. However, in the last few months that we spent working on NMR in the lab, we consistently observed a slow beating of a few kHz when taking such time traces. We show two examples of this in Figure 6.1, observed on NVA2 and NVA3 respectively, at a magnetic field near the ESLAC, and with a π-pulse spacing chosen such that the

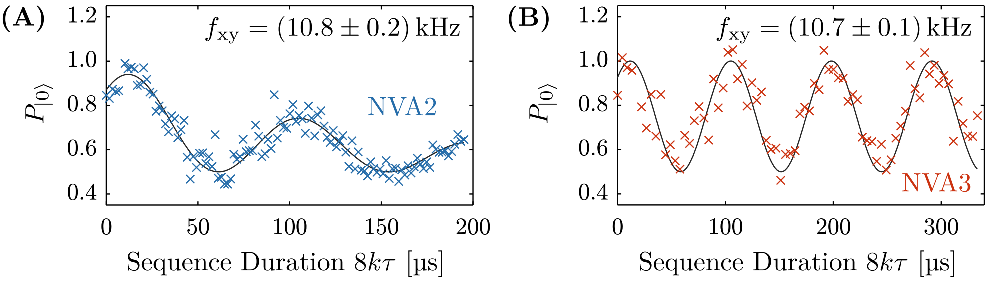

Figure 6.1: XY8-k time traces show a slow beating frequency of about 10.7 kHz modulated into the exponential T_2^{xy} spin decay curve. We observe this behavior both on **(A)** the shallow NVA2 at 513 G, and on **(B)** the much deeper NVA3 at 515 G. The oscillation persists for the entire spin coherence lifetime, that is these cases $T_2^{\mathrm{xy}} = (156 \pm 13)$ µs for NVA2, and more than 2 ms for NVA3. These data were taken on MW resonance, $\delta = 0$.

sequence is sensitive to $f_{\mathrm{NMR}} \approx 1.8\,\mathrm{MHz}$, far away from the proton NMR resonance. Both of these time traces show a slow beating of $f_{\mathrm{xy}} \approx 10.7\,\mathrm{kHz}$ modulated into the exponential decay envelope given by the respective NV's T_2^{xy} coherence time. Here, we obtain $T_2^{\mathrm{xy}} = (156 \pm 13)\,\mu\mathrm{s}$ for the shallow NVA2, such that there are only a few periods of the oscillation before the NV spin has fully dephased, and $T_2^{\mathrm{xy}} > 2\,\mathrm{ms}$ for the much deeper NVA3, allowing us to take many oscillation cycles. Taking Spin-Lock time traces under equivalent conditions results in a single exponential decay without any sign of such a kHz-frequency oscillation.

6.1 Dependency on Detuning and Magnetic Field

Interestingly, we find that the frequency f_{xy} of this oscillation depends very sensitively on the detuning δ of the applied MW drive. In particular, we observe a surprisingly asymmetric behaviour of f_{xy}, in that it is very different for positive and negative detunings. This asymmetry is shown in Figure 6.2, where we measure f_{xy} as a function of δ at 515 G, $f_{\mathrm{NMR}} \approx 1.8\,\mathrm{MHz}$ and a π-pulse duration of 192 ns. The data are taken on each of two separate NVs, NVA3 and NVA4, that both have long coherence times $T_2^{\mathrm{xy}} > 2\,\mathrm{ms}$, which allows us to measure many oscillation periods to minimize the error on the frequency fit. The experiment reveals that both NVs show the same asymmetric frequency pattern. There is a local maximum in f_{xy} at a negative detuning of $-485\,\mathrm{kHz}$ and $-610\,\mathrm{kHz}$ respectively. For even larger negative detuning, f_{xy} eventually diverges, while for a positive detuning of more than 300 kHz it is approaching zero. The fact that the result is so similar for two different NVs is an indicator that the beatings are not due to a NV specific local effect, such as coherent coupling to a single nearby crystal defect, strain or stress in the particular nanopillar, or dirt on its surface.

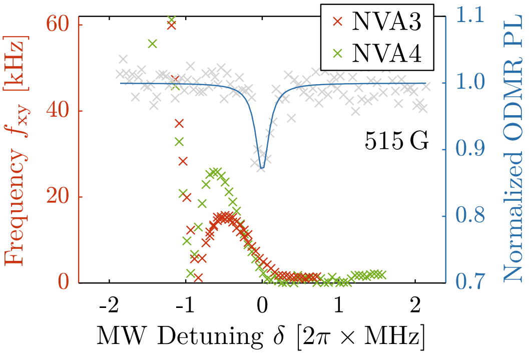

Figure 6.2: Frequency f_{xy} of the beating observed in XY8-k time traces, taken as a function of MW detuning on both NVA3 and NVA4. We find a surprisingly asymmetric behaviour that is very similar on both NVs. The blue line is a fit to a super-low power pulsed ODMR on NVA3. These data were taken at a magnetic field of 515 G, with a π-pulse of 192 ns and at $f_{\mathrm{NMR}} \approx 1.8\,\mathrm{MHz}$ that is far away from the proton NMR.

Figure 6.2 also shows a super-low power pulsed ODMR experiment with a width of only 206 kHz, that was taken on NVA3 at 515 G just prior to the f_{xy} measurements. In this ODMR spectrum, there is only a single hyperpolarized line, and no asymmetry or secondary dips, in particular not at the negative detuning where the beating frequency is large. Note that we obtain a similar ODMR on NVA4, however we do not plot it here. The ODMR data indicate that the investigated NVs are neither a doublet of two NVs, nor is there any strong coupling to P1-centers or nearby ^{13}C, since all these

things should show up in the pulsed ODMR experiments. We therefore exclude such coherent interaction with other nearby spins as the origin of the observed beating. This conclusion is supported by the fact that we are working an isotopically purified diamond which has a very low likelihood of ^{13}C nuclei near the NV center.
Since the XY8-k sequence tends to behave poorly when the π-pulses become too long, we investigated whether the beating frequency f_{xy} disappears when we use shorter π-pulse lengths. Interestingly though, the contrary is true, as shown in Figure 6.3. When we shorten the π-pulse length from 192 ns to either 152 ns or 112 ns, we find additional local maxima in f_{xy}, that become more pronounced the shorter the employed pulses.

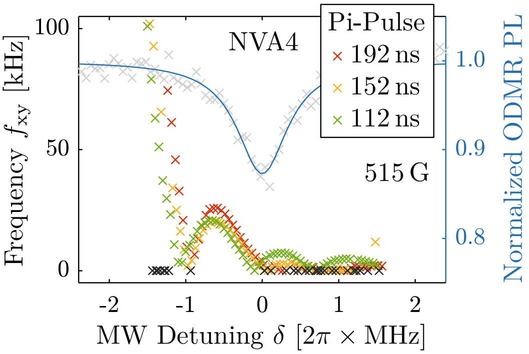

Figure 6.3: Investigation of how the XY8-k beating frequency pattern depends on the employed π-pulse duration. The data reveal that for shorter π-pulses, there are additional local maxima in f_{xy} which become more pronounced the faster the π-pulses become. In this case, we were measuring on NVA4 at a magnetic field of 515 G. The black data points represent time traces where no meaningful beating frequency could be identified.

Finally, in order to test to what extend the ESLAC is relevant in the observation of these beatings, we measure such XY8-k time traces for away from the ESLAC at 305 G. As plotted in Figure 6.4, this has a clear effect on f_{xy}. While there is still a local maxima in f_{xy} at negative detunings, it has been shifted away from the NV spin transition to $\delta = -2250$ kHz and reduced to a maximum of $f_{\mathrm{xy}} = 5.2$ kHz. For a large range around resonance, no beating was observable in the XY8-k time trace at all (indicated by black crosses). Note that for these measurements, we used π-pulses as fast as we could possible achieve, namely 56 ns.

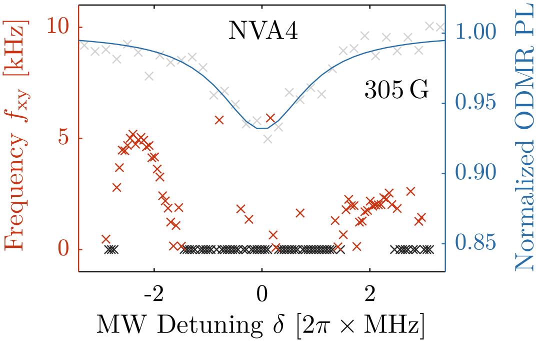

Figure 6.4: Measuring the beating frequency f_{xy} in XY8-k traces on NVA4 at a magnetic field of 305 G far away from the ESLAC, with very fast π-pulses of 56 ns, reveals that the f_{xy} frequency pattern changes a lot. The local maxima at negative detuning is shifted away from MW resonance, to $\delta = -2250$ kHz, and the maximal f_{xy} reduces to to 5.2 kHz. The black crosses represent measurements where no beating frequency could be identified.

6.2 Dependency on Experiment Hardware

Apart from the experiments described so far, we undertook many efforts to investigate whether the observed XY8-k beating could be an experimental artefact. Historically, starting from March 2024, we have consistently seen such beatings in XY8-k time traces, and in XY8-k NMR spectra we obtain wildly distorted backgrounds that we suspect to be related to these beatings. Before March 2024, however, we have never had such issues, instead we have always obtained smooth backgrounds in XY8-k NMR. Furthermore, we have not seen any beatings in the four time traces we have recorded before March 2024. Based on this, it is likely that something in our experimental setup broke in spring 2024 and is introducing the beatings we see.

For this reason, we have thoroughly checked and replaced every piece of hardware relevant to playing the XY8-k sequence: from the signal generators, amplifier and antenna, to every single co-axial cable and SMA interface. The only thing that had an immediate effect on the XY8-k oscillation was exchanging the circulator that we place after the amplifier to prevent harmful back-reflections from damaging the amplifier and SHFSG. Doing so has temporarily removed the beatings entirely, however, running XY8-k NMR for a few days with a new circulator has slowly been reintroducing the beatings. We speculate that there might be too much MW power in the circulator such that it is slowly breaking and thereby giving rise to the XY8-k beating we observe. We have ordered a new circulator with a higher MW power tolerance, but we have not yet been able to check whether the XY8-k beatings persist when using this new device.

6.3 Outlook

In summary, we have reported on a slow kHz-frequency beating in XY8-k time traces, whose frequency scales with the MW detuning in a highly reproducible and surprisingly asymmetric fashion. Moreover, the beating frequency appears to depend on both ESLAC proximity and π-pulse duration. Such asymmetric behaviour near the ESLAC could be indicative of interesting physics. The ESLAC itself is asymmetric with regard to where exactly the spin level anti-crossings occurs, which could perhaps explain the asymmetry we observe. However, we have also given arguments that the beatings might just as well be caused by damaged MW hardware – a hypothesis we have not yet been able to test any further.

We note that the harmonic features that we observed in the XY8-k NMR spectrum of NVB1 (see Figure 4.1) could perhaps be related to the oscillations that we described here. While this seems unlikely given that all harmonic features immediately disappeared when we switched to NVA2, it has also been NVA2 that has shown these oscillations very consistently half a year later. In addition, we point out that both the beating pattern and the XY8-k contaminations reduce in intensity when the applied magnetic field is decreased to fields far away from the ESLAC. This is an indicator that they might indeed be related. Both the NMR contaminations and the time trace beatings – as well as their potential relation to each other – need further investigation.

Appendix

A.1 Home-Built Measurement Setup

All experiments described in this work were conducted on a home-built confocal microscope setup. In this section, this setup is described in detail. In section A.1.1, the optical part of the setup is discussed. Then, in section A.1.2, we describe the special magnetic arrangement that allows for the precise control of an external magnetic field necessary to precisely align it with the NV symmetry axis. Afterwards, in section A.1.3, the microwave generation is described, where we explain how the Zurich Instruments SHFSG device is used to play arbitrary microwave pulse sequences and at the same time synchronize all involved experiment components.

A.1.1 The Optical Setup

Essentially, our home-built setup is a confocal microscope. We use a green laser with 515 nm wavelength (Cobolt 06-MLD) whose output we couple into an optical fiber (ThorLabs P3-460B-FC-2). This fiber guides the green laser light to the confocal optics, that are assembled on one large breadboard, as shown in Figure A.1. First, the laser is out-coupled from the fiber with an objective (Olympus LMPLFLN10x, $\mathrm{NA} = 0.5$) on a linear translation mount (ThorLabs SM1ZA). Afterwards, the collimated laser beam passes a bandpass filter (ThorLabs FL514.5-10) which ensures that only green light of (514.5 ± 10.0) nm is transmitted. Two subsequent mirrors (ThorLabs BB2-E02), mounted on kinematic retention mounts (ThorLabs Polaris-K1E) allow for precise laser beam alignment. Then, the laser reaches the dichroic mirror (Lasermux LM01-552-25), the center piece of the microscope that separates the green illumination from the red photoluminescence. Here, the green light is reflected and sent to the mirror on top of a piezo scanner (XYZ Piezo Flexure Stage P-517.3CD) that sends the light downwards to the main objective (Olympus LMPLFLN100x, $\mathrm{NA} = 0.8$) which focuses the collimated green beam onto the diamond sample. Since the objective is attached to the piezo scanner, it is possible to accurately move the laser focus across the diamond. The scanner's movement range is approximately 100 µm in X and Y, and 20 µm in Z.

The red light emitted by the NV defect in the diamond is collected by the same objective that focuses the green onto the diamond, and therefore the collected PL moves along the same optical path as the green, but in opposite direction. At the

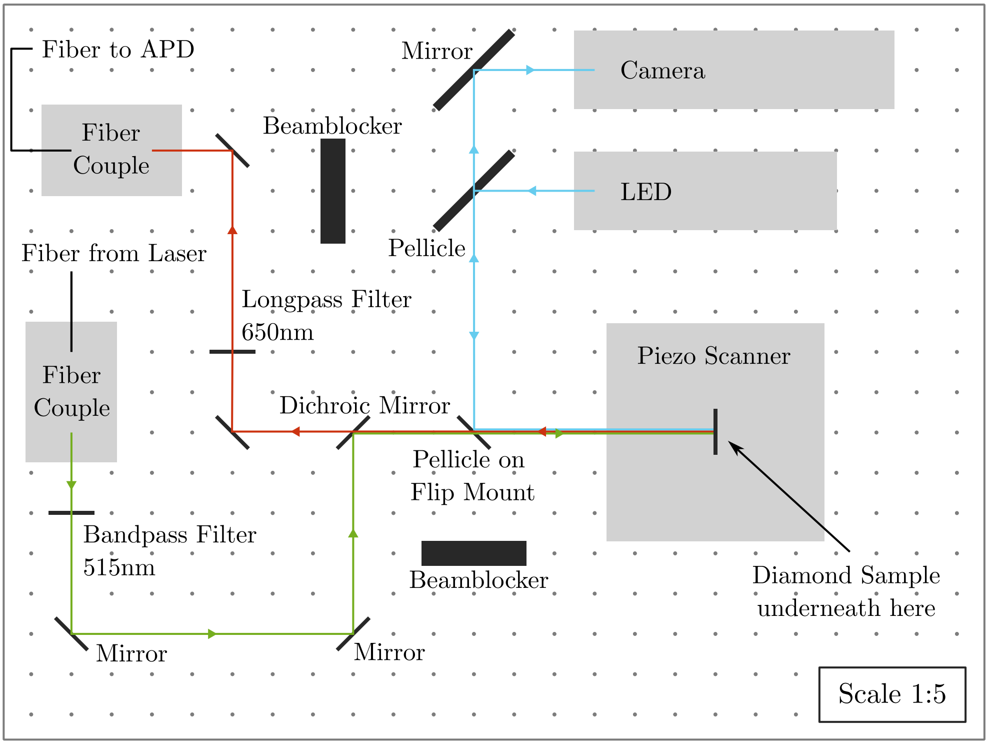
Fiber to APD
Fiber Couple
Beamblocker
Mirror
Camera
LED
Pellicle
Fiber from Laser
Longpass Filter 650nm
Fiber Couple
Piezo Scanner
Dichroic Mirror
Pellicle on Flip Mount
Bandpass Filter 515nm
Beamblocker
Diamond Sample underneath here
Mirror
Mirror
Scale 1:5

Figure A.1: True to scale schematic of the breadboard where all the optics of our home-built confocal microscope are assembled. Green laser light is focused onto the diamond underneath the piezo scanner. The emitted red PL is collected and separated from the green laser light by a dichroic mirror. A LED lamp provides back focal plane illumination, such that a simple camera can image the diamond surface.

dichroic mirror, the red light is transmitted and thereby separated from the green laser light. Similar to the green path, the red path has two mirrors (ThorLabs BB2-E02) on kinetic mounts (ThorLabs Polaris-K1E) for beam alignment. In addition, there is an optical longpass filer (ThorLabs FELH0650) with a cut-off wavelength of 650 nm, which removes the NV^- phonon sideband. Then, the red light is coupled into a telecom wavelength fiber (ThorLabs SMF-28-J9 Custom), which delivers the red PL to an avalanche photon detector (APD, Excelitas SPCM-CD) that counts the amount of red photons.

The setup also hosts back focal plane illumination with blue-green light of 490 nm provided by a LED lamp (ThorLabs M490L4). This light is sent from the LED to the diamond via two pellicles, a large 2-inch one directly at the LED output (ThorLabs BP245B1), and a small 1-inch one (ThorLabs BP109) mounted on a motorized flip mount (ThorLabs MFF101). With this flip mount, the LED path can be entirely removed from the green-red path. To view the laser spot on the diamond or the illuminated back focal plane, there is a camera (Watec WAT-120N+) in the LED path, that collects a fraction of all light returning from the diamond.

A.1.2 Goniometric Magnet Stage

The breadboard described in the previous section is fixed on several dynamically damped posts (ThorLabs DP12A/M) for vibration isolation, leaving space underneath for the diamond and the magnetic arrangement. This arrangement is depicted in Figure A.2. The diamond is mounted flat on a manual XYZ stage (Newport M-562-XYZ). For the (001)-oriented diamond crystals we typically work with, this means that one of the four possible NV directions, (111), $(1\bar{1}\bar{1})$, $(\bar{1}1\bar{1})$, or $(\bar{1}\bar{1}1)$, is lying in the X-Z-plane, tilted by 54° with respect to Z. Therefore, in order to produce a static magnetic field that is aligned with this particular NV orientation, a permanent neodymium disk magnet (supermagnete.ch GTN-32) is positioned such that its rotation symmetry axis lies in the X-Z-plane at 54°, pointing at the laser focal spot, as shown in Figure A.2. This is achieved with a manual XY stage (ThorLabs PT1/M) and a custom made aluminium wedge with a top surface at 54°.

In addition, this permanent magnet is mounted on a goniometric stage (SmarAct SGO-60.5r2dl-7 and SGO-77.5r2dl-1) that can rotate the magnet in two orthogonal directions with ±5° angular range each. This allows for fine tuning the alignment of the static magnetic field and the NV axis with sub millidegree accuracy. Finally, there is a linear motor (ThorLabs ZFS25B) that controls the axial distance between the magnet and the diamond sample. This enables control over the magnetic field strength in an automated fashion. Note that the goniometer's center of rotation is

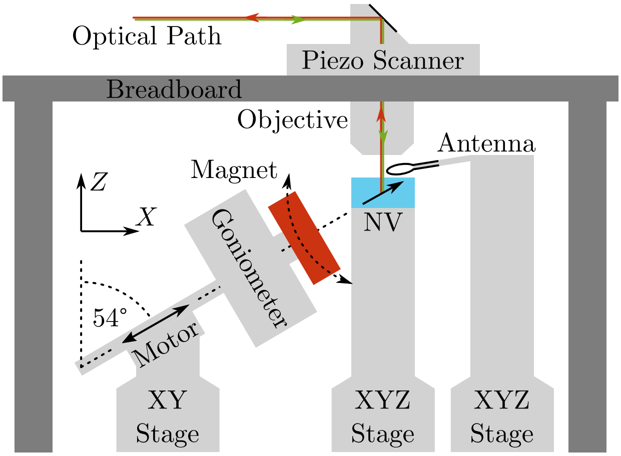

Figure A.2: Visualization of the magnetic arrangement. A permanent neodymium disk magnet (red) is mounted on a goniometric stage at an angle of about 54°, such that it is roughly aligned with the NV axis of a (001) diamond crystal (blue). The goniometer's two angular degrees of freedom then allow for rotation of the magnet about the NV position with sub millidegree precision, such that the magnet's field vector can carefully be aligned with the NV axis with high precision. The optics are assembled on a breadboard above this magnetic setup, and an objective focusses the laser onto the diamond. A piezo scanner moves this laser spot. Microwave delivery is realized by a gold wire loop antenna positioned in close proximity to the NV.

only the diamond, if the distance from the magnet to diamond is chosen such that the magnetic field at the diamond's position is roughly 500 G.
Apart from the optics and the magnetic setup, the experiment requires a third crucial component: A microwave (MW) field for coherent spin control. This MW is delivered to the NV with a home-made gold wire loop antenna, which is brought into close proximity to the NV with a manual XYZ stage (Newport M-462-XYZ-M). This is depicted in Figure A.2.

A.1.3 Sequence Generation with the SHFSG

The AC signal sent through this antenna is generated by a Zurich Instruments SHFSG. This SHFSG has four main channels, and each of them is equipped with its own local oscillator and an arbitrary waveform generator (AWG) core. This means that each channel can play a microwave tone with an arbitrary waveform envelope in its microwave output port. We use these waveforms to effectively pulse the microwave output. In particular, we play Gaussian ramps with constant amplitude in between these ramps. The duration of this flat part between the ramps is what we sweep in Rabi-type experiments. Conveniently, the SHFSG provides full control over the phase of the output, which allows us to implement the necessary phase shifts between pulses for Spin-Lock and XY8-k experiments. Note that the SHFSG can output any frequency between DC and 8.5 GHz with up to 0 dBm power, and it has a timing resolution on the AWG core of 0.5 ns.
The microwave path of our experimental setup, shown in blue in Figure A.3, starts at the first SHFSG channel (ch.01) that plays the microwave signal we need for coherent driving of the NV spin, in either a continuous wave (CW) fashion, or with pulses as described above. Low-loss coaxial SMA cables then carry the signal to an amplifier (Mini-Circuits ZHL-15W-422-S+) that has an approximate gain of 46 dB, up to a saturation power of 41 dBm (=15 W). Then, the amplified signal is sent through a circulator (Fairview Mircowave SFC2040A). The sole purpose of the circulator is to gate any back reflection coming from its output to an attenuator (MiniCircuits BW-S30W20+) and subsequent terminator (ThorLabs FT500). This ensures that these back reflections do not arrive in the amplifier which could potentially damage the SHFSG or the amplifier itself. Finally, the signal is sent through the gold wire loop antenna, which is basically nothing but a thin gold wire short-cutting the conductance and ground of the coaxial cable. There is a DC Block (MiniCircuits BLK-18-S+) in front of the antenna to cut off large DC signals that cause unnecessary heating in the antenna's thin gold wire.

The SHFSG can not only play microwave signals, but it can also provide digital trigger pulses with 0.5 ns timing precision. Each channel has such a digital marker output port, and an additional trigger input port to listen to such triggers. These digital marker pulses are used to trigger, pulse and synchronize all the components necessary to run the experiment. In the following, we discuss in detail how this is done.
The second SHFSG channel, ch.02, sends triggers to the DAQ card to count the ticks from the APD. These triggers are required to bin the counted ticks such that they can be assigned to the correct experiment repetition. The third SHFSG channel, ch.03, pulses the laser (green in Figure A.3), to control precisely when the NV is

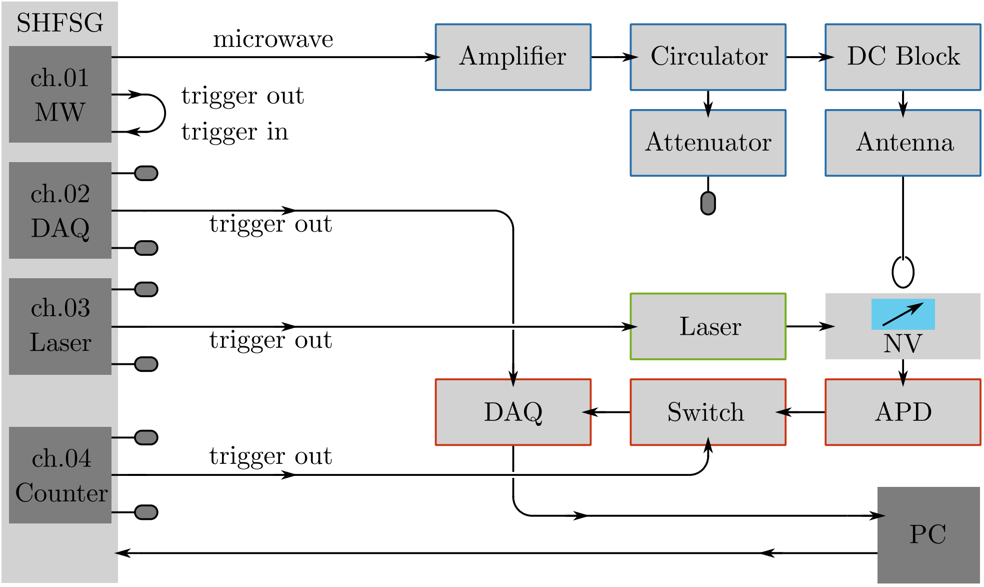

Figure A.3: The SHFSG serves as microwave source, AWG and pulse synchronization clock. The first channel plays the microwave signal, that is fed into the microwave generation part of the setup (blue frames). Channels 2 and 4 pulse the DAQ card and the APD counter switch, providing the means for PL collection (red frames), and channel 3 pulses the laser (green frame). By triggering channel 1 with its own trigger output, all channels can be synchronized.

illuminated with green light. Our laser can be pulsed directly with such a digital trigger; we do not need an acousto-optic modulator (AOM) for this. Finally, ch.04 controls the counter window. This is necessary because the APD is counting the red PL all the time, however, in a pulsed experiment we only want to collect the PL in a well defined readout window. This is realized by gating the APD counts with a switch (MiniCircuits ZASWA-2-50DR+) before sending them to the DAQ card. The SHFSG ch.04 opens and closes this switch.

In order to synchronize the microwave signal of ch.01 with the digital trigger pulses of ch.02-04 we use the trigger output of ch.01, as shown in Figure A.3, where a global trigger pulse is played and sent straight back into the trigger input of ch.01. All other channels are listening to this trigger input, and act simultaneously upon detecting a falling edge, see Figure A.4 (A). In addition, to synchronize the post-sequence pulses (in particular laser and counter), each channel is playing the entire sequence (i.e. the waveform envelopes) in its signal output, yet only ch.01 has the output enabled (i.e. a MW modulated into these waveforms), see Figure A.4 (A). This way, all channels are dynamically synchronized, but only ch.01 is outputting a non-zero MW signal. The nice benefit of this is that in principle, one could just turn on the MW output of ch.02 (i.e. modulate a signal into the played waveform) with a different frequency than ch.01 and very easily implement double frequency pulses to do double resonance experiments.

(A) Sequence as programmed on the computer

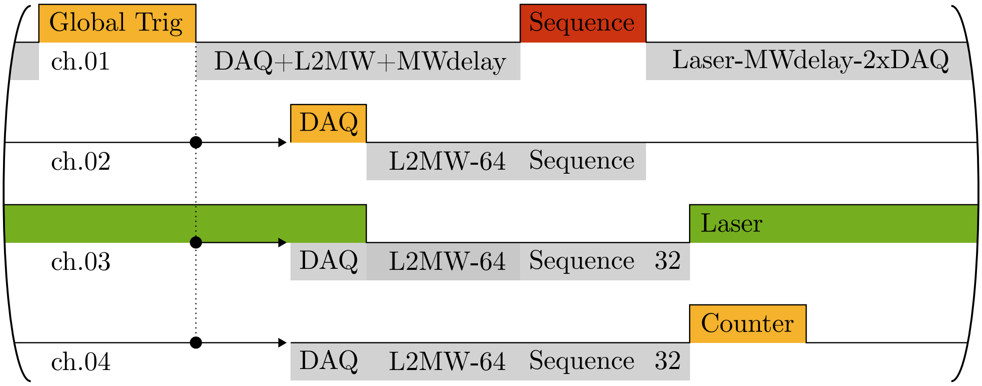
Global Trig
Sequence
ch.01
DAQ+L2MW+MWdelay
Laser-MWdelay-2xDAQ
DAQ
ch.02
L2MW-64
Sequence
Laser
ch.03
DAQ
L2MW-64
Sequence
32
Counter
ch.04
DAQ
L2MW-64
Sequence
32

(B) Sequence as played by SHFSG

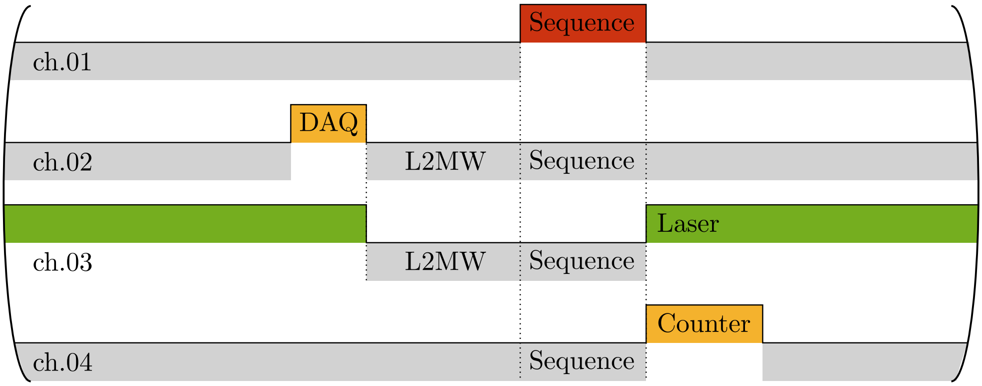
Sequence
ch.01
DAQ
ch.02
L2MW
Sequence
Laser
ch.03
L2MW
Sequence
Counter
ch.04
Sequence

Figure A.4: Synchronization of the experiment components. The first SHFSG channel (ch.01) plays a global trigger to itself, while the other three channels (ch.02-04) listen to that trigger. To account for delays of the device, such as non-zero reaction times to triggers (black arrows) or slow response to opening microwave channels (MWdelay), there are multiple timing corrections in the sequence (indicated by "+32" and "−64" which are corrections in nanoseconds). Panel **(A)** shows how the experiment is programmed in LabOne on the computer, and **(B)** shows the resulting output of the SHFSG as one could measure with an oscilloscope. Numbers are given in nanoseconds.

Unfortunately, there are various different delays happening in the device. For instance, the device has non-zero reaction times when answering to triggers or playing microwave pulses. To account for these, multiple timing corrections are added to the sequence. Figure A.4 (A) shows the experiment framework as implemented on the computer in the SHFSG's LabOne code, while Figure A.4 (B) depicts what the device actually plays, e.g. what one would observe with an oscilloscope if they were to measure the different outputs. Here "MWdelay" denotes just this delay. Furthermore, and "L2MW" is the laser to microwave delay that is played to allow the NV spin population to relax into $|0\rangle$ after optical pumping. In Figure A.4, delay are depicted in grey, and non-zero outputs are highlighted in color.

Note that there are more timing delays introduced by the hardware. For example, microwave components, or different coaxial cable lengths, or even the laser itself, etc, all introduce nanosecond delays. However, we did not look into these. The crucial timings for our experiments are on one hand the length and position of the π-pulses within a given sequence (which is ensured by the LabOne code), and on the other hand a clean interface between the end of the pulse sequence's last pulse and the beginning of the laser and counter, which we optimized by maximizing ODMR contrast via the timings shown in Figure A.4 (A).

A.2 Diamond Samples

In this thesis, we have worked with various different NVs hosted in three different diamond samples. For simplicity, we call these three diamond samples diamond A, B and C, while in our research group's internal nomenclature, their names are 60010, 00010F and 60012. In the following, we describe these three diamond samples, how their NV defects were created and what nanostructures have been fabricated on them.

Diamond A

The majority of our experimental results were obtained on what we call diamond sample A (respectively 60010 in our group's internal nomenclature). It is an "electronic grade" single-crystal diamond sample from Element Six, with a (001) oriented crystal surface, and one edge along the (110) direction. On this diamond substrate, an approximately 80 µm thick layer of ultra-pure ^{12}C-enriched diamond has been grown. This means that there is less than 10 ppm of ^{13}C isotopes in the diamond lattice of this layer. That is a negligible amount for our experiments; and we therefore call this diamond layer "isotopically purified".

The top 50 µm of the isotopically purified layer have been sliced off, and both sides of the resulting 50 µm thin diamond have been polished by Almax. This polish reduces the surface roughness to a point where surface light scattering is small enough such that it is possible to focus a Gaussian laser beam through the surface.

We then creature NVs via ^{15}N ion implantation and annealing, and subsequently fabricate parabolic nanopillars. We describe this process in detail in section A.2.1. Importantly, due to implantation of ^{15}N and a small natural abundance of ^{14}N in this diamond, we obtain NVs formed by either nitrogen isotope. The ^{15}N defects are always shallow, meanwhile the ^{14}N defects can be located anywhere in the sample.

Diamond B

The diamond we call diamond B (respectively 00010F in our group's internal nomenclature) is another "electronic grade" diamond from Element Six. It too has a (001) oriented crystal surface, and one edge along the (110) direction. However, opposite to diamond A, no further diamond growth was performed on this diamond. Instead, it was straight away sliced and polished by Almax down to a thickness of about 60 µm.

Afterwards, NVs and nanopillars were created in the same fashion as on diamond A, see section A.2.1.
The two key differences compared to diamond A is that diamond B was implanted with ^{14}N ions, such that its NV centers are exclusively formed by ^{14}N. In addition, diamond B is not ^{12}C enriched, which means that there is plenty of ^{13}C present its lattice, resulting in shorter T_2^* coherence times of the NV electron spins.

Diamond C

Diamond C (respectively 60012) has been grown on a CVD diamond substrate along the (113) crystal orientation. This special growth direction, combined with using a ^{12}C and ^{15}N enriched gas mixture for growth, facilitates nitrogen incorporation and allows for the creation of NVs that are preferentially oriented along the NV-axis lying closest to the growth plane, such that approximately 73% of the NVs in the grown crystal point in the same direction [171]. Created with this growth technique, diamond C is a 15 µm thick (113) diamond layer with an estimated NV density of $\sim$ 300 ppb and a P1-center density of $\sim$0.1 ppm [172]. Opposite to diamond A and B, no further nanofabrication was performed on this diamond. This diamond serves as a sample for ensemble measurements. In particular, we have used it to demonstrate that the all-optical sensing scheme we present in chapter 2 works on an entire NV ensemble.

A.2.1 NV Creation and Nanopillar Fabrication

Let us now discuss the NV creation and nanostructures fabrication performed on diamonds A and B. The NVs were created by ion implantation and subsequent sample annealing [173]. For implantation, as depicted in Figure A.5 (A), high-energy ions are shot at the diamond. Specifically, we employ singly charged nitrogen ions, either ^{14}N or ^{15}N, with a flux of 10^{11} cm^{-2} and at a 7° angle with respect to the dia-

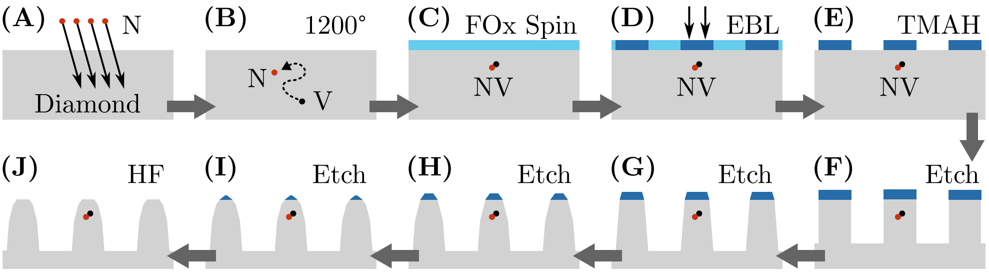

Figure A.5: Visualization of the nanopillar fabrication process of diamond A and B. First, **(A)** Nitrogen ion implantation creates substitutional nitrogen atoms and plenty of crystal vacancies, and **(B)** subsequent annealing forms stable NV centers. For pillar fabrication, **(C)** a FOx masks is spun, and **(D)** written with an electron beam. Finally, **(E)** the mask is developed in TMAH to remove the unwritten parts. Afterwards, **(F)-(I)** the diamond is etched in a plasma of O_2 and CF_4. By stepwise increasing the CF_4 concentration, the resulting nanopillar is etched into a parabolic shape. In the end, **(J)** the mask is entirely removed with HF.

	Diamond A	**Diamond B**
Nitrogen Ion Species	^{15}N	^{14}N
Ion Energy [keV]	6	12
Dose [ions/cm^2]	10^{11}	10^{11}
Incident Angle [°]	7	7
Company	CuttingEdge	Innovion
Nominal Implantation Depth [nm]	9	18

Table A.1: List of nitrogen ion implantation parameters for diamond A and B.

mond surface. The ion energy is different for the diamonds, as shown in table A.1, resulting in different implantation depths. In particular, stopping range of ions in matter (SRIM) simulations [168] predict a nominal implantation depth of about 9 nm for diamond A [174], and about twice of that for diamond B. However, since SRIM does not consider certain effects such as crystal channelling of ions, it systematically underestimates the predicted implantation depths [51, 169].

Bombarding the sample with such high energy nitrogen ions does not only implant these ions into the diamond lattice, but each single ion also creates a trace of vacancies in the lattice. These vacancies need to be coupled with one of the implanted nitrogen ions to form a NV center. This is why after implantation, the diamond is annealed; that means it is baked in a home-built vacuum oven at high temperature. At temperatures above 600°C the vacancies start moving in the carbon lattice [175], until they are adjacent to a substitutional nitrogen ion, where they bind together to form a stable NV center, as depicted in Figure A.5 (B). We employed the recipe from [173], where the temperature is increased stepwise with 1 h ramps up to a maximum temperature of 1200 °C, see table A.2. Note that today, we know that this temperature is slightly too high and can lead to significant surface graphitization, reducing the resulting depth of the NVs, or even worse, remove the entire layer of implanted nitrogen [141, 175]. This is why today, the maximal temperature we anneal at is 1100 °C. In addition, we have learned that doing much longer ramps of 6 h between temperature steps reduces the pressure in the chamber which helps with further minimizing diamond surface graphitization [141].

To increase PL collection efficiency, parabolic diamond pillars were fabricated on the diamond surface subsequent to NV creation [176], in a way such that there is a high chance of finding a single NV in the apex of the pillar. The main reason why such

Duration [min]	60	240	60	480	60	120	120
Start [°C]	20	400	400	800	800	1200	1200
End [°C]	400	400	800	800	1200	1200	20

Table A.2: Annealing parameters for the process done with diamond A and B.

Baking	5 min at 120 °C
Spin FOx	5 µL with 6000 RPM for 60 s
Baking	5 min at 120 °C
Spin Electra	6 µL with 2500 RPM for 60 s
Baking	5 min at 120 °C

Table A.3: List of FOx spinning parameters for diamond A and B.

parabolic nanopillars are desirable is that they have wave-guiding properties. Simply put, these pillars' geometry acts like a parabolic mirror in that it focuses light modes inside the pillar onto the NV in its apex due to total internal reflection. This means that focussing the laser through the diamond onto the base of the pillar leads to not only an enhanced laser focus onto the NV in the pillar tip, it also helps collecting the isotropically emitted red photons and channels them in a single direction: Back to where the laser came from. For our experiment architecture (see Figure A.1.2), this means that such nanostructures increase the obtained PL signal by a factor of 10 to 50, and at the same time they drastically reduce the necessary laser power to saturate the NV, from up to a few milliwatts to a only about 50 µW. Apart from these wave-guiding properties, these nanopillars have a second crucial advantage compared to working with NVs in bulk diamond: The pillar architecture allow us to reliably find the exact same NV within a diamond. While for bulk samples it is near impossible to discern between single NVs, it is simple to create nanopillars in a systematic and labelled fashion so they can be individually identified.

These parabolic nanopillars are created by electron-beam lithography, following the recipe from [176]. For this, we first spin a DuPont FOx-16 mask layer onto the diamond surface, Figure A.5 (C), followed by a thin layer of Allresist Electra that is electrically conductive and helps with discharging the sample during the exposure to the electron beam. The parameters for spinning are shown in table A.3.

After FOx spinning, the diamond sample is mounted in an electron beam lithography system, where an electron beam of 30 keV and 4 mC/cm^2 is used to write the pillar field structures into the mask. This is shown in Figure A.5 (D). Importantly, we write each pillar with two concentric circular areas of different radii to obtain an trapezoidal mask cross-section. Afterwards, the mask is developed in TMAH for 30 s, which removes all the unwritten parts, see Figure A.5 (E). Then, in an inductively coupled plasma reactive ion etching (ICP-RIE) system, the diamond is etched with a plasma of O_2 and CF_4 gas, removing diamond in all parts not covered by the mask. This way, the pillars are formed as shown in Figure A.5 (F). While the mask is very resistant against a pure oxygen plasma, it is attacked more the higher the CF_4 concentration in the plasma. Therefore, to shape them into the desired parabolic shape, multiple etch steps of increasing CF_4 concentration are performed, as depicted in Figure A.5 (G-I). An exact list of parameters for each of these etching steps in shown in table A.4 and A.5 respectively. Finally, once the desired pillar shape is achieved, the remainder of the mask is removed from the pillar tips with HF acid, see Figure A.5 (J).

An optical microscope image of the finished result is shown in Figure A.6 (A). Note that apart from the pillar themselves, we have also written wall-like features to help differentiating between pillar fields. Each of these fields has 90 pillars and a label to facilitate the identification. In order to not etch the entire diamond but only the relevant area, we have used a quartz mask to protect a large part of the diamond. This has lead to the etch marks around the written pillar fields. Furthermore, in Figure A.6 (B, C), there are scanning electron microscope (SRM) images that show an example of how a single finished pillar looks. In this particular images, the mask is still on top of the pillar.

If the unetched top surface's radius of the pillar is matched to the average distance between NVs in the diamond before fabrication, one can achieve single NVs in a large portion of the pillars. However, in the case of diamond A, the NV density after annealing was very low, and we would have needed to create giant pillars with a diameter of more than 1 µm in order to achieve a single NV probability of $> 50\%$. Unfortunately,

Repetitions	Duration	CF_4 [sccm]	O_2 [sccm]	Power [W]	Pressure [Pa]
10x	4 s	2	50	500, 50	0.5
10x	120 s	0	50	500, 110	0.5
8x	3 s	2	50	500, 50	0.5
8x	120 s	0	50	500, 110	0.5
15x	60 s	2	50	500, 50	0.5
2x	50 s	3	50	500, 50	0.5
1x	37 s	6	50	500, 50	0.5
1x	13 s	10	50	500, 50	0.5
1x	10 s	12	50	500, 50	0.5

Table A.4: List of parameters for the etch steps on diamonds A.

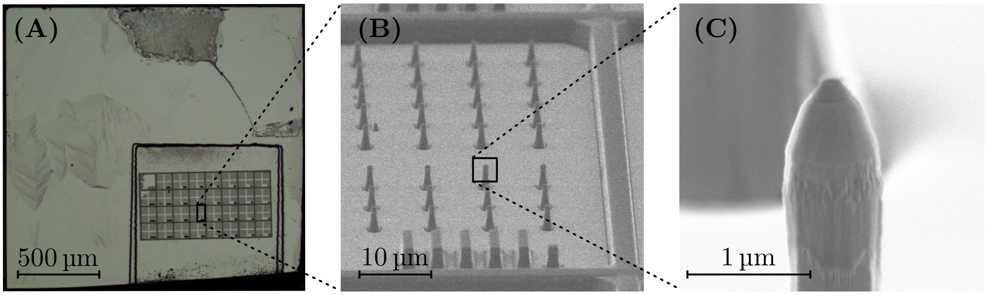

Figure A.6: Microscope images of the fabricated nanostructures on diamond A. **(A)** Optical microscope image of the entire diamond sample, showing the pillarfield structure in the botton right. **(B)** Scanning electron microscope image of a few pillars. The bottom right features are labels used to identify each pillar field. **(C)** Zoom onto one pillar tip demonstrating the parabolic shape, where the FOx mask is still on top.

Repetitions	Duration	CF_4 [sccm]	O_2 [sccm]	Power [W]	Pressure [Pa]
10x	4 s	2	50	500, 50	0.5
10x	120 s	0	50	500, 110	0.5
15x	60 s	2	50	500, 50	0.5
2x	45 s	3	50	500, 50	0.5
1x	30 s	6	50	500, 50	0.5
1x	22 s	8	50	500, 50	0.5

Table A.5: List of exact parameters for the etch steps on diamond B.

pillars this large are expected to have very poor wave-guiding properties. This is why we instead opted for a top diameter of around 400 nm which has previously been proven to have excellent optical qualities, and in turn deal with only about one to five NVs per 100 pillars. In the end, the pillars on diamond A turned out to have an average top diameter 375 nm diameter, and a pillar height of about 6.5 µm.
Surprisingly though, none of the approximately 500 pillars we have checked contained any NVs. We suspect that this is due to either a faulty etch – other people who etched within the same months have observed the same disappearance of NVs – or possibly too high temperatures in the annealing process, or even the combination of both. After thoroughly cleaning the etching machine, and trying again with fresh FOx material, we have successfully etched pillars onto diamond B (see below), and observed an NV per pillar ratio as expected based on the pre-fabrication NV density. In particular, the same annealing recipe was used for diamond B (see table A.2).
In order to create new NVs in the finished pillars of diamond A, using the existing

	Isotope	PL (kcps)	$T_{1\rho}^{\mathrm{off}}$ (µs)	T_2^* (µs)	Comment
NVA1	^{15}N	540	28 - 47	7.4	Has become NV^0
NVA2	^{15}N	390	8 - 1190	11.3	Fast $T_{1\rho}$ degradation
NVA3	^{14}N	150	2000 - 2500	35.5	Too deep for NMR
NVA4	^{14}N	110	2200 - 5000	70.0	Too deep for NMR
NVB1	^{14}N	620	188	2.0	
NVB2	^{14}N	400	414 - 459	-	D_2 Termination

Table A.6: List of NVs. Name nomenclature is "NV[host diamond][NV number]". The respective PL number given in the table is an approximate mean value for the expected PL at 50 µW green laser power. The shown $T_{1\rho}$ decoherence times are values from measurements under default conditions, e.g. with a clean diamond surface and a spin-locking frequency of 1.8 to 3.0 MHz. For NVs that have shown differences in separate $T_{1\rho}$ measurements, we list the smallest and largest value ever measured.

vacancies and implanted ^{15}N ions, the diamond was annealed for a second time after fabrication, once more utilizing the same recipe (see table A.2). This second anneal worked well, giving rise to roughly 1 NV per 50 pillars. Ultimately, we found four good NVs in this diamond. The key properties of these four NV centers, denoted NVA1 to NVA4, are shown in table A.6. The results of chapter 2 were obtained on NVA1. NMR experiments were taken on all of these NVs. Particularly, the two ^{14}N-NVs, NVA3 and NVA4, were used to investigate the XY8-k oscillations described in chapter 6.
On diamond B, the fabrication went smoothly without this issue of vanishing NVs post etch. Here, the resulting pillars are 5.4 µm tall, with a top diameter of approximately 300 nm. While there are many pillars with single NVs in this diamond, we have mainly worked with two of them, NVB1 and NVB2. Their key properties are shown in table A.6.

A.3 Spin-Lock NMR Depth Determination

Here, we derive the mathematical framework to describe the proton dip in a Spin-Lock NMR spectrum in a quantitatively accurate manner, such that the depth d of an employed single NV can be fitted. This theoretical work was done by collaborators of ours: Aaron Daniel and Patrick Potts. The credit for this derivation goes to them.

A.3.1 Hamiltonian Description in the Lab Frame

The situation is the following: We consider a single NV located in a diamond at a depth d, and an ensemble of spin-1/2 nuclei on the diamond surface – in this case specifically ^{1}H hydrogen nuclei, i.e. proton spins. In addition, a static magnetic field is applied along the NV symmetry axis, such that by virtue of the Zeeman interaction, all electronic spin state degeneracies are lifted. This allows us to operate on the two lowest energy states, an effective two level system spanned by $|0\rangle$ and $|-1\rangle$. Finally, we use microwave radiation to drive the spin transition between $|0\rangle$ and $|-1\rangle$, in particular to play a Spin-Lock sequence (see section 1.5.5). In the laboratory frame, the Hamiltonian for this system is

$$\hat{\mathcal{H}} = \hbar\omega_0\hat{\sigma}_z + \hbar\gamma_{\mathrm{NV}}\boldsymbol{B}_{\mathrm{MW}}\cdot\hat{\boldsymbol{\sigma}} + \hbar\gamma_{\mathrm{NV}}\boldsymbol{B}_{\mathrm{N}}\cdot\boldsymbol{\sigma} + \hbar\omega_L\sum_j \hat{I}_z^j\,. \tag{A.1}$$

Here, the first term describes the energy splitting $\hbar\omega_0$ of the $|0\rangle$ and $|-1\rangle$ electronic energy levels. The NV electron spin operators $\hat{\boldsymbol{\sigma}} = (\hat{\sigma}_x, \hat{\sigma}_y, \hat{\sigma}_z)$ describing this two-level system comprised of $|0\rangle$ and $|-1\rangle$ are the same as defined in section 1.3.1. The second term is the coupling of the NV spin to the applied MW pulse's magnetic field $\boldsymbol{B}_{\mathrm{MW}}$, and the third term represents the coupling of the NV spin to the magnetic field $\boldsymbol{B}_{\mathrm{N}}$ produced by the nuclear spins on the diamond surface. Finally, the last term describes the Zeeman splitting of the nuclear hydrogen spins due to the applied field, where ω_L denotes their Larmor frequency and $\hat{\boldsymbol{I}} = (\hat{I}_x, \hat{I}_y, \hat{I}_z)$ are the nuclear spin operators for a spin-1/2 particle, just as defined in the main text in equation (1.7). Note that we do not include any term that describes the effect of the NV spin's magnetic field on the spin bath.

Assumption: In the formulation of equation (A.1) we neglect any direct influence that the NV's magnetic field might exert on the nuclear spin bath.

Based on this Hamiltonian, we will model the evolution of the NV spin throughout the spin-locking pulse of the Spin-Lock sequence, and in particular we will compute the final quantum state. For this we make an assumption on the initial quantum state right at the beginning of the spin-locking pulse: Namely, we assume perfect $\pi/2$-pulses, such that the first $\pi/2$-pulse of the Spin-Lock sequence perfectly rotates the NV spin from $|0\rangle$ (into which it was optically pumped) to $|+\rangle$ (eigenstate of $\hat{\sigma}_x$, see section 1.3.1).

Assumption: We assume that the initial $\pi/2$-pulse of the Spin-Lock sequence is free of errors, such that it initializes the NV spin into $|+\rangle$.

In the following, we derive an expression for the probability of detecting the $|+\rangle$ state at the end of the spin-locking pulse, given that the system was in $|+\rangle$ at the start of that pulse. We do this by applying the time-evolution corresponding to equation (A.1). To evaluate this time evolution analytically, we first transform to an appropriate frame of reference, specifically a doubly rotating frame, and apply a rotating wave approximation.

A.3.2 First Rotating Wave Approximation

In a first step, we transform to the rotating interaction frame, using the transformation rule from the main text, equation (1.11),

$$\hat{\mathcal{H}}_{\text{rot}} = \hat{U}\hat{\mathcal{H}}\hat{U}^\dagger + i\hbar\,\frac{\partial \hat{U}}{\partial t}\,\hat{U}^\dagger\,, \tag{A.2}$$

with the unitary rotation operator

$$\hat{U} = \exp\Big(i\omega_0 t \cdot \hat{\sigma}_z + i\omega_L t \sum_j \hat{I}_z^j\Big) = \hat{U}_{\text{NV}}\hat{U}_{\text{N}}\,, \tag{A.3}$$

where $\hat{U}_{\text{NV}}$ and $\hat{U}_{\text{N}}$ are the rotation operators that act on just the NV or nuclear spin subspace respectively. Perform this rotation results in

$$\begin{aligned}\hat{\mathcal{H}}_{\text{rot}} = {}& \hat{U}\hbar\omega_0\hat{\sigma}_z\hat{U}^\dagger + \hat{U}\sum_j \hbar\omega_L \hat{I}_z^j\hat{U}^\dagger + i\hbar\,\frac{\partial \hat{U}}{\partial t}\,\hat{U}^\dagger \\ & + \hat{U}\hbar\gamma_{\text{NV}}\boldsymbol{B}_{\text{MW}}\cdot\boldsymbol{\sigma}\,\hat{U}^\dagger + \hat{U}\hbar\gamma_{\text{NV}}\boldsymbol{B}_{\text{N}}\cdot\hat{\sigma}\hat{U}^\dagger\,.\end{aligned} \tag{A.4}$$

There are five individual terms in $\hat{\mathcal{H}}_{\text{rot}}$. The first three are easy to compute, because they commute with $\hat{U}$ and $\hat{U}^\dagger$, yielding

$$\hat{U}\hbar\omega_0\hat{\sigma}_z\hat{U}^\dagger = \hbar\omega_0\hat{\sigma}_z \,, \tag{A.5}$$

$$\hat{U}\sum_j \hbar\omega_L \hat{I}_z^j \hat{U}^\dagger = \sum_j \hbar\omega_L \hat{I}_z^j \,, \tag{A.6}$$

$$i\hbar\,\frac{\partial \hat{U}}{\partial t}\,\hat{U}^\dagger = -\hbar\omega_0\hat{\sigma}_z - \sum_j \hbar\omega_L \hat{I}_z^j \,. \tag{A.7}$$

Importantly, the sum of these three terms is zero, such that they are perfectly cancelling each other out. Out of the two remaining terms, let us first consider

$$\begin{aligned}
\hat{U}\hbar\gamma_{\text{NV}}\boldsymbol{B}_{\text{MW}}\cdot\boldsymbol{\sigma}\,\hat{U}^\dagger &= \hbar\gamma_{\text{NV}}\left(B_{\text{MW}}^x\hat{U}\hat{\sigma}_x\hat{U}^\dagger + B_{\text{MW}}^y\hat{U}\hat{\sigma}_y\hat{U}^\dagger + B_{\text{MW}}^z\hat{U}\hat{\sigma}_z\hat{U}^\dagger\right) \\
= \hbar\gamma_{\text{NV}}\Big(B_{\text{MW}}^x(\cos(\omega_0 t)\hat{\sigma}_x - \sin(\omega_0 t)\hat{\sigma}_y) & \\
+B_{\text{MW}}^y(\cos(\omega_0 t)\hat{\sigma}_y + \sin(\omega_0 t)\hat{\sigma}_x) + B_{\text{MW}}^z\hat{\sigma}_z\Big) & \\
= \hbar\gamma_{\text{NV}}\underbrace{\begin{pmatrix}\cos(\omega_0 t) & \sin(\omega_0 t) & 0\\ -\sin(\omega_0 t) & \cos(\omega_0 t) & 0\\ 0 & 0 & 1\end{pmatrix}\cdot\boldsymbol{B}_{\text{MW}}}_{:=\boldsymbol{B}_{\text{MW}}^{\text{rot}}}\cdot\hat{\boldsymbol{\sigma}}\,, &
\end{aligned} \tag{A.8}$$

where in the last line, we have introduced the rotated magnetic field $\boldsymbol{B}_{\text{MW}}^{\text{rot}}$. Next, we aim to evaluate this field, and for this we must make an assumption on the exact form of the of the MW field's lab frame magnetic field $\boldsymbol{B}_{\text{MW}}$.

Assumption: We assume that the microwave field is linearly polarized, i.e. that it takes the form $\boldsymbol{B}_{\text{MW}} = \boldsymbol{B}_{\text{MW}_0}\cos(\omega_0 t)\,.$

This allows us to compute

$$\boldsymbol{B}_{\text{MW}}^{\text{rot}} = \begin{pmatrix}\cos(\omega_0 t) & \sin(\omega_0 t) & 0\\ -\sin(\omega_0 t) & \cos(\omega_0 t) & 0\\ 0 & 0 & 1\end{pmatrix}\cdot\boldsymbol{B}_{\text{MW}_0}\cos(\omega_0 t) \tag{A.9}$$

$$= \begin{pmatrix}\frac{1}{2}\left(B_{\text{MW}_0}^x + B_{\text{MW}_0}^x\cos(2\omega_0 t) + B_{\text{MW}_0}^y\sin(2\omega_0 t)\right)\\ \frac{1}{2}\left(B_{\text{MW}_0}^y + B_{\text{MW}_0}^y\cos(2\omega_0 t) - B_{\text{MW}_0}^x\sin(2\omega_0 t)\right)\\ B_{\text{MW}_0}^z\cos(\omega_0 t)\end{pmatrix} \tag{A.10}$$

$$\approx \frac{1}{2}\begin{pmatrix}B_{\text{MW}_0}^x\\ B_{\text{MW}_0}^y\\ 0\end{pmatrix}, \tag{A.11}$$

where we have performed the rotating wave approximation in the last line by dropping the fast oscillating terms, i.e. terms that that rotate at $\pm\omega_0$ or faster.

Assumption: We assume that the frequency ω_0 is large enough such that the rotating frame approximation becomes valid.

Without loss of generality we now choose our coordinate system such that the y-component of the field vanishes. By introducing the Rabi frequency of the MW field,

$$\Omega_R := \gamma_{\mathrm{NV}} B^x_{\mathrm{MW}_0} , \tag{A.12}$$

we can write finally express the fourth term of $\hat{\mathcal{H}}_{\mathrm{rot}}$ in a simple form, yielding

$$\hat{U} \hbar \gamma_{\mathrm{NV}} \boldsymbol{B}_{\mathrm{MW}} \cdot \boldsymbol{\sigma} \, \hat{U}^\dagger = \hbar \Omega_R \, \hat{\sigma}_x . \tag{A.13}$$

Now, we turn to calculating the fifth and last term in $\hat{\mathcal{H}}_{\mathrm{rot}}$ which contains both operators of the NV center and the proton spins

$$\hat{U} \hbar \gamma_{\mathrm{NV}} \boldsymbol{B}_{\mathrm{N}} \cdot \hat{\sigma} \hat{U}^\dagger = \hbar \gamma_{\mathrm{NV}} \sum_k \left(\hat{U}_{\mathrm{N}} B^k_{\mathrm{N}} \hat{U}^\dagger_{\mathrm{N}} \right) \left(\hat{U}_{\mathrm{NV}} \hat{\sigma}_k \hat{U}^\dagger_{\mathrm{NV}} \right) . \tag{A.14}$$

We first turn to the second factor in equation (A.14). Analogously to the what we did above to evaluate the fourth term shown above, we execute the rotation and apply the rotating frame approximation, and find that

$$\sum_k \hat{U}_{\mathrm{NV}} \hat{\sigma}_k \hat{U}^\dagger_{\mathrm{NV}} \boldsymbol{e}_k = \begin{pmatrix} \cos(\omega_0 t) & -\sin(\omega_0 t) & 0 \\ \sin(\omega_0 t) & \cos(\omega_0 t) & 0 \\ 0 & 0 & 1 \end{pmatrix} \cdot \boldsymbol{\sigma} \underset{\mathrm{RWA}}{\simeq} \begin{pmatrix} 0 \\ 0 \\ \hat{\sigma}_z \end{pmatrix} . \tag{A.15}$$

What is left to do is to compute the first factor in equation (A.14), that is to rotate the magnetic field $\boldsymbol{B}_{\mathrm{N}}$ generated by the nuclear hydrogen spins into the rotating frame with the operator $\hat{U}_{\mathrm{N}}$. For this, we make an assumption on the proton spin bath in that we model the spins as non-interacting pure magnetic dipoles.

Assumption: We assume the surface proton spin ensemble to be a collection of non-interacting pure magnetic dipoles.

Analogous to [51], we begin with the general formula for the magnetic field due to a magnetic dipole as can be found in any textbook on electrodynamics such as [177], yielding

$$\boldsymbol{B}_{\mathrm{dipole}}(\boldsymbol{u}) = \frac{\mu_0}{4\pi} \frac{1}{u^3} \left[3(\boldsymbol{m} \cdot \boldsymbol{e}_u) \boldsymbol{e}_u - \boldsymbol{m} \right] . \tag{A.16}$$

Here $\boldsymbol{u}$ is the vector from the center of the magnetic dipole to the location where the magnetic field is measured, and $\boldsymbol{e}_u$ is a unit vector in the direction of $\boldsymbol{u}$. For the magnetic dipole due to a proton spin, the magnetic moment $\boldsymbol{m}$ is given by the operator projections of the nuclear spin operators $\boldsymbol{I}^j$, such that

$$\boldsymbol{B}_{\mathrm{proton}}(\boldsymbol{u}) = \frac{\hbar \gamma_{\mathrm{H}}}{2} \frac{\mu_0}{4\pi} \frac{1}{u^3} \left[3(\boldsymbol{I} \cdot \boldsymbol{e}_u) \boldsymbol{e}_u - \boldsymbol{I} \right] , \tag{A.17}$$

Finally, to obtain the full magnetic field, we compute the linear superposition of the magnetic fields due to all surface spins, and find

$$\boldsymbol{B}_{\mathrm{N}}(t)=\sum_j\frac{\hbar\gamma_{\mathrm{H}}}{2}\frac{\mu_0}{4\pi}\frac{1}{u_j^3}\left[3\left(\boldsymbol{I}^j(t)\cdot\boldsymbol{e}_u^j)\boldsymbol{e}_u^j-\boldsymbol{I}^j\right)\right]\,. \tag{A.18}$$

We now focus on the components of $\boldsymbol{B}_{\mathrm{N}}(t)$, that are

$$\begin{aligned}B_{\mathrm{N}}^k&=\sum_j\overbrace{\frac{\hbar\gamma_{\mathrm{H}}}{2}\frac{\mu_0}{4\pi}\frac{1}{u_j^3}}^{:=D_j}\left[3\left(\boldsymbol{I}^j(t)\cdot\boldsymbol{e}_u^j)(e_u^j)_k-\hat{I}_k^j\right)\right]\\&=\sum_j D_j\left[3\left((e_u^j)_x(e_u^j)_k\hat{I}_x^j+(e_u^j)_y(e_u^j)_k\hat{I}_y^j+(e_u^j)_z(e_u^j)_k\hat{I}_z^j\right)-\hat{I}_k^j\right]\,,\end{aligned} \tag{A.19}$$

where we introduced the pre-factor $D_j=\frac{\hbar\gamma_{\mathrm{H}}}{2}\frac{\mu_0}{4\pi}\frac{1}{u_j^3}$. The transformation of each component to the rotating frame is given by

$$\begin{aligned}\hat{U}_{\mathrm{N}}B_{\mathrm{N}}^k\hat{U}_{\mathrm{N}}^\dagger=\sum_j D_j&\left[3\left((e_u^j)_x(e_u^j)_k e^{i\omega_L\hat{I}_z^jt}\hat{I}_x^je^{-i\omega_L\hat{I}_z^jt}+(e_u^j)_z(e_u^j)_k\hat{I}_z^j\right.\right.\\&\left.\left.+(e_u^j)_y(e_u^j)_ke^{i\omega_L\hat{I}_z^jt}\hat{I}_y^je^{-i\omega_L\hat{I}_z^jt}\right)-e^{i\omega_L\hat{I}_z^jt}\hat{I}_k^je^{-i\omega_L\hat{I}_z^jt}\right]\,.\end{aligned} \tag{A.20}$$

Since we will ultimately multiply with equation (A.15), we only need to consider the case $k=z$. With this, we get

$$\begin{aligned}B_{\mathrm{N},z}^{\mathrm{rot}}(t)&:=\left(\hat{U}_{\mathrm{N}}B_{\mathrm{N}}^k\hat{U}_{\mathrm{N}}^\dagger\right)_{k=z}\\&=\sum_j D_j\left[3\left((e_u^j)_x(e_u^j)_z\left(\cos(\omega_Lt)\hat{I}_x^j-\sin(\omega_Lt)\hat{I}_y^j\right)\right.\right.\\&\qquad+(e_u^j)_y(e_u^j)_z\left(\cos(\omega_Lt)\hat{I}_y^j+\sin(\omega_Lt)\hat{I}_x^j\right)\\&\qquad\left.\left.+(e_u^j)_z(e_u^j)_z\hat{I}_z^j\right)-\hat{I}_z^j\right]\\&=\sum_j D_j\left[3\left(\boldsymbol{e}_u^j\cdot\begin{pmatrix}\cos(\omega_Lt)&-\sin(\omega_Lt)&0\\\sin(\omega_Lt)&\cos(\omega_Lt)&0\\0&0&1\end{pmatrix}\cdot\boldsymbol{I}^j\right)(e_u^j)_z-\hat{I}_z^j\right]\,.\end{aligned} \tag{A.21}$$

Thus, we finally obtain the the rotating frame Hamiltonian by combining equations (A.13), (A.14), (A.15) and (A.21), which yields

$$\hat{\mathcal{H}}^{\mathrm{rot}}=\hbar\Omega_R\,\hat{\sigma}_x+\hbar\gamma_{\mathrm{NV}}B_{\mathrm{N},z}^{\mathrm{rot}}(t)\,\hat{\sigma}_z\,, \tag{A.22}$$

where the Rabi frequency Ω_R is given by equation (A.12), and the rotating frame magnetic field $B_{\mathrm{N},z}^{\mathrm{rot}}(t)$ of the nuclear proton ensemble is given by equation (A.21).

A.3.3 Second Rotating Wave Approximation

We now bring the rotating frame Hamiltonian $\hat{\mathcal{H}}_{\text{rot}}$ into a doubly rotating frame. To that end, we transform equation (A.22) using the transformation rule from equation (A.3), with the unitary rotation operator $\hat{R}$,

$$\hat{R} = \exp(i\omega_L t \cdot \hat{\sigma}_x)\,, \tag{A.23}$$

which leads to the following Hamiltonian in the doubly rotating frame,

$$\begin{aligned} \hat{\mathcal{H}}_{\text{rotrot}} &= \hbar(\Omega_R - \omega_L)\,\hat{\sigma}_x + \hbar\gamma_{\text{NV}} B^{\text{rot}}_{\text{N},z}(t)\,\hat{R}\,\hat{\sigma}_z \hat{R}^\dagger \\ &= \hbar\Delta\hat{\sigma}_x + \hbar\gamma_{\text{NV}} B^{\text{rot}}_{\text{N},z}(t)\,\big(\cos(\omega_L t)\hat{\sigma}_z + \sin(\omega_L t)\hat{\sigma}_y\big)\,, \end{aligned} \tag{A.24}$$

where we have introduced the detuning $\Delta = \Omega_R - \omega_L$ that describes the offset between applied MW Rabi frequency and the Larmor frequency of the proton spins. For $\Delta = 0$, the Hartmann-Hahn resonance condition is met, meaning the NMR dip we ultimately aim to model is expected to be located at $\Delta = 0$, that is $\Omega_R = \omega_L$. Therefore, for our experimental conditions, Ω_R and ω_L are always very similar.

Assumption: The MW Rabi frequency Ω_R and the proton Larmor frequency ω_L are assumed to be very similar (= fulfilled Hartmann-Hahn condition).

Under this assumption, it is true that Ω_R and ω_L are both much larger than their difference $\Delta = \Omega_R - \omega_L$. We can there perform another rotating wave approximation by dropping all terms that oscillate with Ω_R, ω_L, or faster. This simplifies the expressions for the magnetic field coefficients in equation (A.24), resulting in

$$B_y := B^{\text{rot}}_{\text{N},z}(t)\sin(\Omega_R t) \approx \sum_j D_j \left[\frac{3}{2}\left(\boldsymbol{e}^j_u \cdot \begin{pmatrix} 0 & 1 & 0 \\ -1 & 0 & 0 \\ 0 & 0 & 0 \end{pmatrix} \cdot \boldsymbol{I}^j\right)(e^j_u)_z\right]\,, \tag{A.25}$$

$$B_z := B^{\text{rot}}_{\text{N},z}(t)\cos(\Omega_R t) \approx \sum_j D_j \left[\frac{3}{2}\left(\boldsymbol{e}^j_u \cdot \begin{pmatrix} 1 & 0 & 0 \\ 0 & 1 & 0 \\ 0 & 0 & 0 \end{pmatrix} \cdot \boldsymbol{I}^j\right)(e^j_u)_z\right]\,. \tag{A.26}$$

With this RWA, the doubly rotating Hamiltonian from (A.24) becomes time-independent and reads

$$\begin{aligned} \hat{\mathcal{H}}_{\text{rotrot}} &\approx \hbar\Delta\hat{\sigma}_x + \hbar\gamma_{\text{NV}} B_y \hat{\sigma}_y + \hbar\gamma_{\text{NV}} B_z \hat{\sigma}_z \\ &= \hbar\gamma_{\text{NV}} \boldsymbol{B}^{\text{eff}}_{\text{rotrot}} \cdot \hat{\boldsymbol{\sigma}}\,, \end{aligned} \tag{A.27}$$

where we have defined the effective magnetic field in the doubly rotating frame,

$$\boldsymbol{B}^{\text{eff}}_{\text{rotrot}} = \begin{pmatrix} \Delta/\gamma_{\text{NV}} \\ B_y \\ B_z \end{pmatrix}. \tag{A.28}$$

Crucially, opposite to $\hat{\mathcal{H}}$ and $\hat{\mathcal{H}}_{\mathrm{rot}}$, the doubly rotating Hamiltonian $\hat{\mathcal{H}}_{\mathrm{rotrot}}$ is time-independent, and therefore the quantum evolution can be expressed and evaluated in a straightforward fashion. Specifically, in this case the time propagator is given by

$$\begin{aligned}\hat{N}(t) &= \exp\left(\frac{-it}{\hbar}\,\hat{\mathcal{H}}_{\mathrm{rotrot}}\right) = \exp\left(-it\gamma_{\mathrm{NV}}\boldsymbol{B}^{\mathrm{eff}}_{\mathrm{rotrot}}\cdot\hat{\boldsymbol{\sigma}}\right) \\ &= \hat{\mathbb{I}}\,\cos\left(\frac{t\gamma_{\mathrm{NV}}}{2}|\boldsymbol{B}^{\mathrm{eff}}_{\mathrm{rotrot}}|\right) - 2i\left(\frac{\hat{\boldsymbol{\sigma}}\cdot\boldsymbol{B}^{\mathrm{eff}}_{\mathrm{rotrot}}}{|\boldsymbol{B}^{\mathrm{eff}}_{\mathrm{rotrot}}|}\right)\sin\left(\frac{t\gamma_{\mathrm{NV}}}{2}|\boldsymbol{B}^{\mathrm{eff}}_{\mathrm{rotrot}}|\right).\end{aligned} \tag{A.29}$$

A.3.4 Plus State Population

With the time-evolution operator $\hat{N}(t)$ we have derived in equation (A.29), we can finally compute the probability $P_{|+\rangle}$ to find the system in state $|+\rangle$ at the end of the spin-locking pulse, given that it was in $|+\rangle$ at the start of said pulse. Since the experiments are conducted in the rotating frame (due to how the MW phase reference is constant throughout an experimental run), we calculate $P_{|+\rangle}$ in the rotating frame. It is given by

$$\begin{aligned}P_{|+\rangle} &= \left|\langle +|\,\hat{R}^{\dagger}(\tau)\hat{N}(\tau)\hat{R}(\tau)\,|+\rangle\right|^2 \\ &= \left|\cos\left(\frac{\tau\gamma_{\mathrm{NV}}}{2}|\boldsymbol{B}^{\mathrm{eff}}_{\mathrm{rotrot}}|\right) - \sin\left(\frac{\tau\gamma_{\mathrm{NV}}}{2}|\boldsymbol{B}^{\mathrm{eff}}_{\mathrm{rotrot}}|\right)\times\frac{i\Delta}{\gamma_{\mathrm{NV}}\left|\boldsymbol{B}^{\mathrm{eff}}_{\mathrm{rotrot}}\right|}\right|^2 \\ &= \frac{1}{2}\left(1+\frac{\Delta^2+\gamma_{\mathrm{NV}}^2B^2\,\cos\left(\frac{1}{2}\tau\sqrt{\Delta^2+\gamma_{\mathrm{NV}}^2B^2}\right)}{\Delta^2+\gamma_{\mathrm{NV}}^2B^2}\right),\end{aligned} \tag{A.30}$$

where in the last line, we have introduced the total magnetic field amplitude B as

$$B := \sqrt{B_y^2+B_z^2}\,, \tag{A.31}$$

such that

$$\gamma_{\mathrm{NV}}|\boldsymbol{B}^{\mathrm{eff}}_{\mathrm{rotrot}}| = \sqrt{\Delta^2+\gamma_{\mathrm{NV}}^2B^2}\,. \tag{A.32}$$

A.3.5 Spin Bath Noise Statistics

The probability $P_{|+\rangle}$ we have derived in equation (A.30) is only valid if the magnetic field components B_y and B_z that the surface protons generate is constant. However, this is not an accurate description of reality, because these protons are affected by noise, such as for example temperature fluctuations, and therefore B_y and B_z (and thus also $B=(B_y^2+B_z^2)^{1/2}$) are fluctuating in time. We will now address this noise, and incorporate it into our model of $P_{|+\rangle}$. For this, we consider a very simple case: We assume slow noise, such that the magnetic fields B_y and B_z are constant throughout one experiment repetition (but take on different values in different experimental runs).

This is justified by the very long nuclear coherence times of the protons compared to our typical spin-locking duration of $\tau \approx 100\,\mu\mathrm{s}$.

Assumption: We assume the nuclear magnetic fields B_y and B_z to be constant over the duration τ of our time-evolution.

Under this assumption, based on heuristic arguments involving the central limit theorem, we now model B_y and B_z with Gaussian distributions $\mathcal{N}$ that have zero mean and variance σ^2. Consequently, their Euclidean norm $B = (B_x^2 + B_y^2)^{1/2}$ is described by the Rayleigh distribution $R(B, \sigma^2)$ which yields

$$R(B,\sigma^2) = \frac{B}{\sigma^2} \exp\left(\frac{-B^2}{2\sigma^2}\right), \tag{A.33}$$

where σ^2 is the variance of B_y and B_z. Therefore, we can express the expectation value of $P_{|+\rangle}$ (that depends on B) as

$$E\left[P_{|+\rangle}\right] = \int_0^\infty P_{|+\rangle}\ R(B,\sigma^2)\ \mathrm{d}B\,. \tag{A.34}$$

What is left to do in order to evaluate $E\left[P_{|+\rangle}\right]$ from equation (A.34) in a quantitative fashion is to rigorously describe the variance σ^2 of B_y and B_z. For that end, we model the surface protons as a thermal quantum state, given by

$$\hat{\rho}_{\mathrm{th}} = \frac{1}{Z} \exp\left(-\sum_j \frac{\omega_L \hat{I}_z^j}{k_B T}\right), \tag{A.35}$$

where Z is the partition function that serves as normalization,

$$Z = \mathrm{Tr}\left[\exp\left(-\sum_j \frac{\omega_L \hat{I}_z^j}{k_B T}\right)\right] = \prod_j 2\cosh\left(\frac{\omega_L}{2k_B T}\right). \tag{A.36}$$

The last equality in equation (A.36) can be seen from

$$\begin{aligned} \mathrm{Tr}\left[\exp\left(-\frac{\omega_L \hat{I}_z^j}{k_B T}\right)\right] &= \langle 0|\exp\left(-\frac{\omega_L \hat{I}_z^j}{k_B T}\right)|0\rangle + \langle -1|\exp\left(-\frac{\omega_L \hat{I}_z^j}{k_B T}\right)|-1\rangle \\ &= \exp\left(\frac{-\omega_L}{2k_B T}\right) + \exp\left(\frac{+\omega_L}{2k_B T}\right) \\ &= 2\cosh\left(\frac{\omega_L}{2T}\right). \end{aligned} \tag{A.37}$$

In the following, we will continue to work under the assumption of an infinite temperature, $T \to \infty$. This might be a bad approximation of reality, and at some point, we should extend our model to general temperature states.

Assumption: We describe the proton spin bath with an infinite temperature thermal state $\hat{\rho}_{\mathrm{th}}$.

Given the infinite temperature thermal state $\hat{\rho}_{\mathrm{th}}$ of the proton spin bath, we can now determine the variance σ^2 of both B_y and B_z. In particular, this variance is given by the following difference of expectation values:

$$\sigma^2_{y/z} = \left\langle \hat{B}^2_{y/z} \right\rangle_{\mathrm{th}} - \left\langle \hat{B}_{y/z} \right\rangle^2_{\mathrm{th}} = \mathrm{Tr}\left[\hat{\rho}_{\mathrm{th}} \hat{B}^2_{y/z}\right] - \mathrm{Tr}\left[\hat{\rho}_{\mathrm{th}} \hat{B}_{y/z}\right]^2 . \tag{A.38}$$

As one would expect for an infinite temperature thermal state, where $\langle \hat{I}^j_x \rangle_{\mathrm{th}}$ and $\langle \hat{I}^j_y \rangle_{\mathrm{th}}$ are zero, the term $\langle \hat{B}_{y/z} \rangle_{\mathrm{th}}$ is also vanishing, as can be seen from

$$\begin{aligned} \langle \hat{B}_z \rangle_{\mathrm{th}} = \mathrm{Tr}\left[\hat{\rho}_{\mathrm{th}} \hat{B}_z\right] &= \sum_j \frac{+3D_j (e^j_u)_z}{2} \Big(+(e^j_u)_x \,\mathrm{Tr}\Big[\hat{\rho}_{\mathrm{th}} \hat{I}^j_x\Big] + (e^j_u)_y \,\mathrm{Tr}\Big[\hat{\rho}_{\mathrm{th}} \hat{I}^j_y\Big]\Big) \\ &= \sum_j \frac{+3D_j (e^j_u)_z}{2} \Big(+(e^j_u)_x \langle \hat{I}^j_x \rangle_{\mathrm{th}} + (e^j_u)_y \langle \hat{I}^j_y \rangle_{\mathrm{th}} \Big) = 0 \,, \end{aligned} \tag{A.39}$$

$$\begin{aligned} \langle \hat{B}_y \rangle_{\mathrm{th}} = \mathrm{Tr}\left[\hat{\rho}_{\mathrm{th} \hat{B}_y}\right] &= \sum_j \frac{-3D_j (e^j_u)_z}{2} \Big(-(e^j_u)_y \,\mathrm{Tr}\Big[\hat{\rho}_{\mathrm{th}} \hat{I}^j_x\Big] + (e^j_u)_x \,\mathrm{Tr}\Big[\hat{\rho}_{\mathrm{th}} \hat{I}^j_y\Big]\Big) \\ &= \sum_j \frac{-3D_j (e^j_u)_z}{2} \Big(-(e^j_u)_y \langle \hat{I}^j_x \rangle_{\mathrm{th}} + (e^j_u)_x \langle \hat{I}^j_y \rangle_{\mathrm{th}} \Big) = 0 \,. \end{aligned} \tag{A.40}$$

Therefore, the variance $\sigma^2_{y/z}$ equals the expectation value of $\hat{B}^2_{y/z}$. We will now determine this value in detail for B_z, and the calculation for B_y is entirely similar and will yields the identical result. First, we write out the full expression, resulting in

$$\begin{aligned} \langle \hat{B}^2_z \rangle_{\mathrm{th}} = \sum_j \sum_i \frac{9}{4} D_j D_i \, (e^j_u)_z (e^i_u)_z & \\ \times \Big((e^j_u)_x (e^i_u)_x \langle \hat{I}^j_x \hat{I}^i_x \rangle_{\mathrm{th}} &+ (e^j_u)_x (e^i_u)_y \langle \hat{I}^j_x \hat{I}^i_y \rangle_{\mathrm{th}} \\ &+ (e^j_u)_y (e^i_u)_x \langle \hat{I}^j_y \hat{I}^i_x \rangle_{\mathrm{th}} + (e^j_u)_y (e^i_u)_y \langle \hat{I}^j_y \hat{I}^i_y \rangle_{\mathrm{th}} \Big) \,. \end{aligned} \tag{A.41}$$

We then individually calculate the expectation values that appear in (A.41),

$$\langle \hat{I}^j_x \hat{I}^i_x \rangle_{\mathrm{th}} = \delta_{ij} \langle (\hat{I}^j_x)^2 \rangle_{\mathrm{th}} = \frac{1}{4}\, \delta_{ij} \langle \hat{\mathbb{I}} \rangle_{\mathrm{th}} = \frac{1}{4}\, \delta_{ij} \,, \tag{A.42}$$

$$\langle \hat{I}^j_y \hat{I}^i_y \rangle_{\mathrm{th}} = \delta_{ij} \langle (\hat{I}^j_y)^2 \rangle_{\mathrm{th}} = \frac{1}{4}\, \delta_{ij} \langle \hat{\mathbb{I}} \rangle_{\mathrm{th}} = \frac{1}{4}\, \delta_{ij} \,, \tag{A.43}$$

$$\langle \hat{I}^j_x \hat{I}^i_y \rangle_{\mathrm{th}} = \delta_{ij} \langle \hat{I}^j_x \hat{I}^j_y \rangle = +i\delta_{ij} \langle \hat{I}^j_z \rangle = -i\delta_{ij} \tanh\left(\frac{\omega_L}{2T}\right) \xrightarrow{\text{infinite } T} 0 \,, \tag{A.44}$$

$$\langle \hat{I}^j_y \hat{I}^i_x \rangle_{\mathrm{th}} = \delta_{ij} \langle \hat{I}^j_y \hat{I}^j_x \rangle = -i\delta_{ij} \langle \hat{I}^j_z \rangle = +i\delta_{ij} \tanh\left(\frac{\omega_L}{2T}\right) \xrightarrow{\text{infinite } T} 0 \,, \tag{A.45}$$

and thus equation (A.41) becomes

$$\langle \hat{B}^2_z \rangle_{\mathrm{th}} = \frac{9}{16} \sum_j D^2_j \big((e^j_u)_z\big)^2 \Big[\big((e^j_u)_x\big)^2 + \big((e^j_u)_y\big)^2\Big] . \tag{A.46}$$

Analogously, we find the identical expression for $\langle \hat{B}_y^2 \rangle_{\text{th}}$,

$$\langle \hat{B}_y^2 \rangle_{\text{th}} = \frac{9}{16} \sum_j D_j^2 \big((e_u^j)_z\big)^2 \Big[\big((e_u^j)_x\big)^2 + \big((e_u^j)_y\big)^2\Big] . \tag{A.47}$$

In order to evaluate the sum over the all protons spins (denoted by j), we change the summation to an integration. In particular, we will consider three different scenarios: Either an infinitely extended two-dimensional layer of protons on the diamond surface with a surface density ρ_A, which leads to a surface integral over the area $\mathrm{d}A$,

$$\sum_j \rightarrow \int \rho_A \, \mathrm{d}A \, , \tag{A.48}$$

or an infinitely large volume of protons with a volume density ρ_V that fill the entire space over the diamond surface, which results in a volume integral over $\mathrm{d}V$,

$$\sum_j \rightarrow \int \rho_V \, \mathrm{d}V \, , \tag{A.49}$$

or the combination of both, that is a surface ensemble of surface density ρ_A and a volume ensemble of spin density ρ_V,

$$\sum_j \rightarrow \sum_{\substack{\text{Surface}\\ \text{Spins}}} + \sum_{\substack{\text{Volume}\\ \text{Spins}}} \rightarrow \int \rho_A \, \mathrm{d}A \, + \, \int \rho_V \, \mathrm{d}V \, , \tag{A.50}$$

This means that equations (A.46) and (A.47) become

$$\langle \hat{B}_{y/z}^2 \rangle_{\text{th}}^{A} = \frac{9}{16} \left(\frac{\hbar \gamma_{\text{H}}}{2} \frac{\mu_0}{4\pi} \right)^2 \rho_A \int \frac{u_z^2}{|\boldsymbol{u}|^{10}} (u_x^2 + u_y^2) \, \mathrm{d}A \, , \tag{A.51}$$

$$\langle \hat{B}_{y/z}^2 \rangle_{\text{th}}^{V} = \frac{9}{16} \left(\frac{\hbar \gamma_{\text{H}}}{2} \frac{\mu_0}{4\pi} \right)^2 \rho_V \int \frac{u_z^2}{|\boldsymbol{u}|^{10}} (u_x^2 + u_y^2) \, \mathrm{d}V \, , \tag{A.52}$$

and

$$\begin{aligned} \langle \hat{B}_{y/z}^2 \rangle_{\text{th}}^{AV} = \frac{9}{16} \left(\frac{\hbar \gamma_{\text{H}}}{2} \frac{\mu_0}{4\pi} \right)^2 \Bigg[\, & \rho_A \int \frac{u_z^2}{|\boldsymbol{u}|^{10}} (u_x^2 + u_y^2) \, \mathrm{d}A \\ & + \rho_V \int \frac{u_z^2}{|\boldsymbol{u}|^{10}} (u_x^2 + u_y^2) \, \mathrm{d}V \Bigg] \, , \end{aligned} \tag{A.53}$$

where the superscripts A, V and AV stand for "area" and "volume" to indicate what kind of proton bath is considered, and where we have used that

$$D_j = \left(\frac{\hbar \gamma_{\text{H}}}{2} \frac{\mu_0}{4\pi} \right) \frac{1}{u_j^3} \, , \qquad \text{and} \qquad (e_u^j)_k = \frac{u_k^j}{|\boldsymbol{u}|} \, . \tag{A.54}$$

To solve these integrals, we use cylindrical coordinates. In these coordinates, the following terms read

$$\boldsymbol{u} = \begin{pmatrix} r\cos(\phi) \\ r\sin(\phi) \\ d \end{pmatrix} \qquad \mathrm{d}A = r \, \mathrm{d}r \, \mathrm{d}\phi \qquad \mathrm{d}V = r \, \mathrm{d}r \, \mathrm{d}\phi \, \mathrm{d}z \, , \tag{A.55}$$

where we choose the origin of the coordinate system to be the single NV located at a depth d in the diamond lattice. Substitution of equation (A.55) into (A.51) then finally let us solve the integral, which ultimately yields the analytic expression for the magnetic field variance σ_A^2 at he NV's position, produced by a two-dimensional ensemble of surface protons located on the diamond surface,

$$\begin{aligned}\sigma_A^2 = \langle \hat{B}_{y/z}^2 \rangle_{\mathrm{th}}^A &= \frac{9\,(\hbar\gamma_{\mathrm{H}}\mu_0)^2}{1024\,\pi^2}\,\rho_A \int_0^\infty \int_0^{2\pi} \frac{d^2}{(r^2+d^2)^5}\, r^3\,\mathrm{d}r\,\mathrm{d}\phi \\ &= \frac{(\hbar\gamma_{\mathrm{H}}\mu_0)^2}{4096\,\pi} \cdot \left(3\,\frac{\rho_A}{d^4}\right) .\end{aligned} \tag{A.56}$$

Similarly, by substituting the cylindrical coordinates into (A.52), we obtain the solution for the magnetic field variance σ_V^2 of a three-dimensional finite layer of of protons, located between z coordinates $d+L_1$ and $d+L_2$ relative to the NV center, yielding

$$\begin{aligned}\sigma_V^2 = \langle \hat{B}_{y/z}^2 \rangle_{\mathrm{th}}^V &= \frac{9\,(\hbar\gamma_{\mathrm{H}}\mu_0)^2}{1024\,\pi^2}\,\rho_V \int_0^\infty \int_0^{2\pi} \int_{d+Z1}^{d+Z2} \frac{(d+z)^2}{(r^2+(d+z)^2)^5}\, r^3\,\mathrm{d}r\,\mathrm{d}\phi\,\mathrm{d}z \\ &= \frac{(\hbar\gamma_{\mathrm{H}}\mu_0)^2}{4096\,\pi} \cdot \left(\frac{\rho_V}{(d+Z_1)^3} - \frac{\rho_V}{(d+Z_2)^3}\right) .\end{aligned} \tag{A.57}$$

Notably, for an infinitely large layer in direct contact with the diamond surface, i.e. for $Z_1 = 0$ and $Z_2 \to \infty$, this becomes

$$\sigma_{V,\infty}^2 = \frac{(\hbar\gamma_{\mathrm{H}}\mu_0)^2}{4096\,\pi} \cdot \left(\frac{\rho_V}{d^3}\right) . \tag{A.58}$$

Finally, for a combination of both a surface and a volume ensemble of protons, we use our cylindrical coordinates to solve equation (A.53) and thereby find

$$\begin{aligned}\sigma_{AV}^2 = \langle \hat{B}_{y/z}^2 \rangle_{\mathrm{th}}^{AV} &= \frac{9\,(\hbar\gamma_{\mathrm{H}}\mu_0)^2}{1024\,\pi^2} \Bigg[\rho_A \int_0^\infty \int_0^{2\pi} \frac{d^2}{(r^2+d^2)^5}\, r^3\,\mathrm{d}r\,\mathrm{d}\phi \\ &\qquad + \rho_V \int_0^\infty \int_0^{2\pi} \int_{d+Z1}^{d+Z2} \frac{(d+z)^2}{(r^2+(d+z)^2)^5}\, r^3\,\mathrm{d}r\,\mathrm{d}\phi\,\mathrm{d}z\Bigg] \\ &= \frac{(\hbar\gamma_{\mathrm{H}}\mu_0)^2}{4096\,\pi} \cdot \left(3\,\frac{\rho_A}{d^4} + \frac{\rho_V}{(d+Z_1)^3} - \frac{\rho_V}{(d+Z_2)^3}\right) ,\end{aligned} \tag{A.59}$$

demonstrating that $\sigma_{AV}^2 = \sigma_A^2 + \sigma_V^2$.

A.3.6 Final Result

With the results of the previous section, we can now formulate the final result for the expectation value of the probability $P_{|+\rangle}$ to find the system in state $|+\rangle$ at the end of the spin-locking pulse with duration τ. Specifically, we combine equations (A.30), (A.33) and (A.34), to find that

$$E\left[P_{|+\rangle}\right] = \int_0^\infty P_{|+\rangle} \cdot R\left(B, \sigma^2\right)\,\mathrm{d}B \tag{A.60}$$
$$= \int_0^\infty \frac{B}{2\sigma^2}\left(1 + \frac{\Delta^2 + \gamma_{\mathrm{NV}}^2 B^2 \cos\left(\frac{1}{2}\tau\sqrt{\Delta^2 + \gamma_{\mathrm{NV}}^2 B^2}\right)}{\Delta^2 + \gamma_{\mathrm{NV}}^2 B^2}\right) \cdot \exp\left(\frac{-B^2}{2\sigma^2}\right)\mathrm{d}B\,,$$

where the magnetic variance σ^2 depends on whether the proton ensemble on the diamond surface is present in the form of a two-dimensional area (A), a three-dimensional volume (V), or a combination of both (AV). The variances in these three cases, as derived in equations (A.56), (A.57) and (A.59), are given by

$$\sigma_A^2 = \frac{\left(\hbar\gamma_{\mathrm{H}}\mu_0\right)^2}{4096\,\pi} \cdot \left(3\,\frac{\rho_A}{d^4}\right), \tag{A.61}$$

$$\sigma_V^2 = \frac{\left(\hbar\gamma_{\mathrm{H}}\mu_0\right)^2}{4096\,\pi} \cdot \left(\frac{\rho_V}{(d+Z_1)^3} - \frac{\rho_V}{(d+Z_2)^3}\right), \tag{A.62}$$

$$\sigma_{AV}^2 = \frac{\left(\hbar\gamma_{\mathrm{H}}\mu_0\right)^2}{4096\,\pi} \cdot \left(\frac{\rho_V}{(d+Z_1)^3} - \frac{\rho_V}{(d+Z_2)^3} + 3\,\frac{\rho_A}{d^4}\right) = \sigma_A^2 + \sigma_V^2\,, \tag{A.63}$$

where d is the depth the of single NV used to sense the proton spin bath. So far we were not able to solve equation (A.60) analytically, however, we can numerically fit our Spin-Lock NMR data with it. In order to do that, we need to convert the expectation value $E\left[P_{|+\rangle}\right]$ into the units of spin contrast $\mathcal{S}_c$ in which we plot our NMR spectra (see section 3.1.1 for the definition of $\mathcal{S}_c$). To do this conversion, we point out that these two quantities are linearly related to each other, while spanning different numerical ranges. Specifically, in the case where there is no spin relaxation due to the surface protons occurs, that is if the state of the system at the end of the spin-locking pulse is $|+\rangle$, we obtain $E\left[P_{|+\rangle}\right] = 1$ and $\mathcal{S}_c = 1$. Thus, in this limit the two quantities are equal. However, if the system has fully decayed into the statistical mixture $\frac{1}{2}\,|+\rangle\langle+| + \frac{1}{2}\,|-\rangle\langle-|$ (= Bloch sphere origin) by the end of the spin-locking pulse, we find $E\left[P_{|+\rangle}\right] = \frac{1}{2}$ and $\mathcal{S}_c = 0$. Overall, these arguments lead to the following linear relationship,

$$\mathcal{S}_c = 2 \cdot E\left[P_{|+\rangle}\right] - 1\,. \tag{A.64}$$

This expression for $\mathcal{S}_c$ is what we use to fit to the Spin-Lock data in chapter 5. In particular, and most importantly, this allows us to fit the depth d of the employed NV. The other free parameters are the proton spin density ρ_A respectively ρ_V, that can also be fitted, or – given a known NMR target – be fixed to literature values; and the proton layer coordinates Z_1 and Z_2, where we usually assume $Z_1 = 0$ such that Z_2 simply denotes the thickness of the proton layer (which we either fit or set to infinity). Finally, the NMR detuning $\Delta = f_{\mathrm{NMR}} - \omega_L$ describes the x-axis of the NMR spectrum, the duration τ is given by the experiment settings, and $\hbar$, γ_{H} and μ_0 are natural constants for which we plug in literature values.

A.4 Redfield Relaxation Theory

The Redfield theory evolves around the Redfield equation. This equation is a Markovian master equation that describes the time evolution of a quantum system that is weakly coupled to an environment. In our case, the quantum system at hand is the electronic spin of the NV center (we here omit the hyperfine structure), and the environment is given by weak magnetic fluctuations. Casting the Redfield equation into a matrix form leads to the Redfield superoperator from which it is straightforward to extract specific spin relaxation times, such as T_1, T_2^* or $T_{1\rho}$. The notation and general approach we present here is adapted from the lecture of Spielman [124], and the books of Slichter [104] and Kowalewski [105].
This section is structured as follows: First, in section A.4.1 we will derive the general form of the Redfield master equation and the corresponding Redfield superoperator. Afterwards, in sections A.4.2 and A.4.3 we will evaluate the superoperator for an undriven NV electron spin to compute T_1 and T_2^*, and for the driven case to determine $T_{1\rho}$.

A.4.1 Derivation of the Redfield Superoperator

Consider the Hamiltonian $\hat{\mathcal{H}} = \hat{\mathcal{H}}_0 + \hat{\mathcal{H}}_1(t)$ and let $\hat{\mathcal{H}}_1(t)$ be a weak perturbation of the time independent part $\hat{\mathcal{H}}_0$. Notably, such a weak coupling is a strong assumption, and the entire derivation we present here is only valid for the case of such weak environments.

Assumption: We assume that the environment is weakly coupled, such that a perturbative treatment of the interaction Hamiltonian is valid.

The time evolution of a system described by the density matrix $\hat{\rho}$ is given by the Von-Neumann equation and reads

$$\frac{\mathrm{d}}{\mathrm{d}t}\hat{\rho}(t) = \frac{-i}{\hbar}\left[\hat{\mathcal{H}}, \hat{\rho}(t)\right]. \tag{A.65}$$

Transforming to the interaction picture with the transformation rule given by equation (1.11) with $\hat{U} = \exp\left(\frac{it}{\hbar}\hat{\mathcal{H}}_0\right)$ leads to the rotating frame equation of motion, yielding

$$\frac{\mathrm{d}}{\mathrm{d}t}\hat{\rho}^{\mathrm{rot}}(t) = \frac{-i}{\hbar}\left[\hat{\mathcal{H}}_1^{\mathrm{rot}}(t), \hat{\rho}^{\mathrm{rot}}(t)\right], \tag{A.66}$$

where the superscript (rot) denotes the rotating frame. We proceed with a formal integration of this equation by expanding into the Dyson series, and thereby find

$$\begin{aligned}\hat{\rho}^{\mathrm{rot}}(t) = \hat{\rho}^{\mathrm{rot}}(t_0) &- \frac{i}{\hbar}\int_{t_0}^{t}\left[\hat{\mathcal{H}}_1^{\mathrm{rot}}(t'), \hat{\rho}^{\mathrm{rot}}(t')\right]\mathrm{d}t' \\ &- \frac{1}{\hbar^2}\int_{t_0}^{t}\int_{t_0}^{t'}\left[\hat{\mathcal{H}}_1^{\mathrm{rot}}(t'), \left[\hat{\mathcal{H}}_1^{\mathrm{rot}}(t''), \hat{\rho}^{\mathrm{rot}}(t'')\right]\right]\mathrm{d}t'\mathrm{d}t'' + \ldots\end{aligned} \tag{A.67}$$

Here, we cut off the series after the first three terms which equals a second order perturbation approach. This is valid under the assumption of a weak environment. In addition, we take the ensemble average, indicated in the following by overlines. For the NV system, this ensemble average corresponds to the average over many different experimental runs. Further, we assume a non-biased environment, such that $\overline{\hat{\mathcal{H}}_1^{\mathrm{rot}}(t)} = 0$. Hence, the second term of the Dyson series is eliminated when we apply the ensemble average.

Assumption: We assume a non-biased environment, such that the ensemble average of the interaction Hamiltonian with the environment is zero.

We are therefore only left with the first and third term, reading

$$\overline{\hat{\rho}^{\mathrm{rot}}(t)} = \overline{\hat{\rho}^{\mathrm{rot}}(t_0)} - \frac{1}{\hbar^2}\int_{t_0}^{t}\int_{t_0}^{t'} \overline{\left[\hat{\mathcal{H}}_1^{\mathrm{rot}}(t'), \left[\hat{\mathcal{H}}_1^{\mathrm{rot}}(t''), \hat{\rho}^{\mathrm{rot}}(t'')\right]\right]}\mathrm{d}t'\mathrm{d}t''\,, \tag{A.68}$$

and taking the derivative with respect to time yields

$$\frac{\mathrm{d}}{\mathrm{d}t}\overline{\hat{\rho}^{\mathrm{rot}}(t)} = -\frac{1}{\hbar^2}\int_{t_0}^{t} \overline{\left[\hat{\mathcal{H}}_1^{\mathrm{rot}}(t), \left[\hat{\mathcal{H}}_1^{\mathrm{rot}}(t''), \hat{\rho}^{\mathrm{rot}}(t'')\right]\right]}\mathrm{d}t''\,. \tag{A.69}$$

Next, we now apply the Markov approximation. To that end, we replace $\hat{\rho}^{\mathrm{rot}}(t'')$ in the time integral with $\hat{\rho}^{\mathrm{rot}}(t)$, which is valid under the assumption that the dynamics of the system at time t are only dependent on $\hat{\rho}^{\mathrm{rot}}(t)$ and not on $t'' < t$; or put differently, we assume that there is no memory in the system.

Assumption: We work in the Markov approximation that assumes that there no memory in the system, such that the dynamics of $\hat{\rho}^{\mathrm{rot}}(t)$ only depend on the state of the system at time t and not on $t'' < t$.

In addition to the Markov approximation, we insert a Boltzmann correction by introducing a thermal equilibrium state $\hat{\rho}_{\mathrm{eq}}^{\mathrm{rot}}$ the system decays towards. Such a thermal density matrix looks as follows

$$\hat{\rho}_{\mathrm{eq}}^{\mathrm{rot}} = \sum_j \exp\left(\frac{-E_j}{k_B T}\right)|\Psi_j\rangle\langle\Psi_j|\,, \tag{A.70}$$

where k_B is the Boltzmann constant, $|\Psi_j\rangle$ are the eigenstates of $\hat{\mathcal{H}}_1^{\mathrm{rot}}(t)$ with eigenenergy E_j, and T is the thermal equilibrium temperature. Performing the Born-Markov approximation and the Boltzmann correction ultimately leads to

$$\frac{\mathrm{d}}{\mathrm{d}t}\overline{\hat{\rho}^{\mathrm{rot}}(t)} = -\frac{1}{\hbar^2}\int_{t_0}^{t} \overline{\left[\hat{\mathcal{H}}_1^{\mathrm{rot}}(t), \left[\hat{\mathcal{H}}_1^{\mathrm{rot}}(t''), \hat{\rho}^{\mathrm{rot}}(t) - \hat{\rho}_{\mathrm{eq}}^{\mathrm{rot}}\right]\right]}\mathrm{d}t''\,. \tag{A.71}$$

Next, we substitute $\tau := t - t''$ and assume $t_0 \to \infty$, such that

$$\frac{\mathrm{d}}{\mathrm{d}t}\overline{\hat{\rho}^{\mathrm{rot}}(t)} = -\frac{1}{\hbar^2}\int_{0}^{\infty} \overline{\left[\hat{\mathcal{H}}_1^{\mathrm{rot}}(t), \left[\hat{\mathcal{H}}_1^{\mathrm{rot}}(t-\tau), \hat{\rho}^{\mathrm{rot}}(t) - \hat{\rho}_{\mathrm{eq}}^{\mathrm{rot}}\right]\right]}\mathrm{d}\tau\,. \tag{A.72}$$

Finally, by transforming back to the lab frame, we obtain the general form of the Redfield equation, which yields

$$\frac{\mathrm{d}}{\mathrm{d}t}\overline{\hat{\rho}(t)} = -\frac{i}{\hbar}\left[\hat{\mathcal{H}}_0, \overline{\hat{\rho}(t)}\right] - \frac{1}{\hbar^2}\int_0^\infty \overline{\left[\hat{\mathcal{H}}_1(t), \left[\hat{\mathcal{H}}_1(t-\tau), \hat{\rho}(t)\right]\right]}\mathrm{d}\tau\,. \tag{A.73}$$

This is the general Redfield equation, as you would commonly find it in other work. It is valid in the Markov approximation and for weakly coupled, non-biased environments. The first term of the Redfield equation describes the coherent evolution, as it equals the Liouville–Von Neumann equation for the unperturbed Hamiltonian $\hat{\mathcal{H}}_0$. The second term deals with the perturbation due to the environment.

The Redfield Superoperator

Next, we will proceed to derive a different form of the Redfield equation that will turn out to be easy to evaluate for the Ramsey and Spin-Lock problems. To that end, we first note that it is always possible to find the decomposition

$$\hat{\mathcal{H}}_1(t) = \sum_{q=-N}^{N} F_q(t)\hat{A}_q \qquad \text{where } \left[\hat{\mathcal{H}}_0, \hat{A}_q\right] = \hbar e_q \hat{A}_q \text{ and } \hat{A}_{-q} := \hat{A}_q^\dagger\,. \tag{A.74}$$

Since $\hat{\mathcal{H}}_1(t)$ is hermitian, it must always contain both $\hat{A}_q$ and $\hat{A}_q^*$. For simplicity, we therefore define $\hat{A}_q^* := \hat{A}_{-q}$. Note that this definition also implies that $e_{-q} = -e_q$, as one can show by using equation (A.74). Using this special decomposition of $\hat{\mathcal{H}}_1(t)$ into operators $\hat{A}_q$ leads to a new expression for the rotating frame Hamiltonian, yielding

$$\hat{\mathcal{H}}_1^{\mathrm{rot}}(t) = \sum_q F_q(t)\hat{A}_q \exp(-ie_q t)\,. \tag{A.75}$$

Plugging this identity into the integral (A.72) yields

$$\begin{aligned}\frac{\mathrm{d}}{\mathrm{d}t}\overline{\hat{\rho}^{\mathrm{rot}}(t)} = &-\frac{1}{\hbar^2}\sum_{p,q}\Bigg(\left[\hat{A}_p, \left[\hat{A}_q, \overline{\hat{\rho}^{\mathrm{rot}}(t)} - \overline{\hat{\rho}^{\mathrm{rot}}_{\mathrm{eq}}}\right]\right] \\ &\times \int_0^\infty \overline{F_p(t)F_q(t-\tau)}\ \exp(-ie_p t)\exp(-ie_q(t-\tau))\,\mathrm{d}\tau\Bigg)\,.\end{aligned} \tag{A.76}$$

In the integral that shows up in this expression only the terms with $e_p = -e_q$ evaluate to non-zero contributions. And since $e_{-q} = -e_q$, we can set $p = -q$. After performing these simplifications, one obtains a new integral that has only a very small imaginary part which is responsible for dynamic frequency shifts. We neglect this shifts here, and thus replace the integral with its real part. Overall, this leads to

$$\begin{aligned}\frac{\mathrm{d}}{\mathrm{d}t}\overline{\hat{\rho}^{\mathrm{rot}}(t)} = &-\frac{1}{2\hbar^2}\sum_{q}\Bigg(\left[\hat{A}_{-q}, \left[\hat{A}_q, \overline{\hat{\rho}^{\mathrm{rot}}(t)} - \overline{\hat{\rho}^{\mathrm{rot}}_{\mathrm{eq}}}\right]\right] \\ &\times \int_{-\infty}^\infty \overline{F_{-q}(t)F_q(t-\tau)}\ \exp(-ie_q\tau)\mathrm{d}\tau\Bigg)\,.\end{aligned} \tag{A.77}$$

Finally, transforming back to the lab frame yields

$$\frac{\mathrm{d}}{\mathrm{d}t}\overline{\hat{\rho}(t)} = -\frac{i}{\hbar}\left[\hat{\mathcal{H}}_0, \overline{\hat{\rho}(t)}\right] - \hat{\hat{\Gamma}}\left\{\overline{\hat{\rho}(t)} - \overline{\hat{\rho}_{\mathrm{eq}}}\right\} \,, \tag{A.78}$$

where $\hat{\hat{\Gamma}}$ is the Redfield superoperator

$$\hat{\hat{\Gamma}}\left\{\hat{\rho}\right\} = \frac{1}{2\hbar^2}\sum_q \int_{-\infty}^{\infty} \overline{F_{-q}(t)F_q(t-\tau)}\exp(-ie_q\tau)\left[\hat{A}_{-q}, \left[\hat{A}_q, \hat{\rho}\right]\right]\mathrm{d}\tau\,. \tag{A.79}$$

Matrix Form of the Redfield Equation

Let us now cast the Redfield equation from (A.78) into a convenient matrix form. To that end, let us assume that $\hat{\mathcal{H}}_0$ describes a spin-1/2 system, such as the NV subsystem spanned by the electronic spin states $|-1\rangle$ and $|0\rangle$. We can then use the spin-1/2 operators $\hat{\boldsymbol{\sigma}} = (\hat{\sigma}_0, \hat{\sigma}_x, \hat{\sigma}_y, \hat{\sigma}_z)$ as a basis for the matrix vector space of $\overline{\hat{\rho}(t)}$ to introduce a vector representation of $\overline{\hat{\rho}(t)}$, yielding

$$\overline{\hat{\rho}(t)} = \sum_j \overline{\langle\hat{\sigma}_j\rangle}\cdot\hat{\sigma}_j \qquad \text{where } \overline{\langle\hat{\sigma}_j\rangle} = 2\cdot\mathrm{Trace}\left(\hat{\sigma}_j\cdot\overline{\hat{\rho}(t)}\right)\,, \tag{A.80}$$

where $\hat{\sigma}_0 = \frac{1}{2}\mathbb{I}_2$ is half the two-dimensional unity operator, and the $\hat{\sigma}$ operators are the same as in section 1.3.1 with the same matrix representations as the operator $\hat{\boldsymbol{I}}$ in (1.7). Incorporating this vector representation into the Redfield equation from (A.78) results in

$$\begin{aligned}\frac{\mathrm{d}}{\mathrm{d}t}\overline{\langle\hat{\sigma}_j\rangle} = \sum_k \Bigg(& -i\overline{\langle\hat{\sigma}_k\rangle}\cdot 2\cdot\mathrm{Trace}\left(\hat{\sigma}_j\cdot\left[\hat{\mathcal{H}}_0, \hat{\sigma}_k\right]\right) \\ & - \left(\overline{\langle\hat{\sigma}_k\rangle} - \overline{\langle\hat{\sigma}_k\rangle}_{\mathrm{eq}}\right)\cdot\underbrace{2\cdot\mathrm{Trace}\left(\hat{\sigma}_j\cdot\hat{\Gamma}\left\{\hat{\sigma}_k\right\}\right)}_{:=R_{jk}}\Bigg)\,.\end{aligned} \tag{A.81}$$

This equation describes the time-dependent evolution of the expectation value of the j^{th} spin component. The first term describes the coherent evolution of the spin system, whereas the second term gives the perturbative effect of the environment. If we identify the $\overline{\langle\hat{\sigma}_k\rangle}$ as entries in a vector, we can treat the two traces in this equation as matrices. The second matrix, which we denote as the Redfield relaxation matrix R_{jk}, is therefore accounting for the decay of component $\overline{\langle\hat{\sigma}_j\rangle}$ due to noise associated with component $\overline{\langle\hat{\sigma}_k\rangle}$. To be precise, its matrix elements are the corresponding decay rates.

A.4.2 Derivation of T_1 and T_2^*

To explicitly get expressions for the T_1 and T_2^* decay rates with the Redfield formalism, we consider the two-level system given by the $|0\rangle$, $|-1\rangle$ two-level manifold of the NV center's electronic ground-state. Let $|0\rangle$ and $|-1\rangle$ be split in energy by $\hbar w_0$. We then assume that a Ramsey FID sequence is applied to that system (see section 1.5.2).

Under this sequence, the spin is brought into a superposition state that then is left to evolve freely, thus being subject to both T_1 relaxation and T_2^* dephasing. The Hamiltonian describing the free evolution during the Ramsey sequence in the lab frame with weak random magnetic field noise $B_k(t)$ along all three axes is given by

$$\hat{\mathcal{H}}_{\text{Ramsey}} = \hbar\omega_0\hat{\sigma}_z + \sum_{k=x,y,z} \hbar\gamma_{\text{NV}} B_k(t)\hat{\sigma}_k \,. \tag{A.82}$$

Here, we identify the first term as a time independent term $\hat{\mathcal{H}}_0$, and the rest as the weak perturbation $\hat{\mathcal{H}}_1(t)$. The operators $\hat{A}_q$ that fulfil

$$\left[\hat{\mathcal{H}}_0, \hat{A}_q\right] = \hbar e_q \hat{A}_q \,, \tag{A.83}$$

are therefore

$$\begin{aligned} \hat{A}_0 &= \hat{\sigma}_z \\ \hat{A}_1 &= \hat{\sigma}_x + i\hat{\sigma}_y \\ \hat{A}_{-1} &= \hat{\sigma}_x - i\hat{\sigma}_y \end{aligned} \tag{A.84}$$

with

$$\begin{aligned} e_0 &= 0 \\ e_1 &= \omega_0 \\ e_{-1} &= -\omega_0 \,. \end{aligned} \tag{A.85}$$

The decomposition of $\hat{\mathcal{H}}_1(t) = \sum_q F_q(t)\hat{A}_q$ into the $\hat{A}_q$ yields

$$\begin{aligned} \hat{\mathcal{H}}_1(t) = &\underbrace{\hbar\gamma_{\text{NV}} B_z(t)}_{F_0(t)}\ \hat{A}_0 + \underbrace{\frac{\hbar\gamma_{\text{NV}}}{2}\Big(B_x(t) + iB_y(t)\Big)}_{F_1(t)}\ \hat{A}_1 \\ &+ \underbrace{\frac{\hbar\gamma_{\text{NV}}}{2}\Big(B_x(t) - iB_y(t)\Big)}_{F_{-1}(t)}\ \hat{A}_{-1} \,. \end{aligned} \tag{A.86}$$

Now that we have determined all the $\hat{A}_q$, e_q and $F_q(t)$, we can calculate the Redfield relaxation matrix R_{jk} that we defined in equation (A.81) via the Redfield superoperator $\hat{\Gamma}$ from equation (A.79), yielding

$$\begin{aligned} R_{jk} = 2\cdot\text{Trace}\Bigg(&\hat{\sigma}_j \cdot \frac{1}{2\hbar^2}\sum_{q=-1}^{+1}\left[\hat{A}_{-q}, \left[\hat{A}_q, \hat{\sigma}_k\right]\right] \\ &\times \int_{-\infty}^{\infty} \overline{F_{-q}(t)F_q(t-\tau)}\,\exp(-ie_q\tau)\,\mathrm{d}\tau\Bigg) \,. \end{aligned} \tag{A.87}$$

As a first step, we will evaluate the integrals in this expression. To that end, we make the usual assumption that the magnetic noise exhibits an exponentially decaying autocorrelation function

$$\overline{B_q(t)B_p(t-\tau)} = \delta_{p,q}\, B_{\text{rms},q}^2\, \exp(-|\tau|/\tau_c) \,, \tag{A.88}$$

where $\delta_{p,q}$ is the Kronecker delta function. Using this autocorrelation function, we find that

$$\begin{aligned}\overline{F_0(t)F_0(t-\tau)} &= \hbar^2\gamma_{\mathrm{NV}}^2\, B_{\mathrm{rms},z}^2\, \exp(-|\tau|/\tau_c) \\ \overline{F_{\mp1}(t)F_{\pm1}(t-\tau)} &= \hbar^2\gamma_{\mathrm{NV}}^2\, \frac{1}{4}\left(B_{\mathrm{rms},x}^2 + B_{\mathrm{rms},y}^2\right)\, \exp(-|\tau|/\tau_c)\,,\end{aligned} \tag{A.89}$$

such that

$$\begin{aligned}\frac{1}{2\hbar^2}\int_{-\infty}^{\infty} \overline{F_0(t)F_0(t-\tau)}\exp(-ie_0\tau)\,\mathrm{d}\tau &= \gamma_{\mathrm{NV}}^2\, S_z(0) \\ \frac{1}{2\hbar^2}\int_{-\infty}^{\infty} \overline{F_{\mp1}(t)F_{\pm1}(t-\tau)}\exp(-ie_{\pm1}\tau)\,\mathrm{d}\tau &= \frac{\gamma_{\mathrm{NV}}^2}{4}\Big(S_x(\pm\omega_0) + S_y(\pm\omega_0)\Big)\,,\end{aligned} \tag{A.90}$$

where $S(w)$ is given as in (1.21). Plugging these integral expressions into equation (A.87) results in

$$\begin{aligned}R_{jk} =\; & 2\,\gamma_{\mathrm{NV}}^2 S_z(0)\cdot\mathrm{Trace}\left(\hat\sigma_j\cdot[\hat\sigma_z,[\hat\sigma_z,\hat\sigma_k]]\right) \\ &+ \frac{\gamma_{\mathrm{NV}}^2}{2}\Big(S_x(+\omega_0) + S_y(+\omega_0)\Big)\cdot\mathrm{Trace}\left(\hat\sigma_j\cdot[(\hat\sigma_x - i\hat\sigma_y),[(\hat\sigma_x + i\hat\sigma_y),\hat\sigma_k]]\right) \\ &+ \frac{\gamma_{\mathrm{NV}}^2}{2}\Big(S_x(-\omega_0) + S_y(-\omega_0)\Big)\cdot\mathrm{Trace}\left(\hat\sigma_j\cdot[(\hat\sigma_x + i\hat\sigma_y),[(\hat\sigma_x - i\hat\sigma_y),\hat\sigma_k]]\right)\,.\end{aligned} \tag{A.91}$$

This expression for R_{jk} can easily be evaluated by calculating the commutators. Additionally, we simplify by using the fact that $S(w)$ is even, i.e. we set $S(\pm\omega_0) = S(\omega_0)$. Ultimately, R_{jk}'s diagonal entries are then determined as follows

$$\begin{aligned}\frac{1}{T_1} &= R_{zz} = \gamma_{\mathrm{NV}}^2\Big(S_x(\omega_0) + S_y(\omega_0)\Big) \\ \frac{1}{T_2^*} &= R_{xx} = R_{yy} = \frac{1}{2}\gamma_{\mathrm{NV}}^2\Big(S_x(\omega_0) + S_y(\omega_0)\Big) + \gamma_{\mathrm{NV}}^2\, S_z(0)\,.\end{aligned} \tag{A.92}$$

which are equations (1.22) and (1.23) in the main text. They agree perfectly with the results from Slichter [104].

A.4.3 Derivation of $T_{1\rho}$

In this section, we present the detailed derivation of $T_{1\rho}$. This derivation is similar to the calculations we did in the previous section, but instead of Ramsey's free induction decay, we now consider a Spin-Lock sequence. The Spin-Lock lab frame Hamiltonian with random magnetic noise along all three spatial axes reads

$$\hat{\mathcal{H}}_{\mathrm{SL}} = \hbar\omega_0\hat\sigma_z + \hbar\Omega_R\cos(\omega_0 t)\hat\sigma_x + \sum_{k=x,y,z}\hbar\gamma_{\mathrm{NV}}B_k(t)\hat\sigma_k\,. \tag{A.93}$$

In order to apply the Redfield theory, the two time dependent terms have to be weak in terms of amplitude compared the to time independent first term. Sadly, this is not true for this Hamiltonian, as in general $\hbar\Omega_R$ is not necessarily small in comparison to $\hbar\omega_0$ (for our experiments this is actually always true, however, we aim to provide a more general derivation that is valid without making this assumption). To address this problem, we transform to the rotating frame using the transformation rule given by equation (1.11), with $\hat{U} = \exp(i\omega_0 t\hat{\sigma}_z)$. After applying the rotating wave approximation (see section 1.3.1), we find

$$\begin{aligned} \hat{\mathcal{H}}_{\mathrm{SL}}^{\mathrm{rot}} = \, & \hbar\Omega_R\hat{\sigma}_x \\ & + \hbar\gamma_{\mathrm{NV}}\Big(B_x(t)\cos(\omega_0 t) + B_y(t)\sin(\omega_0 t)\Big)\,\hat{\sigma}_x \\ & + \frac{\hbar\gamma_{\mathrm{NV}}}{2}\Big(B_y(t)\cos(\omega_0 t) - B_x(t)\sin(\omega_0 t) + iB_z(t)\Big)\,(\hat{\sigma}_y + i\hat{\sigma}_z) \\ & + \frac{\hbar\gamma_{\mathrm{NV}}}{2}\Big(B_y(t)\cos(\omega_0 t) - B_x(t)\sin(\omega_0 t) - iB_z(t)\Big)\,(\hat{\sigma}_y - i\hat{\sigma}_z)\,. \end{aligned} \tag{A.94}$$

Here, the Redfield theory can be applied, since the amplitudes of the time dependent terms are given by $\hbar\gamma_{\mathrm{NV}}B_k$ which by definition are magnetic fluctuations that are weak compared to $\hbar\Omega_R$. We therefore identify the first term as the time independent term $\hat{\mathcal{H}}_0^{\mathrm{rot}}$ and the rest as the perturbation $\hat{\mathcal{H}}_1^{\mathrm{rot}}(t)$. The operators $\hat{A}_q$ that fulfil

$$\Big[\hat{\mathcal{H}}_0^{\mathrm{rot}}, \hat{A}_q\Big] = \hbar e_q\hat{A}_q \tag{A.95}$$

are then

$$\begin{aligned} \hat{A}_0 &= \hat{\sigma}_x \\ \hat{A}_1 &= \hat{\sigma}_y + i\hat{\sigma}_z \\ \hat{A}_{-1} &= \hat{\sigma}_y - i\hat{\sigma}_z \end{aligned} \tag{A.96}$$

with

$$\begin{aligned} e_0 &= 0 \\ e_1 &= \Omega_R \\ e_{-1} &= -\Omega_R \end{aligned} \tag{A.97}$$

Thus, the decomposition of $\hat{\mathcal{H}}_1^{\mathrm{rot}}(t) = \sum_q F_q(t)\hat{A}_q$ is already given directly by the last three terms in (A.94). We therefore deduct

$$\begin{aligned} \hat{F}_0(t) &= \hbar\gamma_{\mathrm{NV}}\Big(B_x\cos(\omega_0 t) + B_y\sin(\omega_0 t)\Big) \\ \hat{F}_{\pm 1}(t) &= \frac{\hbar\gamma_{\mathrm{NV}}}{2}\Big(B_y\cos(\omega_0 t) - B_x\sin(\omega_0 t) \pm iB_z(t)\Big)\,. \end{aligned} \tag{A.98}$$

Now that we have determined all the $\hat{A}_q$, e_q and $F_q(t)$, we can calculate the Redfield relaxation matrix R_{jk} that we defined in equation (A.81) via the Redfield superoperator $\hat{\Gamma}$ from equation (A.79). This yields

$$\begin{aligned} R_{jk} = 2\cdot\mathrm{Trace}\Bigg(&\hat{\sigma}_j\cdot\frac{1}{2\hbar^2}\sum_{q=-1}^{+1}\Big[\hat{A}_{-q},\Big[\hat{A}_q,\hat{\sigma}_k\Big]\Big] \\ & \times\int_{-\infty}^{\infty}\overline{F_{-q}(t)F_q(t-\tau)}\exp(-ie_q\tau)\,\mathrm{d}\tau\Bigg)\,. \end{aligned} \tag{A.99}$$

To evaluate this expression, we begin with finding good expressions for the integrand $\overline{F_{-q}(t)F_q(t-\tau)}$. In the same fashion as in the previous section, we make the usual assumption that the magnetic noise exhibits an exponentially decaying autocorrelation function

$$\overline{B_q(t)B_p(t-\tau)} = \delta_{p,q}\, B^2_{\mathrm{rms},q}\, \exp(-|\tau|/\tau_c)\,, \tag{A.100}$$

where $\delta_{p,q}$ is the Kronecker delta functions, and thus we find that

$$\begin{aligned}\overline{F_0(t)F_0(t-\tau)} &= \hbar^2\gamma^2_{\mathrm{NV}}\, \exp(-|\tau|/\tau_c) \\ &\quad \times \left(\frac{1}{2}\left(B^2_{\mathrm{rms},x} + B^2_{\mathrm{rms},y}\right)\cos(\omega_0\tau) + \frac{1}{2}\left(B^2_{\mathrm{rms},x} - B^2_{\mathrm{rms},y}\right)\cos(2\omega_0 t - \omega_0\tau)\right) \\ &\approx \frac{1}{2}\hbar^2\gamma^2_{\mathrm{NV}}\, \exp(-|\tau|/\tau_c) \times \left(\left(B^2_{\mathrm{rms},x} + B^2_{\mathrm{rms},y}\right)\cos(\omega_0\tau)\right),\end{aligned} \tag{A.101}$$

where in the last line, we assume that the noise is isotropic, e.g. that $B^2_{\mathrm{rms},x} \approx B^2_{\mathrm{rms},y}$, which means that we can neglect the second term and simplify the rest. With the same assumption, we also find that

$$\begin{aligned}&\overline{F_{\mp1}(t)F_{\pm1}(t-\tau)} \\ &\approx \frac{1}{4}\hbar^2\gamma^2_{\mathrm{NV}}\, \exp(-|\tau|/\tau_c) \times \left(\frac{1}{2}\left(B^2_{\mathrm{rms},x} + B^2_{\mathrm{rms},y}\right)\cos(\omega_0\tau) + B^2_{\mathrm{rms},z}\right).\end{aligned} \tag{A.102}$$

Next, we evaluate the sum and the integral in equation (A.99) using the expressions from (A.101) and (A.102), and thereby find

$$\begin{aligned}R_{jk} =& \gamma^2_{\mathrm{NV}}\, \mathrm{Trace}\big(\hat\sigma_j \cdot [\hat\sigma_x, [\hat\sigma_x, \hat\sigma_k]]\big) \cdot \Big(S_x(\omega_0) + S_y(\omega_0)\Big) \\ &+ \frac{\gamma^2_{\mathrm{NV}}}{2}\, \mathrm{Trace}\big(\hat\sigma_j \cdot [(\hat\sigma_y + i\hat\sigma_z), [(\hat\sigma_y - i\hat\sigma_z), \hat\sigma_k]]\big) \cdot \Bigg(S_z(\Omega_R) \\ &\qquad + \frac{1}{4}\Big(S_x(\omega_0 + \Omega_R) + S_y(\omega_0 + \Omega_R)\Big) \\ &\qquad + \frac{1}{4}\Big(S_x(\omega_0 - \Omega_R) + S_y(\omega_0 - \Omega_R)\Big)\Bigg) \\ &+ \frac{\gamma^2_{\mathrm{NV}}}{2}\, \mathrm{Trace}\big(\hat\sigma_j \cdot [(\hat\sigma_y - i\hat\sigma_z), [(\hat\sigma_y + i\hat\sigma_z), \hat\sigma_k]]\big) \cdot \Bigg(S_z(\Omega_R) \\ &\qquad + \frac{1}{4}\Big(S_x(\omega_0 + \Omega_R) + S_y(\omega_0 + \Omega_R)\Big) \\ &\qquad + \frac{1}{4}\Big(S_x(\omega_0 - \Omega_R) + S_y(\omega_0 - \Omega_R)\Big)\Bigg),\end{aligned} \tag{A.103}$$

where the noise spectral density $S_k(\omega)$ is defined as in equation (1.21). Finally, we obtain $T_{1\rho} := 1/R_{xx}$ by evaluating the commutators in equation (A.103) for $j = k =$

x. Hence we get

$$\frac{1}{T_{1\rho}} = R_{xx} = \gamma_{\mathrm{NV}}^2 \, S_z(\Omega_R) + \frac{\gamma_{\mathrm{NV}}^2}{4}\Big(S_x(\omega_0+\Omega_R) + S_y(\omega_0+\Omega_R)\Big) + \frac{\gamma_{\mathrm{NV}}^2}{4}\Big(S_x(\omega_0-\Omega_R) + S_y(\omega_0-\Omega_R)\Big)\,. \tag{A.104}$$

This is the general result for $T_{1\rho}$. In our experiments, we employ weak microwave driving where the spin-locking field amplitude Ω_R is typically three orders of magnitude smaller than the spin transition ω_0 (compare a few MHz to a few GHz). Therefore, for our experimental conditions, we can further simplify by replacing $S(\omega_0 \pm \Omega_R)$ with $S(\omega_0)$, such that

$$\frac{1}{T_{1\rho}} = R_{xx} = \gamma_{\mathrm{NV}}^2 \, S_z(\Omega_R) + \frac{1}{2}\gamma_{\mathrm{NV}}^2\Big(S_x(\omega_0) + S_y(\omega_0)\Big) \tag{A.105}$$

which is (1.28) in the main text.

A.5 Construction of Transition Superoperators

Here, we derive the matrix representations of the transition superoperators required for the numerical model introduced in section 2.1.3. In general, the system $\hat{\rho}$ is in a state comprised of two subsystems, the nuclear and electron spins, can thus mathematically be written as $\hat{\rho} = \hat{\rho}_I \otimes \hat{\rho}_S$. The nuclear subspace is 2-dimensional with spin operators $\hat{I}_{x,y,z}$ as defined in (1.7), whereas the electronic subsystem is 3-dimensional with corresponding spin operators $\hat{S}_{x,y,z}$ from (1.2). Based on this, we can develop the matrix representations of the required superoperators, where we closely follow the procedure laid out in [130]. Note that in order to stay close to the expressions from [130] as possible, we inverted the order of nuclear and electronic subsystems compared to how we typically treat it within this thesis: Usually, we list the electron spin first, but within the numerical model, we list the nuclear spin first.

Partial Trace Superoperator

The action of the partial trace superoperator can be understood by considering

$$\hat{\hat{T}}^e\left(\hat{\rho}_I \otimes \hat{\rho}_S\right) = \mathrm{Trace}\left\{\hat{\rho}_S\right\} \cdot \hat{\rho}_I\,. \tag{A.106}$$

The matrix representation of $\hat{\hat{T}}^e$ is determined following the procedure form [130], and reproduced here for completeness:

$$\{\hat{\hat{T}}^e\}_{\alpha\beta} = \begin{cases} 1 & , \text{ if } m = n \\ 0 & , \text{ else} \end{cases} \tag{A.107}$$

where

$$\begin{aligned} \alpha &= (i-1)\cdot d_I + j \\ \beta &= (((i-1)\cdot d_S + m) - 1)\cdot d_S \cdot d_I + (j-1)\cdot d_S + n\,, \end{aligned} \tag{A.108}$$

where $i, n = (1, 2, \dots d_I)$ count through the degrees of freedom of the first subspace (nuclear spin in this case), and $j, m = (1, 2, \dots d_S)$ count through the degrees of freedom of the second subspace (NV electron spin). The resulting matrix is 4x36 dimensional.

Direct Product Superoperator

The action of the direct product superoperator $\hat{\hat{S}}^{\otimes}_{0,\pm1}$ is given by

$$\hat{\hat{S}}^{\otimes}_{0,\pm1}\hat{\rho}_I = \hat{\rho}_I \otimes \hat{\rho}_{m_S=0,\pm1}\,, \tag{A.109}$$

where $\hat{\rho}_{m_S=0,\pm1}$ describes the density operator corresponding to a electron $m_S = \{0, \pm1\}$ eigenstate. The corresponding matrix representation is constructed by [130]

$$\{\hat{\hat{S}}^{\otimes}_{0,\pm1}\}_{\alpha\beta} = \{\hat{\kappa}_{0,\pm1}\}_{mn} \tag{A.110}$$

where

$$\begin{aligned} &\alpha = (((i-1)\cdot d_S + m) - 1)\cdot d_S \cdot d_I + (j-1)\cdot d_S + n \\ &\beta = (i-1)\cdot d_I + j\,, \end{aligned} \tag{A.111}$$

and

$$\hat{\kappa}_{+1} = \begin{pmatrix} 1 & 0 & 0 \\ 0 & 0 & 0 \\ 0 & 0 & 0 \end{pmatrix} \qquad \hat{\kappa}_{0} = \begin{pmatrix} 0 & 0 & 0 \\ 0 & 1 & 0 \\ 0 & 0 & 0 \end{pmatrix} \qquad \hat{\kappa}_{-1} = \begin{pmatrix} 0 & 0 & 0 \\ 0 & 0 & 0 \\ 0 & 0 & 1 \end{pmatrix}. \tag{A.112}$$

The numbers i, j, n, m, d_S and d_I are the same as defined above. The resulting dimensionality of this matrix is 36x4.

Projection Superoperator

Finally, we define the matrix representation for the projection superoperator,

$$\hat{\hat{P}}_{0,\pm1} = \sum_{k=1}^{4} \hat{\rho}^{k}_{0,\pm1} \cdot (\hat{\rho}^{k}_{0,\pm1})^T \tag{A.113}$$

where $\hat{\rho}^{k}_{0,\pm1} = \hat{\kappa}^{k}_{\text{nuc}} \otimes \hat{\kappa}_{0,\pm1}$ is the 36x1 column vector representation of the joint 6x6 density matrix operator and

$$\hat{\kappa}^{1}_{\text{nuc}} = \begin{pmatrix} 1 & 0 \\ 0 & 0 \end{pmatrix} \qquad \hat{\kappa}^{2}_{\text{nuc}} = \begin{pmatrix} 0 & 1 \\ 0 & 0 \end{pmatrix} \qquad \hat{\kappa}^{3}_{\text{nuc}} = \begin{pmatrix} 0 & 0 \\ 1 & 0 \end{pmatrix} \qquad \hat{\kappa}^{4}_{\text{nuc}} = \begin{pmatrix} 0 & 0 \\ 0 & 1 \end{pmatrix}. \tag{A.114}$$

While $\hat{\hat{T}}^{e}$ and $\hat{\hat{S}}^{\otimes}_{0,\pm1}$ both change the dimensionality of the state they operate on, $\hat{\hat{P}}_{0,\pm1}$ is a square 36x36 matrix and thus preserves dimensionality. The sum in equation (A.113) ensures that the projection operator projects onto a particular electronic spin state, while leaving the nuclear spin unchanged. Note that this matrix element construction procedure is not given in [130] but has been developed by us ourselves.

A.6 Magnetic Field Map for All-Optical Precession Data

In the following we elaborate on how we obtained the values for $B_\perp$ and D_0^{gs} used in the plots in chapter 2. To control the external magnetic field we used a permanent magnet mounted on a 2-axis goniometer, as described in section A.1.2. However since the distance between the magnet-goniometer assembly and the diamond is tuned to set the strength of the magnetic bias field $\boldsymbol{B}_{\mathrm{ext}}$, the center of rotation of the goniometer will in general not be precisely at the position of the NV center (this special case is only true for one specific value of $\boldsymbol{B}_{\mathrm{ext}}$ that we measured to be at approximately 500 G). It is therefore not entirely accurate to simply measure $|\boldsymbol{B}_{\mathrm{ext}}|$ and take $B_\perp$ as $\sin(\phi) \cdot |\boldsymbol{B}_{\mathrm{ext}}|$, since the rotation itself will also (slightly) change the distance between the magnet and the diamond. It is more accurate to do ODMR measurements and thereby experimentally determine the exact magnetic field for a range of goniometer

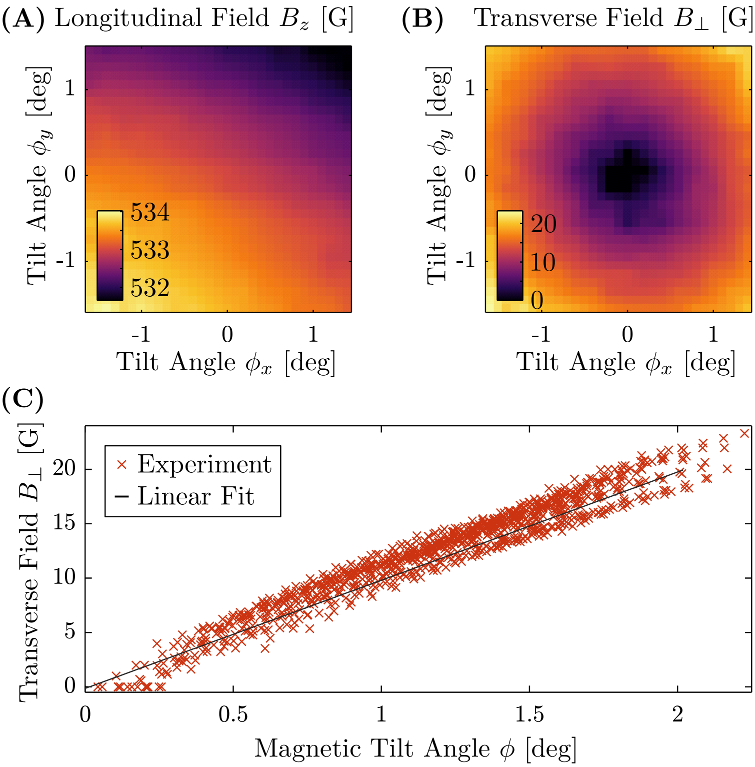

Figure A.7: Magnetic field map based on ODMR measurements **(A)** Parallel magnetic field component B_z and **(B)** transverse magnetic field component $B_\perp$ as a function of tilt angles ϕ_x and ϕ_y, measured via optically detected magnetic resonance. Each of the shown pixels corresponds to one pixel in Figure 2.5 and 2.6. The total magnetic field is $|\boldsymbol{B}_{\mathrm{ext}}| = 533\,\mathrm{G}$. **(C)** Measured transverse magnetic field as a function of total tilt angle ϕ, revealing a linear dependence with slope 10.01 G/deg, allowing for a simple conversion of $B_\perp$ to corresponding Φ and vice versa.

angular displacements. We carefully measured such a magnetic map as a function of the two goniometer angles, at a bias field of $|\boldsymbol{B}_{\text{ext}}| = 533\,\text{G}$, because at this particular field most of the data in this paper were obtained.

The first step of the procedure was to measure the contrast C of the ^{15}N FID signal as a function of the two goniometer angles, as shown in Figure 2.6 (A) in the main text. We know that for the goniometer orientation corresponding to the center pixel where C goes to zero, the magnetic field is perfectly aligned with the NV axis, i.e. $B_\perp = 0$ for this pixel. Knowing this, we measured the full magnetic resonance spectrum ODMR of the NV center on this pixel, and fit the resulting two transitions ($|0\rangle$ to either $|\pm1\rangle$) to the ground state nuclear spin Hamiltonian from (1.4), with B_z and D_0^{gs} as free parameters, enforcing the condition that $B_\perp = 0$. From this fit we obtained the value for the zero field splitting for this particular NV center as $D_0^{\text{gs}} = 2870.760402$ MHz. In the second step we measured ODMR spectra as a function of the two goniometer angles, and once more fit the measured transitions with Hamiltonian (1.4), this time with B_z and $B_\perp$ as the free parameters. Finally, we interpolate both $B_z(\phi_x, \phi_y)$ and $B_\perp(\phi_x, \phi_y)$ to twice the pixel density in order to match the experimental data from Figures 2.5 and 2.6. The results of the procedure are shown in Figure A.7. We also plot $B_\perp$ against total tilt angle $\phi = (\phi_x^2 + \phi_y^2)^{1/2}$, revealing a near linear relationship with a slope of $10.01\,\text{G/deg}$.

Throughout chapter 2, whenever we plot experimental and simulated data against $B_\perp$ (in particular in Figures 2.5 and 2.6) we have used the magnetic field map presented here to obtain the conversion from goniometer position to magnetic field. Further, in order to determine the ideal magnetic tilt angle corresponding to $B_\perp = 8.6$ G from Figure 2.6 (B), we used the slope from Figure A.7 (C).

The experimentally measured magnetic field map is valid only at 533 G. Therefore, for datasets where we swept the distance between the magnet and the diamond in order to vary the strength of the bias field, we instead just report the tilt angle as defined directly by the goniometer.

A.7 Optimization of SNR in Immersion Oil NMR

In section 5.3.1, we presented NMR measurements with and without immersion oil. For these experiments, we have seen that the nuclear magnetic field at the NV center's position is dominated by the ubiquitous surface spins because the addition of immersion oil made only little difference in terms of NMR contrast and SNR. Since our fitting routine depends crucially on the this tiny difference between the two spectra, we needed to integrate these NMR experiments for quite a long time. To speed up these measurements and enable more robust fitting of the data, it would be advantageous to maximize the SNR difference between the two NMR spectra. Here, we study how one can maximize this SNR difference.

In section 3.1.2, we have derived a model that simulates how the Spin-Lock SNR depends on τ, and that allows us to determine the ideal τ_{opt} with which the SNR is maximized. We now use this model, in particular equation (3.8), to simulate the difference $\Delta\text{SNR}(\tau) = \text{SNR}_{\text{Oil}}(\tau) - \text{SNR}_{\text{Bare}}(\tau)$. For this, we use representative values for our system: Let the PL difference be $\Delta_{01} = 100\,\text{kcps}$, the experimental overhead be $T_0 = 3.5\,\mu\text{s}$, and the noise variance on the spin readout be $\sigma = 0.5$. Furthermore, we assume that on off-resonance with the proton spins, we measure the relaxation time $T_{1\rho} = (250 \pm 5)\,\mu\text{s}$. On Hartmann-Hahn resonance with the proton spins, this decay is faster, here we set $T_{1\rho}^{\text{res}}(\text{Bare}) = (100 \pm 5)\,\mu\text{s}$, and after adding immersion oil, we let the decay time decrease even more to $T_{1\rho}^{\text{res}}(\text{Oil}) = (85 \pm 5)\,\mu\text{s}$. The result of this is plotted in Figure A.8 (A), where the error stems from the uncertainty of the $T_{1\rho}$ values.

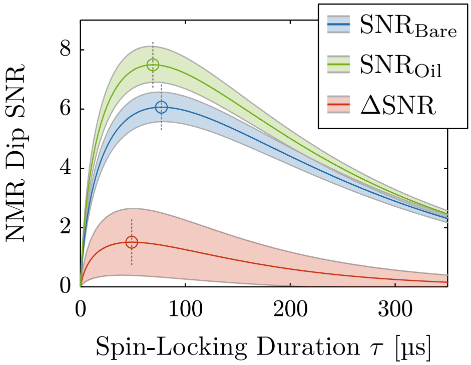

Figure A.8: The $\text{SNR}(\tau)$ predicted by equation (3.8), for $\Delta_{01} = 100\,\text{kcps}$, $\sigma = 0.5$, $T_0 = 3.5\,\mu\text{s}$, $T_{1\rho}^{\text{off}} = (250 \pm 5)\,\mu\text{s}$, $T_{1\rho}^{\text{off}}(\text{Bare}) = (100 \pm 5)\,\mu\text{s}$ and $T_{1\rho}^{\text{off}}(\text{Oil}) = (85 \pm 5)\,\mu\text{s}$. The resulting $\text{SNR}(\tau)$ for bare diamond and oil-coated diamond, as well as their difference ΔSNR, are maximized for different values for τ. In this case, at $\tau_{\text{opt}}^{\text{Bare}} \approx (77.0 \pm 1.9)\,\mu\text{s}$, $\tau_{\text{opt}}^{\text{Oil}} = (47.9 \pm 3.2)\,\mu\text{s}$ and $\tau_{\text{opt}}^{\Delta} = (36.3 \pm 0.9)\,\mu\text{s}$.

The key result is that the three different SNR curves are maximized for different choices for τ, as indicated by the circle markers. In the experiments we presented in section 5.3.1, we have always chosen τ such that SNR_{Bare} is maximized. Based on the simulation shown here, we now see that this is not ideal for ΔSNR.

The curves shown in Figure A.8 depend strongly on the ratio of the coherence times in the presence and absence of oil, $\mathcal{R} = T_{1\rho}^{\text{res}}(\text{Oil})/T_{1\rho}^{\text{res}}(\text{Bare})$. This ratio quantifies how much the nuclei in the oil contribute to the magnetic signal collected by the NV in NMR. Particularly, in the limit of $\mathcal{R} = 1$, the presence of immersion oil makes no difference in the NMR, and for $\mathcal{R} = 0$, the oil's magnetic signal is so strong that it causes an immediate full decay of the NV spin.

In Figure A.9 (A), we present the ideal τ values one needs to choose to maximize the three different SNRs, plotted as a function of $\mathcal{R}$. For our experiments where $\mathcal{R} \approx 0.85$, the simulation predicts that $\tau_{\text{opt}}^{\Delta}$ is about 2/3 of $\tau_{\text{opt}}^{\text{Bare}}$. If $\mathcal{R}$ was lower (which would be the case for less dense surface spins or a shallower NV), the discrepancy in the ideal values of $\tau_{\text{opt}}^{\text{Bare}}$ and $\tau_{\text{opt}}^{\Delta}$ becomes even larger.

Finally, to quantify how detrimental it is to measure at a suboptimal τ, we calculate the relative difference in SNR, that is $\Delta\text{SNR}/\sum\text{SNR}$, for a choice of τ equal to either $\tau_{\text{opt}}^{\text{Bare}}$, $\tau_{\text{opt}}^{\text{Oil}}$, or $\tau_{\text{opt}}^{\Delta}$ respectively. This is plotted in Figure A.9 (B). For our experimental regime where $\mathcal{R} > 0.8$, the difference is actually very minute. Therefore, our choice of $\tau = \tau_{\text{opt}}^{\text{Bare}}$ for the experiments in section 5.3.1 is fine, and using $\tau_{\text{opt}}^{\text{Oil}}$ or $\tau_{\text{opt}}^{\Delta}$ would only lead to a very small improvement in ΔSNR.

However, for systems where $\mathcal{R} < 0.5$, measuring at $\tau_{\text{opt}}^{\text{Bare}}$ instead of $\tau_{\text{opt}}^{\Delta}$ is highly suboptimal, because in this regime there is a significant difference in the resulting ΔSNR. Interestingly, independent of $\mathcal{R}$, ΔSNR is nearly identical for $\tau_{\text{opt}}^{\text{Oil}}$ and $\tau_{\text{opt}}^{\Delta}$. Hence, when calibrating an experiment where ΔSNR is desired to be large, it is perfectly fine to use either of these values for τ.

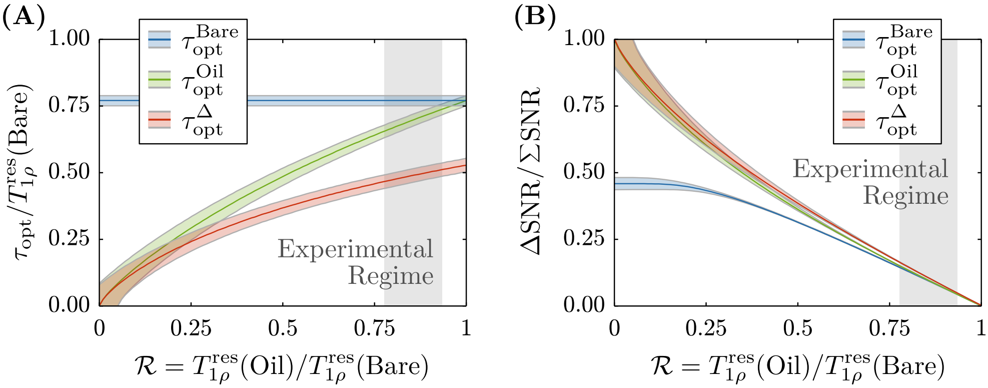

Figure A.9: Optimization of the SNR in proton NMR with and without immersion oil, where $T_{1\rho}^{\mathrm{res}}(\mathrm{Bare})$ is held constant and $T_{1\rho}^{\mathrm{res}}(\mathrm{Oil})$ is varied. **(A)** Visualization of the three different ideal tau values as a function of the relaxation time ratio $\mathcal{R}$. The grey box highlights our experimental regime, where $\tau_{\mathrm{opt}}^{\Delta}$ is smaller than $\tau_{\mathrm{opt}}^{\mathrm{Bare}}$. **(B)** The relative different in ΔSNR as a function of $\mathcal{R}$ reveals that for our experimental regime it makes little difference to use $\tau_{\mathrm{opt}}^{\mathrm{Bare}}$ instead of the ideal $\tau_{\mathrm{opt}}^{\Delta}$.

In summary, our analysis has shown that depending on what specific SNR one wants to optimize, a different value for the spin-locking duration τ needs to be used. In particular when studying ΔSNR, it is not ideal to measure at $\tau_{\mathrm{opt}}^{\mathrm{Bare}}$ – which is what we have done throughout this chapter – however for our experimental conditions this suboptimal choice leads to a negligible reduction in ΔSNR compared to the optimal case.

Finally, note that the SNR model is applicable to NMR with the XY8-k sequence in an analogous manner (see section 4.2). For this reason, the same conclusions can be drawn for XY8-k NMR. The only difference is that instead of the spin-locking duration τ, the XY8 block repetition number k is the control parameter for such SNR optimization.

Bibliography

[1] S. S. Gill, O. Cetinkaya, S. Marrone, D. Claudino, D. Haunschild, L. Schlote, H. Wu, C. Ottaviani, X. Liu, S. P. Machupalli, K. Kaur, P. Arora, J. Liu, A. Farouk, H. H. Song, S. Uhlig, and K. Ramamohanarao, *Quantum Computing: Vision and Challenges*, (arXiv:2403.02240) (2024).

[2] H. Dutta and A. K. Bhuyan, *Quantum Communication: From Fundamentals to Recent Trends, Challenges and Open Problems*, (arXiv:2406.04492) (2024).

[3] C. Degen, F. Reinhard, and P. Cappellaro, *Quantum sensing*, Rev. Mod. Phys. **89**, 035002 (2017).

[4] The LIGO Scientific Collaboration, *A gravitational wave observatory operating beyond the quantum shot-noise limit*, Nature Phys **7**, 962 (2011).

[5] R. Kleiner, D. Koelle, F. Ludwig, and J. Clarke, *Superconducting quantum interference devices: State of the art and applications*, Proceedings of the IEEE **92**, 1534 (2004).

[6] M. J. Biercuk, H. Uys, J. W. Britton, A. P. VanDevender, and J. J. Bollinger, *Ultrasensitive detection of force and displacement using trapped ions*, Nature Nanotech **5**, 646 (2010).

[7] J. Chaste, A. Eichler, J. Moser, G. Ceballos, R. Rurali, and A. Bachtold, *A nanomechanical mass sensor with yoctogram resolution*, Nature Nanotech **7**, 301 (2012).

[8] F. Guzman Cervantes, L. Kumanchik, J. Pratt, and J. M. Taylor, *High sensitivity optomechanical reference accelerometer over 10 kHz*, Applied Physics Letters **104**, 221111 (2014).

[9] J. M. Taylor, P. Cappellaro, L. Childress, L. Jiang, D. Budker, P. R. Hemmer, A. Yacoby, R. Walsworth, and M. D. Lukin, *High-sensitivity diamond magnetometer with nanoscale resolution*, Nature Phys **4**, 810 (2008).

[10] F. Dolde, H. Fedder, M. W. Doherty, T. Nöbauer, F. Rempp, G. Balasubramanian, T. Wolf, F. Reinhard, L. C. L. Hollenberg, F. Jelezko, and J. Wrachtrup, *Electric-field sensing using single diamond spins*, Nature Phys **7**, 459 (2011).

[11] M. Chipaux, L. Toraille, C. Larat, L. Morvan, S. Pezzagna, J. Meijer, and T. Debuisschert, *Wide bandwidth instantaneous radio frequency spectrum analyzer based on nitrogen vacancy centers in diamond*, Applied Physics Letters **107**, 233502 (2015).

[12] H. Tabuchi, Y. Matsuzaki, N. Furuya, Y. Nakano, H. Watanabe, N. Tokuda, N. Mizuochi, and J. Ishi-Hayase, *Temperature sensing with RF-dressed states of nitrogen-vacancy centers in diamond*, Journal of Applied Physics **133**, 024401 (2023).

[13] M. W. Doherty, V. V. Struzhkin, D. A. Simpson, L. P. McGuinness, Y. Meng, A. Stacey, T. J. Karle, R. J. Hemley, N. B. Manson, L. C. Hollenberg, and S. Prawer, *Electronic Properties and Metrology Applications of the Diamond NV- Center under Pressure*, Phys. Rev. Lett. **112**, 047601 (2014).

[14] P. Kehayias, M. J. Turner, R. Trubko, J. M. Schloss, C. A. Hart, M. Wesson, D. R. Glenn, and R. L. Walsworth, *Imaging crystal stress in diamond using ensembles of nitrogen-vacancy centers*, Phys. Rev. B **100**, 174103 (2019).

[15] M. P. Ledbetter, K. Jensen, R. Fischer, A. Jarmola, and D. Budker, *Gyroscopes based on nitrogen-vacancy centers in diamond*, Phys. Rev. A **86**, 052116 (2012).

[16] J. F. Barry, M. J. Turner, J. M. Schloss, D. R. Glenn, Y. Song, M. D. Lukin, H. Park, and R. L. Walsworth, *Optical magnetic detection of single-neuron action potentials using quantum defects in diamond*, Proceedings of the National Academy of Sciences **113**, 14133 (2016).

[17] D. R. Glenn, R. R. Fu, P. Kehayias, D. Le Sage, E. A. Lima, B. P. Weiss, and R. L. Walsworth, *Micrometer-scale magnetic imaging of geological samples using a quantum diamond microscope*, Geochemistry, Geophysics, Geosystems **18**, 3254 (2017).

[18] F. Casola, T. van der Sar, and A. Yacoby, *Probing condensed matter physics with magnetometry based on nitrogen-vacancy centres in diamond*, Nat Rev Mater **3**, 1 (2018).

[19] X. Wang, W. Li, B. Moran, B. C. Gibson, L. T. Hall, D. A. Simpson, A. N. Kealy, and A. D. Greentree, *Quantum Diamond Magnetometry for Navigation in GNSS Denied Environments*, in J. T. Freymueller and L. Sánchez (editors), *Gravity, Positioning and Reference Frames*, pp. 87–92 (Springer Nature Switzerland, Cham) (2024).

[20] M. W. Doherty, N. B. Manson, P. Delaney, F. Jelezko, J. Wrachtrup, and L. C. L. Hollenberg, *The nitrogen-vacancy colour centre in diamond*, Physics Reports **528**, 1 (2013).

[21] G. Balasubramanian, P. Neumann, D. Twitchen, M. Markham, R. Kolesov, N. Mizuochi, J. Isoya, J. Achard, J. Beck, J. Tissler, V. Jacques, P. R. Hemmer, F. Jelezko, and J. Wrachtrup, *Ultralong spin coherence time in isotopically engineered diamond*, Nature Mater **8**, 383 (2009).

[22] N. Bar-Gill, L. M. Pham, A. Jarmola, D. Budker, and R. L. Walsworth, *Solid-state electronic spin coherence time approaching one second*, Nature Communications **4**, 1743 (2013).

[23] T. A. Kennedy, J. S. Colton, J. E. Butler, R. C. Linares, and P. J. Doering, *Long coherence times at 300 K for nitrogen-vacancy center spins in diamond grown by chemical vapor deposition*, Appl. Phys. Lett. **83**, 4190 (2003).

[24] J. Harrison, M. J. Sellars, and N. B. Manson, *Optical spin polarisation of the N-V centre in diamond*, Journal of Luminescence **107**, 245 (2004).

[25] J.-P. Tetienne, L. Rondin, P. Spinicelli, M. Chipaux, T. Debuisschert, J.-F. Roch, and V. Jacques, *Magnetic-field-dependent photodynamics of single NV defects in diamond: an application to qualitative all-optical magnetic imaging*, New J. Phys. **14**, 103033 (2012).

[26] A. Gruber, A. Dräbenstedt, C. Tietz, L. Fleury, J. Wrachtrup, and C. v. Borczyskowski, *Scanning Confocal Optical Microscopy and Magnetic Resonance on Single Defect Centers*, Science **276**, 2012 (1997).

[27] P. Maletinsky, S. Hong, M. S. Grinolds, B. Hausmann, M. D. Lukin, R. L. Walsworth, M. Loncar, and A. Yacoby, *A robust scanning diamond sensor for nanoscale imaging with single nitrogen-vacancy centres*, Nature Nanotechnology **7**, 320 (2012).

[28] M. Fujiwara, S. Sun, A. Dohms, Y. Nishimura, K. Suto, Y. Takezawa, K. Oshimi, L. Zhao, N. Sadzak, Y. Umehara, Y. Teki, N. Komatsu, O. Benson, Y. Shikano, and E. Kage-Nakadai, *Real-time nanodiamond thermometry probing in vivo thermogenic responses*, Sci Adv **6**, eaba9636 (2020).

[29] V. Jacques, P. Neumann, J. Beck, M. Markham, D. Twitchen, J. Meijer, F. Kaiser, G. Balasubramanian, F. Jelezko, and J. Wrachtrup, *Dynamic Polarization of Single Nuclear Spins by Optical Pumping of Nitrogen-Vacancy Color Centers in Diamond at Room Temperature*, Phys. Rev. Lett. **102**, 057403 (2009).

[30] A. Jarmola, I. Fescenko, V. M. Acosta, M. W. Doherty, F. K. Fatemi, T. Ivanov, D. Budker, and V. S. Malinovsky, *Robust optical readout and characterization of nuclear spin transitions in nitrogen-vacancy ensembles in diamond*, Phys. Rev. Research **2**, 023094 (2020).

[31] M. Pfender, N. Aslam, P. Simon, D. Antonov, G. Thiering, S. Burk, F. Fávaro de Oliveira, A. Denisenko, H. Fedder, J. Meijer, J. A. Garrido, A. Gali, T. Teraji, J. Isoya, M. W. Doherty, A. Alkauskas, A. Gallo, A. Grüneis, P. Neumann, and J. Wrachtrup, *Protecting a Diamond Quantum Memory by Charge State Control*, Nano Lett. **17**, 5931 (2017).

[32] G. Waldherr, J. Beck, P. Neumann, R. S. Said, M. Nitsche, M. L. Markham, D. J. Twitchen, J. Twamley, F. Jelezko, and J. Wrachtrup, *High-dynamic-range magnetometry with a single nuclear spin in diamond*, Nature Nanotech **7**, 105 (2012).

[33] O. Sahin, E. de Leon Sanchez, S. Conti, A. Akkiraju, P. Reshetikhin, E. Druga, A. Aggarwal, B. Gilbert, S. Bhave, and A. Ajoy, *High field magnetometry with hyperpolarized nuclear spins*, Nat Commun **13**, 5486 (2022).

[34] A. Ajoy and P. Cappellaro, *Stable three-axis nuclear-spin gyroscope in diamond*, Phys. Rev. A **86**, 062104 (2012).

[35] A. Jarmola, S. Lourette, V. M. Acosta, A. G. Birdwell, P. Blümler, D. Budker, T. Ivanov, and V. S. Malinovsky, *Demonstration of diamond nuclear spin gyroscope*, Science Advances **7**, eabl3840 (2021).

[36] G. de Lange, Z. H. Wang, D. Ristè, V. V. Dobrovitski, and R. Hanson, *Universal Dynamical Decoupling of a Single Solid-State Spin from a Spin Bath*, Science **330**, 60 (2010).

[37] B. Naydenov, F. Dolde, L. T. Hall, C. Shin, H. Fedder, L. C. L. Hollenberg, F. Jelezko, and J. Wrachtrup, *Dynamical decoupling of a single-electron spin at room temperature*, Phys. Rev. B **83**, 081201 (2011).

[38] M. J. Biercuk, A. C. Doherty, and H. Uys, *Dynamical decoupling sequence construction as a filter-design problem*, J. Phys. B: At. Mol. Opt. Phys. **44**, 154002 (2011).

[39] A. Lazariev, S. Arroyo-Camejo, G. Rahane, V. K. Kavatamane, and G. Balasubramanian, *Dynamical sensitivity control of a single-spin quantum sensor*, Sci Rep **7**, 6586 (2017).

[40] C. A. Ryan, J. S. Hodges, and D. G. Cory, *Robust Decoupling Techniques to Extend Quantum Coherence in Diamond*, Phys. Rev. Lett. **105**, 200402 (2010).

[41] B. Myers, A. Das, M. Dartiailh, K. Ohno, D. Awschalom, and A. Bleszynski Jayich, *Probing Surface Noise with Depth-Calibrated Spins in Diamond*, Phys. Rev. Lett. **113**, 027602 (2014).

[42] Y. Romach, C. Müller, T. Unden, L. Rogers, T. Isoda, K. Itoh, M. Markham, A. Stacey, J. Meijer, S. Pezzagna, B. Naydenov, L. McGuinness, N. Bar-Gill, and F. Jelezko, *Spectroscopy of Surface-Induced Noise Using Shallow Spins in Diamond*, Phys. Rev. Lett. **114**, 017601 (2015).

[43] D. B. Bucher, D. P. L. Aude Craik, M. P. Backlund, M. J. Turner, O. Ben Dor, D. R. Glenn, and R. L. Walsworth, *Quantum diamond spectrometer for nanoscale NMR and ESR spectroscopy*, Nat Protoc **14**, 2707 (2019).

[44] R. D. Allert, K. D. Briegel, and D. B. Bucher, *Advances in nano- and microscale NMR spectroscopy using diamond quantum sensors*, Chem. Commun. **58**, 8165 (2022).

[45] K. S. Liu, A. Henning, M. W. Heindl, R. D. Allert, J. D. Bartl, I. D. Sharp, R. Rizzato, and D. B. Bucher, *Surface NMR using quantum sensors in diamond*, Proceedings of the National Academy of Sciences **119**, e2111607119 (2022).

[46] J. M. Abendroth, K. Herb, E. Janitz, T. Zhu, L. A. Völker, and C. L. Degen, *Single-Nitrogen–Vacancy NMR of Amine-Functionalized Diamond Surfaces*, Nano Lett. **22**, 7294 (2022).

[47] H. J. Mamin, M. Kim, M. H. Sherwood, C. T. Rettner, K. Ohno, D. D. Awschalom, and D. Rugar, *Nanoscale Nuclear Magnetic Resonance with a Nitrogen-Vacancy Spin Sensor*, Science **339**, 557 (2013).

[48] I. Lovchinsky, A. O. Sushkov, E. Urbach, N. P. de Leon, S. Choi, K. De Greve, R. Evans, R. Gertner, E. Bersin, C. Müller, L. McGuinness, F. Jelezko, R. L. Walsworth, H. Park, and M. D. Lukin, *Nuclear magnetic resonance detection and spectroscopy of single proteins using quantum logic*, Science **351**, 836 (2016).

[49] M. Kost, J. Cai, and M. B. Plenio, *Resolving single molecule structures with Nitrogen-vacancy centers in diamond*, Sci Rep **5**, 11007 (2015).

[50] C. Müller, X. Kong, J.-M. Cai, K. Melentijević, A. Stacey, M. Markham, D. Twitchen, J. Isoya, S. Pezzagna, J. Meijer, J. F. Du, M. B. Plenio, B. Naydenov, L. P. McGuinness, and F. Jelezko, *Nuclear magnetic resonance spectroscopy with single spin sensitivity*, Nature Communications **5**, 1 (2014).

[51] L. M. Pham, S. J. DeVience, F. Casola, I. Lovchinsky, A. O. Sushkov, E. Bersin, J. Lee, E. Urbach, P. Cappellaro, H. Park, A. Yacoby, M. Lukin, and R. L. Walsworth, *NMR technique for determining the depth of shallow nitrogen-vacancy centers in diamond*, Physical Review B **93** (2016).

[52] S. Castelletto, L. Rosa, J. Blackledge, M. Z. Al Abri, and A. Boretti, *Advances in diamond nanofabrication for ultrasensitive devices*, Microsyst Nanoeng **3**, 1 (2017).

[53] E. Janitz, K. Herb, L. A. Völker, W. S. Huxter, C. L. Degen, and J. M. Abendroth, *Diamond surface engineering for molecular sensing with nitrogen—vacancy centers*, J. Mater. Chem. C **10**, 13533 (2022).

[54] L. Jiang, J. S. Hodges, J. R. Maze, P. Maurer, J. M. Taylor, D. G. Cory, P. R. Hemmer, R. L. Walsworth, A. Yacoby, A. S. Zibrov, and M. D. Lukin, *Repetitive Readout of a Single Electronic Spin via Quantum Logic with Nuclear Spin Ancillae*, Science **326**, 267 (2009).

[55] B. Shields, Q. Unterreithmeier, N. de Leon, H. Park, and M. Lukin, *Efficient Readout of a Single Spin State in Diamond via Spin-to-Charge Conversion*, Phys. Rev. Lett. **114**, 136402 (2015).

[56] D. A. Hopper, R. R. Grote, S. M. Parks, and L. C. Bassett, *Amplified Sensitivity of Nitrogen-Vacancy Spins in Nanodiamonds Using All-Optical Charge Readout*, ACS Nano **12**, 4678 (2018).

[57] D. Hopper, H. Shulevitz, L. Bassett, D. A. Hopper, H. J. Shulevitz, and L. C. Bassett, *Spin Readout Techniques of the Nitrogen-Vacancy Center in Diamond*, Micromachines **9**, 437 (2018).

[58] V. M. Acosta, E. Bauch, M. P. Ledbetter, C. Santori, K.-M. C. Fu, P. E. Barclay, R. G. Beausoleil, H. Linget, J. F. Roch, F. Treussart, S. Chemerisov, W. Gawlik, and D. Budker, *Diamonds with a high density of nitrogen-vacancy centers for magnetometry applications*, Phys. Rev. B **80**, 115202 (2009).

[59] B. L. Dwyer, L. V. Rodgers, E. K. Urbach, D. Bluvstein, S. Sangtawesin, H. Zhou, Y. Nassab, M. Fitzpatrick, Z. Yuan, K. De Greve, E. L. Peterson, H. Knowles, T. Sumarac, J.-P. Chou, A. Gali, V. Dobrovitski, M. D. Lukin, and N. P. de Leon, *Probing Spin Dynamics on Diamond Surfaces Using a Single Quantum Sensor*, PRX Quantum **3**, 040328 (2022).

[60] J.-P. Tetienne, R. W. de Gille, D. A. Broadway, T. Teraji, S. E. Lillie, J. M. McCoey, N. Dontschuk, L. T. Hall, A. Stacey, D. A. Simpson, and L. C. L. Hollenberg, *Spin properties of dense near-surface ensembles of nitrogen-vacancy centers in diamond*, Phys. Rev. B **97**, 085402 (2018).

[61] A. Healey, L. Hall, G. White, T. Teraji, M.-A. Sani, F. Separovic, J.-P. Tetienne, and L. Hollenberg, *Polarization Transfer to External Nuclear Spins Using Ensembles of Nitrogen-Vacancy Centers*, Phys. Rev. Appl. **15**, 054052 (2021).

[62] Z. Yuan, M. Fitzpatrick, L. V. H. Rodgers, S. Sangtawesin, S. Srinivasan, and N. P. de Leon, *Charge state dynamics and optically detected electron spin resonance contrast of shallow nitrogen-vacancy centers in diamond*, Phys. Rev. Res. **2**, 033263 (2020).

[63] K. Ohashi, T. Rosskopf, H. Watanabe, M. Loretz, Y. Tao, R. Hauert, S. Tomizawa, T. Ishikawa, J. Ishi-Hayase, S. Shikata, C. L. Degen, and K. M. Itoh, *Negatively Charged Nitrogen-Vacancy Centers in a 5 nm Thin 12C Diamond Film*, Nano Lett. **13**, 4733 (2013).

[64] J. D. A. Wood, J.-P. Tetienne, D. A. Broadway, L. T. Hall, D. A. Simpson, A. Stacey, and L. C. L. Hollenberg, *Microwave-free nuclear magnetic resonance at molecular scales*, Nat Commun **8**, 15950 (2017).

[65] R. Fukuda, P. Balasubramanian, I. Higashimata, G. Koike, T. Okada, R. Kagami, T. Teraji, S. Onoda, M. Haruyama, K. Yamada, M. Inaba, H. Yamano, F. M. Stürner, S. Schmitt, L. P. McGuinness, F. Jelezko, T. Ohshima, T. Shinada, H. Kawarada, W. Kada, O. Hanaizumi, T. Tanii, and J. Isoya, *Lithographically engineered shallow nitrogen-vacancy centers in diamond for external nuclear spin sensing*, New J. Phys. **20**, 083029 (2018).

[66] M. Loretz, S. Pezzagna, J. Meijer, and C. L. Degen, *Nanoscale nuclear magnetic resonance with a 1.9-nm-deep nitrogen-vacancy sensor*, Appl. Phys. Lett. **104**, 033102 (2014).

[67] S. J. DeVience, L. M. Pham, I. Lovchinsky, A. O. Sushkov, N. Bar-Gill, C. Belthangady, F. Casola, M. Corbett, H. Zhang, M. Lukin, H. Park, A. Yacoby, and R. L. Walsworth, *Nanoscale NMR spectroscopy and imaging of multiple nuclear species*, Nature Nanotech **10**, 129 (2015).

[68] Z. Xu, M. L. Palm, W. Huxter, K. Herb, J. M. Abendroth, K. Bouzehouane, O. Boulle, M. S. Gabor, J. Urrestarazu Larranaga, A. Morales, J. Rhensius, G. Puebla-Hellmann, and C. L. Degen, *Minimizing Sensor-Sample Distances in Scanning Nitrogen-Vacancy Magnetometry*, ACS Nano **19**, 8255 (2025).

[69] D. Bluvstein, Z. Zhang, and A. C. B. Jayich, *Identifying and Mitigating Charge Instabilities in Shallow Diamond Nitrogen-Vacancy Centers*, Phys. Rev. Lett. **122**, 076101 (2019).

[70] J. R. Maze, A. Gali, E. Togan, Y. Chu, A. Trifonov, E. Kaxiras, and M. D. Lukin, *Properties of nitrogen-vacancy centers in diamond: the group theoretic approach*, New J. Phys. **13**, 025025 (2011).

[71] A. Gali, *Ab initio theory of the nitrogen-vacancy center in diamond*, Nanophotonics **8**, 1907 (2019).

[72] A. Gali, M. Fyta, and E. Kaxiras, *Ab initio supercell calculations on nitrogen-vacancy center in diamond: Electronic structure and hyperfine tensors*, Phys. Rev. B **77**, 155206 (2008).

[73] L. J. Rogers, R. L. McMurtrie, M. J. Sellars, and N. B. Manson, *Time-averaging within the excited state of the nitrogen-vacancy centre in diamond*, New J. Phys. **11**, 063007 (2009).

[74] G. Davies, M. F. Hamer, and W. C. Price, *Optical studies of the 1.945 eV vibronic band in diamond*, Proceedings of the Royal Society of London. A. Mathematical and Physical Sciences **348**, 285 (1997).

[75] L. J. Rogers, S. Armstrong, M. J. Sellars, and N. B. Manson, *Infrared emission of the NV centre in diamond: Zeeman and uniaxial stress studies*, New J. Phys. **10**, 103024 (2008).

[76] R. Giri, R. H. Jensen, D. Khurana, J. Bocquel, I. P. Radko, J. Lang, C. Osterkamp, F. Jelezko, K. Berg-Sorensen, U. L. Andersen, and A. Huck, *Charge Stability and Charge-State-Based Spin Readout of Shallow Nitrogen-Vacancy Centers in Diamond*, ACS Appl. Electron. Mater. **5**, 6603 (2023).

[77] G. Davies, S. C. Lawson, A. T. Collins, A. Mainwood, and S. J. Sharp, *Vacancy-related centers in diamond*, Phys. Rev. B **46**, 13157 (1992).

[78] J. H. N. Loubser and J. A. v. Wyk, *Electron spin resonance in the study of diamond*, Rep. Prog. Phys. **41**, 1201 (1978).

[79] G. D. Fuchs, V. V. Dobrovitski, R. Hanson, A. Batra, C. D. Weis, T. Schenkel, and D. D. Awschalom, *Excited-State Spectroscopy Using Single Spin Manipulation in Diamond*, Phys. Rev. Lett. **101**, 117601 (2008).

[80] J. Cavanagh, W. J. Fairbrother, A. G. P. III, and N. J. Skelton, *Protein NMR Spectroscopy: Principles and Practice* (Elsevier) (1995).

[81] M. Steiner, P. Neumann, J. Beck, F. Jelezko, and J. Wrachtrup, *Universal enhancement of the optical readout fidelity of single electron spins at nitrogen-vacancy centers in diamond*, Phys. Rev. B **81**, 035205 (2010).

[82] S. Felton, A. M. Edmonds, M. E. Newton, P. M. Martineau, D. Fisher, D. J. Twitchen, and J. M. Baker, *Hyperfine interaction in the ground state of the negatively charged nitrogen vacancy center in diamond*, Phys. Rev. B **79**, 075203 (2009).

[83] A. Gali, *Identification of individual 13C isotopes of nitrogen-vacancy center in diamond by combining the polarization studies of nuclear spins and first-principles calculations*, Phys. Rev. B **80**, 241204 (2009).

[84] Y. Ting and D. Williams, *Nuclear Gyromagnetic Ratios. IV*, Physical Review **89**, 595 (1953).

[85] G. Thiering and A. Gali, *Theory of the optical spin-polarization loop of the nitrogen-vacancy center in diamond*, Phys. Rev. B **98**, 085207 (2018).

[86] R. Fischer, A. Jarmola, P. Kehayias, and D. Budker, *Optical polarization of nuclear ensembles in diamond*, Phys. Rev. B **87**, 125207 (2013).

[87] M. L. Goldman, M. W. Doherty, A. Sipahigil, N. Y. Yao, S. D. Bennett, N. B. Manson, A. Kubanek, and M. D. Lukin, *State-selective intersystem crossing in nitrogen-vacancy centers*, Phys. Rev. B **91**, 165201 (2015).

[88] M. Goldman, A. Sipahigil, M. Doherty, N. Yao, S. Bennett, M. Markham, D. Twitchen, N. Manson, A. Kubanek, and M. Lukin, *Phonon-Induced Population Dynamics and Intersystem Crossing in Nitrogen-Vacancy Centers*, Phys. Rev. Lett. **114**, 145502 (2015).

[89] L. Robledo, H. Bernien, T. v. d. Sar, and R. Hanson, *Spin dynamics in the optical cycle of single nitrogen-vacancy centres in diamond*, New J. Phys. **13**, 025013 (2011).

[90] A. Gupta, L. Hacquebard, and L. Childress, *Efficient signal processing for time-resolved fluorescence detection of nitrogen-vacancy spins in diamond*, J. Opt. Soc. Am. B, JOSAB **33**, B28 (2016).

[91] C. Zhang, F. Shagieva, M. Widmann, M. Kübler, V. Vorobyov, P. Kapitanova, E. Nenasheva, R. Corkill, O. Rhrle, K. Nakamura, H. Sumiya, S. Onoda, J. Isoya, and J. Wrachtrup, *Diamond Magnetometry and Gradiometry Towards Subpicotesla dc Field Measurement*, Phys. Rev. Applied **15**, 064075 (2021).

[92] N. B. Manson, J. P. Harrison, and M. J. Sellars, *Nitrogen-vacancy center in diamond: Model of the electronic structure and associated dynamics*, Phys. Rev. B **74**, 104303 (2006).

[93] A. Batalov, C. Zierl, T. Gaebel, P. Neumann, I.-Y. Chan, G. Balasubramanian, P. R. Hemmer, F. Jelezko, and J. Wrachtrup, *Temporal Coherence of Photons Emitted by Single Nitrogen-Vacancy Defect Centers in Diamond Using Optical Rabi-Oscillations*, Phys. Rev. Lett. **100**, 077401 (2008).

[94] V. M. Acosta, A. Jarmola, E. Bauch, and D. Budker, *Optical properties of the nitrogen-vacancy singlet levels in diamond*, Phys. Rev. B **82**, 201202 (2010).

[95] E. Van Oort and M. Glasbeek, *Electric-field-induced modulation of spin echoes of N-V centers in diamond*, Chemical Physics Letters **168**, 529 (1990).

[96] L. Rondin, J.-P. Tetienne, T. Hingant, J.-F. Roch, P. Maletinsky, and V. Jacques, *Magnetometry with nitrogen-vacancy defects in diamond*, Rep. Prog. Phys. **77**, 056503 (2014).

[97] S. Hong, M. S. Grinolds, L. M. Pham, D. L. Sage, L. Luan, R. L. Walsworth, and A. Yacoby, *Nanoscale magnetometry with NV centers in diamond*, MRS Bulletin **38**, 155 (2013).

[98] A. Boretti, L. Rosa, J. Blackledge, and S. Castelletto, *Nitrogen-vacancy centers in diamond for nanoscale magnetic resonance imaging applications*, Beilstein J. Nanotechnol. **10**, 2128 (2019).

[99] J. F. Barry, J. M. Schloss, E. Bauch, M. J. Turner, C. A. Hart, L. M. Pham, and R. L. Walsworth, *Sensitivity optimization for NV-diamond magnetometry*, Rev. Mod. Phys. **92**, 015004 (2020).

[100] A. Dréau, M. Lesik, L. Rondin, P. Spinicelli, O. Arcizet, J.-F. Roch, and V. Jacques, *Avoiding power broadening in optically detected magnetic resonance of single NV defects for enhanced dc magnetic field sensitivity*, Phys. Rev. B **84**, 195204 (2011).

[101] J. R. Maze, A. Dréau, V. Waselowski, H. Duarte, J.-F. Roch, and V. Jacques, *Free induction decay of single spins in diamond*, New J. Phys. **14**, 103041 (2012).

[102] M. Kim, H. Mamin, M. Sherwood, K. Ohno, D. Awschalom, and D. Rugar, *Decoherence of Near-Surface Nitrogen-Vacancy Centers Due to Electric Field Noise*, Phys. Rev. Lett. **115**, 087602 (2015).

[103] T. Rosskopf, A. Dussaux, K. Ohashi, M. Loretz, R. Schirhagl, H. Watanabe, S. Shikata, K. Itoh, and C. Degen, *Investigation of Surface Magnetic Noise by Shallow Spins in Diamond*, Phys. Rev. Lett. **112**, 147602 (2014).

[104] C. Slichter, *Principles of Magnetic Resonance*, Springer Series in Solid-State Sciences **2** (1980).

[105] J. Kowalewski and L. Mäler, *Nuclear Spin Relaxation in Liquids*, Series in Chemical Physics (Taylor & Frances, New York) **2** (2006).

[106] P. S. Hubbard, *Nuclear Magnetic Relaxation by Intermolecular Dipole-Dipole Interactions*, Phys. Rev. **131**, 275 (1963).

[107] J. Gugler, T. Astner, A. Angerer, J. Schmiedmayer, J. Majer, and P. Mohn, *Ab initio calculation of the spin lattice relaxation time T1 for nitrogen-vacancy centers in diamond*, Phys. Rev. B **98**, 214442 (2018).

[108] A. G. Redfield, *On the Theory of Relaxation Processes*, IBM Journal of Research and Development **1**, 19 (1957).

[109] M. Cambria, A. Norambuena, H. Dinani, G. Thiering, A. Gardill, I. Kemeny, Y. Li, V. Lordi, A. Gali, J. Maze, and S. Kolkowitz, *Temperature-Dependent Spin-Lattice Relaxation of the Nitrogen-Vacancy Spin Triplet in Diamond*, Phys. Rev. Lett. **130**, 256903 (2023).

[110] A. Jarmola, V. M. Acosta, K. Jensen, S. Chemerisov, and D. Budker, *Temperature- and Magnetic-Field-Dependent Longitudinal Spin Relaxation in Nitrogen-Vacancy Ensembles in Diamond*, Phys. Rev. Lett. **108**, 197601 (2012).

[111] L. Cywinski, R. M. Lutchyn, C. P. Nave, and S. Das Sarma, *How to enhance dephasing time in superconducting qubits*, Phys. Rev. B **77**, 174509 (2008).

[112] L. Childress, M. V. Gurudev Dutt, J. M. Taylor, A. S. Zibrov, F. Jelezko, J. Wrachtrup, P. R. Hemmer, and M. D. Lukin, *Coherent Dynamics of Coupled Electron and Nuclear Spin Qubits in Diamond*, Science **314**, 281 (2006).

[113] E. L. Hahn, *Spin Echoes*, Phys. Rev. **80**, 580 (1950).

[114] H. Y. Carr and E. M. Purcell, *Effects of Diffusion on Free Precession in Nuclear Magnetic Resonance Experiments*, Phys. Rev. **94**, 630 (1954).

[115] T. Gullion, D. B. Baker, and M. S. Conradi, *New, compensated Carr-Purcell sequences*, Journal of Magnetic Resonance (1969) **89**, 479 (1990).

[116] C. J. Lee, D. Suter, and A. Pines, *Theory of multiple-pulse NMR at low and zero fields*, Journal of Magnetic Resonance (1969) **75**, 110 (1987).

[117] A. M. Souza, G. A. Álvarez, and D. Suter, *Robust Dynamical Decoupling for Quantum Computing and Quantum Memory*, Phys. Rev. Lett. **106**, 240501 (2011).

[118] J. Medford, L. Cywinski, C. Barthel, C. M. Marcus, M. P. Hanson, and A. C. Gossard, *Scaling of Dynamical Decoupling for Spin Qubits*, Phys. Rev. Lett. **108**, 086802 (2012).

[119] M. Loretz, J. Boss, T. Rosskopf, H. Mamin, D. Rugar, and C. Degen, *Spurious Harmonic Response of Multipulse Quantum Sensing Sequences*, Phys. Rev. X **5**, 021009 (2015).

[120] T. Staudacher, F. Shi, S. Pezzagna, J. Meijer, J. Du, C. A. Meriles, F. Reinhard, and J. Wrachtrup, *Nuclear Magnetic Resonance Spectroscopy on a (5-Nanometer)* ^{3} *Sample Volume*, Science **339**, 561 (2013).

[121] M. Loretz, T. Rosskopf, and C. L. Degen, *Radio-Frequency Magnetometry Using a Single Electron Spin*, Phys. Rev. Lett. **110**, 017602 (2013).

[122] F. Yan, S. Gustavsson, J. Bylander, X. Jin, F. Yoshihara, D. G. Cory, Y. Nakamura, T. P. Orlando, and W. D. Oliver, *Rotating-frame relaxation as a noise spectrum analyser of a superconducting qubit undergoing driven evolution*, Nature Communications **4**, 2337 (2013).

[123] S. R. Hartmann and E. L. Hahn, *Nuclear Double Resonance in the Rotating Frame*, Phys. Rev. **128**, 2042 (1962).

[124] D. Spielman, *In Vivo MR: Relaxation Theory and Contrast Mechanisms*, Lecture **7-11** (2019).

[125] A. Wickenbrock, H. Zheng, L. Bougas, N. Leefer, S. Afach, A. Jarmola, V. M. Acosta, and D. Budker, *Microwave-free magnetometry with nitrogen-vacancy centers in diamond*, Appl. Phys. Lett. **109**, 053505 (2016).

[126] H. Zheng, Z. Sun, G. Chatzidrosos, C. Zhang, K. Nakamura, H. Sumiya, T. Ohshima, J. Isoya, J. Wrachtrup, A. Wickenbrock, and D. Budker, *Microwave-Free Vector Magnetometry with Nitrogen-Vacancy Centers along a Single Axis in Diamond*, Phys. Rev. Applied **13**, 044023 (2020).

[127] C. Cohen-Tannoudji, J. Dupont-Roc, and G. Grynberg, *Atom-Photon Interactions: Basic Processes and Applications* (Wiley), , complement B1, page 45 (1998).

[128] J. H. Choi, *Partitioning Method and Van Vleck's Perturbation Theory*, Progress of Theoretical Physics **53**, 1641 (1975).

[129] M. Chen, M. Hirose, and P. Cappellaro, *Measurement of transverse hyperfine interaction by forbidden transitions*, Phys. Rev. B **92**, 020101 (2015).

[130] S. Knecht, A. N. Pravdivtsev, J.-B. Hövener, A. V. Yurkovskaya, and K. L. Ivanov, *Quantitative description of the SABRE process: rigorous consideration of spin dynamics and chemical exchange*, RSC Adv. **6**, 24470 (2016).

[131] D. Budker and M. Romalis, *Optical magnetometry*, Nature Phys **3**, 227 (2007).

[132] S. Sangtawesin, C. A. McLellan, B. A. Myers, A. C. B. Jayich, D. D. Awschalom, and J. R. Petta, *Hyperfine-enhanced gyromagnetic ratio of a nuclear spin in diamond*, New J. Phys. **18**, 083016 (2016).

[133] M. H. Metsch, K. Senkalla, B. Tratzmiller, J. Scheuer, M. Kern, J. Achard, A. Tallaire, M. B. Plenio, P. Siyushev, and F. Jelezko, *Initialization and Readout of Nuclear Spins via a Negatively Charged Silicon-Vacancy Center in Diamond*, Phys. Rev. Lett. **122**, 190503 (2019).

[134] D. A. Broadway, S. E. Lillie, N. Dontschuk, A. Stacey, L. T. Hall, J.-P. Tetienne, and L. C. L. Hollenberg, *High precision single qubit tuning via thermo-magnetic field control*, Appl. Phys. Lett. **112**, 103103 (2018).

[135] G. Chatzidrosos, *A perfect imperfection: Quantum magnetometry and applications using nitrogen-vacancy defects in diamond*, Ph.D. thesis, Johannes Gutenberg-Universität Mainz (2021).

[136] N. El-Sheimy and A. Youssef, *Inertial sensors technologies for navigation applications: state of the art and future trends*, Satellite Navigation **1**, 2 (2020).

[137] R. Patel, L. Zhou, A. Frangeskou, G. Stimpson, B. Breeze, A. Nikitin, M. Dale, E. Nichols, W. Thornley, B. Green, M. Newton, A. Edmonds, M. Markham, D. Twitchen, and G. Morley, *Subnanotesla Magnetometry with a Fiber-Coupled Diamond Sensor*, Phys. Rev. Applied **14**, 044058 (2020).

[138] I. I. Rabi, J. R. Zacharias, S. Millman, and P. Kusch, *A New Method of Measuring Nuclear Magnetic Moment*, Phys. Rev. **53**, 318 (1938).

[139] R. R. Ernst, G. Bodenhausen, and A. Wokaun, *Principles of Nuclear Magnetic Resonance in One and Two Dimensions*, (Clarendon Press) (1990).

[140] P. Glover and S. P. Mansfield, *Limits to magnetic resonance microscopy*, Rep. Prog. Phys. **65**, 1489 (2002).

[141] S. Sangtawesin, B. L. Dwyer, S. Srinivasan, J. J. Allred, L. V. Rodgers, K. De Greve, A. Stacey, N. Dontschuk, K. M. O Donnell, D. Hu, D. A. Evans, C. Jaye, D. A. Fischer, M. L. Markham, D. J. Twitchen, H. Park, M. D. Lukin, and N. P. de Leon, *Origins of Diamond Surface Noise Probed by Correlating Single-Spin Measurements with Surface Spectroscopy*, Phys. Rev. X **9**, 031052 (2019).

[142] W. Zheng, S. Zhang, J. Jiang, Y. He, R. Stöhr, A. Denisenko, J. Wrachtrup, X. C. Zeng, K. Bian, E.-G. Wang, and Y. Jiang, *Observation of liquid-solid transition of nanoconfined water at ambient temperature*, (arXiv:2412.15001) (2024).

[143] P. Fernández-Acebal and M. B. Plenio, *Sensing phases of water via nitrogen-vacancy centres in diamond*, Sci Rep **8**, 13453 (2018).

[144] F. Bruckmaier, R. D. Allert, N. R. Neuling, P. Amrein, S. Littin, K. D. Briegel, P. Schätzle, P. Knittel, M. Zaitsev, and D. B. Bucher, *Imaging local diffusion in microstructures using NV-based pulsed field gradient NMR*, Science Advances **9**, eadh3484 (2023).

[145] M. Holz, S. R. Heil, and A. Sacco, *Temperature-dependent self-diffusion coefficients of water and six selected molecular liquids for calibration in accurate 1H NMR PFG measurements*, Phys. Chem. Chem. Phys. **2**, 4740 (2000).

[146] R. Mills, *Self-diffusion in normal and heavy water in the range 1-45.deg.*, J. Phys. Chem. **77**, 685 (1973).

[147] Z. Li, X. Kong, H. Sun, G. Qu, P. Yu, T. Xie, Z. Zhao, G. Shi, Y. Wang, F. Shi, and J. Du, *Discovery of an anomalous non-evaporating sub-nanometre water layer in open environment*, (arXiv:2412.17636) (2024).

[148] Z.-H. Zhang, J. A. Zuber, L. V. Rodgers, X. Gui, P. Stevenson, M. Li, M. Batzer, M. Grimau Puigibert, B. J. Shields, A. M. Edmonds, N. Palmer, M. L. Markham, R. J. Cava, P. Maletinsky, and N. P. de Leon, *Neutral Silicon Vacancy Centers in Undoped Diamond via Surface Control*, Phys. Rev. Lett. **130**, 166902 (2023).

[149] M. V. Hauf, B. Grotz, B. Naydenov, M. Dankerl, S. Pezzagna, J. Meijer, F. Jelezko, J. Wrachtrup, M. Stutzmann, F. Reinhard, and J. A. Garrido, *Chemical control of the charge state of nitrogen-vacancy centers in diamond*, Phys. Rev. B **83**, 081304 (2011).

[150] M. Kaviani, P. Deak, B. Aradi, T. Frauenheim, J.-P. Chou, and A. Gali, *Proper Surface Termination for Luminescent Near-Surface NV Centers in Diamond*, Nano Lett. **14**, 4772 (2014).

[151] B. M. Nichols, J. E. Butler, J. N. Russell, and R. J. Hamers, *Photochemical Functionalization of Hydrogen-Terminated Diamond Surfaces: A Structural and Mechanistic Study*, J. Phys. Chem. B **109**, 20938 (2005).

[152] L. V. H. Rodgers, S. T. Nguyen, J. H. Cox, K. Zervas, Z. Yuan, S. Sangtawesin, A. Stacey, C. Jaye, C. Weiland, A. Pershin, A. Gali, L. Thomsen, S. A. Meynell, L. B. Hughes, A. C. B. Jayich, X. Gui, R. J. Cava, R. R. Knowles, and N. P. de Leon, *Diamond surface functionalization via visible light–driven C–H activation for nanoscale quantum sensing*, Proceedings of the National Academy of Sciences **121**, e2316032121 (2024).

[153] J. A. Zuber, *Optical spectroscopy of shallow silicon vacancy centers in diamond nanostructures*, Thesis, University of Basel (2024).

[154] N. Stojilovic, *Why Can't We See Hydrogen in X-ray Photoelectron Spectroscopy?*, J. Chem. Educ. **89**, 1331 (2012).

[155] O. R. Opaluch, N. Oshnik, R. Nelz, and E. Neu, *Optimized Planar Microwave Antenna for Nitrogen Vacancy Center Based Sensing Applications*, Nanomaterials **11**, 2108 (2021).

[156] J. C. Hermann, R. Rizzato, F. Bruckmaier, R. D. Allert, A. Blank, and D. B. Bucher, *Extending radiowave frequency detection range with dressed states of solid-state spin ensembles*, npj Quantum Inf **10**, 1 (2024).

[157] J. D. A. Wood, D. A. Broadway, L. T. Hall, A. Stacey, D. A. Simpson, J.-P. Tetienne, and L. C. L. Hollenberg, *Wide-band nanoscale magnetic resonance spectroscopy using quantum relaxation of a single spin in diamond*, Physical Review B **94** (2016).

[158] T. Ishikawa, A. Yoshizawa, Y. Mawatari, H. Watanabe, and S. Kashiwaya, *Influence of Dynamical Decoupling Sequences with Finite-Width Pulses on Quantum Sensing for AC Magnetometry*, Phys. Rev. Appl. **10**, 054059 (2018).

[159] J. Casanova, Z.-Y. Wang, J. F. Haase, and M. B. Plenio, *Robust dynamical decoupling sequences for individual-nuclear-spin addressing*, Phys. Rev. A **92**, 042304 (2015).

[160] Z.-Y. Wang, J. E. Lang, S. Schmitt, J. Lang, J. Casanova, L. McGuinness, T. S. Monteiro, F. Jelezko, and M. B. Plenio, *Randomization of Pulse Phases for Unambiguous and Robust Quantum Sensing*, Phys. Rev. Lett. **122**, 200403 (2019).

[161] Z. Wang, J. Casanova, and M. B. Plenio, *Enhancing the Robustness of Dynamical Decoupling Sequences with Correlated Random Phases*, Symmetry **12**, 730 (2020).

[162] K. Zeng, X. Yu, M. B. Plenio, and Z.-Y. Wang, *Wide-Band Unambiguous Quantum Sensing via Geodesic Evolution*, Phys. Rev. Lett. **132**, 250801 (2024).

[163] I. Schwartz, J. Scheuer, B. Tratzmiller, S. Müller, Q. Chen, I. Dhand, Z.-Y. Wang, C. Müller, B. Naydenov, F. Jelezko, and M. B. Plenio, *Robust optical polarization of nuclear spin baths using Hamiltonian engineering of nitrogen-vacancy center quantum dynamics*, Science Advances **4**, eaat8978 (2018).

[164] J. M. Boss, K. S. Cujia, J. Zopes, and C. L. Degen, *Quantum sensing with arbitrary frequency resolution*, Science **356**, 837 (2017).

[165] Z. Jiang, H. Cai, R. Cernansky, X. Liu, and W. Gao, *Quantum sensing of radio-frequency signal with NV centers in SiC*, Science Advances **9**, eadg2080 (2023).

[166] L. Thiel, Z. Wang, M. A. Tschudin, D. Rohner, I. Gutiérrez-Lezama, N. Ubrig, M. Gibertini, E. Giannini, A. F. Morpurgo, and P. Maletinsky, *Probing magnetism in 2D materials at the nanoscale with single-spin microscopy*, Science **364**, 973 (2019).

[167] A. Dubois, D. Broadway, A. Stark, M. Tschudin, A. Healey, S. Huber, J.-P. Tetienne, E. Greplova, and P. Maletinsky, *Untrained Physically Informed Neural Network for Image Reconstruction of Magnetic Field Sources*, Phys. Rev. Appl. **18**, 064076 (2022).

[168] J. F. Ziegler, J. P. Biersack, and M. D. Ziegler, *SRIM: The Stopping and Range of Ions in Matter*, (SRIM) (2012).

[169] D. M. Toyli, C. D. Weis, G. D. Fuchs, T. Schenkel, and D. D. Awschalom, *Chip-Scale Nanofabrication of Single Spins and Spin Arrays in Diamond*, Nano Lett. **10**, 3168 (2010).

[170] B. E. Herzog, D. Cadeddu, F. Xue, P. Peddibhotla, and M. Poggio, *Boundary between the thermal and statistical polarization regimes in a nuclear spin ensemble*, Applied Physics Letters **105**, 043112 (2014).

[171] M. Lesik, T. Plays, A. Tallaire, J. Achard, O. Brinza, L. William, M. Chipaux, L. Toraille, T. Debuisschert, A. Gicquel, J. F. Roch, and V. Jacques, *Preferential orientation of NV defects in CVD diamond films grown on (113)-oriented substrates*, Diamond and Related Materials **56**, 47 (2015).

[172] P. Balasubramanian, C. Osterkamp, O. Brinza, M. Rollo, I. Robert-Philip, P. Goldner, V. Jacques, F. Jelezko, J. Achard, and A. Tallaire, *Enhancement of the creation yield of NV ensembles in a chemically vapour deposited diamond*, Carbon **194**, 282 (2022).

[173] Y. Chu, N. de Leon, B. Shields, B. Hausmann, R. Evans, E. Togan, M. J. Burek, M. Markham, A. Stacey, A. Zibrov, A. Yacoby, D. Twitchen, M. Loncar,

H. Park, P. Maletinsky, and M. Lukin, *Coherent Optical Transitions in Implanted Nitrogen Vacancy Centers*, Nano Lett. **14**, 1982 (2014).

[174] S. Pezzagna, B. Naydenov, F. Jelezko, J. Wrachtrup, and J. Meijer, *Creation efficiency of nitrogen-vacancy centres in diamond*, New J. Phys. **12**, 065017 (2010).

[175] T. Yamamoto, T. Umeda, K. Watanabe, S. Onoda, M. L. Markham, D. J. Twitchen, B. Naydenov, L. P. McGuinness, T. Teraji, S. Koizumi, F. Dolde, H. Fedder, J. Honert, J. Wrachtrup, T. Ohshima, F. Jelezko, and J. Isoya, *Extending spin coherence times of diamond qubits by high-temperature annealing*, Phys. Rev. B **88**, 075206 (2013).

[176] N. Hedrich, D. Rohner, M. Batzer, P. Maletinsky, and B. J. Shields, *Parabolic Diamond Scanning Probes for Single-Spin Magnetic Field Imaging*, Phys. Rev. Applied **14**, 064007 (2020).

[177] D. J. Griffiths, *Introduction to Electrodynamics* (Cambridge University Press) (2017).

Acknowledgements

I have spent the last few years of my life studying NV physics in the lab. And among all the countless things that I have learned in this exciting time, I was taught one particularly important lesson: Scientific success is always a team effort! All the results I have so proudly presented in this thesis would not have been possible if it was not for the help and support of many fantastic people, who have all contributed to this PhD project in one way or another. I would now like to take the opportunity to express my gratitude to those who have had the greatest influence on me and my research.

First of all, I sincerely thank Patrick Maletinsky. Not only were you the first to spark my interest in NV physics when I listened to your quantum optics course back in 2018, but you also gave me the opportunity to do my master's and PhD degree in your group, where you foster a pleasantly harmonious atmosphere between group members – an environment I have always greatly appreciated. Your enthusiastic and infectious fascination for science, your ability to approach scientific problems from a point of view I had not even considered, and your trust in giving me all the freedom I needed, really pushed this project forward.
The second supervisor of my PhD project is Patrick Potts. Thank you for your open ear in our yearly meetings, and for your expert opinion on how to properly model our Spin-Lock experiments. Last but not least, the third member of my doctoral committee is Dominik Bucher. I am grateful that you have agreed to be the external referee for my thesis. It is no small task to read and review such a long thesis.

The person that has had by far the largest impact on this thesis is my closest co-worker: Dear Tobias, thank you so much for tackling this project together with me. You've shown me how to handle things in a systematic, thoughtful and pragmatic way; you've taught me the importance of precise scientific language, and you were my rock when I lost track of where our project was standing and where it was (supposed to be) going. Together, we published my very first paper, laughed at xkcd comics while our magnet was aligning, and fought through experimental mishaps – I'll never forget how the two of us crawled through room 3.17 for nearly two hours, frantically searching for our precious diamond sample with our phone lights.

I owe special thanks to a few more people who have made a decisive contribution to the success of this thesis: Dear Patrik – yes, so many Patri(c)ks! – you have only

been around for the last bit of my PhD, but your inexhaustible experimental drive was such a great help in the lab. Thank you in particular for taking the lead in the deuterium experiments, where you did an outstanding job! Dear Aaron, thank you for our fantastic collaboration. Together with Patrick Potts, you have developed the mathematical framework to describe our Spin-Lock NMR experiments, and it's been a pleasure to work with someone so open-minded and flexible like you. Dear Johannes, you have supervised me before Tobias has joined the project. In this time, you've taught me everything I know about MW pulse generation, helped me fabricate my first nanopillars, and you have generously allowed me to disassemble your setup to build a new one in its place! Dear Brendan, Juanita and Silvia, thanks for the endless support with nano-fabrication, a task I neither liked nor was particularly good at. You helped me achieve good results nonetheless. Dear Clément, David and Minghao, you all weren't directly part of my specific project, yet you always had an open ear for my problems. I thank you for valuable discussions and constructive feedback. Dear Mark, thank you for teaching me the basics of laser optics, and for contributing to this PhD project with technical support for the SHFSG even after you left the university. Finally, dear Josh, we have accompanied each other throughout this near-eleven year long journey as physicists at this university, a time in which we became good friends. Together, we have tackled exams and FP experiments, discovered our passion for quantum physics, suffered through midsummer acid-cleans, and lightened up each other's mood with Schoggi-Gipfeli and Pokémon battles when things weren't going as planned. I thank you for this lovely comradeship.

Next, I'd like to cordially thank all the other wonderful people in the quantum sensing group for their valuable scientific input, interesting discussions at lunch and in the office, ice-cream breaks, great group events, lunch pick-ups, and for keeping their diamond entries up-to-date in the diamond wiki. I thank especially Tobias, but also Aaron, Clément, Josh, Minghao, Patrik and Silvia for proof-reading parts of this thesis and for providing valuable feedback. Furthermore, I thank the technical support of the university, in particular Sascha Martin and his machine shop team for manufacturing the excellent customized aluminium parts required for my experiment, and Arnold Lücke for his help in building the nitrogen gas cooling contraption.

Experimental science is a double-edged sword. As exciting and fascinating as it can be, there are days or even weeks where things in the lab just don't work out – be it data not making any sense, stuff breaking or us experimentalist making silly mistakes. I would like to thank my best friends, Kevin, Anja and Cello, for helping me deal with such frustrating and stressful periods. Thank you for listening to my problems, for spending time with me when I needed to clear my mind from brooding over work, and for cheering me up in Discord with your goofy humour after an exhaustingly long day of thesis-writing. Thanks for your friendship, it means so much to me.

Finally, I thank Andrea, my favourite person. You have accompanied me throughout my entire PhD journey; and your love and endless support have given me the strength to push through even the most difficult times. Knowing that you always believe in me, and that you will stand by my side no matter what challenges I might face next, is one of the greatest gifts in my life. For that I thank you and love you.

Curriculum Vitae

Personal Details

Name	Beat Bürgler
Date of Birth	September 22, 1994
Nationality	Switzerland

Education

2020 – 2025	University of Basel, PhD in Experimental Physics
2017 – 2020	University of Basel, Master of Science in Physics
	Master thesis in the group of Prof. P. Maletsinky
	Depth Determination of Single NV Centers *via Spin-Locked Hydrogen Sensing*
2014 – 2017	University of Basel, Bachelor of Science in Physics
	Bachelor thesis in the group of Prof. P. Maletsinky
	Towards Measuring the $T_{1\rho}$ *Spin Decay Time* *in NV Color Centers in Diamond*
2010 – 2013	Gymnasium Muttenz, Swiss Matura

Publications

[178] B. Bürgler, T.F. Sjolander, O. Brinza, A. Tallaire, J. Achard and P. Maletinsky, *All-Optical Nuclear Quantum Sensing using Nitrogen-Vacancy Centers in Diamond*, npj Quantum Information 9, 56 (2023)

[179] J. Kölbl, M. Kaspercyzk, B. Bürgler, A. Barfuss, P. Maletinsky, *Determination of intrinsic effective fields and microwave polarizations by high-resolution spectroscopy of single NV center spins*, New Journal of Physics **21**, 113039 (2019)

June 19, 2025

Dancing like Flames
After All that I've Done
I'll Salt the Earth and Disappear
In a Sea of Fire

– Lorna Shore –